

MULTISCALE PORE STRUCTURE CHARACTERIZATION AND PORE
NETWORK MODELING OF MIDDLE EAST CARBONATES

A THESIS SUBMITTED TO
THE GRADUATE SCHOOL OF NATURAL AND APPLIED SCIENCES
OF
MIDDLE EAST TECHNICAL UNIVERSITY

BY

SATI ASLI GÜNDOĞAR

IN PARTIAL FULFILLMENT OF THE REQUIREMENTS
FOR
THE DEGREE OF DOCTOR OF PHILOSOPHY
IN
THE DEPARTMENT OF PETROLEUM AND NATURAL GAS ENGINEERING

FEBRUARY 2017

Approval of the Thesis:

**MULTISCALE PORE STRUCTURE CHARACTERIZATION AND PORE
NETWORK MODELING OF MIDDLE EAST CARBONATES**

submitted by **SATI ASLI GÜNDOĞAR** in partial fulfillment of the requirements for
the degree of **Doctor of Philosophy in Petroleum and Natural Gas Engineering**
Department, Middle East Technical University by,

Prof. Dr. Gülbin Dural Ünver
Dean, Graduate School of **Natural and Applied Sciences** _____

Prof. Dr. Serhat Akin
Head of Department, **Petroleum and Natural Gas Engineering** _____

Prof. Dr. Serhat Akin
Supervisor, **Petroleum and Natural Gas Engineering Dept., METU** _____

Examining Committee Members:

Prof. Dr. Mahmut Parlaktuna
Petroleum and Natural Gas Engineering Dept., METU _____

Prof. Dr. Serhat Akin
Petroleum and Natural Gas Engineering Dept., METU _____

Prof. Dr. Nurkan Karahanoğlu
Geological Engineering Dept., METU _____

Assoc. Prof. Dr. Ö. İnanç Türeyen
Petroleum and Natural Gas Engineering Dept., ITU _____

Asst. Prof. Dr. F. Emre Artun
Petroleum and Natural Gas Engineering Dept., METU NCC _____

Date: 03.02.2017

I hereby declare that all information in this document has been obtained and presented in accordance with academic rules and ethical conduct. I also declare that, as required by these rules and conduct, I have fully cited and referenced all material and results that are not original to this work

Name, Last name : Satı Aslı Gündoğar

Signature :

ABSTRACT

MULTISCALE PORE STRUCTURE CHARACTERIZATION AND PORE NETWORK MODELING OF MIDDLE EAST CARBONATES

Gündoğar, Satı Aslı

Ph.D., Department of Petroleum and Natural Gas Engineering

Supervisor: Prof. Dr. Serhat Akın

February 2017, 254 pages

The complex interplay between structural and wettability heterogeneities is responsible for the limited pore network modeling studies on carbonates. In this study, our purpose is to develop structurally representative pore networks of Middle East carbonates and to predict their macroscopic difficult-to-measure relative permeability and capillary pressure hysteresis curves and residual oil trends under mixed-wettability conditions.

In comparison with the conventional pore-scale models, particular emphasis is put on multiscale pore structure characterization of complex carbonates. Scanning electron microscopy (SEM) imaging at multiple magnifications (75X and 750X) as well as physical core measurements, namely helium pycnometry and high-pressure (33,000 psi) mercury intrusion porosimetry (MIP) are employed to determine quantitative pore network descriptors. Mosaics constructed from overlapping low magnification (75X) views reveal abundant evidence of unresolved microporosity within the carbonate samples. Multiscaled SEM pore-size distributions incorporate microporous features as small as 0.077 μm and macropores as large as 310 μm into a single pore system. A pore body-throat classification method is developed with an initial premise of strong spatial size correlation between pore bodies and their connected throats. Six pore classes are

identified with unique pore- and throat-size distributions. The average coordination number ranges mostly from 3 to 5, and irregular triangle-shaped cross-sections dominate the carbonate pore geometry. The pore body to throat aspect ratio is generally large (>2.5), indicating the potential for significant residual oil saturation.

A novel quasi-static two-phase flow simulator is developed for a complete primary drainage-secondary imbibition-secondary drainage cycle with arbitrary wettability. Incorporating wettability alteration and contact angle hysteresis, the critical roles of corner wetting films and intermediate layers on fluid continuity and accordingly on recovery are investigated. The model predictions display a significant dependency on the interaction of pore structure, wettability, and saturation history. During spontaneous imbibition, snap-off becomes dominant in the systems with high aspect ratio and results in large amounts of trapped oil. It is shown that residual oil saturation is lower for more strongly oil-wet systems by means of the abundant presence of oil layers, while the endpoint water relative permeability increases gradually with the oil-wetness. The continuity of a phase is deduced to be the critical factor for its relative permeability rather than its abundance in the pore system. It is concluded that our newly proposed network model succeeds to represent experimentally hard-to-measure capillary pressure and relative permeability hysteresis trends for mixed-wet systems.

Keywords: carbonate rocks, image analysis, pore network modeling, mixed-wettability, intermediate oil layer, residual oil

ÖZ

ORTA DOĞU KARBONATLARININ ÇOK ÖLÇEKLİ GÖZENEK YAPISININ KARAKTERİZASYONU VE GÖZENEK AĞI MODELLEMESİ

Gündoğar, Satı Aslı

Doktora, Petrol ve Doğal Gaz Mühendisliği Bölümü

Tez Yöneticisi : Prof. Dr. Serhat Akın

Şubat 2017, 254 sayfa

Yapısal ve ıslanım-lık-lık heterojenlikleri arasındaki karmaşık ilişki, karbonatların gözenek ağı çalışmalarının sınırlı sayıda olmasından sorumludur. Bu çalışmada amacımız, Orta Doğu karbonatlarının yapısal eşdeğerde gözenek ağlarını oluşturmak ve onların iri ölçekli, ölçümü zor gö-re-li geçi-r-genlik ve kılcal basınç histeresis eğrilerini ve kalan petrol eğilimlerini karma ıslanım-lık-lık koşullarında tahmin etmektir.

Geleneksel gözenek-ölçekli modellere kıyasla, karmaşık karbonatların çok ölçekli gözenek yapısı karakterizasyonu üzerinde özellikle durulmuştur. Nicel gözenek ağı tanımlayıcılarını belirlemek için çoklu büyültmelerde (75X ve 750X) taramalı elektron mikroskopisi (SEM) görüntülemesi ile birlikte helyum piknometrisi ve yüksek-basınçlı (33,000 psi) civa intrüzyon porozimetresi kullanılmıştır. Üst üste binmiş düşük büyültme (75X) görüntülerinden oluşturulan mozaikler karbonat örneklerinin içerisindeki çözölemeyen mikro gözenekliliğin bol miktardaki kanıtını açığa çıkarmıştır. Çok ölçekli SEM gözenek boyut dağılımları 0.077 μm 'ye kadar küçüklükteki mikro gözenek özelliklerini ve 310 μm 'ye kadar büyüklükteki makro gözenekleri tek bir gözenek sisteminde toplamıştır. Gözenek gövdeleri ve onlara bağlı geçitler arasında kuvvetli uzamsal boyut korelasyonu önvarsayımıyla, bir gözenek gövde-geçit

sınıflandırma metodu geliştirilmiştir. Kendilerine ait gövde ve geçit boyut dağılımları olan altı gözenek sınıfı tanımlanmıştır. Ortalama koordinasyon numarası çoğunlukla 3 ile 5 arasında değişmektedir ve çeşitkenar üçgen-şekilli arakesitler karbonat gözenek geometrisine hakimdir. Gözenek gövdesinin geçide olan boyut (aspekt) oranının genellikle büyük olması (>2.5) ciddi miktarda kalan petrol saturasyonuna potansiyel oluşturmaktadır.

Değişken ıslanımıcılıkta tam bir birincil drenaj-ikincil imbibisyon-ikincil drenaj döngüsü için yeni bir yarı-statik iki-fazlı akış simülatörü geliştirilmiştir. Islanımıcılık değişimi ve kontak açısı histeresisini içeren, köşe ıslanma filmleri ve ara katmanların akışkan bütünlüğü ve dolayısıyla üretimindeki kritik rolleri incelenmiştir. Model tahminleri gözenek yapısı, ıslanımıcılık ve saturasyon geçmişinin etkileşimine önemli bağımlılık göstermektedir. Kendiliğinden imbibisyonda, yüksek aspekt oranına sahip sistemlerde ‘snap-off’ baskınlaşmakta ve çok miktarda petrol tutulmasıyla sonuçlanmaktadır. Petrol ıslanımıcılığıyla beraber suyun görel geçirgenliğinin bitim noktası değeri giderek artarken, daha kuvvetli petrol ıslanımıcılı sistemlerde yoğun petrol katmanı varlığına bağılı olarak daha düşük kalan petrol saturasyonu olduğu gösterilmiştir. Bir fazın gözenek sistemindeki miktarından ziyade devamlılığının o fazın görel geçirgenliği için kritik etken olduğu çıkarımı yapılmıştır. Yeni önerilen ağ modelimizin, deneysel olarak ölçümü zor kılcal basınç ve görel geçirgenlik histeresis eğilimlerini karma ıslanımıcılı sistemler için tasvir etmekte başarılı olduğu sonucuna varılmıştır.

Anahtar Sözcükler: karbonat kayaçlar, görüntü analizi, gözenek ağı modelleme, karma ıslanımıcılık, petrol ara katmanı, kalan petrol

Dedicated to my family

In loving memory of my father (1958 – 2015)

ACKNOWLEDGMENTS

First of all, I am deeply indebted to my supervisor Prof. Dr. Serhat Akin for his fundamental role in my doctoral work. His guidance, empathy, encouragements, and patience throughout the research were so valuable for me. I am eternally grateful to him for promoting my Stanford experience which covers a significant part of my thesis. I would also like to thank him for giving me freedom to extend the scope of this research, at the same time for continuing to contribute valuable feedback and advice.

I gratefully acknowledge the members of my Ph.D. committee, Prof. Dr. Mahmut Parlaktuna, Prof. Dr. Nurkan Karahanoğlu, Assoc. Prof. Dr. Ö. İnanç Türeya, and Asst. Prof. Dr. F. Emre Artun, for their time and valuable feedback on this thesis.

I am very thankful to Prof. Anthony Kovalchuk under whose advisorship at Stanford University SUPRI-A Research Group for broadening my technical and scientific horizons. Despite my short-term visiting status, he was always very understanding and helpful to me. I am particularly thankful to Dr. Cynthia Ross from SUPRI-A for her continuous and invaluable contributions on both laboratory and research aspects throughout my work at Stanford. I feel so privileged to have the opportunity to study with her. I also acknowledge that the pore network model code of Dr. Liping Jia written for strongly water-wet diatomites has served as a precious starting point for the development of my own code for mixed-wet carbonates.

I am grateful to end such tough times with the support, enjoy and friendship of my precious friends: Elnur Aliyev, Murat Anıl Erdoğan, Berkin Dörtdivanlıoğlu, Nilay Güngör, Tuğçe Taşcı, Elif Karatay, Ayşe Ökeşli Armlovich, Sophie Roman, and Sergey Klevtsov at Stanford and Selin Güven Erge, Tuğçe Özdemir, İnanç Alptuğ, Emre Özgür, Sevtaç Bülbül, Tuğçe Bayram Ertürk, and Tuğrul Taş at METU, and my cherished

friends Zeycan Kurban Özyazıcı, Delal Şeker, Ahmet Sönmez, Şermin Yavuz Çınar and Aycan Demir. I will always remember the moments we shared together.

I would like to express my biggest thanks to my beloved family for their constant, unconditional love, support, and sacrifices. Without them, it would never have been possible to accomplish this study. I dedicate this dissertation to them, especially to the memory of my father, whose role in my life remains immense.

This study is financially supported by The Scientific and Technological Research Council of Turkey (TUBITAK) under 2214/A International Research Fellowship Program and 2211/A National Scholarship Program for Ph.D. Students.

Additional support was provided by Stanford University Petroleum Research Institute (SUPRI-A) Industrial Affiliates for tuition (12-months) and scholarship (3-months) throughout my research period at Stanford University. These contributions are gratefully acknowledged. Part of this work was performed in the Benson (He pycnometry and MIP) and SUMAC (SEM) laboratory facilities, the GIS computer lab in Branner Library at Stanford University.

NOMENCLATURE

Symbol	Description
γ	: interfacial tension (N.m ⁻¹)
μ	: viscosity (Pa.s)
v	: fluid velocity (m.s ⁻¹)
ρ	: fluid density (kg.m ⁻³)
N_{Ca}	: capillary number
R	: inscribed radius (m)
R_{eff}	: effective radius of the bulk phase (m)
G	: shape factor
β_i	: half-angle of corner i in a triangular pore (°)
Z	: coordination number
Z_{2DA}	: two-dimensional average coordination number
α	: aspect ratio
n	: network model size
n_x, n_y, n_z	: network dimensions
δ, η	: truncated Weibull distribution shape parameters
ϕ	: porosity
ϕ_{SEM}	: SEM porosity
$\bar{\phi}$: average porosity
L_c	: lattice constant (or interpore distance) (m)
L	: pore length (m)
L_{ws}	: length of corner water (m)
L_{os}	: oil length contacting with wall (m)
L_{ow}	: length of oil-water meniscus
L_i	: distance of arc meniscus to apex in corner i (m)
A	: pore cross-sectional area (m ²)
A_{eff}	: effective area occupied by oil (m ²)
A_{wc}	: corner water area (m ²)
A_b	: bulk area (m ²)
A_c	: area covering corner water and oil layer (m ²)

A_{cor}	: area covering water in corner, oil and water layers (m^2)
V	: pore volume (m^3)
P	: pore perimeter (m)
P_{eff}	: effective perimeter occupied by oil (m)
I_k	: pore-body filling mechanisms
k	: number of adjacent oil-filled throats connected to a pore body
A	: geometrical constants in R_{eff}
κ	: geometry factor used in snap-off criterion
θ_c	: contact angle ($^\circ$)
θ_R	: receding contact angle during primary drainage ($^\circ$)
θ_r	: receding contact angle during secondary drainage ($^\circ$)
θ_A	: advancing contact angle ($^\circ$)
θ_h	: hinging contact angle ($^\circ$)
θ_A^{ww}	: advancing contact angle in water-wet pores ($^\circ$)
θ_A^{mw}	: advancing contact angle in mixed-wet pores ($^\circ$)
θ_A^{\max}	: maximum advancing contact angle for spontaneous piston-type flow ($^\circ$)
$\theta_{A,so}^{\max}$: maximum advancing angle for spontaneous snap-off ($^\circ$)
θ_r^{\min}	: minimum receding angle for spontaneous secondary drainage ($^\circ$)
f_{mw}	: mixed-wet fraction by number
f_{mw_N}	: mixed-wet fraction by number in nodes
f_{mw_L}	: mixed-wet fraction by number in links
P_c	: capillary pressure ($P_o - P_w$) (Pa)
P_c^e	: threshold capillary (entry) pressure (Pa)
P_c^*	: breakthrough capillary pressure (Pa)
$P_{c,i}^{crit}$: critical capillary pressure controlling oil layer collapse (Pa)
$P_{c,i}^{stab}$: critical capillary pressure controlling water layer stability (Pa)
$P_{c,pd}^{\max}$: maximum capillary pressure of primary drainage (Pa)
P_c^{\min}	: minimum capillary pressure of secondary imbibition (Pa)

$P_{c, sd}^{\max}$: maximum capillary pressure of secondary drainage (Pa)
ΔP	: pressure difference (Pa)
r	: radius of curvature (m)
r_d	: primary drainage entry radius of curvature (m)
r_{pt}	: piston-type imbibition entry radius of curvature (m)
r_{sd}	: secondary drainage entry radius of curvature (m)
k_a	: absolute permeability (mD)
k_r	: relative permeability
$k_{rw}(S_{or})$: endpoint water relative permeability
q	: flow rate (m^3s^{-1})
g	: hydraulic conductance ($\text{m}^4\text{Pa}^{-1}\text{s}^{-1}$)
B	: dimensionless corner resistance factor
S	: saturation
S_{wi}	: water saturation at the end of primary drainage
S_{wirr}	: water saturation at the end of secondary drainage
S_{or}	: residual oil saturation at the end of secondary imbibition
S_{wc}	: corner water saturation
S_{ol}	: oil layer saturation
S_{wl}	: water layer saturation

Subscripts / Superscripts

o	: oil
w	: water (wetting phase)
s	: solid pore wall
p	: pore (or phase only in permeability calculations)
t	: throat
i	: individual corner in a triangular pore
T	: total
ww	: water-wet
mw	: mixed-wet
ol	: oil layer
wl	: water layer
owl	: oil water layers
$_N$: node

<i>_L</i>	: link
<i>pd</i>	: primary drainage
<i>imb</i>	: secondary imbibition
<i>sd</i>	: secondary drainage
<i>pt</i>	: piston-type
<i>so</i>	: snap-off
<i>pb</i>	: pore-body filling
max	: maximum
min	: minimum
<i>crit</i>	: critical
<i>stab</i>	: stability

Abbreviations

PNM	: pore network modeling
SEM	: scanning electron microscopy
E-D	: erosion-dilation
LPA	: large pore areas
MIP	: mercury intrusion porosimetry
PC	: pore class
CC	: correlation coefficient
MS-P	: Mason, Stowe and Princen method
CPU	: central processing unit
PD	: primary drainage
SI	: secondary imbibition
SD	: secondary drainage

SI Metric Conversion Factors

$\text{cp} \times 10^3 = \text{Pa.s}$	$\mu\text{m} \times 10^6 = \text{m}$	$\text{rad} \times 57.2958 = \text{deg}$
$\text{psi} \times 6.895 = \text{kPa}$	$\text{mD} \times 10^{15} = \text{m}^2$	$\text{in} \times 2.54 = \text{m}$

TABLE OF CONTENTS

ABSTRACT	v
ÖZ.....	vii
DEDICATION	ix
ACKNOWLEDGMENTS.....	x
NOMENCLATURE.....	xii
TABLE OF CONTENTS	xvi
LIST OF TABLES	xx
LIST OF FIGURES.....	xxi
CHAPTERS	
1 INTRODUCTION.....	1
2 LITERATURE REVIEW.....	5
2.1 Carbonate pore system characterization and classification	5
2.2 Pore space representation	7
2.2.1 Pore space imaging techniques	8
2.2.1.1 X-ray micro-computed tomography (micro-CT)	8
2.2.1.2 Scanning electron microscopy (SEM)	9
2.2.2 Mercury intrusion porosimetry (MIP).....	10
2.3 Constructing pore network models.....	10
2.3.1 Direct mapping methods	11
2.3.2 Process-based methods.....	12
2.3.3 Statistical methods.....	13
2.4 Pore network descriptors – shape, spatial correlation and connectivity.....	14
2.4.1 Shape of pore cross-section.....	14
2.4.2 Spatial correlation in network construction	17
2.4.3 Connectivity within the pore network.....	18
2.5 Types of network modeling.....	21
2.5.1 Quasi-static models	21
2.5.2 Dynamic models.....	22
2.6 Fluid flow predictions through pore network modeling.....	22
2.6.1 Pore level displacements	24
2.6.2 Wettability classification.....	25
2.6.3 Wettability alteration and intermediate oil layers	26

2.6.4	Wettability effects on pore network modeling flow predictions.....	28
3	STATEMENT OF THE PROBLEM	33
4	PORE STRUCTURE CHARACTERIZATION OF MIDDLE EAST CARBONATES AND NETWORK MODEL INPUT DATA	35
4.1	Materials	35
4.2	Methods	39
4.2.1	SEM imaging	39
4.2.1.1	Mosaicking.....	42
4.2.1.2	Resolution effect	43
4.2.1.3	Image processing	45
4.2.1.4	SEM porosity	48
4.2.1.5	Sampling	49
4.2.1.6	Multiscale SEM porosity	52
4.2.2	Core measurements	55
4.2.2.1	Helium pycnometry	55
4.2.2.2	Mercury intrusion porosimetry (MIP)	56
4.3	Pore network elements	61
4.3.1	Image-based pore size distribution.....	61
4.3.2	MIP throat size distribution.....	63
4.3.3	Combination of image (SEM) and MIP distributions	64
4.3.4	Pore – throat classification method	66
4.3.5	Aspect ratio	70
4.3.6	Coordination number	71
4.3.7	Shape factor.....	72
5	PORE NETWORK CONSTRUCTION AND PORE-LEVEL FLOW EQUATIONS 75	
5.1	Pore network construction.....	75
5.1.1	Shape of pore cross-section and corner half-angles.....	77
5.1.2	Determination of pore throat and body sizes	81
5.1.2.1	Pore throat size determination	81
5.1.2.2	Aspect ratio and pore body inscribed radius.....	86
5.1.2.3	Pore body and throat size distributions.....	90
5.1.3	Pore body and throat lengths.....	94
5.2	Fluid flow in the network	96

5.2.1	Primary drainage and threshold capillary pressure	99
5.2.1.1	Wettability alteration and contact angle hysteresis.....	103
5.2.2	Secondary imbibition and threshold capillary pressure	105
5.2.2.1	Piston-type advancement	105
5.2.2.2	Pore body filling	110
5.2.2.3	Oil layer formation and stability	112
5.2.2.4	Snap-off.....	113
5.2.3	Secondary drainage and threshold capillary pressure	117
5.2.3.1	Water layer formation and stability	121
5.2.4	Macroscopic fluid transport properties	122
5.2.4.1	Fluid areas and saturations.....	123
5.2.4.2	Fluid conductance, absolute and relative permeabilities	126
5.2.5	Summary of displacement processes.....	130
6	NETWORK SIMULATION RESULTS.....	131
6.1	Primary drainage simulation results	131
6.2	Mixed-wettability development.....	144
6.3	Secondary imbibition simulation results	146
6.4	Secondary drainage simulation results	160
7	SENSITIVITY STUDIES OF WETTABILITY AND PORE STRUCTURE EFFECTS ON TWO-PHASE FLOW PROPERTIES	179
7.1	Effect of advancing contact angle during secondary imbibition	179
7.2	Effect of receding contact angle during secondary drainage.....	185
7.3	Effect of initial water saturation on transport properties and residual oil	189
7.4	Effect of mixed-wettability fraction on transport properties and residual oil	193
7.5	Effect of the structural properties on transport properties and residual oil	199
7.5.1	Network model size.....	199
7.5.2	Shape factor.....	202
8	CONCLUSIONS	207
9	RECOMMENDATIONS FOR FUTURE WORK.....	213
	REFERENCES.....	217
	APPENDICES.....	241
A.	MOSAIC IMAGES OF CARBONATE SAMPLES	241
B.	ALGORITHMS FOR TWO-PHASE FLOW SIMULATIONS IN THE PORE NETWORKS.....	247

B.1	Algorithm of primary drainage simulation	247
B.2	Algorithm of secondary imbibition simulation.....	248
B.3	Algorithm of secondary drainage simulation.....	250
CURRICULUM VITAE		253

LIST OF TABLES

TABLES

Table 4.1 – Petrophysical properties of whole carbonate core plugs.....	37
Table 4.2 – E-D output parameters compiled by image and individual pore objects.	47
Table 4.3 – Porosity of 75X, 750X, and multiscale SEM-derived data.	48
Table 4.4 – Matrix density (g/cm^3) measurements using He pycnometry and MIP.	56
Table 4.5 – Porosity data from He pycnometry, MIP, and SEM methods as well as whole core plug porosity measurements.	59
Table 4.6 – MIP permeability determination (Swanson’s Method).	60
Table 4.7 – Cumulative Hg volume, pore body size range, weighted average pore body and throat sizes, aspect ratio, percent proportions of each class per sample.....	69
Table 4.8 – Average coordination numbers at low and high magnifications.....	72
Table 5.1 – Volume/number proportions of porosity attributed to each PC.	86
Table 5.2 – SEM and MIP-derived average aspect ratios with their minimum and maximum limits.....	88
Table 5.3 – Network-measured aspect ratio and lattice constant.	89
Table 6.1 – Fluid properties used in flow simulations.	134
Table 6.2 – Primary drainage simulation results for $\theta_R = 0^\circ$	136
Table 6.3 – Number fraction of mixed-wet nodes and links and their overall in carbonate networks for $\theta_R = 0^\circ$	145
Table 6.4 – Contact angle ranges of different wettability cases used in secondary imbibition runs.	147
Table 6.5 – Secondary imbibition simulation results for carbonate samples under different wettability cases.....	148
Table 7.1 – Simulation results of a complete flooding cycle at varying $P_{c, pd}^{\max}$ cases for water-wet system of C013.....	190
Table 7.2 – Simulation results of a complete flooding cycle at varying $P_{c, pd}^{\max}$ cases for oil-wet system of C013.	191
Table 7.3 – Simulation results of a complete flooding cycle at varying f_{mw} cases for oil-wet system of C013.	195
Table 7.4 – Simulation results of a complete flooding cycle at varying f_{mw_N} cases for oil-wet system of C013.	198

LIST OF FIGURES

FIGURES

Figure 1.1 – Multistage workflow of the pore network modeling approach.	3
Figure 2.1 – Intergranular pores, vugs and fissures in carbonates from left to right (Schlumberger, 2007).	6
Figure 2.2 – Different regular shape geometries used for shape approximation of real pores in pore network modeling studies include a) circular, b) square, c) triangle and d) star-shaped (GBP).	15
Figure 2.3 – Different network structures a) 2D regular triangular networks (Chatzis and Dullien, 1977), b) cubic network with maximum $Z = 26$ (Raoof and Hassanizadeh, 2010).	19
Figure 2.4 – Fluid configuration in a mixed-wet star-shaped pore just after water invasion during forced imbibition (Radke et al., 1992).	27
Figure 2.5 – Corner water and intermediate oil layers in mixed-wet micromodel waterflood experiments (Buckley, 1995, 1996).	27
Figure 2.6 – Residual oil saturation as a function of contact angle during water injection (Blunt, 1997b).	30
Figure 2.7 – Waterflood recovery curves for the four wettability cases (Blunt, 1997b).	30
Figure 2.8 – Trapped oil saturation in response to advancing contact angle (Al-Futaisi and Patzek, 2003).	31
Figure 2.9 – Effect of advancing contact angle on secondary drainage flow regimes (Al-Futaisi and Patzek, 2003).	31
Figure 4.1 – Slabbed core images of carbonate reservoir section in the study well.	37
Figure 4.2 – SEM/EDS elemental analysis.	38
Figure 4.3 – Carbonate thin sections.	40
Figure 4.4 – SEM/EDS instrument.	40
Figure 4.5 – SEM images of the same region at low and high magnifications.	41
Figure 4.6 – Image segmentation from a) grayscale to b) binary mode and c) correction of incomplete epoxy impregnation regions by painting.	42
Figure 4.7 – Mosaicking of SEM overlapping images.	43
Figure 4.8 – Binary mosaics of C013, C016, C019, and C021.	44
Figure 4.9 – Resolution effect in C013 grayscale mosaic.	44
Figure 4.10 – Idealized erosion-dilation on example 2D pores (Ehrlich et al., 1984).	46
Figure 4.11 – Erosion-dilation results after 1, 5, 7, and 9 (last) cycles on an example 2D pore (Ehrlich et al., 1991a).	46
Figure 4.12 – Cumulative SEM pore size distributions for a) mosaics (75X) and b) high magnification images (750X) of carbonate samples.	49

Figure 4.13 – Sampling tests for a) C013, b) C016, c) C019, and d) C021 at high magnification.....	51
Figure 4.14 – Cumulative pore size distributions for 75X, 750X, and multiscale SEM-derived data of carbonate samples	54
Figure 4.15 – Helium pycnometry run for C019.....	56
Figure 4.16 – High pressure mercury injection profile of carbonate samples.	58
Figure 4.17 – Inflection point on Hg-air P_c curve.....	60
Figure 4.18 – Image-derived pore size distributions of C019 at a) 75X and b) 750X magnifications as well as multiscale SEM data c) in areal frequency and d) in pore counts.	62
Figure 4.19 – High-pressure MIP throat size distributions of a) all carbonates and replicates for b) C013 and c) C019.	64
Figure 4.20 – MIP throat size and multiscale SEM pore size versus cumulative porosity (% volume or area).	66
Figure 4.21 – Determination of throat size ranges for each pore class (PC).....	67
Figure 4.22 – Porosity proportion of each pore class (PC) per sample.....	70
Figure 4.23 – Average coordination number distributions at high magnification.	72
Figure 4.24 – Polygonal cross-sections having same shape factor with real pore space (Valvatne and Blunt, 2004).	73
Figure 4.25 – Edge effect due to incomplete pore element accepted as infinite in E-D. .	73
Figure 4.26 – Cumulative distribution of shape factor at a) 75X, b) 750X, and c) multiscale SEM data.....	74
Figure 5.1 – Schematic view of a) network model structure (modified from Diaz et al., 1987) and b) regular 3D cubic network for $n = 15$	76
Figure 5.2 – Irregular triangle-shaped pore cross-section.....	78
Figure 5.3 – Distribution of shape factor vs intermediate half-angle in irregular triangles (Reproduced from Patzek, 2001).	78
Figure 5.4 – Corner half-angles of individual pore bodies for $G \in [0.01, 0.04811]$	79
Figure 5.5 – SEM-derived shape factor distributions for a) $G \in (0,0.04811]$ and b) $G \in [0.01,0.04811]$	80
Figure 5.6 – Network-generated shape factor distributions in a) pore bodies and b) throats.	80
Figure 5.7 – Experimental (MIP) and model-predicted throat size distributions of C019 for disordered networks (a1 to a7).	82
Figure 5.8 – Experimental (MIP) and model-predicted throat size distributions of C019 for different spatially-ordered networks (c1 to c5).	83
Figure 5.9 – Comparison of experimental (MIP) versus model-predicted (PNM) throat size distributions of carbonate samples.	84

Figure 5.10 – Diagram of volume/number ratio of porosity attributed to each PC per sample.	86
Figure 5.11 – Pore throat and body size distributions representative of unconsolidated (left; sphere-pack) and consolidated (right; Berea sandstone) porous media.	87
Figure 5.12 – Network-measured aspect ratio distributions of carbonate networks in ascending order.	90
Figure 5.13 – Normalized network pore elements against pore body and throat radii for carbonate samples: a) C013, b) C016, c) C019, and d) C021.	91
Figure 5.14 – Network-measured pore body and throat size frequency distributions of a) C013, b) C016, c) C019, and d) C021.	93
Figure 5.15 – Throat length between neighboring pore bodies I and J	94
Figure 5.16 – Network-measured throat length distributions of carbonate networks in ascending order.	95
Figure 5.17 – A sketch of main terminal meniscus and corner arc meniscus in a triangular capillary tube during oil drainage.	97
Figure 5.18 – Main terminal meniscus (a) and corner arc meniscus (b) in a capillary tube with triangular cross-section.	98
Figure 5.19 – Possible fluid configurations during primary drainage, secondary imbibition, and secondary drainage processes.	99
Figure 5.20 – Oil-occupied area and lengths used in MS-P method for a single corner of an irregular triangular cross-section (Modified from Fig. 10 in Ma et al., 1996).	101
Figure 5.21 – Fluid configurations in a corner with pinned oil/water interface during imbibition (Modified from Fig. 5 in Ma et al., 1996).	106
Figure 5.22 – Normalized threshold capillary pressure of a) piston-type displacement and b) snap-off for $\theta_R = 0^\circ$, $P_{c,N}^{\max} = 2$ (Reproduced from Øren et al., 1998).	108
Figure 5.23 – Different types of pore body filling mechanisms for $Z = 4$: a) I_1 , b) I_2 , c) I_3 , d) I_0 ($k = 0$ for snap-off) (Blunt and Scher, 1995).	110
Figure 5.24 – Threshold capillary pressures of pore body filling mechanisms (I_k) in ascending order.	112
Figure 5.25 – The arc menisci configurations during a) spontaneous and b) forced snap-off events (Reproduced from Valvatne, 2004).	115
Figure 5.26 – Piston-type and snap-off capillary entry pressures (left) and their difference in individual throats (right; gray dots) and sorted in ascending order (right; red curve).	117
Figure 5.27 – Visualization of corner interfaces and contact angles in a) Configuration G and b) Configuration I for the sharpest corner i of triangular pore cross-section.	124
Figure 5.28 Any sectional plane ($x = 8$) within the pore network perpendicular to flow direction ($n = 15$).	127

Figure 5.29 – Number of nodes in pressure matrix of a) water and b) oil phases under unit pressure difference during primary drainage ($n = 15$).....	129
Figure 6.1 – Cumulative and incremental volume curves of high-pressure MIP throat size distribution for C013.....	133
Figure 6.2 – Pore occupancy histograms for a) nodes and b) links in C013 during primary drainage (PD).....	135
Figure 6.3 – Predicted primary drainage P_c curves of carbonate networks for $\theta_R = 0^\circ$	136
Figure 6.4 – Predicted primary drainage k_r curves of carbonate networks for $\theta_R = 0^\circ$	136
Figure 6.5 – Corner water saturation S_{wc} in carbonate networks during primary drainage at $\theta_R = 0^\circ$	141
Figure 6.6 – Predicted primary drainage P_c and k_r curves of C013 at different θ_R ..	143
Figure 6.7 – Predicted primary drainage P_c and k_r curves of C019 at different θ_R ..	143
Figure 6.8 – Corner water saturation S_{wc} of a) C013 and b) C019 during primary drainage at different θ_R	144
Figure 6.9 – Pore occupancy histograms for a) nodes and b) links of C013 during secondary imbibition.	146
Figure 6.10 – Number of pore-level displacement events during secondary imbibition	149
Figure 6.11 – Cumulative number of pore-level displacement events in links stepwise during secondary imbibition (<i>Case 1</i>).	150
Figure 6.12 – Secondary imbibition P_c and k_r curves of carbonate networks for <i>Case 1</i>	152
Figure 6.13 – Secondary imbibition P_c and k_r curves of carbonate networks for <i>Case 2</i>	154
Figure 6.14 – Oil layer saturation in a) node and b) link systems of C013 during forced imbibition under <i>Case 2</i>	156
Figure 6.15 – Secondary imbibition P_c and k_r curves of carbonate networks for <i>Case 3</i>	158
Figure 6.16 – Oil layer saturation in a) node and b) link systems of C013 during forced imbibition under <i>Case 3</i>	159
Figure 6.17 – Distribution of the receding and advancing angles in water-wet (ww) and mixed-wet (mw) nodes/links of C013 under <i>Case 3</i>	161
Figure 6.18 – Secondary drainage P_c^e of water-filled a) nodes and b) links of C013 under <i>Case 1</i>	162

Figure 6.19 – Secondary drainage P_c^e of water-filled a) nodes and b) links of C013 under <i>Case 2</i>	163
Figure 6.20 – Secondary drainage P_c^e of water-filled a) nodes and b) links of C013 under <i>Case 3</i>	164
Figure 6.21 – P_c hysteresis curves of C013 for a) <i>Case 1</i> , b) <i>Case 2</i> , c) <i>Case 3</i>	166
Figure 6.22 – P_c hysteresis curves of C016 for a) <i>Case 1</i> , b) <i>Case 2</i> , c) <i>Case 3</i>	167
Figure 6.23 – P_c hysteresis curves of C019 for a) <i>Case 1</i> , b) <i>Case 2</i> , c) <i>Case 3</i>	168
Figure 6.24 – P_c hysteresis curves of C021 for a) <i>Case 1</i> , b) <i>Case 2</i> , c) <i>Case 3</i>	169
Figure 6.25 – Experimental P_c hysteresis curves of water-wet sandstone (a) and two mixed-wet limestone samples from the same formation (b-c) (Masalmeh, 2001).	170
Figure 6.26 – Number frequencies of piston-type displacements in nodes and links of C013 for <i>Case 3</i> during secondary drainage	171
Figure 6.27 – Oil layer saturation in previously water-filled pores of C013 under a) <i>Case 2</i> and b) <i>Case 3</i> during secondary drainage.	172
Figure 6.28 – Oil (a) and water layer saturations (b) of C013 during secondary drainage for <i>Case 2</i>	174
Figure 6.29 – Oil (a) and water layer saturations (b) of C013 during secondary drainage for <i>Case 3</i>	174
Figure 6.30 – k_r hysteresis curves in a flooding cycle of C013 for a) <i>Case 1</i> , b) <i>Case 2</i> , c) <i>Case 3</i>	177
Figure 7.1 – Secondary imbibition P_c curves of a) C013 and b) C019 as a function of advancing contact angle.	181
Figure 7.2 – Residual oil saturation in a) C013 and b) C019 as a function of advancing contact angle during secondary imbibition.	184
Figure 7.3 – Secondary imbibition pore-level displacement events in a) C013 and b) C019 in response to average advancing contact angle.....	184
Figure 7.4 – The average advancing contact angle with its corresponding average receding contact angle in mixed-wet pores.	185
Figure 7.5 – Irreducible water saturation in a) C013 and b) C019 as a function of θ_r during secondary drainage with constant S_{wi} of 0.166 and 0.02.	187
Figure 7.6 – Secondary drainage pore-level displacement events in a) C013 and b) C019 in response to average receding contact angle	187
Figure 7.7 – Secondary imbibition P_c curves at varying $P_{c,pd}^{\max}$ cases for water-wet system of C013.....	190

Figure 7.8 – Secondary imbibition P_c curves at varying $P_{c,pd}^{\max}$ cases for oil-wet system of C013.....	191
Figure 7.9 – The change in S_{or} and S_{wirr} in response to S_{wi} for a) water-wet and b) oil-wet systems of C013.	192
Figure 7.10 – Secondary imbibition P_c and k_r curves at varying f_{mw} cases for oil-wet system of C013.....	195
Figure 7.11 – Secondary imbibition P_c and k_r curves at varying f_{mw_N} cases for oil-wet system of C013.	198
Figure 7.12 – P_c and k_r curves of water-wet networks with different model sizes for a) C013 and b) C019.	200
Figure 7.13 – P_c and k_r curves of oil-wet networks with different model sizes for a) C013 and b) C019.	201
Figure 7.14 – Corner half-angles of individual pore elements in ascending order for a) $G \in [0.01, 0.04811]$, b) $G = 0.024$, and c) $G = 0.048$	203
Figure 7.15 – P_c and k_r curves of water-wet networks with different shape factors for a) C013 and b) C019.	204
Figure 7.16 – P_c and k_r curves of oil-wet networks with different shape factors for a) C013 and b) C019.	205
Figure A.1 – C013 Mosaic..	242
Figure A.2 – C016 Mosaic..	243
Figure A.3 – C019 Mosaic.	244
Figure A.4 – C021 Mosaic..	245

CHAPTER 1

INTRODUCTION

Carbonate reservoirs are estimated to contain more than half of the world's conventional hydrocarbon resources (Ahlbrandt et al., 2005). In the Middle East, carbonate formations hold around 70% of proven oil and 90% of gas reserves (Schlumberger, 2007). In light of their importance in future global energy supply, better understanding of the nature of carbonates is of great interest in the petroleum industry. Unlike siliciclastic reservoirs, carbonates have inherently complex multiscale pore systems due to the diversity in depositional environments and subsequent diagenetic processes (Moore, 2001; Knackstedt et al., 2008). They present a major challenge in both reservoir characterization and management due to their internal structure and wettability heterogeneities. These factors exert strong control on fluid flow and lead to lower oil recovery from carbonate fields (Sung et al., 2013).

The promise of a network model is to simplify complex pore structure of real sediments by an interconnected network in which larger pores (pore bodies) are connected via smaller pores (pore throats). Incorporating a detailed description of pore structure and wettability state together with appropriate pore-scale flow physics, pore network modeling enables thorough investigation of a wide range of multiphase flow phenomena which are experimentally hard-to-measure including capillary pressure and relative permeability curves with their hysteresis loops, wettability effects, pore geometry and topology factors, and the presence of corner films and layers in the mixed-wet pores.

Pore network modeling is an effective tool for understanding multiphase flow phenomena, providing more efficient hydrocarbon recovery, effective contaminant removal, and safe carbon dioxide storage. It has successfully predicted multiphase flow

properties for sandstones (Øren et al., 1998; Patzek, 2001; Blunt et al., 2002). Recent studies have attempted to improve traditional network modeling approaches to study heterogeneous carbonates (Al-Kharusi and Blunt, 2007; Gharbi and Blunt, 2012). Over the last few decades, the advancements in high resolution imaging techniques and reconstruction algorithms have provided more sophisticated network representations for multiscale carbonates (Arns et al., 2005; Knackstedt et al., 2006; Biswal et al., 2007; Sok et al., 2010; Jiang et al., 2013).

Pore network modeling is proposed not as a substitute for special core analysis but as a cost-effective complementary tool to assist in understanding, reproducing and, when necessary, predicting experimental results and their associated uncertainties through model inputs that replicate experimental conditions (Xu et al., 1999). It is not feasible to measure the whole range of relevant multiphase flow behavior of a heterogeneous reservoir. Furthermore, in case experimental or field dataset is scarce which is not uncommon in real field data, due to availability limits of rock samples and time consuming experiments, pore network modeling calibrated by available real data can be used to compute flow properties for other regions of the sample with possibly different wettability and pore structure.

Figure 1.1 gives multistage workflow adapted in our thesis work. This thesis is organized in three main parts. First, the quantitative pore network descriptors necessary for the representative network generation of heterogeneous Middle East carbonates are determined via scanning electron microscopy (SEM) image analysis (at 75X and 750X magnifications) and mercury intrusion porosimetry (MIP) measurements. The SEM-derived and MIP pore size distributions are utilized for pore-throat classification. Second, representative 3D network models are constructed using most of the derived structural input parameters. Third, quasi-state flow simulations are conducted within the proposed model for 3 consecutive floods: primary drainage - secondary imbibition - secondary drainage. Our network model is programmed in MATLAB (a registered trademark of TheMathWorks Inc.)

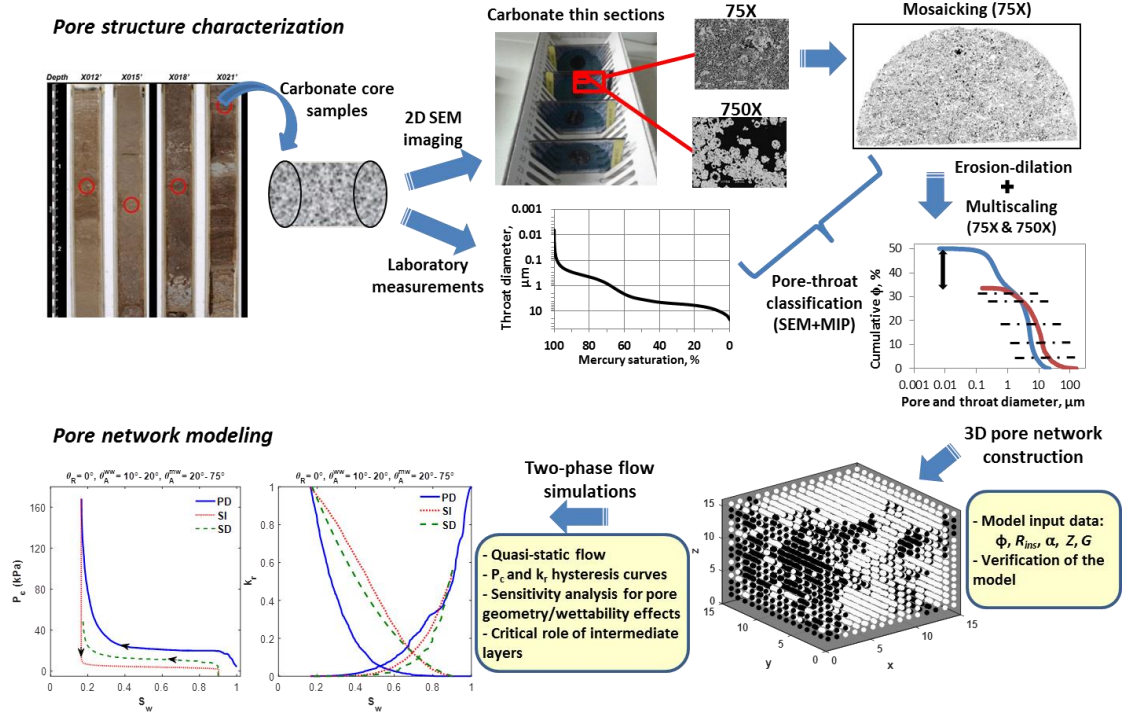


Figure 1.1 – Multistage workflow of the pore network modeling approach.

In **Chapter 2**, different aspects of carbonate pore system characterization and pore network modeling studies that have been reported in the literature are reviewed. The current state of network modeling and the important pore network modeling studies dealing with multiphase flow simulations of mixed-wet carbonates are given.

In **Chapter 3**, the statement of problem is defined and the main parts of multistage workflow adapted in our study are described.

In **Chapter 4**, the pore structure characterization of carbonate samples and the derivation of pore network input parameters are given in detail.

The first part of **Chapter 5** is designated for the development of representative carbonate networks incorporating the previously-derived pore structure inputs with essential modifications. The second part of **Chapter 5** focuses on mathematical basis of flow simulations, including all possible fluid configurations in a single pore for each part of the flooding cycle and the description of the capillary entry pressure for each pore-scale displacement mechanism.

In **Chapter 6**, model simulation results are presented. The consequences of complex interaction between pore structure, wettability status (contact angle) and

saturation history on P_c and k_r curves, pore-level flow mechanisms and residual saturation trends are investigated. The functions of intermediate oil and water layers in the corners of mixed-wet pores during forced imbibition and secondary drainage processes are evaluated, respectively.

In **Chapter 7**, a sensitivity study is carried out to assess the impact of wettability parameters (advancing contact angle, initial water saturation, and the fraction of mixed-wet pores) and pore structure characteristics (shape and model size) on capillary pressure and relative permeability curves, pore-level flow events and residual saturations.

In **Chapter 8**, the essence of our model is explained and the most remarkable points of this thesis work including its methodology, findings, and observations are summarized.

Finally, in **Chapter 9**, the final remarks and some important recommendations about the application and future direction of our newly developed quasi-static pore-scale network model are given.

CHAPTER 2

LITERATURE REVIEW

In this chapter, different aspects in the literature related with our thesis topic, namely carbonate pore system characterization, pore network construction methods including statistical and network extraction approaches and pore network model applications incorporating wettability alteration and contact angle hysteresis are briefly reviewed.

2.1 Carbonate pore system characterization and classification

Petrophysical and multiphase properties (e.g., capillary pressure, absolute and relative permeabilities) controlling fluid distribution and flow responses within the pore space are closely related with local pore-scale properties of the porous rocks (Jerauld and Salter, 1990). Unlike siliciclastic reservoirs, carbonates have inherently complex multiscale pore systems due to the diversity in depositional environments and subsequent diagenetic processes (Lucia, 1995; Moore, 2001; Knackstedt et al., 2008). Fluid flow properties of carbonates depend on the variation in pore type, pore interconnectivity and the microporosity (Knackstedt et al., 2007). In multiscale carbonate pore systems, the pore size variation generally spans four orders of magnitude (Choquette and Pray, 1970). Carbonate reservoirs may have geological variations such as large vugs, fissures and fractures because of depositional and diagenetic processes (**Fig. 2.1**). Micropores are found with other scales of porosity in the carbonate pore systems (Harland et al., 2015). The researchers used different threshold pore sizes to define micropores, including pore diameters less than 1 μm (Pittman, 1971), 10 μm (Cantrell and Hagerty, 1999), or 62.5 μm (Choquette and Pray, 1970).



Figure 2.1 – Intergranular pores, vugs and fissures in carbonates from left to right (Schlumberger, 2007).

Integrating geology, petrophysics, and reservoir engineering disciplines, several carbonate pore classification approaches incorporating depositional texture and petrophysical properties have been proposed in the literature as summarized by Skalinski and Kenter (2015). Despite the valuable contributions of previous studies, carbonates still present a major challenge in characterization due to their structural complexity, mineral instability, and wettability features. These factors exert strong controls on fluid flow and lead to lower oil recovery from carbonate fields (Sung et al., 2013).

Several studies have investigated the size, shape, and relative proportions of pore types and their associated throats in Middle Eastern carbonates (Etris et al., 1988; Funk et al., 1989; Ross et al., 1995). A correlation between total porosity and permeability is uncommon in Middle East carbonates (Saller et al., 2014); rather, the distribution of porosity types and their associated throat sizes control permeability (Morrow, 1971; Li et al., 1986; Etris et al., 1988; Ehrlich et al., 1991b). Marzouk et al. (1998) defined rock texture based on porosity types of a Middle East carbonate reservoir utilizing thin sections and MIP-derived pore-throat size distributions supported by porosity-permeability relations. Based on petrographic studies, Ramakrishnan et al. (2001) classified the carbonate multiporosity system components as intergranular and intragranular pores, vugs, and fractures (**Fig. 2.1**) validating their method with core and log data from Middle East carbonates. Cantrell and Hagerty (1999, 2003) using petrographic and mercury injection techniques found substantial amounts of microporosity throughout Saudi Arabian formations. Masalmeh and Jing (2004) showed that simple static rock types (porosity, permeability and primary drainage capillary pressure) might not be adequate to represent dynamic properties

(imbibition capillary pressure and relative permeability data and residual oil saturation) for the mixed wettability heterogeneous carbonate rocks under water injection. Dynamic special core analysis (SCAL) data including the fluid content information and rock-fluid interactions (i.e. wettability) should also be included in the identification of rock types (Gomes et al., 2008). Knackstedt et al. (2007) suggested correlating 3D image analysis and two-phase network modeling coupled with experimental measurements to examine the complex interaction between flow rate, contact angle, the range and shape of pore body and throat sizes on imbibition relative permeability in realistic carbonate networks. Clerke et al. (2008) and Clerke (2009) proposed a ‘Rosetta Stone’ approach to classify the complex pore systems in a large carbonate reservoir in Saudi Arabia via MIP data type-curve matched by Thomeer functions (Thomeer, 1983) integrating geological, petrophysical, and flow properties. Skalinski and Kenter (2015) developed an eight-step integrated workflow to predict and distribute the dominant petrophysical rock types of carbonates combining geological processes and petrophysics. Initial tests on two giant carbonate fields (from Kazakhstan and the Partitioned Zone (Kuwait–Saudi Arabia)) indicated the applicability of their workflow in variable data scenarios and reservoir types.

2.2 Pore space representation

A pore-scale network model requires, in addition to the physics that describes fluid flow at the pore scale, a 3D representation of the void space of a certain reservoir rock. In pore network modeling approach, the pore space is simplified by a topologically representative network of large pore bodies connected by narrower pore throats. A pore network model gives reasonable predictions of difficult and expensive macroscopic flow properties such as capillary pressure and relative permeability if the pore network captures the real pore structure properties and wettability conditions (contact angles) (Blunt et al., 2002; Valvatne and Blunt, 2004).

2.2.1 Pore space imaging techniques

The most crucial aspect of network construction is to identify pore structure (i.e. geometry and topology) accurately (Celia et al., 1995). Recent development in imaging techniques has enabled better quantifying the rock microstructure. Detailed descriptions of the different imaging techniques applied to pore space characterization are provided in valuable previous reviews (Ketcham and Carlson, 2001; Blunt et al., 2013; Wildenschild and Sheppard, 2013; Xiong et al., 2016). Hence, the imaging techniques will briefly mentioned in this section.

2.2.1.1 X-ray micro-computed tomography (micro-CT)

The standard X-ray micro-CT is a non-destructive and non-invasive technique used to visualize internal pore structures and fluid displacement processes three-dimensionally (Vinegar and Wellington, 1987; Hicks et al., 1992). It has been used to extract 3D pore network for more than two decades in different fields of earth subsurface science (Cnudde and Boone, 2013). Initially, Flannery and coworkers (1987) obtained micro-CT pore-scale images of a rock sample by means of both laboratory measurements and synchrotron beamline sources. Dunsmuir et al. (1991) developed their work in order to elucidate pore system topology and fluid flow in sandstones. Several studies were conducted using the Lattice Boltzmann method on the 3D image-extracted networks (Hazlett, 1995; Turner et al., 2004; Lehmann et al., 2006; Prodanović et al., 2007). One of the teams that have continued to develop the micro-CT technology building a data pool where a large range of rocks are imaged is at the Australian National University in association with colleagues at the University of New South Wales (Turner et al., 2004; Arns et al., 2007; Knackstedt et al., 2010). Based primarily on the X-ray energy (wavelength), the best image resolution is achieved from synchrotron micro-CT, possible up to a few microns (Coenen et al., 2004). However, due to the trade-off between image size and its resolution, while small rock samples with higher resolution better describe pore space, they are not able to exhibit a representative pore size distribution or connectivity (Peng et al., 2012). For this reason, in relatively large-sized

samples, the resolution of micro-CT may not be enough to resolve most of the microporosity features. The unresolved micropores, typically much less than a micron, are abundant in many carbonate reservoirs and unconventional sources, thus in case micropores are disregarded in the network representation, the resultant transport predictions may be in error. To overcome the trade-off between sample size and resolution, Pamukcu and Gualda (2010) suggested combining pore structure information of lower and higher resolution 3D tomograms of larger and smaller samples respectively to represent multiscale crystal size distributions.

2.2.1.2 Scanning electron microscopy (SEM)

The first use of image-obtained pore scale information to create a pore network consisted of 2D serial sectioning of rocks (Koplik et al., 1984; Yanuka et al., 1986). Scanning electron microscopy (SEM) images of thin sections is most widely used to reveal microstructures extracting in 2D down to the nanometer-scale pores and provides rapid information about spatial variations in mineralogy (Xiong et al., 2016). Pore body and throat size distributions can be obtained from analysis of 2D SEM analyses (Gouze et al., 2001). It is sufficient to capture pore elements in low permeable sandstones and carbonates and also to study unconventional shales. The weakness of SEM is that it does not directly give information about 3D connectivity of the pore system. FIB (focused ion beams) provides high resolution in 3D images, but it is time-consuming because less charging of the rock surface during imaging requires refocusing between milling and imaging and sample repositioning (Tomutsa et al., 2007; Curtis et al., 2010). These difficulties restrict FIB applications only to small areas of rock sample which prevents an adequate representation of the sample. The combination of FIB and SEM (FIBSEM) is developed to acquire microstructural properties of very small samples (Tomutsa et al., 2007; Lemmens et al., 2010; Keller et al., 2011). In addition to SEM and FIB, TEM (transmission electron microscopy) is also used to characterize pore space microporosity and topology (Wirth, 2009). Sok et al. (2010) utilized the backscattered scanning electron microscopy (BSEM) and focused ion beam SEM (FIBSEM) to investigate the multimodal pore structure (from 10 nm to 10 cm) of

carbonate rocks. Alternatively, the pore structure descriptors can be derived from a variety of 2D and 3D imaging methods. For example, Beckingham et al. (2013) developed a pore network model to predict permeability based on pore body and throat size distributions obtained from the combination of 2D SEM data of thin sections with connectivity data from 3D image analysis.

2.2.2 Mercury intrusion porosimetry (MIP)

Mercury intrusion porosimetry (MIP) is one of the most common methods used for examining structural characteristics of porous rocks (Giesche, 2006). It is much faster in operation and covers a much more wide range compared to gas adsorption method.

The micropores below the resolution of SEM imaging or the long thin pore throats typically not captured in 2D planes are possible to be analyzed with the aid of MIP experimental data (Gundogar et al., 2016). For adequate characterization of the nanometer-scale pore throat systems and define their pore size distributions, mercury porosimetry as well as gas adsorption analyses and nuclear magnetic resonance have been used (Tsakiroglou et al., 2004). Notice that the only connected (effective) porosity features are accessible during the mercury intrusion (Giesche, 2006). The pore size distribution is extracted from MIP assuming the pore system as a bundle of cylindrical tubes and the limitation of mercury intrusion measurements is so-called ink-bottle phenomenon. Mercury-air capillary pressure models have been utilized for determining pore size ranges and distributions (Chatzis and Dullien, 1977; Ioannidis and Chatzis, 1993a, 2000; Tsakiroglou and Payatakes, 2000). Pore network modeling studies have frequently utilized MIP method in order to tune the parameters of constructed networks to reproduce two-phase mercury-air capillary pressure curves (Mani and Mohanty, 1998; Valvatne and Blunt, 2004; Jia et al., 2007; Al-Kharusi and Blunt, 2007).

2.3 Constructing pore network models

Regardless of the reconstruction approach, the appropriate representation of the real pore space requires sufficient information about pore body and throat sizes, their

shapes, connectivity within the porous medium and also surface wettability character. Throughout the years, three general approaches have been proposed for 3D pore-scale network representation using the input data inferred either from 2D image analyses of thin sections or from 3D X-ray micro-CT images of actual rocks (Xiong et al., 2016):

- direct mapping of a network structure directly onto a specific pore space
- geological process-based (i.e. grain-based or object-based) based on the explicit modeling of the geological rock forming processes
- statistically equivalent network using basic morphologic and topologic properties of actual pore systems

Once the 3D network representation is built, fluid flow can be directly simulated numerically using the Lattice-Boltzmann method. However, this method is computationally ineffective and memory-demanding for multiphase flow and pore network modeling can be used instead (Øren et al., 1998; Patzek, 2001; Joekar-Niasar et al., 2010).

2.3.1 Direct mapping methods

Direct mapping of 3D micro-CT images provides the pore network extraction directly from the pore space and yields an irregular lattice (Piri and Blunt, 2005). Based on digital 3D images, several methods have been proposed to extract skeletons using different algorithms. The first class directly works on the 3D image including medial axis transform (Lindquist et al., 1996; Sheppard et al., 2005) and maximal balls (Silin and Patzek, 2006; Al-Kharusi and Blunt, 2007; Dong and Blunt, 2009; Blunt et al., 2013). The second class uses the pore and grain locations complementarily and are based on Delaunay or Voronoi tessellation (Blunt and King, 1991; Bryant et al., 1993a, 1993b; Øren and Bakke, 2002). Dong et al. (2008) overviewed different micro-CT network extraction methods with the related references for detailed descriptions of the different algorithms. For an overall characterization of core samples, relatively large sample sizes are used; however, in this case the resolution of CT images may not be enough to resolve micropore features. The topologically representative networks representing sandstones may be constructed directly from 3D CT images (Vogel and

Roth, 2001; Sok et al., 2002; Silin et al., 2003; Arns et al., 2005). However, for complex pore systems such as carbonates or mudstones, direct modeling of 3D CT images may lead to unresolved microporosity (Jiang et al., 2007). For this case, 2D SEM images with sufficient resolution can be utilized to construct 3D pore network by means of process-based or statistical methods.

2.3.2 Process-based methods

In process-based reconstruction methods, the petrographical information derived from 2D and 3D images are used for explicit modeling of the geological rock forming processes, such as sedimentation, compaction, and diagenesis. Bryant et al. (1992, 1993a, 1993b) pioneered the use of process-based method to model different physical processes for sedimentary rock generation using a random packing of equal-sized sphere-shaped grains. Their approach provided a significant achievement in pore-scale modeling, because single and multiphase flow properties were successfully predicted for the first time. Their pore network construction approach was developed later by Øren and coworkers (Bakke and Øren, 1997; Øren et al., 1998; Biswal et al., 1999; Lerdahl et al., 2000) incorporating a grain size distribution and other petrographical data obtained from 2D images. The process-based reconstructions have provided promising predictions of single and multiphase flow properties for a variety of water-wet sandstones, and mixed-wet reservoir sample (Øren et al., 1998; Lerdahl et al., 2000; Øren and Bakke, 2002; Valvatne and Blunt, 2004; Piri and Blunt, 2005). Computed physical properties were well-matched with laboratory measurements over a wide range of unconsolidated media such as glass beads and sands and consolidated media including Berea, Bentheimer and Fontainebleau sandstones (Hilfer, 1995; Øren et al., 1998; Øren and Bakke, 2002). The process-based extraction method works well in sedimentary rocks. Many carbonate reservoirs, on the other hand, are exposed to a variety of different complex diagenetic processes and have multiscale pore systems (Lucia, 2007). Therefore, geological reconstruction of carbonates may be challenging and fail to give accurate flow predictions (Blunt, 2001; Al-Kharusi and Blunt, 2008).

2.3.3 Statistical methods

A number of statistical methods have been proposed to recreate 3D images using the measured statistical properties from high resolution 2D images and have been widely applied in complex rocks (Joshi, 1974; Quiblier, 1984; Adler and Thovert, 1998; Manwart and Hilfer, 1999). Statistical methods are more general than the other reconstruction methods because 2D thin sections are often readily available (Blunt et al., 2002). Therefore, statistical methods have been used to describe a wide variety of porous media (Liang et al., 1999; Ioannidis and Chatzis, 2000; Tsakiroglou and Payatakes, 2000; Békri et al., 2000; Hilpert and Miller, 2001). The traditional statistical reconstruction methods are based on using single- (porosity) and two-point correlation functions (the probability of two points separated by a constant distance within the porous system) derived from the quantitative analysis of 2D images to generate a random 3D model that matches the measured statistical data (Adler et al., 1990). To provide more realistic representation of the topology of real porous medium, Okabe and Blunt (2004) developed multipoint statistical method to generate 3D image producing the same pattern of 2D image and thus long-range connectivity. Al-Kharusi and Blunt (2007) used multipoint extraction algorithm of Okabe and Blunt (2004) for network construction of the carbonate core plug from subsurface Oman because its pore space could not readily be resolved using micro-CT scanning. Although the resulting 3D image preserves the typical pore system patterns captured in 2D images, the iterative multi-point statistical methods are computationally very expensive (Ryazanov, 2012).

In clastic systems, process-based approach works well but statistical methods are required for complex pore systems such as carbonates (Blunt, 2001). Besides, direct micro-CT scanning can be used to find the distribution of pore sizes in case imaging tool resolution is sufficient to resolve most of the porous features (Kamath et al., 1998; Xu et al., 1999). In this thesis, a stochastic pore network model is proposed for Middle East carbonate samples where the geometrical and topological input data are derived from quantitative analysis of SEM images along with MIP measurements.

2.4 Pore network descriptors – shape, spatial correlation and connectivity

The microstructure of a porous system controls its flow properties, such as permeability, capillary pressure, and relative permeabilities (Jerauld and Salter, 1990). Accordingly, network models require accurate description of the geometry and connectivity of real pore space in order to produce genuine flow predictions (Blunt et al., 1992; Heiba et al., 1992; Ioannidis and Chatzis, 1993b; Øren and Pinczewski, 1994; Lowry and Miller, 1995; Pereira et al., 1996; Øren et al., 1998; Patzek, 2001; Raoof and Hassanizadeh, 2010). The most important task in pore network construction is to define its pore space features reasonably, i.e., pore body and throat size distributions, spatial correlation between pore body and throat sizes, locations of pore bodies (and thus throat length distributions), and coordination number (i.e. the average number of throats connected to each pore body) (Celia et al., 1995). The following sections provide an overview of previous works dealing with the geometric and topologic properties of pore systems of reservoir rocks.

2.4.1 Shape of pore cross-section

The geometry of each pore element is defined by an inscribed radius and shape factor (i.e. corner half-angles). In pore network modeling studies, to facilitate multiphase fluid flow modeling, highly complex and variable cross-sections of pore bodies and throats in real porous medium are simplified by ideal geometric elements (Valvatne and Blunt, 2004; **Fig. 2.2**). The choice of pore cross-sectional shape has a critical importance in the computational algorithm of a pore network model (Joekar-Niasar et al., 2010). The definition of main network flow properties such as capillary entry pressure and conductances, possible fluid configurations, the existence criteria for corner and intermediate layers, and the resultant transport properties all depend on the geometry of pore bodies and throats (see **Sections 4.3.7** and **5.1.1**).

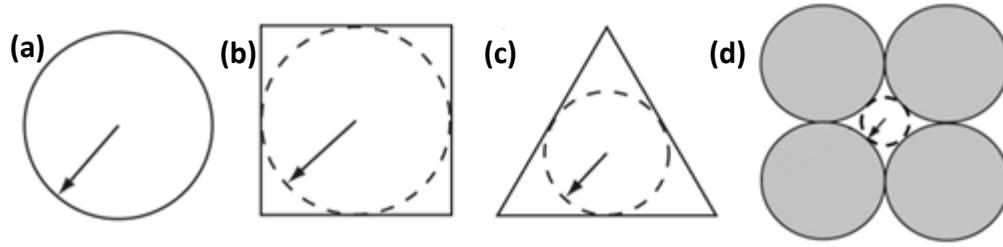


Figure 2.2 – Different regular geometries used for shape approximation of real pores in pore network modeling including a) circular, b) square, c) triangle and d) star-shaped (GBP) (White regions indicate pore space, gray regions indicate grains).

Micromodel experiments have extensively demonstrated the remaining wetting phase in the crevices and grooves of square flow channels after drainage as layers of no more than a few microns in thickness with the non-wetting phase in the center (Lenormand et al., 1983). Although the thin section images display the irregularity of actual pore shapes with many corners in real rock, in the earliest network model studies, for significant simplicity, pore cross-sections were assumed as cylinders with circular cross-section (**Fig. 2.2a**) (Fatt, 1956). However, circular capillary with single-phase occupancy does not allow formation of any surface films, corner or intermediate layers of other phases during flooding processes and results in poor comparison with experiments. Angular pore shapes, on the contrary, allow co-existence of multiple phases in a single pore with corner wetting layers along the pore edges satisfying the micromodel observations and accordingly enhances continuity of wetting phase throughout the pore system. Owing to pore angularity in cross-section, even if wetting phase saturation is very low, corner wetting layers have a significant effect on displacement process (Tuller et al., 1999; Or and Tuller, 1999). Therefore, the use of polygonal pore shapes is essential to reproduce at least qualitatively the multiphase flow phenomena. Modern network models have used different angular cross-section shapes for defining their pore elements such as square (**Fig. 2.2b**) (Blunt, 1997a,b; Fenwick and Blunt, 1998b) or equilateral triangle (**Fig. 2.2c**) in capillary bundle models (Hui and Blunt, 2000; Helland and Skjæveland, 2006a,b) and in network models (Fenwick and Blunt, 1998a). In response to the limitation of triangular pores to equilateral triangles, Mason and Morrow (1991) introduced the dimensionless shape factor quantity which is defined as the ratio of cross-sectional area of a pore element to its corresponding

perimeter-squared (see **Section 4.3.7**). It is used to approximate noncircular and cornered cross-sections of porous media in nature by irregular triangles having the same shape factor in the model. By using the same shape factor of a real pore in its corresponding network element, the idealized pore corners are ensured to capture correct amount of wetting phase during displacement processes (Al-Kharusi and Blunt, 2007). Although real pores are not exact triangles in nature, their corresponding irregular triangular shapes have the essential feature of corner layers and enable successful predictions of multiphase flow properties (Øren et al., 1998; Lerdahl et al., 2000). The corner half-angles of irregular triangles are determined from analytic expressions derived by Patzek and Silin (2001).

In the purpose of more accurate pore characterization, several authors have attempted to use a comprehensive Circle-arbitrary Triangle-Square shaped pores (CTS) approach (Patzek, 2001; Al-Futaisi and Patzek, 2003; Valvatne and Blunt, 2004; Piri and Blunt, 2005; Al-Kharusi and Blunt, 2008; Gharbi and Blunt, 2012). Kovscek et al. (1993) used a grain boundary pore shape (GBP) formed at the junction of four spherical rods to represent the non-convex geometry of pores in their capillary bundle model (**Fig. 2.2d**), followed by Man and Jing (1999, 2000). Helland et al. (2008) proposed a new shape characterization involving n -cornered stars in addition to common CTS shapes in capillary bundles (Ryazanov et al., 2009; 2010). The predictions of model implementing the new proposed pore shape approximation were generally more accurate compared to sole CTS approximation, but poor predictions were obtained for larger pores due to their more irregular and non-convex morphology. Joekar-Niasar et al. (2010) extracted a shape factor distribution from input rock images and represented complex shapes of pore throats by hyperbolic polygons (n -cornered GBPs) and pore bodies by prolate spheroids.

In this thesis, the main idea is to identify the type of pore cross-sections based on SEM-image derived cumulative shape factor distributions. Our carbonate networks are predominantly composed of arbitrary triangular pores (**Section 4.3.7**).

2.4.2 Spatial correlation in network construction

During the construction of equivalent pore networks, pore body and throat sizes can be randomly distributed or spatially correlated. Traditionally, in many network models, pore and throat sizes are independently distributed upon the network lattice despite the overwhelming evidence for the spatial correlation in porous system of reservoir rocks (Øren and Bakke, 2003). Despite any consistent approach clearly describing the function of spatial correlation between pore body and throat, many researchers have realized the importance of this feature in single and multiphase flow simulations and involved it in their network generations (Jerauld and Salter, 1990; Bryant et al., 1993b; Blunt, 1997a; Mani and Mohanty, 1999; Knackstedt et al., 2001; Sok et al., 2002).

Spatial correlation within a pore network can be considered among neighboring pore bodies (body-body), pore throats (throat-throat) or among pore body and the average radius of its connecting pore throats (body-throat). Micromodel studies of Ioannidis et al. (1991) emphasized the significance of the snap-off mechanism during imbibition process. Due to snap-off mechanism (Roof, 1970), the nonwetting phase might be trapped in regions where the aspect ratio (i.e., the size ratio of pore bodies to their connecting throats) is large (Chatzis et al., 1983; Li and Wardlaw, 1986a,b). As carbonates display significantly larger pore-throat aspect ratios than sandstones (Frank et al., 2005), aspect ratio is much more effective in multiphase flow properties of carbonates compared to sandstones (Nguyen et al., 2006; Knackstedt et al., 2006).

Several authors have considered a general correlation between pore body and throat sizes by conditioning that any pore body is always larger than or at least equal to the size of its largest connecting throat (Mayagoitia et al., 1997; Blunt, 1997a; Fenwick and Blunt, 1998a). Many other researchers have applied a strong spatial correlation criterion where large pore bodies in the network were connected to large throats and small pore bodies to small throats (Chatzis and Dullien, 1985; Wardlaw et al., 1987; Diaz et al., 1987; Hilpert et al., 2003). Jerauld and Salter (1990) studied the trends in relative permeability behavior using pore scale modeling and deduced that aspect ratio between pore bodies and throats is the most effective structural property of network. Bryant et al. (1993a) compared permeability predictions in correlated and randomly

distributed networks and showed the necessity of spatial correlations in pore size distribution for accurate permeability predictions. Several studies (Tsakiroglou and Payatakes, 1991; Ioannidis et al., 1993b; Rajaram et al., 1997; Xu et al., 1999; Mani and Mohanty, 1999) showed that a spatially correlated network represents more accurately the pore structure, enables a more efficient displacement and hence reduces the residual saturation of displaced fluid at the end of flooding process.

In this thesis, spatial correlation is proposed between pore bodies and their adjacent throats and incorporated in network construction using average aspect ratios for each pore class per sample derived by the quantitative analysis of SEM-images together with MIP data (see **Section 5.1.2.2**). To determine the inscribed radius of each pore body, the aspect ratio is multiplied by the average radius of the six associating throats. In case that radius is smaller than the largest connecting throat, pore body is set to the size of that largest throat (formalized in **Eq. 5.7**).

2.4.3 Connectivity within the pore network

In the earliest network models, the pore space were idealized as a bundle of capillary tubes and simple analytical solutions were used to simulate fluid flow (Fatt, 1956). However, these simplified networks could not incorporate the interconnectivity of the porous media. In the later studies, 2D or 3D networks were developed for more accurate pore system representation. Again, 2D networks fail to provide a complete representation of the interconnectivity of 3D systems (Chatzis and Dullien, 1977). The primary topological property of a network is the connectivity or coordination number (i.e. the number of pore throats associated to a pore body). As many authors have stated (Chatzis and Dullien, 1977; Wilkinson and Willemsen, 1983; Sok et al., 2002), coordination number has a major impact on flow behavior and on the trapping of residual nonwetting phase during imbibition through piston-type and pore body filling events (Lake, 1989). Most common network models are based on a regular skeleton, typically a cubic lattice with a coordination number of six or less by eliminating throats from the network (Dixit et al., 1998; Fenwick and Blunt, 1998a; Fischer and Celia, 1999; Dixit et al., 2000). Jerauld and Salter (1990) defined a fixed lattice spacing

constant as the distance between the centers of two adjacent pore bodies in a pore network (**Section 5.1.3**). However, using an arbitrary distribution of throat lengths leads to distortion in the network (Blunt, 1997b; Fenwick and Blunt, 1998a; Mogensen and Stenby, 1998). In this case, the pore network acts as a more irregular topology although it is built on a regular skeleton (Blunt et al., 2002). Furthermore, in real porous media, the connectivity can be more than six and follow nonuniform distributions (Kwiecien et al., 1990). To overcome these limitations, different topological descriptions have been suggested in network modeling studies including square or cubic lattices with extra coordination as shown in **Fig. 2.3a** (Chatzis and Dullien, 1977) and **Fig. 2.3b** (Raof and Hassanizadeh, 2010), Delaunay triangulations (Blunt and King, 1991; Bryant et al., 1993b), Voronoi networks (Jerauld and Salter, 1990; Fenwick and Blunt, 1998b), and random networks allowing a variable coordination number (Lowry and Miller, 1995).

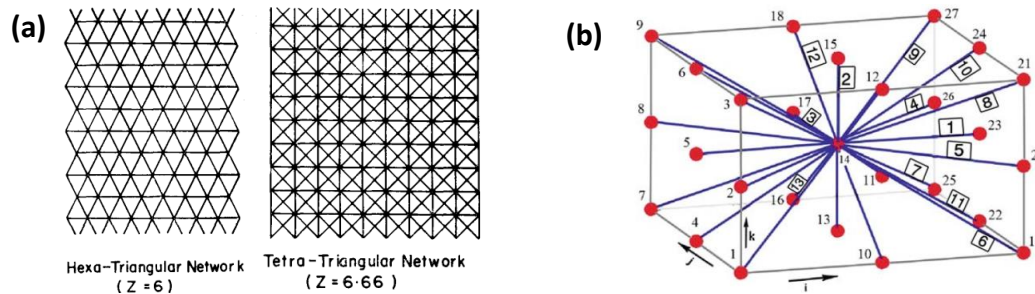


Figure 2.3 – Different network structures a) 2D regular triangular networks (Chatzis and Dullien, 1977), b) cubic network with maximum $Z = 26$ (Raof and Hassanizadeh, 2010).

Several recent studies have conducted to improve traditional network modeling techniques to study multiscale carbonate pore systems (Ioannidis and Chatzis, 2000; Dong et al., 2008; Sok et al., 2010; Blunt et al., 2013; Kallel et al., 2015). Knackstedt et al. (2006) developed a hybrid construction scheme to include both macroporosity and microporosity to the overall carbonate pore systems of two artificial vuggy carbonates, Gambier limestone and a carbonate from West Texas. The resultant networks extracted from 3D images exhibited large variations in topology and geometry between carbonate samples and a clear difference both visually and quantitatively from clastic rocks. The mean coordination numbers of samples were found to be 5.4, 3.6, 5.6, and 3.8, respectively. The weighted Z was much larger for carbonates (>30) indicating the large

connectivity of the larger pore bodies. Al-Kharusi and Blunt (2007) tested a carbonate sample from subsurface Oman using multi-point statistics (Okabe and Blunt, 2004) and found its average coordination number as 5. The coordination number distribution indicated that about 9% of the pores had connections larger than 14. The larger connection between pores might be attributed to the presence of more torturous patterns in carbonates than sandstones embodying many pores together. Zhao et al. (2010) used pore networks of four different rock types: a sand pack, a poorly consolidated sandstone from an Arabian oilfield, Berea sandstone and a granular carbonate using a maximal ball algorithm. The average aspect ratio and coordination numbers were in the range of 2.1-2.9 and 3-5.5, respectively and carbonate sample had the largest aspect ratio ($\alpha = 2.9$) and lower connectivity ($Z = 3$) among all. Bauer et al. (2012) developed a dual method using mercury intrusion method and micro-CT imaging to account for multiscale pore structure of carbonates. Based on the mercury intrusion data, all samples showed bimodal pore system. The extracted networks gave the coordination numbers of the three samples as 3.52, 3.88, and 3.47 which are relatively close. Gharbi and Blunt (2012) studied the effect of wettability and pore space connectivity on waterflood relative permeability for a set of six carbonate samples with different pore structures one of which was from Middle Eastern aquifer. The wettability alteration had a less effect in well-connected carbonates and also lower residual oil saturation was obtained for well-connected samples. Their average aspect ratio ranges from 1.87 to 2.59 while average coordination number from 2.5 to 7.41.

To summarize, based on the reviewed network models, the average coordination number of carbonates generally ranges from around 2 to 8 while it is between 4 and 8 for sandstones (Lindquist et al., 1996; Ioannidis et al., 1997; Bakke and Øren, 1997; Øren et al., 1998; Tsakiroglou and Payatakes, 2000; Øren and Bakke, 2002; Al-Kharusi and Blunt, 2007). In multiscale carbonate systems, microporosity may be significant and due to resolution limit of 3D imaging, it is possible to underestimate the connectivity of their carbonate pore space. In this case, thin section analysis and mercury intrusion porosimetry methods are used to resolve some of the remaining micropores below the resolution. In this study, coordination numbers of carbonate samples are calculated from the quantitative analysis of 2D SEM images at multiple

resolutions (see **Section 4.3.6**). Our findings are consistent with previous carbonate studies (Knackstedt et al., 2006; Sok et al., 2007; Al-Kharusi and Blunt, 2007; Zhao et al., 2010). In our case, the coordination numbers calculated from 2D data are most probably lower than those present in 3D. Due to lack of 3D tomographic images of our samples and presence of abundant microporosity, fixing the system coordination number to 6 is thought as a reasonable assumption (see **Section 5.1**).

2.5 Types of network modeling

Based on the capillary number, N_{Ca} , describing the ratio of viscous forces to capillary forces (Lake, 1989), there are two main types of pore network models: quasi-static and dynamic models. In the case of low capillary number ($< 10^{-6}$; King, 1987; Jadhunandan and Morrow, 1995), flow through pore networks is governed by capillary forces and quasi-static displacement occurs. Otherwise, viscous forces are also significant and dynamic network modeling should be applied regarding both capillary and viscous forces.

2.5.1 Quasi-static models

In quasi-static (capillary-dominated) models, which have been extensively used in network modeling studies, capillary forces control fluid motions and spatial distributions. Displacement simulation is based on invasion-percolation process where fluid-fluid interfaces are rearranged gradually in response to change in local capillary pressure (Chandler et al., 1982; Wilkinson and Willemsen, 1983; Dias and Wilkinson, 1986).

Typical immiscible reservoir displacements and low flow rate coreflooding experiments satisfy low capillary number criterion (Mohanty and Salter, 1982; Dullien, 1992; Blunt and Scher, 1995; Hilfer and Øren, 1996; Blunt, 1997a,b). The reservoir waterflooding displacements have capillary number less than 10^{-7} and also most coreflooding experiments are performed with capillary number lower than 10^{-6} (Lake, 1989; Dullien, 1992; Blunt, 1997b). For this reason, the majority of existing pore

network models has assumed quasi-static flow to compute transport properties (McDougall and Sorbie, 1995; Li and Yortsos, 1995; Øren et al., 1998; Dixit et al., 1999; Patzek, 2001; Blunt et al., 2002; van Dijke and Sorbie, 2002; Al-Futaisi and Patzek, 2003; Valvatne and Blunt, 2004; Piri and Blunt, 2005; Laroche and Vizika, 2005; Kallel et al., 2015). In this thesis, a quasi-static flow is employed at an infinitesimal flow rate where the fluid configurations are dominated by capillary forces and the viscous pressure drop across the network is negligible (see **Section 4.2** for the details).

2.5.2 Dynamic models

Dynamic models are less frequently used in pore network modeling but they become important when the capillary number exceeds 10^{-5} - 10^{-3} or larger (Dullien, 1992; Zhou, 2013). In several circumstances such as polymer flooding (high viscosity), fracture flow (very large flow rate), or surfactant flooding (low interfacial tension), viscous and capillary forces both control flow at the pore scale (Al-Gharbi and Blunt, 2005). In dynamic models, at each time step, inflow rate is applied to each of the phases in the system and the corresponding pressure and interface positions are updated according to the pressure difference criteria. To date, dynamics of multiphase flow have been applied in several works to demonstrate the influence of capillary and viscous forces on multiphase flow properties, oil recovery and pore-scale displacement mechanisms (Koplik and Lasseter, 1985; Blunt and King, 1991; Dahle and Celia, 1999). The flow through thin wetting films is also examined in the dynamic pore network models (Blunt and Scher, 1995; Constantinides and Payatakes, 1996; Hughes and Blunt, 2000; Al-Gharbi and Blunt, 2005; Joekar-Niasar et al., 2010).

2.6 Fluid flow predictions through pore network modeling

The use of network models to represent multiphase flow in porous media was pioneered by Fatt in 1956. The resulting drainage capillary pressure and relative permeability curves had the same characteristics with the experimental curves. He established that

the model including different network lattices gave more similar results to experimental data than the models with a bundle of parallel tubes. He also emphasized that pore size distribution has a significant effect on the model results. After his pioneering work, many publications are encountered mostly in petroleum and environmental applications. By the development of computer process power in the late 1970s, network modeling started to be studied again.

Pore network models predict successfully relative permeability and the effects of wettability for sandstones (Dixit et al., 1999; van Dijke and Sorbie, 2002; Al-Futaisi and Patzek, 2003; Øren and Bakke, 2003; Valvatne and Blunt, 2004). For a comprehensive and consistent physical model to involve the hysteresis phenomenon of multiphase phase, experimental data is a must. In the literature, most of the available experimental data is for water-wet sandstones and hence there is a need for experimental studies for heterogeneous mixed-wet carbonates (Masalmeh, 2001, 2002; Masalmeh and Jiang, 2006). In recent studies, there is substantial emphasis in improving traditional network modeling techniques in order to explore a high range of phenomena such as the effects of wettability study in complex carbonates with nonuniform wettability. Ioannidis and Chatzis (2000) developed a dual network including interconnected channels in vuggy carbonates. They found similar model predictions of capillary pressures. Moctezuma et al. (2003) obtained a dual network model for a vuggy carbonate, including matrix, vugs, and fractures. The representative pore network model was developed by utilizing mercury injection and NMR measurements. Valvatne and Blunt (2004) modeled relatively homogeneous intergranular carbonates and obtained fairly good match for primary drainage capillary pressure curves with experimental data. Using a network extracted from a subsurface carbonate core plug, Al-Kharusi and Blunt (2008) predicted accurately the primary drainage capillary pressure indicating the network sufficiency in pore space representation. With adjusted contact angles, they obtained reasonable relative permeability of oil as well as the residual oil saturation for imbibition and relative permeability of water for secondary drainage. Zhao et al. (2010) examined the impact of wettability for pore network systems extracted from different rock types including sand packs, Middle Eastern sandstone, Berea sandstone, and granular carbonate samples. They concluded that for mixed-wet samples, the most effective

recovery occurred when a small fraction of the medium remained water-wet. Bauer et al. (2012) developed a dual pore network to analyze microporosity in carbonates and achieved good predictions of relative permeability.

2.6.1 Pore level displacements

In 1983, Wilkinson and Willemsen introduced the concept of invasion percolation for describing the theoretical foundation of drainage, in other words, one fluid displacing another in a porous system under the action of capillary forces. There are two types of invasion percolation which are with or without trapping (Knackstedt et al., 2000) depending on the miscibility of the defending phase during the displacement process. The drainage process in water-wet medium is considered as a bond invasion percolation without trapping (Stauffer and Aharony, 1994). As oil displaces water by piston-type displacement, water layers are left in the sharp pore corners and thus the displaced fluid (water) is not trapped due to permanent continuity of water throughout the network (Al-Kharusi and Blunt, 2008).

Using water-wet micromodel experiments, Lenormand et al. (1983) identified three main pore-level displacements during water imbibition: piston-type, pore body filling and snap-off mechanisms. In comparison to primary drainage, water imbibition is somewhat more complex due to the contact angle hysteresis and the co-existence of water and oil in a single pore resulting in competition between flow mechanisms and oil entrapment (Lenormand et al., 1983; Prodanović and Bryant, 2006). It is described as an ordinary invasion percolation with trapping (Al-Futaisi and Patzek, 2003). In secondary drainage, both oil and water is present in the porous system and the water continuity through pore corners similar to primary drainage as well as possible intermediate water layers prevents water trapping during oil re-invasion (Helland and Skjæveland, 2006a). Besides, around one third of the throats remain water-filled (micropores), and so most oil-wet pores are connected by a water-filled region and hence water cannot be trapped (Blunt, 1997b).

2.6.2 Wettability classification

The multiphase properties of the porous medium strongly depend on the wettability of the pore surfaces, i.e. the overall tendency of a rock sample to prefer one phase over another. In an oil-water system, the contact angle measured through the denser (water) phase on a solid surface θ_{ow} is a measure of wettability. Three broad wettability classifications are identified as water-wet ($\theta_{ow} < 90^\circ$), intermediate-wet ($\theta_{ow} \approx 90^\circ$) or, oil-wet ($\theta_{ow} > 90^\circ$). According to the classification of Anderson (1986), $\theta_{ow} < 75^\circ$, $75^\circ < \theta_{ow} < 105^\circ$ and $\theta_{ow} > 105^\circ$ correspond to water-wet, intermediate-wet, and oil-wet systems respectively. In strongly water-wet systems, θ_{ow} is close to 0° and in strongly oil-wet systems, θ_{ow} is close to 180° . For more complex wettability conditions within the same porous medium, McDougall and Sorbie (1995) used uniform and nonuniform (heterogeneous) wettability terms. Uniform wettability means that a porous rock has the same wettability class with nearly the same contact angle throughout the porous system. In the case of nonuniform wettability, the contact angle and accordingly the wettability state of porous rock may vary from pore to pore.

The contact angle hysteresis between different flooding processes is a result of wettability alteration due to ageing and the displacement direction due to surface roughness. Salathiel (1973) used refined oil and crude oil to treat core samples in drainage and imbibition experiments. After primary drainage using refined oil, the imbibition behavior of rock exhibited water-wet character. On the contrary, the core saturated by crude oil behaved as oil-wet during imbibition, because by the adsorption of asphaltenes (surface active components in crude oil), pore walls in contact with oil were exposed to wettability change. Salathiel (1973) referred to these pores as mixed-wet whose central portion is oil-wet and the corners remain water-wet. In several other experimental studies, wettability alteration has been observed (Morrow et al., 1986; Buckley et al., 1996). Using cryo-SEM, Fassi-Fihri et al. (1995) visualized directly nonuniform wettability in a single pore. In some oil-occupied pores where the water film between pore surface and bulk oil remains, some wettability alteration is still possible due to asphaltene diffusion through the water film (Kaminsky and Radke,

1997). For this reason, following oil migration, the network system may involve three different wetting states: strongly water-wet undrained pores, mixed-wet oil-drained pores and intermediate-wet oil-drained pores with remaining water films (Masalmeh, 2003).

In addition to wettability alteration, surface roughness may lead to some degree of hysteresis for different displacement directions: the receding contact angle is lower than the advancing contact angle (Morrow, 1975). The receding contact angle during secondary drainage is different for unaltered and altered pore surfaces. Morrow (1975) showed contact angle hysteresis resulted from surface roughness by using Teflon tubes with different roughness degree. He measured both advancing and receding angles for each model and related them to the intrinsic contact angle. Based on the difference between advancing and receding angles, he defined three models: Class I (no hysteresis), Class II (moderate hysteresis due to little roughness), and Class III (substantial hysteresis due to extensive roughness). Swanson (1980) also observed contact angle hysteresis up to 90° in the experiments which has a critical effect on capillary pressure and relative permeability hysteresis.

In the wettability scenario of our model, both wettability alteration and contact angle hysteresis are implemented for two-phase flow algorithms (e.g., Øren and Bakke, 2003; Al-Futaisi and Patzek, 2003, 2004; Valvatne and Blunt, 2004; Piri and Blunt, 2005; Helland and Skjæveland, 2006a).

2.6.3 Wettability alteration and intermediate oil layers

In Salathiel's experimental study (1973), the residual oil saturation in mixed-wet case was significantly lower than water-wet case. The water breakthrough occurred earlier in mixed-wet case than in water-wet case. However, the additional oil volumes could be produced very slowly for a considerable time after breakthrough using a large number of injected water (1000 PV or more). In mixed-wet systems, Salathiel (1973) explained the higher oil recovery in mixed-wet system by oil flow through thin oil films along the aged surfaces. In addition to surface films, Kovscek et al. (1993) suggested the effect of oil layers in the corners of mixed-wet pores with much larger contribution to oil

recovery (**Fig. 2.4**). In this pore-level scenario, the oil-water interface in the corners remained pinned during water flooding, allowing oil layers to become sandwiched between water in the corners and that in the center. Using this pore level scenario, the experimental trends observed by Salathiel (1973) were reproduced. Using an etched-glass micromodel, Buckley (1995, 1996) conducted oil drainage, wettability alteration and water injection experiments. In the mixed-wet conditions where crude oil with asphaltene was used for drainage, the stable intermediate oil layers were observed between water in the corners and water in the center (**Fig. 2.5**). The corner water connected with water in the center as the oil layers ceased to exist.

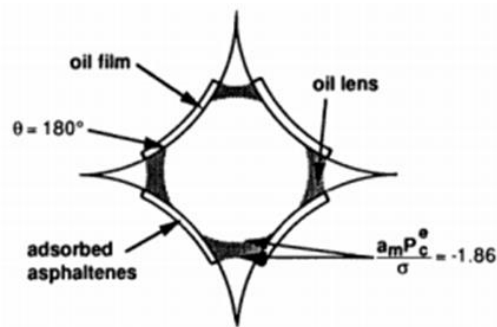


Figure 2.4 – Fluid configuration in a mixed-wet star-shaped pore just after water invasion during forced imbibition (Radke et al., 1992).

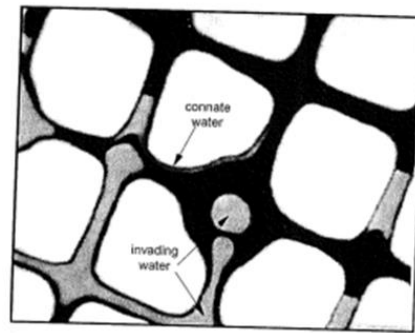


Figure 2.5 – Corner water and intermediate oil layers in mixed-wet micromodel waterflood experiments (Buckley, 1995, 1996).

Recently, Singh et al. (2016) investigated experimentally the effect of wettability of carbonates on oil layers created after a sequential oil and brine flooding in a capillary-controlled regime. Using X-ray micro-CT, they observed that brine displaced oil in mixed-wet large pores leaving oil layers in the pore corners between two water interfaces. For mixed-wet systems, during brine injection, brine invaded only the larger oil-wet throats due to requirement of more negative capillary entry pressure in smaller throats. The displacement of remaining oil saturation with 19 to 37 pore volume brine injection indicated the low conductance of oil through layers. The oil layers formed at strongly oil-wet conditions (180°) were stable throughout the experiments.

Using pore network modeling, Blunt (1997b, 1998) confirmed that oil layers formed in nonuniform pores and throats during forced imbibition allowed the oil phase

to be drained to a significantly low saturation. Blunt (1997b) derived the geometrical criterion for formation and collapse of oil layers in a pore with square cross-section based on the meeting of surrounding oil-water interfaces. The geometrical criterion has been used by many authors in capillary bundle models (Hui and Blunt, 2000; Helland and Skjæveland, 2004) and network models (Blunt, 1997b; Øren et al., 1998; Valvatne and Blunt, 2004; Piri and Blunt, 2005). Van Dijke and Sorbie (2006) developed a thermodynamically based criterion for oil layer existence which was more restrictive than the geometrical criterion proposed by Blunt (1997b). In their approach, oil layer existence was derived using MS-P theory (Mayer and Stowe, 1965; Princen, 1969a, 1969b, 1970) based on free energy variation. Their thermodynamic criterion was implemented into capillary bundle model (Helland and Skjæveland, 2006a) and network models (Ryazanov et al., 2009, 2010). Helland and Skjæveland (2006b) revised their previous results (Helland and Skjæveland, 2006a) by thermodynamical layer approach.

2.6.4 Wettability effects on pore network modeling flow predictions

The wettability effects on multiphase flow properties including capillary pressure and relative permeabilities and residual oil saturation has been extensively investigated in many numerical studies by using pore network modeling (Øren and Bakke, 1998; Patzek, 2001; Al-Futaisi and Patzek, 2003; Valvatne and Blunt, 2004; Piri and Blunt, 2005; Helland and Skjæveland, 2006a,b; Høiland et al., 2007; Al-Kharusi and Blunt, 2008; Dixit et al., 1999; Ryazanov et al., 2010; Sorbie et al., 2011; Kallel et al., 2015). According to many field investigations and experimental results, most of the carbonate reservoirs have heterogeneous wettability (Treiber et al., 1972). McDougall and Sorbie (1995, 1997) predicted trends in relative permeability and recovery efficiency and concluded that optimum recovery would be achieved with about half the pore space being oil-wet, something that had been previously established experimentally (Jadhunandan and Morrow, 1995).

Blunt (1997b) used a cubic network lattice with square pore cross-sections to study effect of wettability and oil layers on residual oil saturation. The receding contact angle is set to be 22.5° at initial. After oil drainage, an oil-wet wettability distribution is

considered in oil-filled pores. The advancing contact angle in water-wet and oil-wet pores were constant and equal to 34° and 180° , respectively. Based on the resulting S_{or} trend against oil-wet fraction f_{mw} (from 0 to 1), S_{or} increases until some critical fraction value (0.59) and then decreases steeply. The maximum recovery was possible for entirely oil-wet case ($f_{mw}=1$). The oil-wet fractions below the critical value of 0.59 led to separate dendritic clusters which could not contribute to oil displacement during the forced imbibition. However, for higher oil-wet fractions, oil-wet pores formed a spanning cluster and enhanced oil displacement through oil layers.

Øren et al. (1998) used the network models extracted from some mixed-wet reservoir rock to study wettability effect on flow properties and residual oil. The receding contact angle was taken as 20° for all network elements. In imbibition, the contact angles assigned to water-wet and oil-wet pores were 40° and 180° , respectively. The dependence of S_{or} with respect to oil-wet fraction in their sensitivity analysis is similar to the findings of Blunt (1997b). Dixit et al. (1999) studied two cases for advancing angle distributions of oil-filled pore throats: MWL (mixed-wet large) and FW (fractionally wet) distributions. The contact angles for their proposed mixed-wet network were 0, $[0^\circ, 89^\circ]$, and $[91^\circ, 180^\circ]$ for θ_R , θ_A^{ww} , and θ_A^{mw} respectively. They could not explicitly model oil layer formation during forced imbibition due to simplified circular pore cross-sections, but still their resulting S_{or} dependence to oil-wet fraction was qualitatively consistent with the previous studies (Blunt, 1997b; Øren et al., 1998)

Sensitivity studies have been performed to analyze the effect of wettability (i.e. contact angle) on flow regimes, residual oil and relative permeabilities (Blunt, 1997b; Al-Futaisi and Patzek, 2003). Blunt (1997b) identified four distinct flow regimes controlling S_{or} trend in response to θ_A during water imbibition (**Fig. 2.6**). Snap-off in strongly water-wet case was responsible for significant oil trapping. For square pore cross-section, snap-off no longer occurred beyond a contact angle of 45° . In the second regime between 45° and 90° , the system was still water-wet but due to inhibited snap-off, S_{or} reduced. Many experiments have stated that oil recovery is larger in weakly water-wet systems compared to strongly water-wet media (Morrow et al., 1986;

Buckley et al., 1996). Since the displacement dominated by piston-type mechanism improved both oil and water continuities, their relative permeabilities were higher than for a strongly water-wet case. The third regime between 90° and 135° represented a weakly oil-wet system where oil layers could not be formed. Due to isolated water clusters and no oil layers, S_{or} was extremely high. The water relative permeability was very low with endpoint value of 10^{-4} as a result of very poor water connectivity across the network. The oil-wet system was realized in the fourth regime ($>135^\circ$) where oil layers were formed and collapsed after some point during waterflooding. With the increase in contact angle, the oil layers remained stable for a greater range of P_c and recovery increased. The oil layers allowed a low S_{or} to be reached during forced imbibition, but due to very small thickness of oil layers, oil conductance and accordingly oil relative permeability dropped to very low values.

According to the waterflooding recovery curves of the different flow regimes (Fig. 2.7), the weakly water-wet medium gave the highest recovery at breakthrough. In the strongly oil-wet medium, significant recovery occurred beyond breakthrough by means of flow through thin oil layers. Due to low conductance of oil layers, more than 100 pore volume of water had to be injected to reach a greater recovery than in weakly water-wet case.

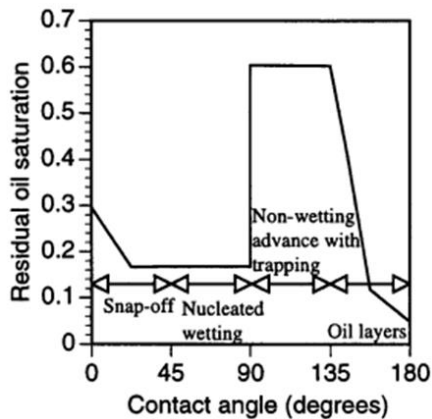


Figure 2.6 – Residual oil saturation as a function of contact angle during water injection (Blunt, 1997b).

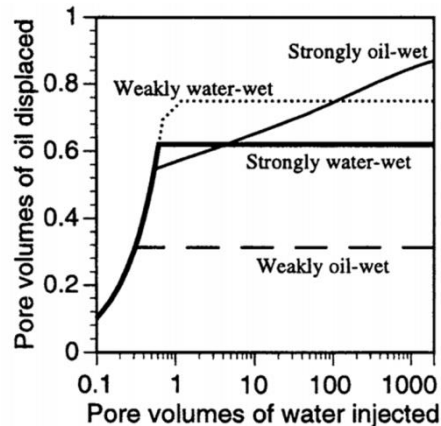


Figure 2.7 – Waterflood recovery curves for the four wettability cases (Blunt, 1997b).

Al-Futaisi and Patzek (2003) developed a two-phase pore network simulator including a realistic representation of pore structure and wettability properties of a sedimentary rock. They represented sensitivity results of S_{or} (**Fig. 2.8**) and displacement mechanisms (**Fig. 2.9**) with respect to a range of advancing contact angles. The significant effect of θ_A on S_{or} was summarized in **Fig. 2.8**. S_{or} decreased dramatically from 38% to nearly 8% as θ_A increased from strongly water-wet system (0°) to the case of weakly water-wet network (90°). With the transition from weakly water-wet to weakly oil-wet case, a sharp jump was noted in S_{or} (from 8% to almost 46%). During forced imbibition in between 90° to 100° , oil layer formation was geometrically impossible (see **Section 5.2.2.3**) resulting in significant amount of residual oil. Just after $\theta_A=100^\circ$, the creation of intermediate oil layers allowed better oil connectivity within the network and less trapping decreased. For θ_A values than 120° , a great number of oil layers were present in the network and so very low S_{or} could be reached.

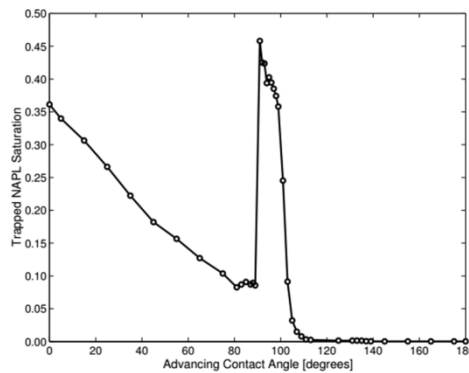


Figure 2.8 – Trapped oil saturation in response to advancing contact angle (Al-Futaisi and Patzek, 2003).

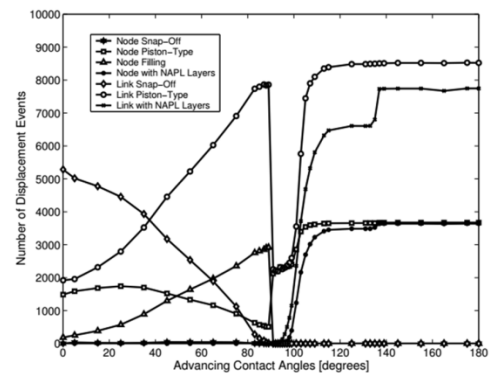


Figure 2.9 – Effect of advancing contact angle on secondary drainage flow regimes (Al-Futaisi and Patzek, 2003).

The sensitivity of θ_A on S_{or} reflected competition between different pore-level displacement mechanisms during imbibition process (**Fig. 2.9**). The dominant snap-off mechanism was responsible for the largest S_{or} observed in strongly water-wet systems. As the contact angle hysteresis increased, snap-off was largely replaced by pore body

filling mechanisms in case pore-throat aspect ratio was not too large. The compact water clusters provided minor oil trapping, therefore less S_{or} . When θ_A exceeded 90° , the imbibition was forced. Pore body filling was completely inhibited and the possible flow regimes changed to be forced snap-off and piston-type displacement with the existence of oil layers in the pore corners.

CHAPTER 3

STATEMENT OF THE PROBLEM

To date, pore network model (PNM) approach has successfully predicted the multiphase flow properties of sandstones. However, there are limited pore network modeling studies of heterogeneous carbonates due to their complex multiscale pore system and nonuniform wettability character. In this thesis, our purpose is to generate representative pore networks of Middle East carbonates incorporating a detailed description of the real void space and to develop a comprehensive flow simulation algorithm under arbitrary wettability conditions. For this reason, a multistage workflow is adapted in our study including three main parts as:

- 1.** Pore structure characterization of carbonate samples for the determination of main geometrical and topological properties of their pore spaces via SEM image analysis (at 75X and 750X magnifications) and physical core measurements.
- 2.** 3D representative network construction and the description of basic quasi-static pore-scale flow equations.
- 3.** Quasi-state flow simulations within the proposed network models for a complete primary drainage-secondary imbibition-secondary drainage cycle. The simulations incorporate wettability alteration and contact angle hysteresis, the corner and intermediate layer flow under mixed-wettability conditions and sensitivity analysis elucidating the effects of surface wettability and pore structure features on two-phase flow behavior.

CHAPTER 4

PORE STRUCTURE CHARACTERIZATION OF MIDDLE EAST CARBONATES AND NETWORK MODEL INPUT DATA

In this chapter, the physical properties of Middle East carbonate samples to be studied throughout the thesis are introduced. Then, for reasonable pore network representation of carbonate samples, the essential geometrical and topological input data derivation with the aid of SEM-image analysis and core measurements namely mercury intrusion porosimetry and helium pycnometry are described in detail.

4.1 Materials

This study is carried out with four carbonate samples, referred to as C013, C016, C019, and C021, from a giant Middle Eastern carbonate oil field. Trimmings from four 1.5-inch (3.81 cm) diameter core plugs (C013, C016, C019, and C021) were collected from a nine-foot interval within the heterogeneous carbonate reservoir.

Slabbed core images with plug locations and petrophysical properties are given in **Fig. 4.1** and **Table 4.1**, respectively. Slabbed core images highlight the diversity in porosity features even in such a short reservoir interval (nine foot). Whole core porosities range from 43 to 51.4% with permeability values from 154 to 225 mD (**Table 4.1**). From the plug data, the largest porosity sample, C013, has the maximum permeability (51.4%, 225 mD), whereas the sample with the next highest permeability, C021, has the smallest porosity of the four samples (43.0%, 212 mD). This complexity occurs when total porosity does not correlate with permeability, which is prevalent in Middle East carbonates (Saller et al., 2014); rather, permeability is controlled by the distribution of porosity types and their associated throat sizes control permeability

(Morrow, 1971; Li et al., 1986; Etris et al., 1988; Ehrlich et al., 1991b), thereby providing, in part, the motivation for this study.

Petrophysical properties of carbonate rocks including porosity, permeability, saturation, and pore size distribution are controlled in part by their mineralogy. Based on elemental analysis via energy dispersive X-ray spectroscopy (EDS), the samples are predominantly dolomite ($\text{CaMg}(\text{CO}_3)_2$). During diagenesis period, dolomite has replaced primary aragonite and calcite (CaCO_3) preserving the original depositional texture while altering its mineralogy (Saller et al., 2014). Dolomitization may contribute to large reservoir porosities by generating secondary intercrystalline microporosity (Sun, 1995; Saller et al., 2014); this is true for our study samples (**Table 4.1**) and is discussed in subsequent sections. Pore-filling cements are also encountered during elemental analysis including calcite (CaCO_3), gypsum ($\text{CaSO}_4 \cdot 2\text{H}_2\text{O}$) and fluorite (CaF_2). In brief, carbonate samples are composed wholly of dolomite with minor amounts of pore-filling calcite, gypsum for C013 and C021, and trace amount of fluorite in C019 and C021 (**Fig. 4.2**).



Figure 4.1 – Slabbed core images of carbonate reservoir section in the study well (The plug locations of cores studied, i.e. C013, C016, C019, and C021 are circled in red on the slabbed core images from left to right, respectively).

Table 4.1 – Petrophysical properties of whole carbonate core plugs.

Sample	ϕ (%)	k_{air} (mD)	Grain density (g/cm ³)
C013	51.35	225	2.803
C016	47.65	162	2.830
C019	46.96	154	2.846
C021	42.97	212	2.800

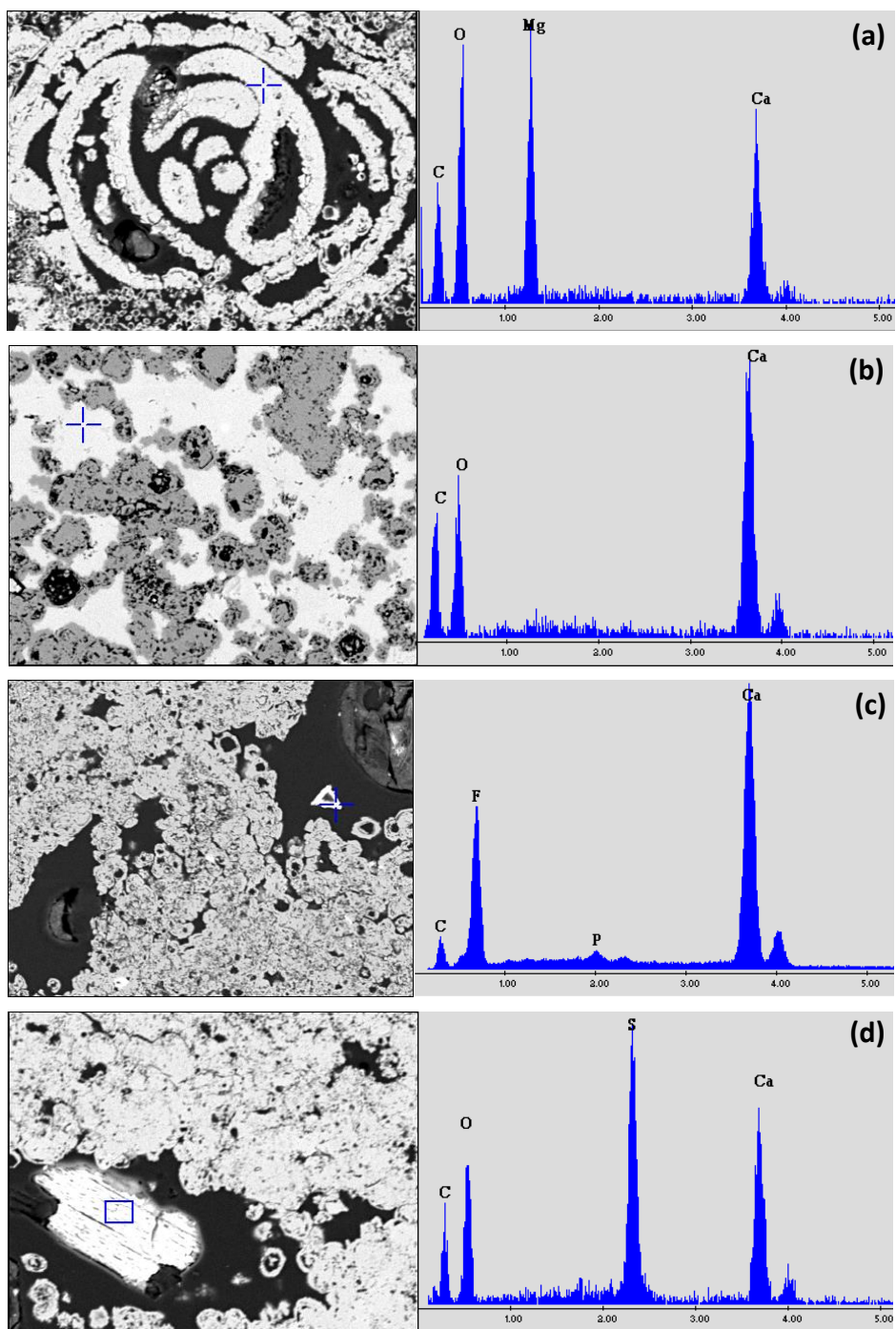


Figure 4.2 – SEM/EDS elemental analysis.

Individual peaks in X-ray spectrum show elevated concentration of particular element.
a) Dolomite, $\text{CaMg}(\text{CO}_3)_2$. b) Calcite, CaCO_3 . c) Fluorite, CaF_2 . d) Gypsum, $\text{CaSO}_4 \cdot 2\text{H}_2\text{O}$.

4.2 Methods

SEM imaging along with associated image processing, helium pycnometry, and mercury intrusion porosimetry (MIP) are employed complementarily to examine pore morphology and topology of carbonate samples. In the following, the basis of each method is described in detail.

4.2.1 SEM imaging

Many carbonates have significant microporous features that are not fully resolvable via current micro-CT scanning tools (Clerke, 2009; Prodanović et al., 2014). SEM imaging of thin sections allows the 2D characterization of pore morphology with sub-micrometer resolution. SEM is an effective nondestructive technique in the analysis of pore structure at microscopic scale. Backscattered electron (BSE) images illustrate the contrasts in rock sample components based on their average atomic number. The dense minerals having higher average atomic number appear as brighter areas than the areas with low average atomic numbers such as epoxy in BSE images. Energy dispersive X-ray spectroscopy (EDS) is useful in qualitative determination of chemical compositions. Each element has characteristic X-ray energies identifying elemental composition of samples (Ross and Kovscek, 2002). BSE images can be used to discriminate between different components.

Prior to SEM imaging, carbonate thin sections (**Fig. 4.3**) are prepared by impregnating with blue-dyed epoxy. Once the epoxy is cured, the samples are cut, the exposed rock surface adhered to a standard petrographic slide, excess material is cutoff, the exposed surface is ground down to 30 μm , and this surface is then polished. Epoxy-impregnation of the samples provides contrast between pore and solid phases during SEM imaging and stabilizes the structure while stressed by cutting, grinding, and polishing. It is noteworthy that epoxy can only fill interconnected portions of the pore network. Circles of double-sided carbon tape are used to fix the thin sections to the mount, and carbon paint is applied to improve conductivity. SEM images were collected using a JEOL JSM 5600LV model coupled with an energy dispersive spectrometer

(EDAX Sapphire Si(Li)) for qualitative elemental analysis and a backscattered electron detector (BSE) (**Fig. 4.4**).

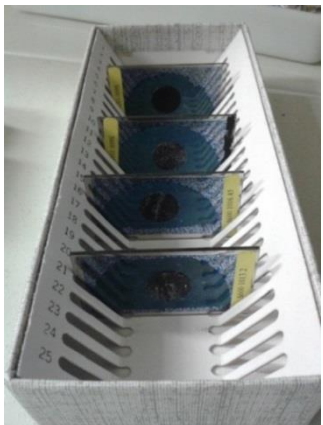


Figure 4.3 – Carbonate thin sections.



Figure 4.4 – SEM/EDS instrument.

In imaging studies, selection of the image resolution (pixel size) and field of view (FOV) are significant as they limit the minimum and maximum pore sizes that can be detected. Due to the ‘trade off’ between image size and resolution, generally multiple magnifications are preferred in pore characterization studies to detect microporosity features together with large-scale macropores (Pamukcu and Gualda, 2010; Jiang et al., 2013).

In this study, SEM images were collected at 75X ($2.63 \mu\text{m}/\text{pixel}$) and 750X ($0.077 \mu\text{m}/\text{pixel}$) magnifications (**Fig. 4.5**). By this way, a large pore size range extending from micropores as small as $0.077 \mu\text{m}$ up to the largest pore encountered at $310 \mu\text{m}$ is captured. The 750X or high magnification images have a FOV measuring 2048 by 1600 pixels ($158 \times 123 \mu\text{m}$) that is smaller than the largest pore detected. The 75X or low magnification images are composed of 640 by 480 pixels ($1683 \times 1262 \mu\text{m}$) containing pores as small as $2.63 \mu\text{m}$ as well as those too large to be imaged at 750X. Accordingly, one 75X pixel corresponds to the area of 1167 pixels at 750X. At low magnification, thin sections in their entirety were scanned requiring 335 to 435 overlapping images per sample. For high magnification, 39 to 77 images were sampled in a loosely-defined grid to represent the entire thin section. The number of high

magnification images depends upon the number of images required to generate stable average SEM porosity values.

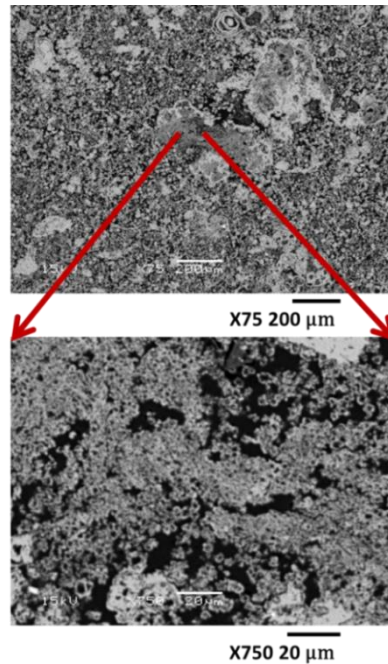


Figure 4.5 – SEM images of the same region at low (75X) and high (750X) magnifications.

Adobe Photoshop CS5.1 was used for preprocessing adjustments, segmentation, correction of misclassified regions, and image compilation. Before image processing, individual 750X and compiled 75X (mosaics) images were segmented from their original grayscale mode (**Fig. 4.6a**) into binary pore and non-pore pixels (**Fig. 4.6b**) by thresholding. The threshold value was chosen using the grayscale intensity histogram in which peaks were associated with either epoxy-filled pores or individual minerals. After choosing the particular threshold value, the size and shape of the resulting pores (black) were visually confirmed. In some cases, portions of the pore space were misclassified as non-pore due to incomplete epoxy impregnation and other issues and thus threshold determination might be somewhat ambiguous. Therefore, these few misclassified solid regions were corrected by painting and cropping for improved pore characterization (**Fig. 4.6c**).

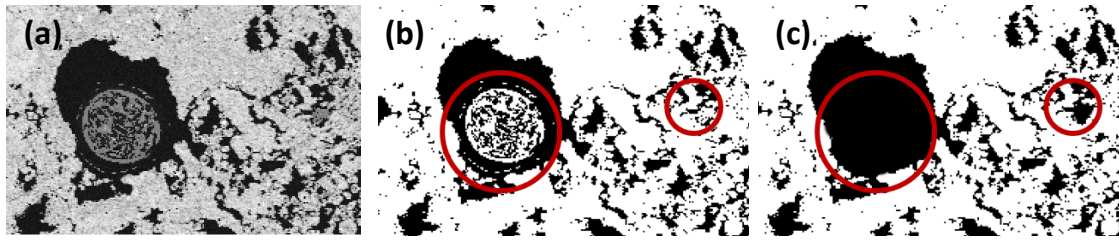


Figure 4.6 – Image segmentation from a) grayscale to b) binary mode and c) correction of incomplete epoxy impregnation regions by painting (Images are 700 μm wide).

4.2.1.1 Mosaicking

Lemmens and Richards (2013) demonstrated mosaic construction prior to image analysis as a tool to resolve small pores while still capturing larger pores. Mosaics enable the analysis of a more representative area of the core plug in a single composite image at nanometer-scale resolution. Their study was aided by mosaicking software that tracks piezoelectric stage alignment while recording overlapping images and automatically adjusting image controls such as brightness and contrast. The resulting tiled images were readily stitched together using automated software.

In contrast, the low resolution 75X images used in this study for mosaic construction were collected on an older SEM with a manually manipulated stage. To resolve even smaller pores, mosaics could be constructed using 750X images (0.077 $\mu\text{m}/\text{pixel}$), but it would not be feasible to collect manually and align the nearly 50,000 required images with 40% overlap (10% each edge). Instead, 335 to 435 overlapping images of the entire thin sections were digitized at low magnification (75X; 2.63 $\mu\text{m}/\text{pixel}$) to construct mosaics of the carbonate thin sections.

For combining or stitching the images together, the automated mosaicking method in Adobe Photoshop CS5.1 was tested, but it did not provide proper alignment of the images due to resolution issues and complexity of the views. Manual image alignment was based on operator's visual assessment. As many as four images may overlap in a region providing confidence in the alignment (**Fig. 4.7**). The low resolution composite mosaics then underwent preprocessing adjustments prior to image compilation to ensure uniform contrast and brightness. After the grayscale mosaics were compiled, they were thresholded into binary mode (pores are black, non-pore regions

are white) and corrected for misclassified regions such as areas affected by incomplete epoxy impregnation (**Fig. 4.6**).

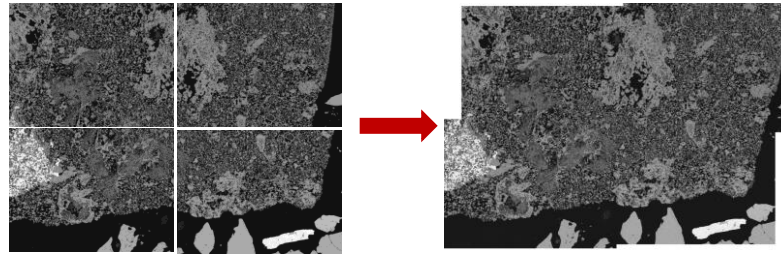


Figure 4.7 – Mosaicking of SEM overlapping images.

The resulting binary mosaics shown in **Fig. 4.8** (their full page versions are given in **Appendix A**) consolidate structural details of entire thin sections in a single composite image and provide a link between pore- and core-scale features. Visual examination of **Fig. 4.8** reveals that all mosaics, except C019, are quite heterogeneous with respect to the distribution of porosity. In addition, C016 contains some small fractures whereas C021 is distinctly bedded with some readily observed large pores. In comparison, C019 appears homogeneous with more uniform size range and distribution of pores.

4.2.1.2 Resolution effect

For sample C013, a mostly white region on the upper left portion appears to be non-porous in the binary image (**Fig. 4.8**, red oval); however, it is porous in the grayscale image (**Fig. 4.9**). To understand the reason for this seemingly misclassified region in the binary image, additional high magnification images were collected from different sections of the C013 mosaic (**Fig. 4.9**). These images reveal that the regional shading in the binary image is controlled by particle and pore size in relation to pixel size. In the extreme case (**Fig. 4.8**, oval; **Fig. 4.9**), pores whose sizes are smaller than one mosaic pixel ($2.63\ \mu\text{m}/\text{pixel}$) cannot be differentiated and are classified as non-porous objects or unresolved pores during thresholding. Microporous regions in the grayscale mosaics (medium gray) result in unresolved porosity in the binary image due to averaging

affects caused by the similar or smaller sizes of particles and pores compared to the pixel size. This type of misclassification is referred to as the “resolution effect”.

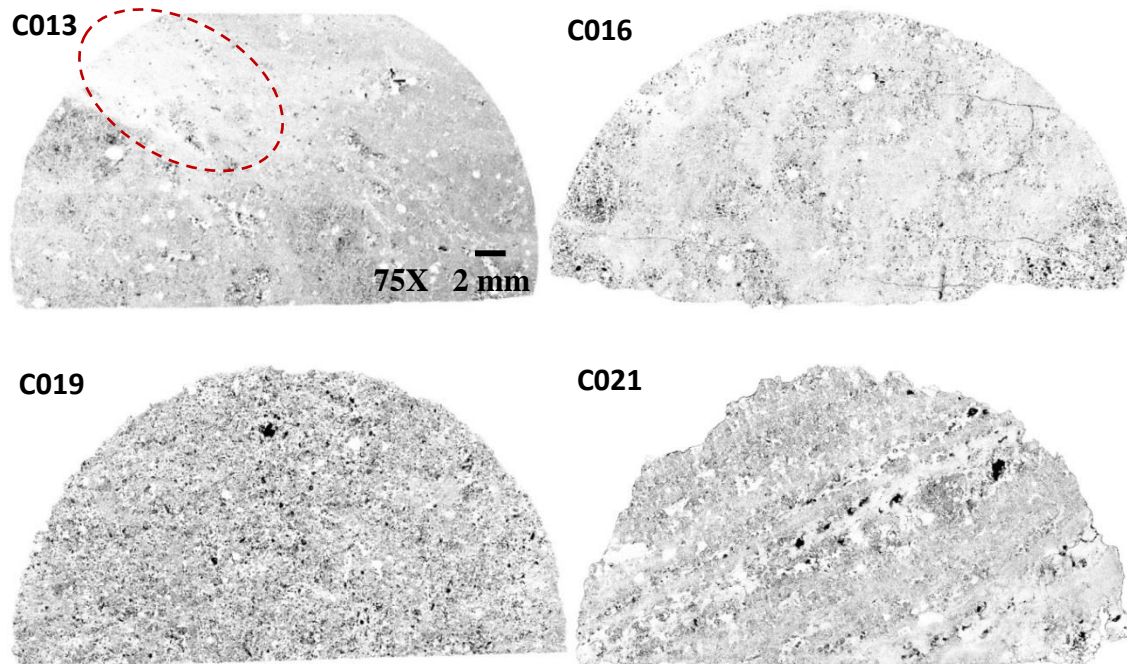


Figure 4.8 – Binary mosaics of C013, C016, C019, and C021 (Epoxy-filled pores are black and rock matrix is white).

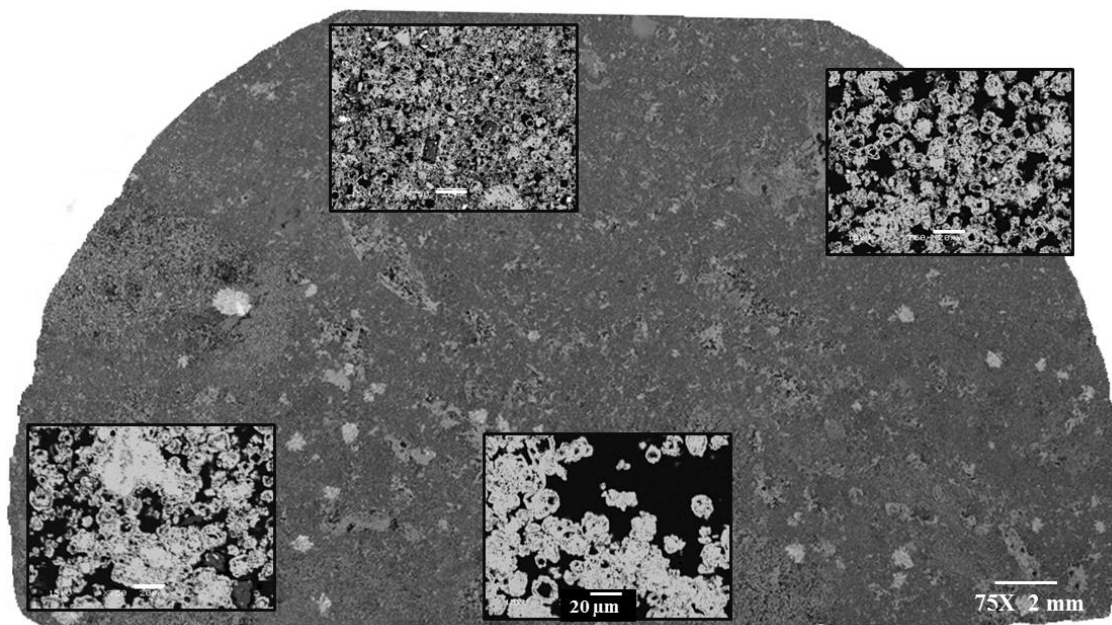


Figure 4.9 – Resolution effect in C013 grayscale mosaic.

4.2.1.3 Image processing

While visual inspection of the images provides useful information, we seek to determine quantitative pore network measures including spatial correlations, connectivity, and size distributions of carbonate pore system. Such pore network elements provide a detailed representation of complex pore systems and serve to populate subsequent models (Øren and Bakke, 2002; Al-Kharusi and Blunt, 2007; Jia et al., 2007; Prodanović et al., 2014).

Erosion-dilation (E-D) is a common morphological image processing technique (Serra, 1982; Heijmans, 1995) that has been applied to 2D pores exposed in thin section (Ehrlich et al., 1984, 1991a; Øren et al., 1998; Ross and Kovscek, 2002). During E-D, a layer of pixels is removed (eroded) from the 2D pores followed by the addition of a layer of pixels (dilation) on the pore remnant (**Figs. 4.10** and **4.11**). Pixels not restored in the subsequent dilation cycle are attributed to roughness elements at that cycle size. This process is repeated for two pixel layers, three pixel layers, and so on until no pore remnant is left. In **Fig. 4.10**, idealized erosion-dilation processes on example 2D pores show the progressive cycles until there is nothing left to dilate (top left), separation of different pore sizes (top right), and distinction between pore body size and shape irregularities (bottom; Ehrlich et al., 1984). **Figure 4.11** indicates erosion and dilation results after 1, 5, 7, and 9 (last) cycles on an example 2D pore. The pore shape smooths progressively as increasingly larger roughness elements are removed. The smooth porosity is the porosity remaining before the entire 2D pore is eroded on the final cycle (in this example, 10th cycle).

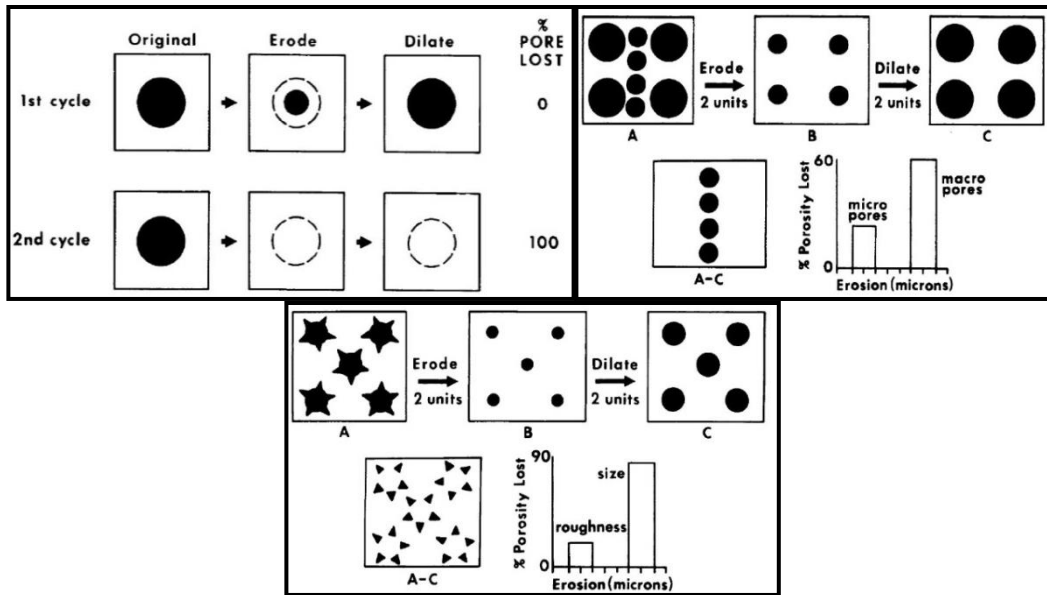


Figure 4.10 – Idealized erosion-dilation on example 2D pores showing the progressive cycles until there is nothing left to dilate (top left), separation of different pore sizes (top right), and distinction between pore body size and shape irregularities (bottom; Ehrlich et al., 1984).

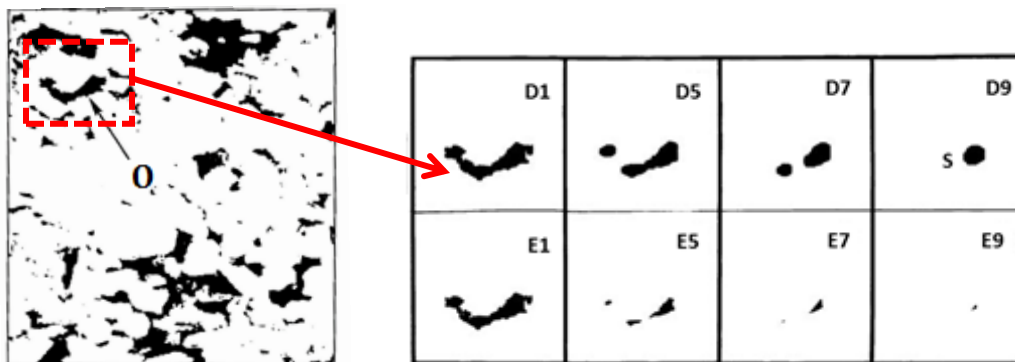


Figure 4.11 – Erosion-dilation results after 1, 5, 7, and 9 (last) cycles on an example 2D pore (O) (Ehrlich et al., 1991a).

Ehrlich and others (1984) developed optimized E-D software that records 2D pore area, size, and perimeter as well as the size and abundance of apparent constrictions where the 2D pore splits into two or more objects. E-D provides a set of variables summarized for each image (**Table 4.2**, left) and its individual 2D pore objects (**Table 4.2**, right). Units are in pixel lengths (perimeter) and pixel counts (area). The resulting E-D cycle number of each pore element is used to determine the smallest dimension of that 2D pore, which is the equivalent of the apparent maximum flow

diameter. Due to different magnifications and, therefore, pixel sizes, cycle numbers do not refer to the same length and are converted to a common pore width or diameter by **Eq. 4.1:**

$$\text{Maximum pore width } (\mu\text{m}) = 2 \times \text{Cycle number} \times \text{Pixel size } (\mu\text{m}) \quad (4.1)$$

Measurements on 2D images are based on established geometrical probabilities that relative areas (such as porosity) exposed in planar sections are equivalent to their relative volumes (Kendall and Moran, 1963). This 2D to 3D relationship also holds true for perimeters, surface area, and parameters calculated therefrom. The image-based structural measurements of 2D pores exposed in thin section are more variable in size and shape in comparison to their actual 3D counterparts (Graton and Fraser, 1935; Sahu, 1968). A unimodal spherical pore network yields a 2D distribution and subsequent average that is smaller than the actual size. Based on Krumbein's work (1935), an average size calculated using the number of 2D pore slices is 76% of the actual diameter whereas a weighted average based on the area of the 2D pore slices is 86% of the actual diameter.

Table 4.2 – E-D output parameters compiled by image (left) and individual pore objects (right).

Parameter	Description	Parameter	Description
X ₁	Number of 2D pores	OBJ	Object number
X ₂	Number of constrictions (2D throats)	Cycle	Number of cycles for the 2D pore
X ₃	Number of 2D pores with constrictions	N _{th}	Number of constrictions or 2D throats
X ₄	Total pore area	T _{area}	Total pore area
X ₅	Smooth pore area	S _{area}	Smooth pore area
X ₆	Rough pore area	R _{area}	Rough pore area
X ₇	Area of 2D pores with constrictions	T _{peri}	Total perimeter
X ₈	Total pore perimeter	S _{peri}	Smooth perimeter
X ₉	Smooth pore perimeter	R _{peri}	Rough perimeter
X ₁₀	Rough pore perimeter		
X ₁₁	Total area		
X ₁₂	Max number of cycles		

4.2.1.4 SEM porosity

SEM-based porosity is the ratio of pore area to total area (X_4 to X_{11} in **Table 4.2**) given by **Eq. 4.2**. The area inputs X_4 and X_{11} are in pixel counts. Total area equals the sample area.

$$\phi_{SEM} = \left(\frac{\text{Total Pore Area}}{\text{Total Area}} \right) \times 100 = \frac{X_4}{X_{11}} \times 100 \quad (4.2)$$

For the mosaics (75X), SEM porosities are found to be 14.9, 11.7, 21.3, and 17.8% of the total sample area for C013, C016, C019, and C021, respectively and given in the first row of **Table 4.3**.

Table 4.3 – Porosity of 75X, 750X, and multiscale SEM-derived data (+ adjusted porosity).

	C013	C016	C019	C021
ϕ (75X), % area	14.9	11.7	21.3	17.8
ϕ (750X), % area	33.6	31.5	32.2	33.0
ϕ (750X_LPA) ⁺ , % area	33.0	30.6	30.0	31.8
ϕ (Multiscaled), % area	33.6	31.9	30.6	31.8

Low and high magnification cumulative pore size distributions are plotted in **Fig. 4.12**. Based on **Fig. 4.12a**, C019 has the greatest porosity attributed to larger pores between 16 and about 90 μm in diameter and the least amount of small pores ($< 16 \mu\text{m}$) in the low resolution mosaics (**Fig. 4.8**). The cumulative distributions of C013, C016, and C021 converge at about 60% pore area and 16 μm pore width revealing that the relative amount of micropores for these three samples is equal to or greater than 40% of the total mosaic porosity (**Fig. 4.12a**). Similar relationships are observed in the high resolution pore size distributions where the amount of microporosity is greatest for C016 followed by C013, C021, and C019, respectively (**Fig. 4.12b**). The trends merge at a pore size of about 2 μm . The main difference between two plots is that C013 has more area attributed to small pores than C016 at 750X whereas the reverse is true for the 75X distributions. Resolution issues as discussed previously account for this change.

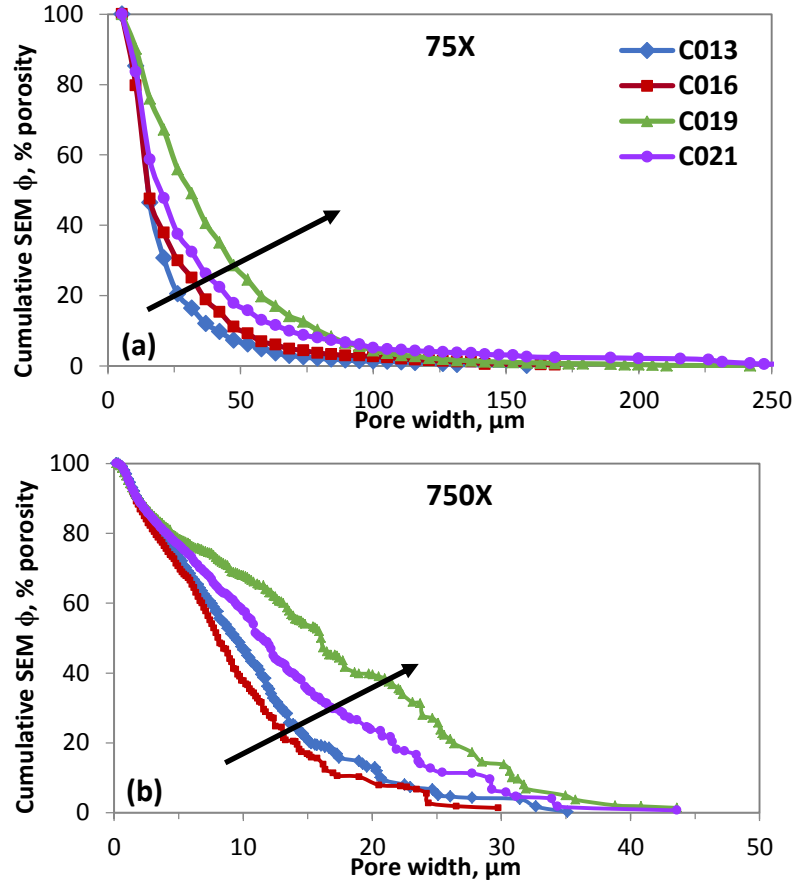


Figure 4.12 – Cumulative SEM pore size distributions for a) mosaics (75X) and b) high magnification images (750X) of carbonate samples (Arrows indicate trend for increasing percentage of large pores).

4.2.1.5 Sampling

A substantial number of views are necessary to ensure that the variability in pore shape and size characteristics contained within a heterogeneous rock is adequately sampled (Ehrlich et al., 1991a; Chatzis et al., 1997). Large numbers of views are required for a stable average porosity given the small fields of view in samples with either scalar heterogeneities or relatively rare large pores (Ross and Kovscek, 2002). In our case, the total and sequential average porosities are used to verify sample set sufficiency at 750X and the reliability of the measurements.

SEM porosity of individual 750X images is calculated again using **Eq. 4.2** except, in this case, total area equals the image area. Sequential average porosity is computed with increasing number of images until the addition or subtraction of an

image does not affect the average porosity. The combined or total average SEM porosity and sequential average SEM porosity per sample are calculated by the following equations:

$$Total \bar{\phi} = \sum_{i=1}^k \phi_i / k \quad (4.3)$$

$$Seq \bar{\phi} = \sum_{i=1}^n \phi_i / n \quad (4.4)$$

where i refers to individual images, k the maximum number of images, and n the number of images included in the average.

The plots of the sampling proficiency determination are shown in **Fig. 4.13** for all samples. In **Fig. 4.13**, blue dots are porosities of individual images, the red line per sample is the total average porosity calculated using all of the views, and orange triangles are the sequential average porosities that stabilize at the total average porosity as the number of individual images included in the sequential average increases. According to **Fig. 4.13a**, C013 requires about 40 views for a stable average porosity. The remaining samples (C016, C019, and C021) are sufficiently sampled using 25, 51, and 50 images, respectively. Once these thresholds have been met, the standard deviations for subsequent sequential porosity averages are 0.21, 0.15, 0.12, and 0.26% area for C013, C016, C019, and C021, respectively, and apply to the 750X average porosities in **Table 4.3**. This establishes that more than enough images were collected to capture heterogeneities in the porosity distribution for each sample.

SEM porosity averages (and ranges) at 750X are found to be 33.6 (5.3 to 51.9), 31.5 (18.0 to 46.5), 32.2 (6.0 to 56.8), and 33.0 (4.3 to 61.8) % image area for C013, C016, C019, and C021, respectively (**Table 4.3**). Porosity averages at 750X are much larger than the porosities measured at 75X (**Table 4.3**). This is due to improved pixel resolution (from 2.63 μm to 0.077 μm), thereby resolving and measuring pores that are as small as 3% of the low resolution pixel size. Conversely, porosity at 750X does not include pores larger than 43.58 μm width. This pore size limitation at 750X results from the limited FOV as well as the E-D processing requirement that most of the pore wall be included within the image for accurate size and perimeter measurements. Exclusion of these large pores skews porosity calculations and requires correction before merging the low and high magnification data into a multiscale pore size distribution.

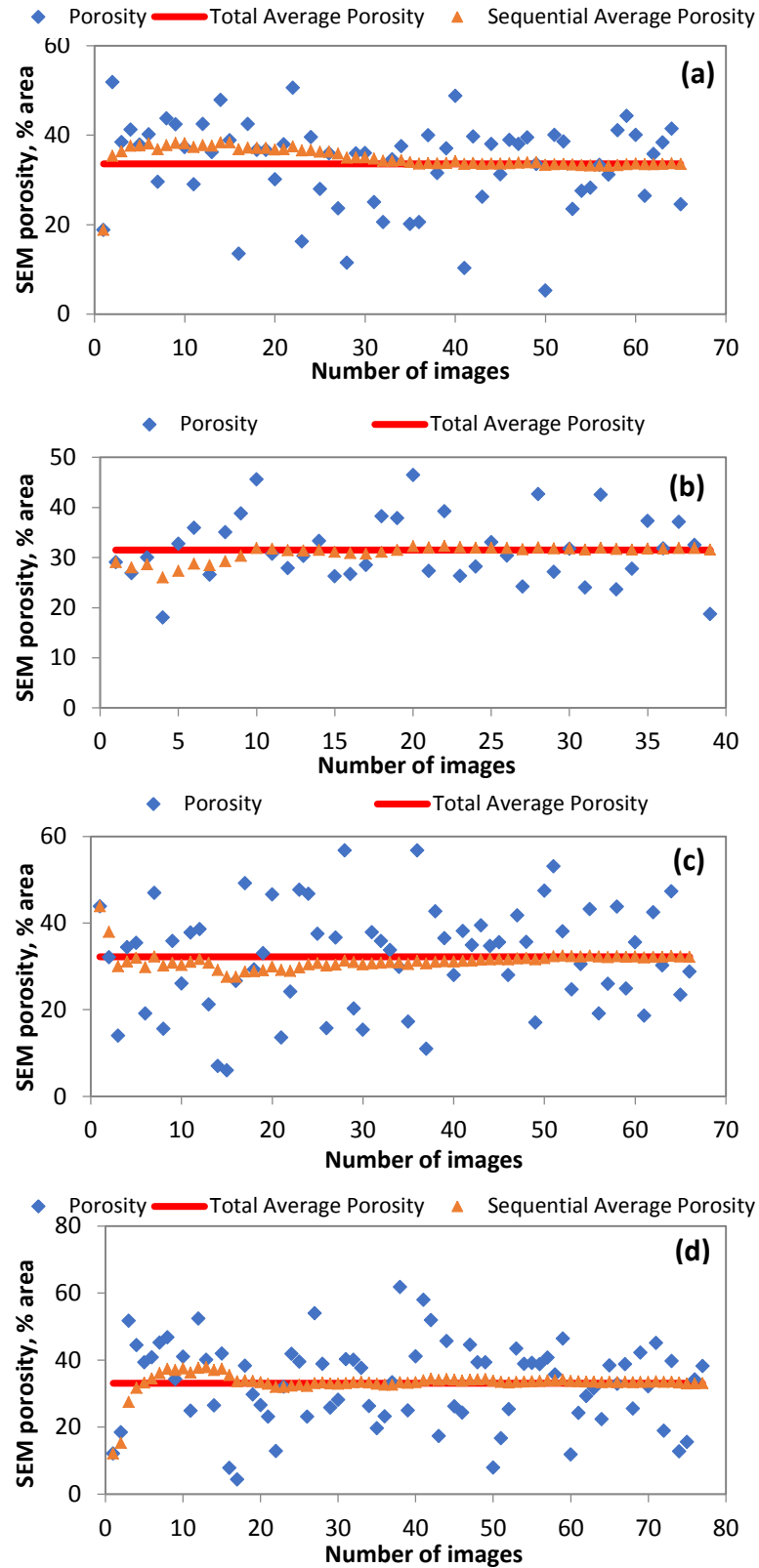


Figure 4.13 – Sampling tests for a) C013, b) C016, c) C019, and d) C021 at high magnification (750X).

4.2.1.6 Multiscale SEM porosity

Image-derived porosities (**Table 4.3**) are less than whole core plug porosities measured in the laboratory (**Table 4.1**). This is particularly true for the low magnification mosaics with porosity values 54.7 to 75.6% less than core porosity measurements. This unresolved porosity is attributed to micropores as indicated by the increase in porosity as image resolution increases (2.63–0.077 μm). Cantrell and Hagerty (1999, 2003) stated that micropores, that are volumetrically significant in Middle East reservoirs, are usually filled with capillary-bound water whereas macropores are filled with oil due to mixed-wet mineral surfaces. Substantial amounts of microporosity cause large immobile water saturations affecting log response, flow behavior, and ultimate recovery of hydrocarbons, confirming the significance of incorporating the full range of complexity from micro- to macro-scale pores in carbonate network modeling.

Before integrating the low and high magnification data into a multiscale pore size distribution, areal correction is required since high and low magnification porosities represent different total areas. While mosaics cover the entire sample area, high magnification images are subsamples of the thin section. Large pores (i.e., those pores that fill the FOV ($> 43.58 \mu\text{m}$) in diameter) are excluded from 750X images, because a significant portion of the pore perimeter lies outside the FOV. The missing porosity associated with large pores affects the total porosity as well as the amount of porosity attributed to large pores thereby skewing the 750X pore size distribution. On the other hand, small pores (typically $< 2.63 \mu\text{m}$) and small scale roughness features along the pore walls cannot be detected in the low resolution mosaics due to the resolution effect. As it is not possible to correct existing data for resolution issues, 750X porosities are renormalized to compensate for the missing large pore areas (LPA) in the total 750X image area (**Table 4.3**). Following this correction, both of the pore size distributions are plotted using a common scale as shown in **Fig. 4.14** (green).

Figure 4.14 depicts the low and high magnification cumulative pore size distributions together with their multiscale curves for all carbonate samples. The overlapping or coincident pore size interval is 5.26 to 35.112 μm for C013, i.e. 5.26 μm is the minimum pore diameter for 75X and 35.112 μm is the maximum for 750X. The

region of pore size overlap is between 5.26 and 29.722 μm for C016, and 5.26 and 43.58 μm for C019 and C021. The 75X and 750X cumulative porosities for C013 converge at 11 to 21 μm whereas they converge from 11 to 16 μm for the remaining samples (**Fig. 4.14**). **Table 4.3** includes 750X porosities after LPA adjustment and final multiscale SEM porosities. Although improved, the multiscale SEM porosity values are still 26.1 to 34.8% smaller than the porosities measured on whole core plugs (**Table 4.1** versus **4.3**).

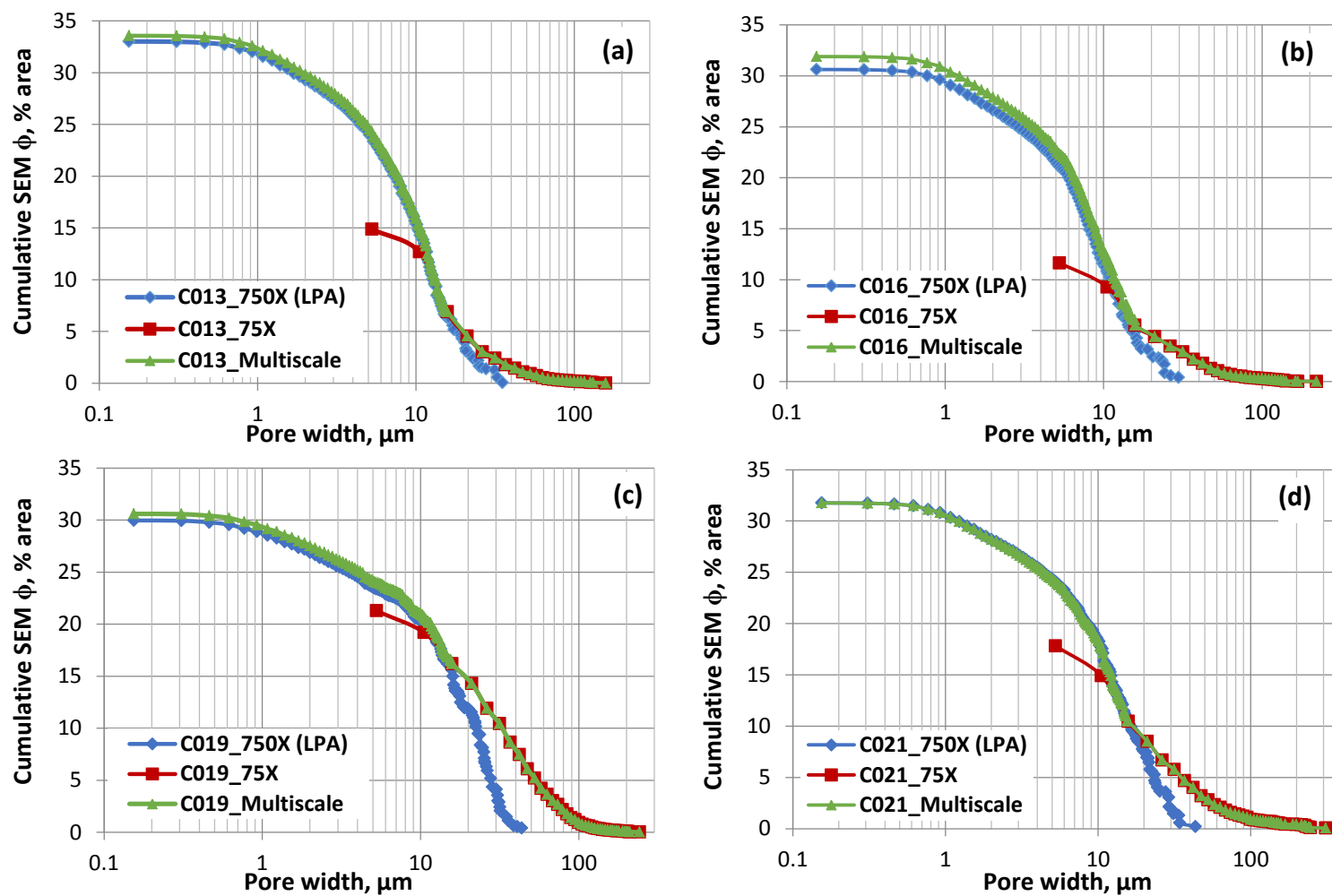


Figure 4.14 – Cumulative pore size distributions for 75X, 750X, and multiscale SEM-derived data of carbonate samples a) C013, b) C016, c) C019, and d) C021.

4.2.2 Core measurements

Helium pycnometry and mercury intrusion porosimetry (MIP) tests are performed to obtain petrophysical core properties, namely porosity, grain density, and capillary pressure data.

4.2.2.1 Helium pycnometry

High precision volume measurements were conducted on small subsamples or chips (0.3 to 1.2 cm) using a Micromeritics AccuPyc II 1340 helium pycnometer. Based on Boyle's Law, pressure before and after helium expansion was recorded and repeated for 999 cycles to measure the matrix volume of samples. Grain volume versus cycle number is plotted in **Fig. 4.15** for C019, yielding 0.273 cm³ grain volume. Grain or matrix density was calculated by dividing the sample mass by the resulting grain volume. Matrix densities calculated from measured volumes and the sample masses are presented in **Table 4.4** (center) along with the replicates for some of the samples. The pycnometer-derived matrix densities of the chips are 0.4 to 1.1% less than the whole plug matrix densities (**Table 4.4**). Both measures provide reasonable density values for carbonates composed primarily of dolomite containing minor amounts of other mineral constituents. Published mineral densities are as follows: dolomite – 2.87 g/cm³, calcite – 2.71 g/cm³, fluorite – 3.18 g/cm³, and gypsum – 2.32 g/cm³ (Edmundson and Raymer, 1979; Crain's Petrophysical Handbook, 2015). One possibility for the lower grain (matrix) density of C013 and C021 compared to C016 and C019 may be their gypsum content (**Table 4.4**). Of the repeat runs, the last measurements are selected to represent the samples in subsequent plots.

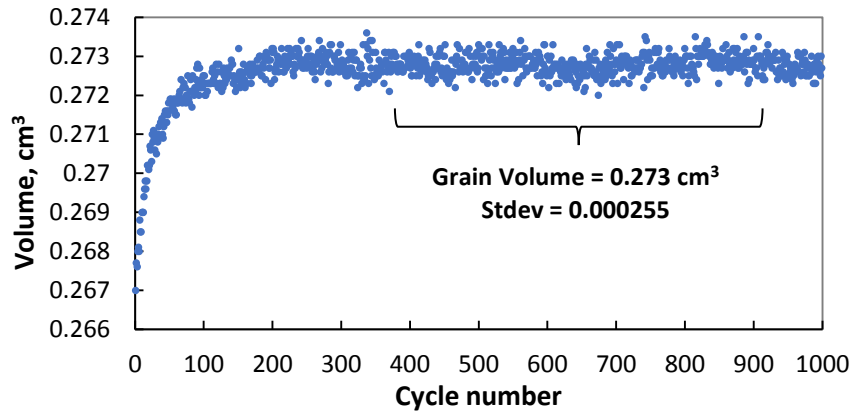


Figure 4.15 – Helium pycnometry run for C019.

Table 4.4 – Matrix density (g/cm³) measurements using He pycnometry and MIP.

Sample	Whole core plug (3.81 cm)	Subsamples (0.3 to 1.2 cm)	
		He Pycnometer	MIP
C013	2.803	2.796	2.650
		2.781	2.622
		2.786	2.685
C016	2.830	2.819	2.713
C019	2.846	-	2.738
		2.821	2.706
		2.813	2.667
C021	2.800	2.788	2.501

4.2.2.2 Mercury intrusion porosimetry (MIP)

Throat size distributions and their pathway configurations are necessary for modeling flow properties of rocks as throats or constrictors control displacement mechanisms in the pore network. Image-derived data provides quantitative information on pore body sizes and geometry, but it does not reveal how pores are connected to each other three dimensionally. Due to the minimal pore volume contributed by throats, the chance of intersecting pore throats within the plane of a thin section is extremely low and, even if they are captured during image scanning, they are classified as micropores for the most part.

Throat sizes and their distribution are measured using mercury porosimetry (Micromeritics AutoPore IV 9500 V1.06 Series) whereby mercury is intruded into the sample at increasing pressures up to 33,000 psia. Throat sizes are calculated using mercury properties and measurement pressure via the Washburn equation (1921). In this manner, the pore volume accessed by throats of increasingly smaller diameters ($\geq 0.0065 \mu\text{m}$) is recorded. The capillary pressure in a throat is always higher than that of a connected pore body. As a result, at the point where threshold capillary pressure P_c^e of a given throat is overcome, non-wetting fluid flows freely into the its connected pore body, those portions with radii larger than or equal to that of the throat.

After correcting for P_c^e (thresholding to remove conforming volume on the outside of the sample from intruding volume), pore throat size distributions of carbonate samples are calculated from their MIP P_c curves as illustrated in **Fig. 4.16**. The trend of the capillary pressure curve of a rock sample gives information about its pore geometry (Rose and Bruce, 1949; Sahimi, 1993). Bimodal trends are obvious in the saturation profiles of C013, C016, and C019 whereas C021, in comparison, does not exhibit the obvious inflection points of the other samples (**Fig. 4.16**). P_c profiles also reveal that C019 is the outlier of the four samples similar to that found in the pore size distributions (**Fig. 4.12**). In **Fig. 4.16**, C019 has more porosity accessed through throats greater than $6 \mu\text{m}$ in diameter compared to the other samples. Conversely, more porosity in C019 is filled via smaller throat diameters (0.237 to $1.7 \mu\text{m}$). The variability in P_c behavior between C019 and the other samples will provide interesting contrasts when constructing pore network models based on these observations.

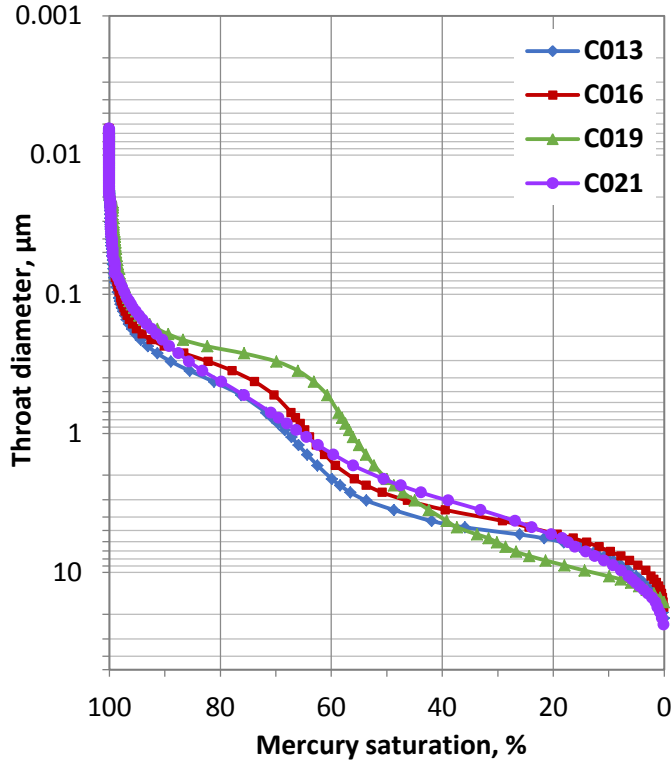


Figure 4.16 – High pressure (33,000 psia) mercury injection profile of carbonate samples.

For MIP tests, small samples or chips may not be adequate to capture fully intrusion information on the largest pore sizes (e.g., 310 μm); therefore, the amount of macroporosity and its potentially larger throat sizes may be under represented. In addition, unfilled porosity is present as either isolated pores or pores connected by throat sizes requiring an entry pressure greater than 33,000 psia. Besides porosity results, the existence of unfilled porosity is also deduced from grain density values generated by MIP runs that are 3.47 to 10.29 % less than those values derived from He pycnometry measurements on the same subsamples (**Table 4.4**).

Porosity values vary depending upon the sample size (3.81 cm diameter core plug vs 0.3 to 1.2 cm chips) and measurement type (helium pycnometry, MIP, and SEM methods) as summarized in **Table 4.5**. Of these methods, helium pycnometry provides the most accurate measure of porosity due to the ability of helium gas with its small elemental size (0.2 nm, Tissot and Welte, 1978) to pass through exceptionally small throats and fill all porosity accessible up to 0.2 nm. Mercury porosimetry leaves some porosity unfilled (3.53 to 12.01% of whole plug porosity; **Table 4.5**) due to maximum

pressure limitation of 33,000 psia equivalent to a throat diameter of 6.5 nm rather than mercury's atomic size (0.31 nm, Bondi, 1964). Porosity measured from SEM images yields the lowest porosity values (32.52 to 35.26% less than whole plug porosity; **Table 4.5**) resulting from unresolved porosity that is either below the pixel resolution (77 nm for 750X) or not filled with epoxy. Of the pore size distribution, these unresolved micropores do not contribute significantly to permeability and, accordingly, multiphase flow properties as indicated in previous experimental studies (Schembre and Kovscek, 2003; Øren et al., 1998).

Whole core plug measures provide overall composite measurements compared to data generated on smaller pieces or chips (**Table 4.5**) due to the significant degree of heterogeneity observed in the mosaics (**Fig. 4.8**). Helium pycnometry on chips provides similar porosity values coming within 0.82 to 2.63% of the whole core plug porosities except for C021 (**Table 4.5**). Unlike the other samples, C021 has a chip porosity that is 13% greater than the plug porosity. This is most likely due to heterogeneity differences between laminations visible within C021 mosaic (**Fig. 4.8**) and those within the core plug. For this project, additional measurements were not possible due to limited sample material.

Table 4.5 – Porosity data from He pycnometry, MIP, and SEM methods as well as whole core plug porosity measurements (Sample sizes are widths).

Sample	Core plug (3.81 cm)	Subsamples (0.3 to 1.2 cm)		
	$\phi_{\text{meas.}}$ (% volume)	$\phi_{\text{meas.}}$ (% volume)		SEM ϕ (% area)
	He Pyc.	He Pyc.	MIP	
C013	51.4	50.0	47.2	33.6
		52.1	49.2	
		51.9	50.0	
C016	47.7	47.3	45.2	31.9
C019	47.0	—	46.4	30.6
		46.5	44.2	
		46.1	43.2	
C021	43.0	48.6	43.0	31.8

For comparison purposes, absolute permeabilities are calculated from MIP data. Swanson (1981) suggested a permeability estimation method using mercury injection capillary pressure data on carbonate samples. In this method, a single point on capillary pressure curve, the maximum ratio of mercury saturation to pressure, $(S_{Hg}/P_c)_{\max}$ point, is determined assuming that all interconnected pore space is filled with mercury at this inflection point and dominate fluid flow. From linear regression, Swanson obtained simple relations of the form,

$$k_w = 290 \left(\frac{S_{Hg}}{P_c} \right)_A^{1.901} \quad (4.5)$$

$$k_w = 0.292 (k_a)^{1.186} \quad (4.6)$$

for determination of brine k_w and air k_a permeabilities. Air permeabilities listed on **Table 4.6** are in good agreement with core measurement range (154 to 225 mD in **Table 4.1**). Of the samples, C013 has the highest Swanson's air permeability followed by C016, C019, and lastly C021 (**Table 4.6**). Repeated mercury injection measurements on C013 yielded Swanson's air permeability values as high as 225.43 mD and as low as 84.93 mD. The low permeability values of C013 most likely correspond to the unresolved porosity pointed out previously in **Fig. 4.8**.

Table 4.6 – MIP permeability determination (Swanson's Method).

Sample	Primary inflection point, $(S_{Hg}/P_c)^*$	k_w , mD	k_a , mD
C013	0.766	195.11	219.54
C016	0.660	131.68	172.93
C019	0.642	125.04	165.55
C021	0.601	110.07	148.68

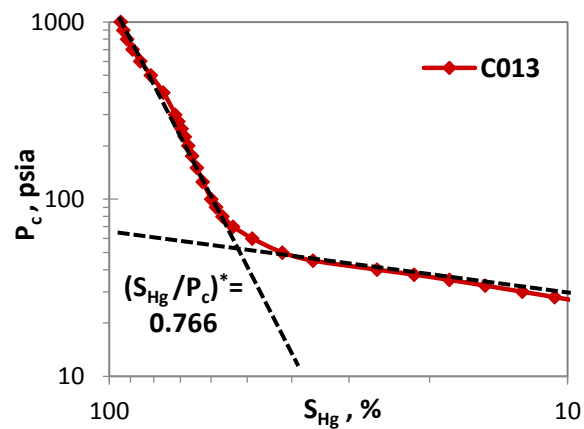


Figure 4.17 – Inflection point on Hg-air P_c curve.

4.3 Pore network elements

Pore network elements, namely pore body and throat size distributions, aspect ratio (pore body to throat size ratio), coordination number (number of throats per pore), shape factor (pore area to perimeter ratio), and their distributions are determined for the characterization of morphology and connectivity of carbonate pore systems.

4.3.1 Image-based pore size distribution

Pore size distributions generated from image data may be viewed as either pore counts or pore area frequency distributions. Pore area frequency distribution indicates the relative abundance (area and therefore volume) of particular pore sizes included in the pore system rather than the number of pores in this size interval. Pore counts or number frequencies give equal weight to individual pores regardless of their size (Krumbein, 1935). Micropores as shown in **Fig. 4.18d** dominate the resulting distributions where the smallest pores (0.077 to 0.154 μm ; first cycle) dominate the number frequency distribution. For image-derived data, the number frequency of micropores may vary depending upon the image resolution and quality; this may introduce bias into pore network models. Therefore, pore area size distributions provide a more appropriate distribution of pore sizes and correspond to the volumetric frequency of sizes within the sample. Although number frequencies may be required in the construction of pore network models, the pore size distribution of the resulting model should mimic that of the area frequency of the measured pore size distribution (Jia, 2005).

Image-derived pore sizes range from 2.63 μm to 241.96 μm at low magnification and from 0.077 μm to more than 43 μm at high magnification for C019 (**Fig. 4.18**). The 75X distribution shown in **Fig. 4.18a** indicates that the majority of the pores are less than or equal to 84 μm in diameter. The equivalent plot for 750X images reveals finer details for pores less than 44 μm in size with at least two modes (at around 1 and 26 μm ; **Fig. 4.18b**). When combined as demonstrated in **Fig. 4.14**, at least 95% of the SEM porosity is attributed to pores less than or equal to 84 μm wide (**Fig. 4.18c**). Comparison of **Figs. 4.18a** and **4.18c** reveals that the first point (smallest pore size bin) of 75X

porosity comprises only 9.8% of the total mosaic porosity versus 21.5% of the multiscale porosity for C019 (**Table 4.3**).

The pore size distribution of 75X mosaic represents a unimodal size distribution (**Fig. 4.18a**); however, 2D pore sizes are equal to or smaller than their actual 3D pore sizes as the maximum diameter is not always transected, yielding a more diffuse pore size distribution. In addition, the 5.26 μm bin widths (includes pore widths of 2.63 to 5.26 μm as dictated by image resolution and the E-D process) may also obscure nuances in the pore size distribution. The multiscale distribution in **Fig. 4.18c** exhibits a similar distribution with 21.5% of the porosity less than 5.2 μm in width and another mode around 10.5 μm in width. Based on the high resolution results, the pore size distribution of carbonates exhibits multimodal behavior (**Fig. 4.18b**).

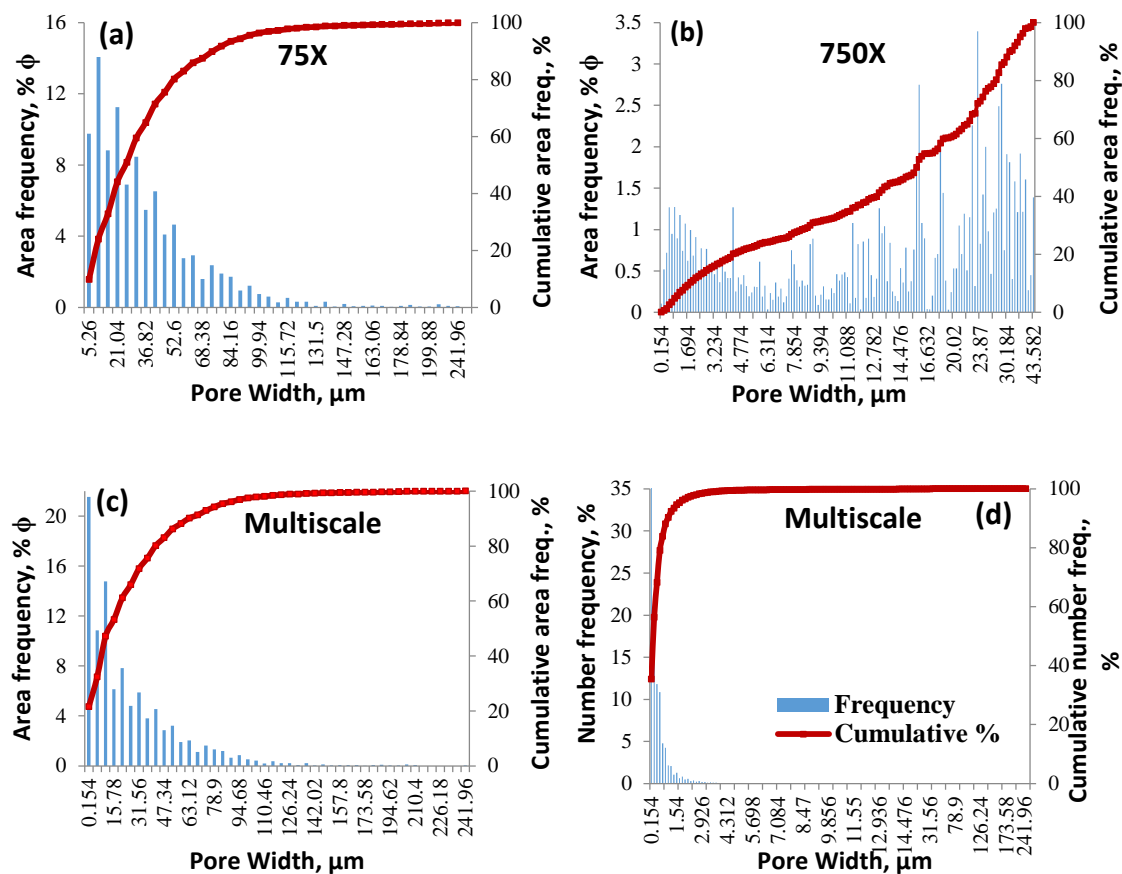


Figure 4.18 – Image-derived pore size distributions of C019 at a) 75X and b) 750X magnifications as well as multiscale SEM data c) in areal frequency and d) in pore counts.

4.3.2 MIP throat size distribution

Despite having the same name, pore size distributions generated by image analysis and mercury intrusion data are not comparable. MIP determines the volume of porosity accessed by increasingly smaller throat sizes rather than the areal abundance of pore body sizes as measured via image analysis. The differential mercury intrusion data vs throat-size distributions are plotted in **Fig. 4.19a**; the last MIP measurements of each sample listed in **Tables 4.4** and **4.5** are used for the distribution plots. Bimodal trends occur in the throat-size distributions of all samples with one mode having throats greater than $0.771\ \mu\text{m}$ in diameter and the other mode occurring for throat diameters less than $0.771\ \mu\text{m}$ (**Fig. 4.19a**). In a similar manner to the pore size distributions via image analysis (**Fig. 4.12**), C019 is the outlier of four samples having the greatest pore volume filled by throats whose sizes are greater than $6\ \mu\text{m}$ (**Fig. 4.19a**). Conversely, more porosity in C019 is filled via smaller throats (0.2 to $0.3\ \mu\text{m}$) than the other samples. The peaks representing each sample align at about 0.24 , 0.53 , 1.71 , 3.56 , 4.74 , 9.69 , and $14.22\ \mu\text{m}$ and differ in the pore volume filled at each throat size. This indicates a consistency between the samples with respect to their throat sizes.

To test the repeatability of throat-size distribution data, mercury intrusion experiments were conducted three times for C013 and C019; the resulting curves are shown in **Figs. 4.19b-c** with related data in **Tables 4.4** and **4.5**. The heterogeneity of C013 (**Fig. 4.19b**) is apparent in differential intrusion curves compared to the relative homogeneity of C019 (**Fig. 4.19c**). Similarly, the C013 mosaic exhibits a heterogeneous porosity distribution compared to that of C019 (**Fig. 4.8**). For the C013 runs (**Fig. 4.19b**), the second run (red) covers a narrower throat size range and begins at a lower throat size ($< 10\ \mu\text{m}$); it probably represents the upper left portion of the sample (**Fig. 4.9**). Likewise, the first run (blue) is most likely from a region with larger, better-resolved porosity whereas the intermediate regions are represented by the intermediate throat size distribution (green, **Fig. 4.19b**). In comparison, all throat size distributions in **Fig. 4.19c** show a good match indicating the pore structure homogeneity of C019 thin section. Of the three measurements for C019, the sample size for the first run (blue, **Fig. 4.19c**) is more than twice the size of the other samples. Hence, the resulting distributions

show that the entirety of the throat size spectrum is characterized regardless of sample size at this scale. The samples for the C013 repeat runs are of similar sizes.

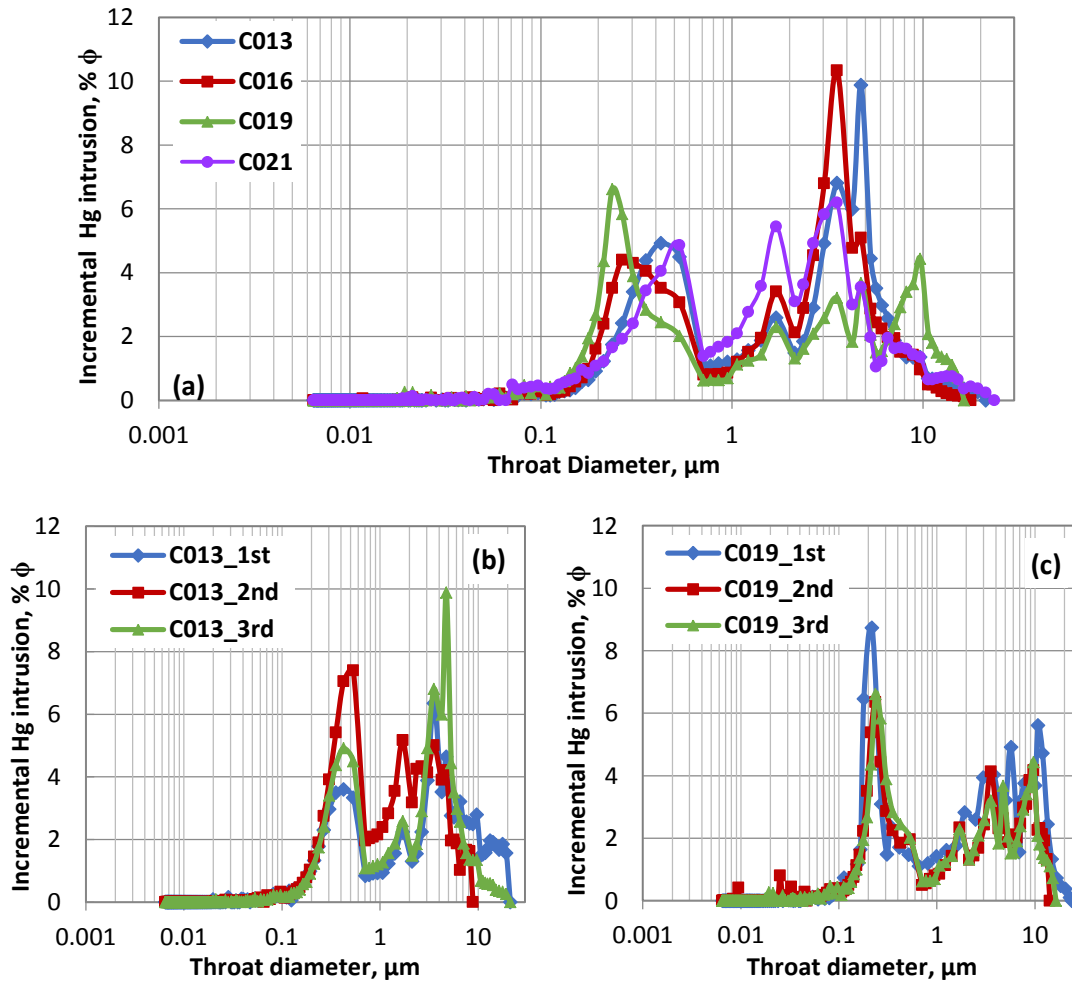


Figure 4.19 – High-pressure MIP throat size distributions of a) all carbonates and replicates for b) C013 and c) C019.

4.3.3 Combination of image (SEM) and MIP distributions

The complementary nature of two measurement types with image analysis determining apparent pore-body size and mercury intrusion measuring throat sizes have been utilized in characterizing entire pore network configurations (Dullien and Batra, 1970; Ehrlich et al., 1991b; McCreesh et al., 1991; Ross et al., 1995; Jia et al., 2007). The resulting size distributions from both methods exhibit wide ranges of pore body (0.077 to 310 μm) and

throat sizes (0.007 to 24 μm) for the carbonates studied. Of note, the minimum limit of the pore size distribution is determined by resolution (or pixel size) for image analysis and the maximum pressure for MIP. Greater coincidence of SEM and mercury intrusion data may be possible with increased maximum pressure ($> 33,000$ psia, smaller throat sizes) and improved resolution (< 0.077 μm pixel size).

Comparison of image analysis and MIP distributions requires expressing the data in equivalent units. MIP data is usually presented as percent or proportion (saturation) of the measured MIP porosity as shown in **Fig. 4.19**. As the porosity values obtained via image analysis and MIP data are not the same (**Table 4.5**), data are plotted as percent bulk volume for MIP and percent sample area for SEM-derived data in **Fig. 4.20**. MIP data includes only connected pores filled with mercury up to 33,000 psia whereas image analysis data is limited by its resolution (i.e., pixel size).

Image analysis-based pore size distributions and their corresponding MIP throat size distributions have a complex relationship. Multiscale SEM porosity (30.6 to 33.6% area) is lower than the MIP porosity (43 to 50% volume), leaving 16.45, 13.30, 12.56, and 11.24% MIP pore volume unresolved via image analysis for samples C013, C016, C019, and C021, respectively (**Fig. 4.20; Table 4.5**). This unresolved 11.24 to 16.45% MIP pore volume is likely attributed to pores smaller than 0.077 μm , which is the pixel size of the high resolution images.

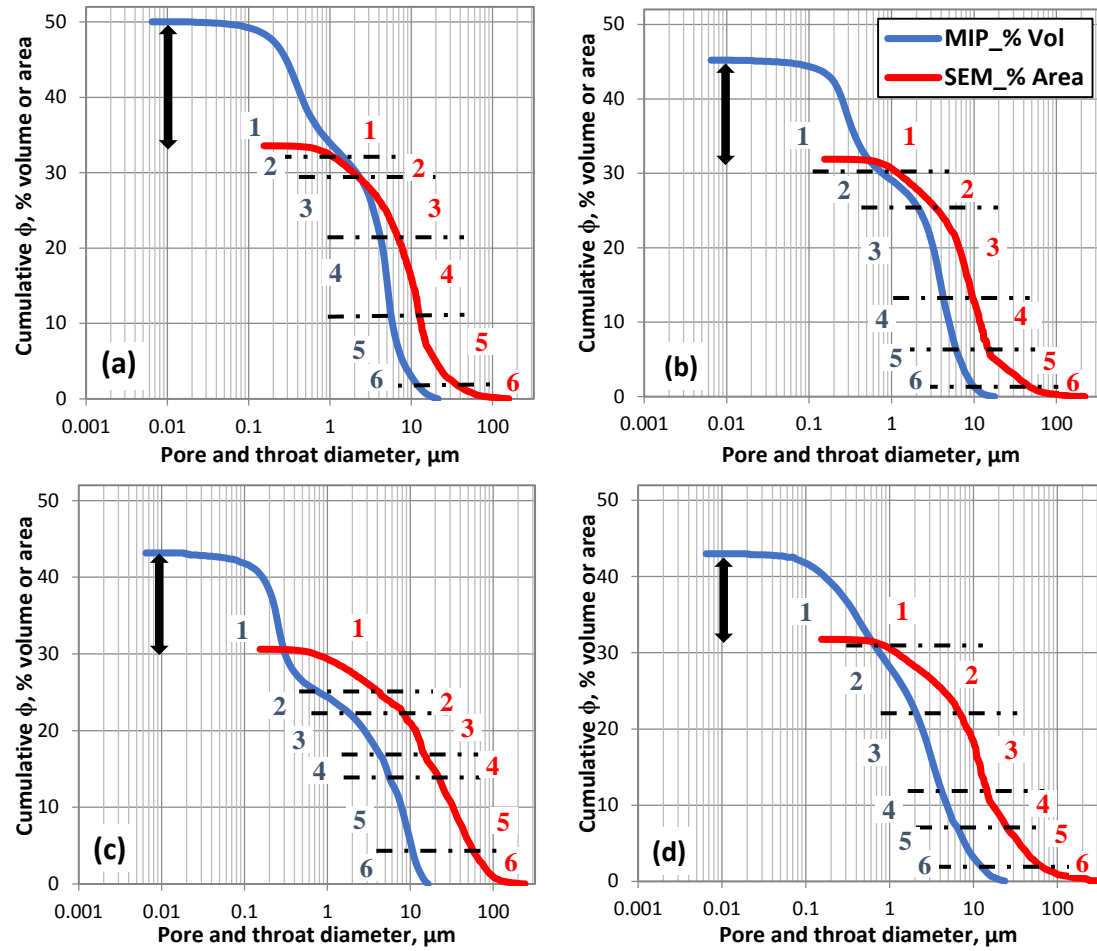


Figure 4.20 – MIP throat size and multiscale SEM pore size versus cumulative porosity (% volume or area) (Arrows indicate unresolved porosity. Dashed lines and numbers delineate the pore classification intervals).

4.3.4 Pore – throat classification method

A fundamental pore-throat classification method is developed by relating mercury volume intruded into throats to its corresponding pore area derived from SEM data. The initial premise of our classification approach is based on a strong spatial correlation between pore body and throat size distributions where larger pores are accessed via larger throats and smaller pore bodies via smaller throats (e.g., Chatzis and Dullien, 1985; Wardlaw et al., 1987; Diaz et al., 1987; Hilpert et al., 2003). This relationship is true for most depositional materials unless subsequent diagenesis has altered this relationship (Berg, 1975; McCreesh et al., 1991). SEM images and petrographic

microscopy of the study samples indicate that their original depositional pore networks are largely intact except for rare patches of diagenetic cement and the addition of intercrystalline microporosity during dolomitization.

Clerke et al. (2008) developed a bimodal pore system classification for the Arab D limestone using mercury injection data alone. In their paper, the capillary pressure histogram is divided into four basic regions. The first interval with large pores is referred to as the macroporosity mode and the remaining three intervals correspond to different types of micropores. In our case, the classification procedure starts with incremental mercury saturation (% porosity) vs throat size plotted on linear scale in **Fig. 4.21**. It is subdivided into six main regions based upon peak locations and inflection points that are common to all samples (**Fig. 4.21**). The resulting pore classes are hereafter referred to as PC1 (the smallest throat size) to PC6 (the largest throat size). Throat diameter ranges are determined by identifying common inflection points for all samples. The seven peaks identified in **Fig. 4.19a** are distributed as follows: PC6 – 14.22 μm , PC5 – 9.69 μm , PC4 – 4.74 μm , PC3 – 3.56 μm , PC2 – 1.71 μm , and PC1 – 0.24 and 0.53 μm . PC1 contains multiple peaks. The pore-throat size ranges are determined as 10.666 to 23.703 μm for PC6, 5.689 to 10.666 μm for PC5, 4.266 to 5.689 for PC4, 2.133 to 4.266 for PC3, and 0.711 to 2.133 μm for PC2, and 0.007 to 0.711 μm for PC1.

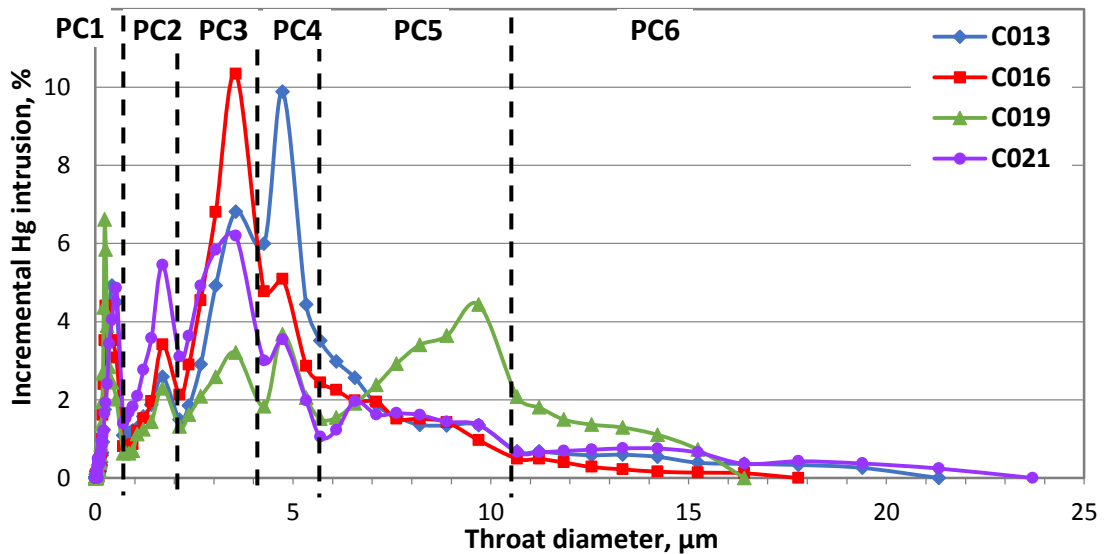


Figure 4.21 – Determination of throat size ranges for each pore class (PC).

In our initial pore classification case (Gundogar et al., 2016), a simpler four pore class (PC1-4) set was used where PC2 to PC4 in **Fig. 4.21** were accepted as a single class; however, when this reduced classification system was applied to pore network construction (**Chapter 5**), calibration of model-derived throat size distributions to experimental MIP measurements was better with more detailed information about the PC size ranges comprising any deflection behavior in throat size distribution curves. For this reason, PC3 created in the previous classification is subdivided into 3 further subclasses based on their common peak locations. (Note: The order of the pore classes with PC1 representing pores accessed by the smallest diameter throats in **Fig. 4.21** differ from Gundogar et al. (2016) in which PC1 represents the pore volume accessed via the largest diameter throats.) After specifying each throat-size interval, the corresponding cumulative mercury volumes occupied in each interval (from the largest throat size up to the throat size at its boundary) are determined per sample as presented in **Table 4.7** and **Fig. 4.20** (blue).

For the next step, pore body sizes are derived by matching MIP volumes from different throat size ranges to corresponding SEM pore areas. Pore body width ranges are established from cumulative SEM pore areas corresponding to equivalent Hg volumes in each class (**Fig. 4.20**, red). It should be kept in mind that the minimum pore body size must be greater than the smallest throat size for each class. As an example, the first interval (PC6) consists of 4.26% of the sample volume with a throat size range of 10.666 to 23.703 μm (MIP data) for C019 (**Table 4.7** and **Fig. 4.20c**). The equivalent sample area (4.26%) for C019 occurs in SEM pore sizes ranging from the largest pore size, 241.96 μm , to 57.86 μm . Likewise, the second interval (PC5) for C019 includes a cumulative sample volume of 13.64% representing a throat size range of 5.689 to 10.666 μm (MIP data); the corresponding SEM area includes pores that are 21.04 to 57.86 μm in width. This process is repeated for each pore class. In the first pore class (PC1) covering the smallest pore bodies and throats, the difference between mercury and SEM porosity is the unresolved porosity. The classification procedure is applied to each sample (**Fig. 4.20**) and the resulting pore body size ranges are listed in **Table 4.7**. For C013, PC2 requires adjustment of the pore body width range as the ideal placement of the threshold between PC1 and PC2 results in a minimum pore body width less than

0.154 μm , which is less than the smallest throat diameter (0.711 μm) for PC2. Complete filling of the SEM porosity (33.6% area) for C013 cannot match the mercury volume cutoff value of PC2 with 35.87% volume (**Table 4.7**). To correct for this, the threshold is shifted to the smallest pore body width that is larger than the smallest throat size in PC2, in this case, 0.924 μm (**Table 4.7**).

Table 4.7 – Cumulative Hg volume, pore body size range, weighted average pore body and throat sizes, aspect ratio, percent proportions of each class per sample (⁺ adjusted size).

Sample	Pore class (PC)	Cumulative Hg volume, % volume	Pore body width range, μm		Average body width, μm	Average throat diameter, μm	Aspect ratio (R_p/R_t)	PC % (% ϕ)
C013	1	50.02	≤ 0.077	0.924	0.648	0.338	1.92	28.3
	2	35.87	0.924 ⁺	3.08	1.411	1.296	1.09	11.8
	3	29.95	3.08	7.084	4.568	3.341	1.37	18.0
	4	20.96	7.084	12.628	9.983	4.871	2.05	20.3
	5	10.80	12.628	31.56	17.591	7.179	2.45	16.6
	6	2.52	31.56	157.8	52.014	13.487	3.86	5.0
C016	1	45.20	≤ 0.077	1.078	0.8	0.298	2.69	32.8
	2	30.37	1.078	3.542	2.139	1.405	1.52	11.4
	3	25.21	3.542	9.702	6.83	3.220	2.12	26.7
	4	13.14	9.702	14.014	11.649	4.855	2.40	12.7
	5	7.38	14.014	52.6	24.501	7.275	3.37	14.0
	6	1.04	52.6	220.92	82.968	12.305	6.74	2.3
C019	1	43.16	≤ 0.077	3.85	1.798	0.253	7.10	41.3
	2	25.32	3.85	8.932	6.434	1.361	4.73	8.7
	3	21.57	8.932	14.63	12.074	3.109	3.88	10.8
	4	16.91	14.63	21.04	18.199	4.937	3.69	7.6
	5	13.65	21.04	57.86	35.102	8.193	4.28	21.7
	6	4.26	57.86	241.96	85.816	12.293	6.98	9.9
C021	1	43.00	≤ 0.077	1.078	0.784	0.315	2.49	29.2
	2	30.47	1.078	7.084	3.722	1.365	2.73	20.3
	3	21.74	7.084	14.784	10.953	3.034	3.61	23.7
	4	11.55	14.784	21.04	17.648	4.819	3.66	8.5
	5	7.88	21.04	52.6	32.218	7.683	4.19	11.9
	6	2.76	52.6	310.34	103.635	14.031	7.39	6.4

The weighted pore body and throat averages are calculated from either volume (MIP) or area (SEM) for each pore class per sample and given in **Table 4.7**. Besides, the porosity proportions attributed to each pore class per sample are listed on the last column of **Table 4.7** and demonstrated in **Fig. 4.22**. In this classification, the largest throats connect PC6 whereas increasingly smaller throats connect sequentially the other classes in descending size order. Of the four samples, the porosity of C019 has proportionally the most PC1 (the smallest pore body and throat sizes) and PC6 (the largest pore body and throat sizes). For pore network modeling (PNM), both PC % and size ranges should be replicated as closely as possible with any necessary adjustments being assigned to the smallest pore class.

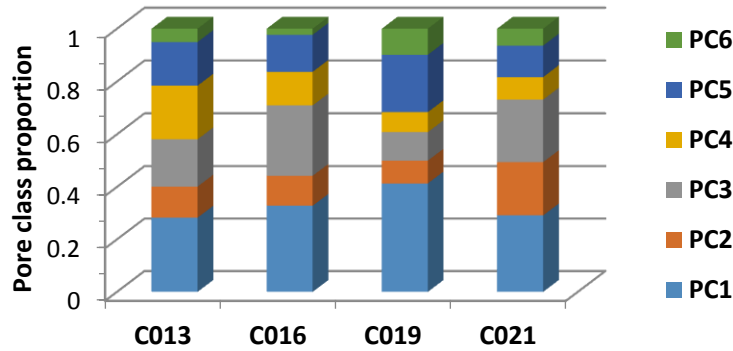


Figure 4.22 – Porosity proportion of each pore class (PC) per sample.

4.3.5 Aspect ratio

Aspect ratio (α) is the radius ratio of pore body to its connected throats and given by

$$\alpha = R_p / R_t \quad (4.7)$$

It is a significant network property affecting both multiphase flow behavior and residual oil saturation of sedimentary rocks (Jerauld and Salter, 1990). In our study, aspect ratio is calculated from weighted average pore body and throat sizes for each pore class per sample (**Table 4.7**). C013 has the lowest aspect ratio for all pore classes (i.e., pore body sizes are not much larger than their associated throats). Samples having sufficiently large aspect ratios are expected to have greater residual oil saturations, because flow is more difficult throughout the porous medium. In case the size contrast between pores and their

connecting throats (aspect ratio) is large, snap-off flow of wetting fluid retaining in corners is possible during water imbibition causing disconnected trapped oil in the medium (Roof, 1970; Akin et al., 2000).

4.3.6 Coordination number

Coordination number (Z) is the average number of throats that are connected to a pore body. Connectivity between pore bodies and throats with possible flow pathways in the porous media has a major effect on reservoir performance and recovery efficiency. Pore connectivity has a stronger effect on permeability than porosity alone (Mohanty and Salter, 1982; Jivkov et al., 2013).

Coordination numbers calculated from 2D data are most likely lower than those present in 3D. To distinguish between the two coordination types, Z values calculated using SEM data are hereafter referred to as 2D coordination number or Z_{2D} . The E-D method reports the total number of constrictions (2D throats, X_2 in **Table 4.2**) and total number of 2D pores with constrictions per image (X_3 ; **Table 4.2**). Their ratio yields average coordination number Z_{2DA} in **Eq. 4.8**. Z_{2DA} of both magnifications (75X and 750X) per sample are listed in **Table 4.8**.

$$Z_{2DA} = \frac{\text{Number of constrictions (2D throats)}}{\text{Number of pores with constrictions}} = \frac{X_2}{X_3} \quad (4.8)$$

The 2D average coordination values are greater at 750X for all samples except C019 that has slightly greater connectivity in the low magnification mosaic (3.37 vs 3.29 in **Table 4.8**). This finding agrees with previous observations of C019 that it has more porosity accessed through throats larger than 6 μm (**Fig. 4.16**). For the other samples, many constrictions are too small to be resolved with a pixel size of 2.63 μm at 75X. With increased magnification and smaller pixel sizes (e.g., 0.077 μm), it is possible to detect more throats in microporous samples. Of significance, the coordination number values for 75X and 750X represent two different scales of connectivity, where throats

measured at 75X are much larger ($\geq 2.63 \mu\text{m}$) than throats ($\geq 0.077 \mu\text{m}$) measured at 750X.

Table 4.8 – Average coordination numbers at low (75X) and high (750X) magnifications.

Sample	Z_{2DA}	
	75X	750X
C013	2.16	4.31
C016	1.67	3.58
C019	3.37	3.29
C021	2.76	4.33

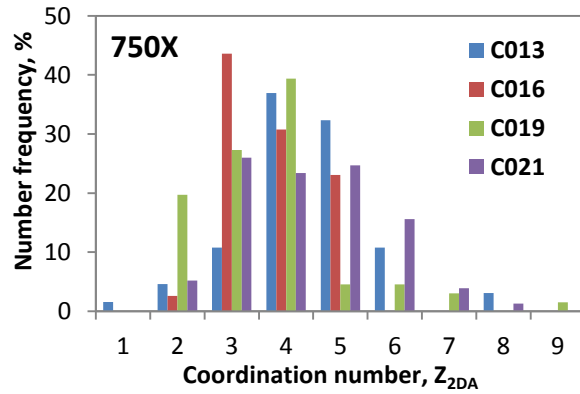


Figure 4.23 – Average coordination number distributions at high magnification (750X).

Coordination numbers for pores less than $43.58 \mu\text{m}$ predominantly range from 3 to 5 as shown by the Z_{2DA} frequency distribution of individual 750X images (**Fig. 4.23**). This finding is consistent with previous studies (Knackstedt et al., 2006; Sok et al., 2007; Al-Kharusi and Blunt, 2007; Zhao et al., 2010). Based on **Fig. 4.23**, Z_{2DA} distribution differs somewhat between the samples with C016 and C019 skewed toward smaller coordination values compared to C013 and C021.

4.3.7 Shape factor

Shape factor (G) is a dimensionless quantity defined as the ratio of cross-sectional area of pore body or throat (X_4 ; **Table 4.2**) to the square of its corresponding perimeter (X_8 ; **Table 4.2**) as given in **Eq. 4.9**. It is used in image analysis to describe numerically the shape of a particle independent of its size. Together with capillary pressure, shape factor determines the amount of wetting fluid retained in the corners of drained pores (Øren et al., 1998).

$$G = \frac{\text{Total pore area}}{(\text{Total pore perimeter})^2} = \frac{X_4}{(X_8)^2} \quad (4.9)$$

Actual pore space is approximated by ideal polygonal elements with square, circular, and triangular cross-sections having equivalent shape factor values (**Fig. 4.24**; Valvatne and Blunt, 2004). Triangle shape factor ranges from zero to 0.04811 (slit-like to equilateral triangles). A square has a shape factor of 0.0625 whereas a circle has a shape factor of 0.07958. Shape factors larger than 0.04811 and less than that of a circle are accepted as composites of squares, circles, and triangles. As symmetry increases, shape factor also increases with the greatest value for circles; therefore, pore elements having higher shape factor than that of circles are most probably due to edge effects (**Fig. 4.25**) and omitted from further consideration.

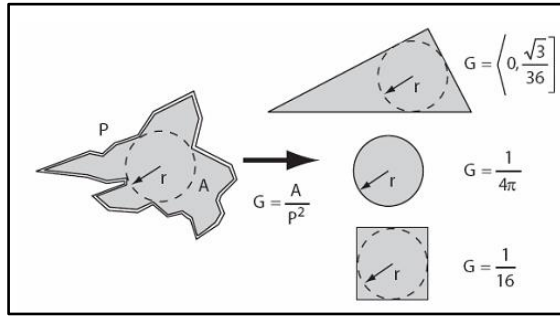


Figure 4.24 – Polygonal cross-sections having same shape factor with real pore space (Valvatne and Blunt, 2004).

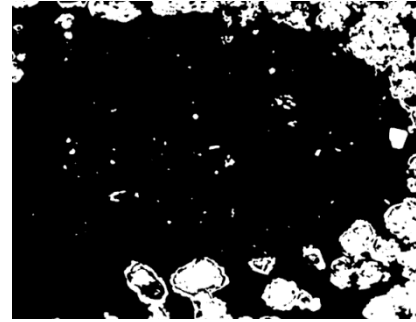


Figure 4.25 – Edge effect due to incomplete pore element accepted as infinite in E-D.

Shape factor cumulative frequency distributions for low and high magnifications as well as multiscale SEM data are shown in **Figs. 4.26a, 4.26b, and 4.26c**, respectively. The resulting distributions indicate that most of the porosity (>75%) can be approximated by triangular cross-sections ($G \leq 0.04811$). For the multiscale SEM data, this value corresponds to 93 to 96% of the total pore area (**Fig. 4.26c**).

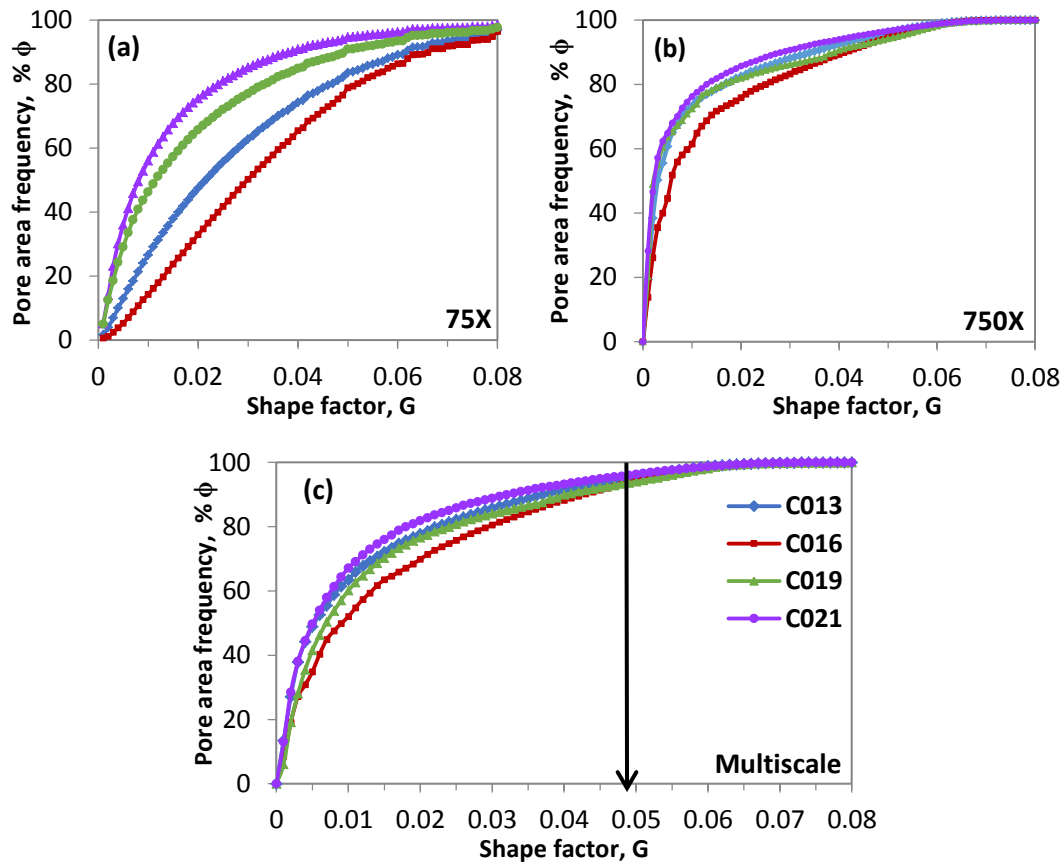


Figure 4.26 – Cumulative distribution of shape factor at a) 75X, b) 750X, and c) multiscale SEM data (Arrow marks the uppermost limit of triangle shape factor range, $G = 0.04811$).

The pore size versus shape factor analysis reveals that values belonging to other symmetrical shapes (squares and circles) are typically small pores for both 75X and 750X distributions. More telling is that the size itself is not a predictor of these equant shapes; rather, circles and squares are associated, in almost every case, with the first two E-D cycles regardless of magnification indicating that non-triangular pores are caused by resolution and E-D itself. In part, this is a function of the pixel size in comparison to the pore size. The more cycles that a pore progresses through, the better the size and shape are characterized (Ehrlich et al., 1991a). Therefore, it is not possible to measure details of angularity and roughness for pores that are one to two pixels wide. Given this point, triangular cross-sections are sufficient to represent the irregularity of complex carbonate pore geometry.

CHAPTER 5

PORE NETWORK CONSTRUCTION AND PORE-LEVEL FLOW EQUATIONS

In this chapter, the properties of our pore network model are described to be used in the course of the study for predicting two-phase flow properties and oil recovery of Middle East carbonates. This model encapsulates network topology and pore space geometry properties, pore-level displacement mechanisms with their appropriate threshold capillary pressures to simulate any sequence of flooding cycles in complex carbonate systems with nonuniform wettability.

In the following two sections, the construction of our stochastic network model using pore structure characterization inputs which are derived from image analysis and core measurements in **Chapter 4** and the pore-level flow mechanisms simulated within the proposed model are presented. If the details of the pore structure specific to a given rock system are known, pore network model makes reasonable estimations of transport properties (Jerauld and Salter, 1990; Sok et al., 2002); therefore, in the upcoming flow simulations, network models of carbonate samples (C013, C016, C019, and C021) will involve most of the topologic and morphologic properties from original carbonate core samples to replicate their nature of porous media as closely as possible.

5.1 Pore network construction

In the present model, a pore-scale 3D cubic network is proposed as the basis of multimodal carbonate porous media (**Fig. 5.1**). The pore space is represented as an assemblage of wider nodes (i.e. pore bodies) interconnected via tubular narrower links (i.e. pore throats) (Wardlaw et al., 1987). Nodes are located at the vertices of the cubic

lattice and links are assigned to the connections between each neighboring pore body couples.

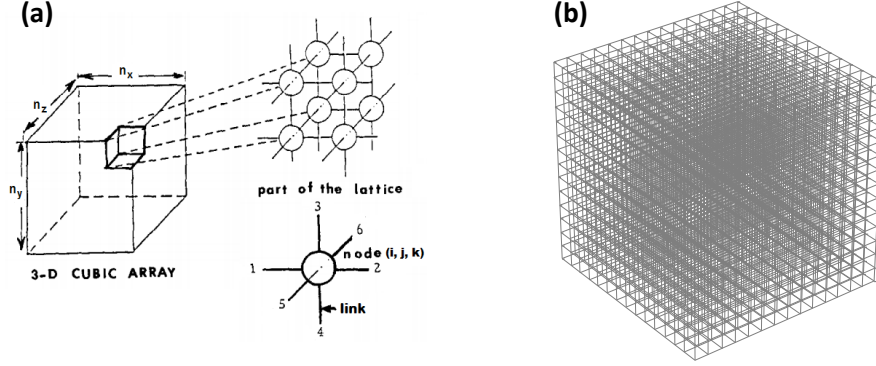


Figure 5.1 – Schematic view of a) network model structure (modified from Diaz et al., 1987) and b) regular 3D cubic network for $n = 15$.

The model size is defined by the number of nodes per edge and denoted by $n_x \times n_y \times n_z$, where n_x , n_y and n_z are the dimensions of the network (**Fig. 5.1a**). The network size is equal in all directions in our cubic system, hence the model size is designated by single n and chosen as $n = 15$ or $n = 20$ depending on the necessity for a larger model ($n = 20$) or not. As larger network models need much more CPU time, the minimum model size overcoming the end effects is preferred (Jerauld and Salter, 1990; Xu et al., 1999; Jia et al., 2007). In preliminary studies (Chatzis and Dullien, 1985; Dullien et al., 1986; Diaz et al., 1987), the network size of 15 nodes per edge and greater were verified to be sufficiently large to enable reproducibility of capillary pressure vs saturation curves. For a cubic system with model size of n nodes per edge, there are n^3 nodes and $3n^2(n+1)$ links in the system. Accordingly, a model with $n = 20$ consists of 8000 nodes and 25200 links in the system whereas a model of $n = 15$ has 3375 nodes and 10800 links. A node or link is addressed by its index in the network model. Indices from the integer number space $[1, 2, 3, \dots, n^3]$ have been assigned sequentially to the nodes according to their coordinates (i, j, k) in the cubic lattice. The spatial orientation of each link, in the same manner, is numbered by the coordinate of its connected node and

by its location on that node from 1 to 6 (**Fig. 5.1a**). Therefore, link indexes are spatially correlated to node indexes over the network (Diaz et al., 1987).

A fixed coordination number, the number of pore throats connected to a single pore body, of 6 is employed in the model. In **Section 4.3.6**, average coordination number is found as predominantly ranging from 3 to 5 (**Fig. 4.23**). The coordination numbers calculated from 2D data are most probably lower than those present in 3D; thus, fixing the system coordination number to 6 is thought as a reasonable assumption. **Figure 5.1b** shows schematically the cubic lattice on the order of 15 nodes per edge ($n = 15$) with coordination number of 6.

In the network, characteristic pore space properties (shape factor, pore body and throat radii uniform along the length, pore class (PC), aspect ratio, length, etc.) obtained from the original samples are assigned to individual nodes and links. Most of these pore-scale input data are quantified using image analysis and mercury injection measurements in **Chapter 4**. The construction procedure of carbonate pore networks is described below.

5.1.1 Shape of pore cross-section and corner half-angles

Dimensionless shape factor ($G = A/P^2$) is used to simplify complex and variable shape of pore cross-sections in real porous medium (Mason and Morrow, 1991). SEM-derived data is used to evaluate shape factor of carbonate samples (**Section 4.3.7**). Shape factor cumulative frequency distributions, given in **Fig. 4.26**, indicate that most of the porosity (93 to 96% for the multiscale SEM data) belongs to triangular shapes ($G \leq 0.04811$). Hence, noncircular and cornered cross-sections of porous media in nature (Dullien, 1992) are approximated by irregular triangles in the model (e.g., Øren et al., 1998; Patzek, 2001; Al-Futaisi and Patzek, 2003, Al-Kharusi and Blunt, 2008). Lenormand et al. (1983) observed the presence of water layers in the corners of square flow channels after drainage in micromodel experiments. Triangle-shaped pore elements have also the essential feature of corners. Pore angularity in cross-section allows the wetting fluid to reside in the sharp corners and so to remain connected across the network while the

nonwetting phase occupies the center. Two or more fluids can, therefore, co-exist and flow through the same pore simultaneously.

A scalene triangular pore with its corner half-angles ($\beta_i, i:1,2,3$) is shown in **Fig. 5.2**. Dividing the pore cross-section to six triangles of equal heights R (**Fig. 5.2**), the corner half-angles of a triangular pore are related to its shape factor by (Øren et al., 1998; Patzek and Silin, 2001)

$$G = \frac{1}{4 \sum_{i=1}^3 \cot \beta_i} = \frac{1}{4} \tan \beta_1 \tan \beta_2 \cot (\beta_1 + \beta_2) \quad (5.1)$$

where β_i are the corner half-angles with the order of $0 \leq \beta_1 \leq \beta_2 \leq \beta_3 \leq 90^\circ$. It is deduced from **Eq. 5.1** that a single G value corresponds to a range of corner half-angles and therefore different triangular shapes as indicated in **Fig. 5.3** (Patzek, 2001).

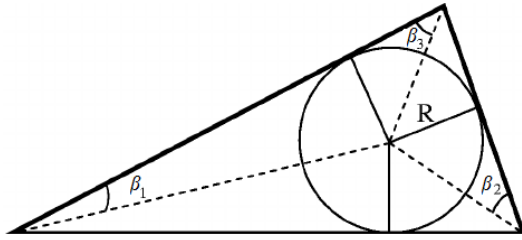


Figure 5.2 – Irregular triangle-shaped pore cross-section.

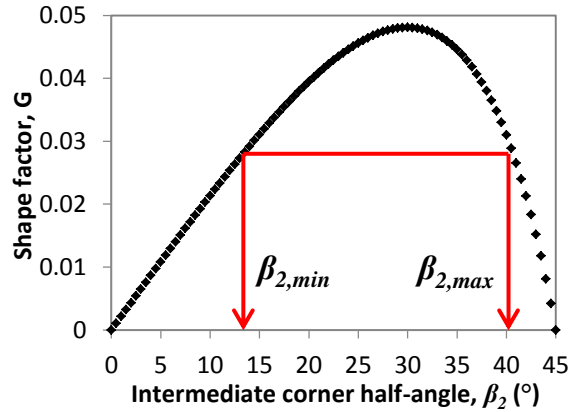


Figure 5.3 – Distribution of shape factor vs intermediate half-angle in irregular triangles (Reproduced from Patzek, 2001).

For the determination of corner half-angles of a triangular pore with a given value of G , firstly, the minimum and maximum values of intermediate half-angle β_2 are calculated from **Eqs. 5.2** and **5.3**, respectively.

$$\beta_{2,\min} = \text{atan} \left(\frac{2}{\sqrt{3}} \cos \left(\frac{\arccos \left(\frac{-12\sqrt{3}G}{3} \right) + \frac{4\pi}{3}}{3} \right) \right) \quad (5.2)$$

$$\beta_{2,\max} = \text{atan} \left(\frac{2}{\sqrt{3}} \cos \left(\frac{\arccos \left(-12\sqrt{3}G \right)}{3} \right) \right) \quad (5.3)$$

Then, β_2 is selected randomly within the allowed range of $\beta_{2,\min} \leq \beta_2 \leq \beta_{2,\max}$. The smallest half-angle β_1 is subsequently calculated from **Eq. 5.4** as

$$\beta_1 = -\frac{1}{2}\beta_2 + \frac{1}{2}\text{asin} \left(\left(\frac{\tan \beta_2 + 4G}{\tan \beta_2 - 4G} \right) \sin \beta_2 \right) \quad (5.4)$$

and finally $\beta_3 = \pi/2 - \beta_1 - \beta_2$. Here, corner half-angles are in radian and converted to degrees to be used in flow equations. In **Fig. 5.4**, the resulting corner half-angles of all node elements in the network are plotted together indicating the order of magnitude clearly ($\beta_1 \leq \beta_2 \leq \beta_3$) with the verification of their summation that is equal to 90° for any given run.

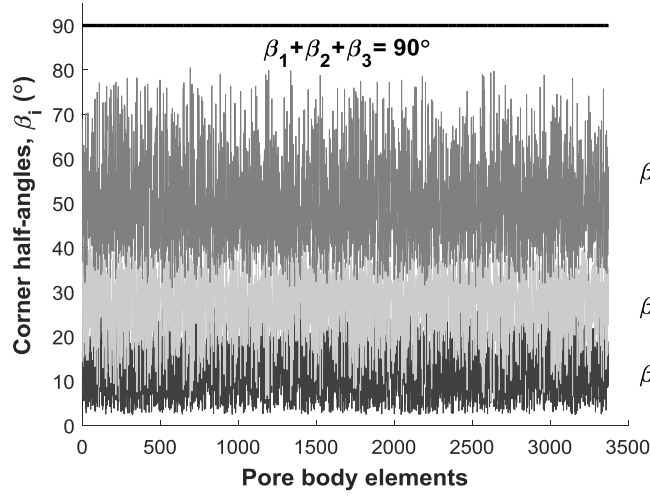


Figure 5.4 – Corner half-angles β_i of individual pore bodies for $G \in [0.01, 0.04811]$.

As shape factor decreases, the difference between maximum and minimum half-angles ($\beta_3 - \beta_1$) increases and, accordingly, pore space becomes more irregular. Although the minimum shape factor of triangular pores is theoretically zero (slit-like), extremely narrow pores are not included in the pore network due to their fracture-like structure (Patzek and Silin, 2001). In the model, the lowest G value is shifted from nearly zero to 0.01 of a sharply-edged triangular shape in which

$\beta_1 \approx 2.5^\circ - 3.5^\circ$ and $\beta_3 \approx 50^\circ - 80^\circ$ (Al-Kharusi and Blunt, 2008). To prevent excessive difference between corner half-angles also guarantees water presence at each corner of a triangular pore after oil migration ($\theta_R + \beta_i < 90^\circ$; see **Section 5.2.1**). The cumulative shape factor distributions compressed from $(0, 0.04811]$ to $[0.01, 0.04811]$ are indicated in **Figs. 5.5a** and **5.5b**, respectively. In **Fig. 5.5b**, cumulative distribution curves for $G \geq 0.01$ are given with their polynomial fits (3rd order) reproducing the experimentally obtained shape factor curves. Then, polynomial fitting parameters are used to randomly distribute shape factors to pore elements. The network model-generated shape factor distributions, given in **Figs. 5.6a** and **5.6b** for pore bodies and throats respectively, show that the resulting distributions replicate the experimental shape factor distributions (correlation coefficient (CC) ≥ 0.987).

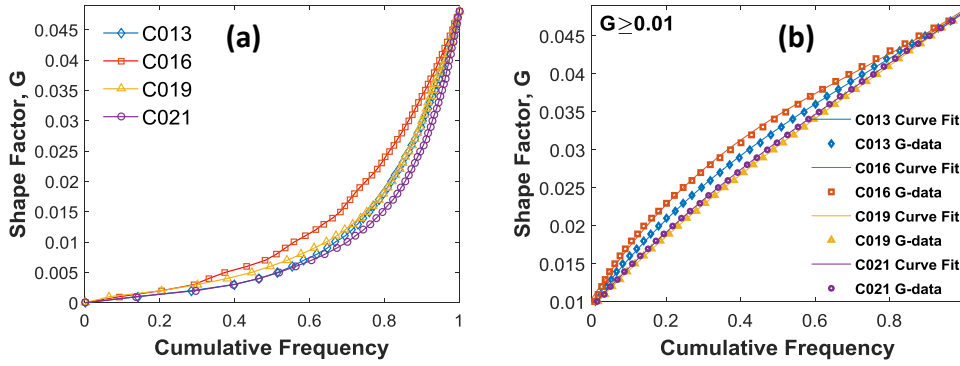


Figure 5.5 – SEM-derived shape factor distributions for a) $G \in (0, 0.04811]$ and b) $G \in [0.01, 0.04811]$.

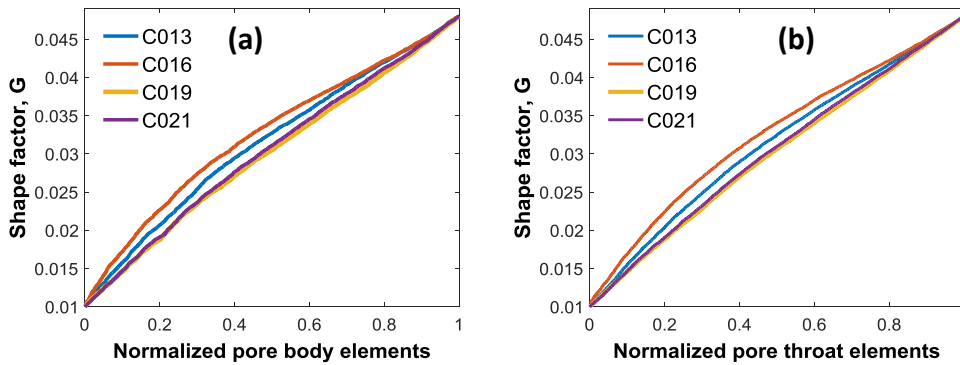


Figure 5.6 – Network-generated shape factor distributions in a) pore bodies and b) throats.

5.1.2 Determination of pore throat and body sizes

Pore throat size distribution plays an important role on the predicted flow properties. Below, the procedure how the inscribed radii of pore throats and their connected pore bodies are determined in the network model is described.

5.1.2.1 Pore throat size determination

In this section, experimental MIP data is used to modify throat size distribution in the network and then, the matched-model is used to evaluate the relative abundance of each PC in the network. As mercury is the nonwetting phase in almost all solid-fluid configurations, the resulting throat size information is not influenced by wettability characteristics of rock surfaces (Valvatne, 2004). MIP-derived throat size distributions and their differential intrusion curves are previously shown in **Figs. 4.16** and **4.19a**, respectively. Mercury intrusion curves exhibit bimodal (dual) behavior for all carbonates studied comprising (I) macroporosity and (II) microporosity regions in their pore systems. The pore throat size distributions range from 0.007 to 24 μm .

Based on the algorithm for throat size adjustment, firstly 3D carbonate network model is constructed incorporating a representative mercury-air system. A large network model is preferred on the order of $n = 20$ for throat size modification. As the starting point, throat sizes in each PC derived from MIP measurements are randomly distributed in the model depending on their volume proportions (PC %) given in **Table 4.7**. Since MIP data is determined from throat sizes, inscribed radii of all pore bodies within the network are assumed constant and equal to the maximum throat radius of each carbonate sample. As the second step, mercury-air capillary entry pressure P_c^e of each pore network element is calculated and converted to its equivalent pore throat radius using mercury-air interfacial tension $\gamma_{Hg/air}$ of 0.485 N.m^{-1} and the receding contact angle $\theta_{Hg/air}$ of 140° (Dandekar, 2006).

Mercury invasion starts from the inlet face, it first meets the pore throats located at the inlet boundary and enters to one of the possible pore throats with the lowest P_c^e . The mercury pressure and, accordingly, capillary pressure ($P_{Hg} - P_{air}$) increase stepwise. Mercury progressively fills the system in this manner. The throat size distribution derived from the initial mercury-air drainage simulation together with the experimental MIP throat size data are given in **Fig. 5.7** for C019. Despite the dual porosity nature of C019, the resulting throat size distributions only match the second region of experimental curve (high pressure interval on the left side of the dashed black line in **Fig. 5.7**). The second region of MIP curve represents microporosity including throat sizes less than $0.711 \mu\text{m}$. Basically, the network system is acting in series with no preferential pathways in this randomly distributed throat network. Thus, the larger throats in the first region of MIP curve (macropores) can only be filled after the smaller throats connecting with the mercury reservoir have been invaded at a pressure higher than that required by their actual dimensions (Xiong et al., 2016) and cannot be recorded progressively during the simulations.

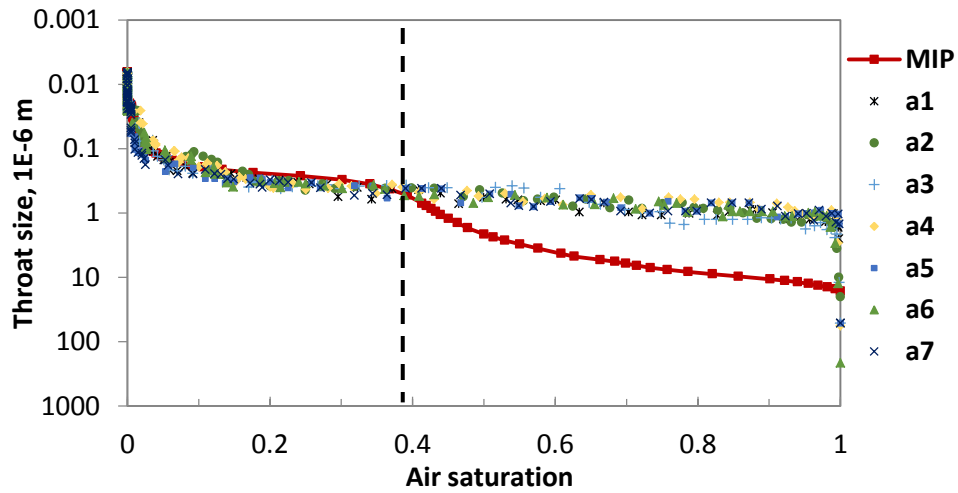


Figure 5.7 – Experimental (MIP) and model-predicted throat size distributions of C019 for disordered networks (a1 to a7).

In order to provide a gradual increase of mercury-air P_c where mercury passes through throats sequentially from wider to smaller ones and eventually to reproduce the target throat size distribution, a spatially ordered network is proposed. The interconnected 3D network is accepted as a bundle of cylindrical capillary tubes where the throats are ranked in descending size order to follow the same pathway of mercury intrusion in porous medium (Valvatne and Blunt, 2004). Pore throats are distributed in the system starting from PC6 (the widest throats) at the inlet face to PC1 (the narrowest throats) at the outlet face. The first trials for mercury-air simulations in spatially ordered networks are given in **Fig. 5.8** for C019. After many adjustments of throat size distributions via variations in arrangement and proportion of six pore classes (PC) identified with their particular size ranges, reasonable matches are obtained between pore model (PNM) predictions and experimental MIP data. The modified throat size distributions and MIP data are plotted together in **Fig. 5.9** for all carbonates studied.

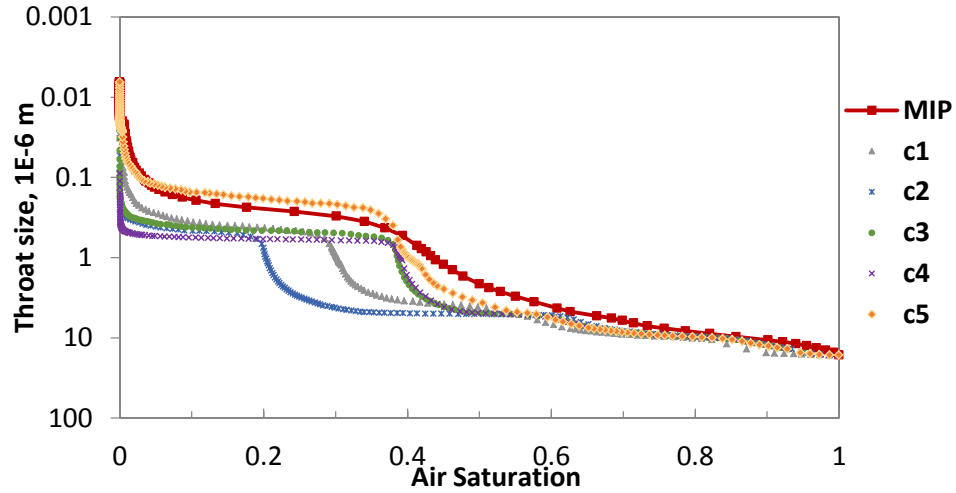


Figure 5.8 – Experimental (MIP) and model-predicted throat size distributions of C019 for different spatially-ordered networks (c1 to c5).

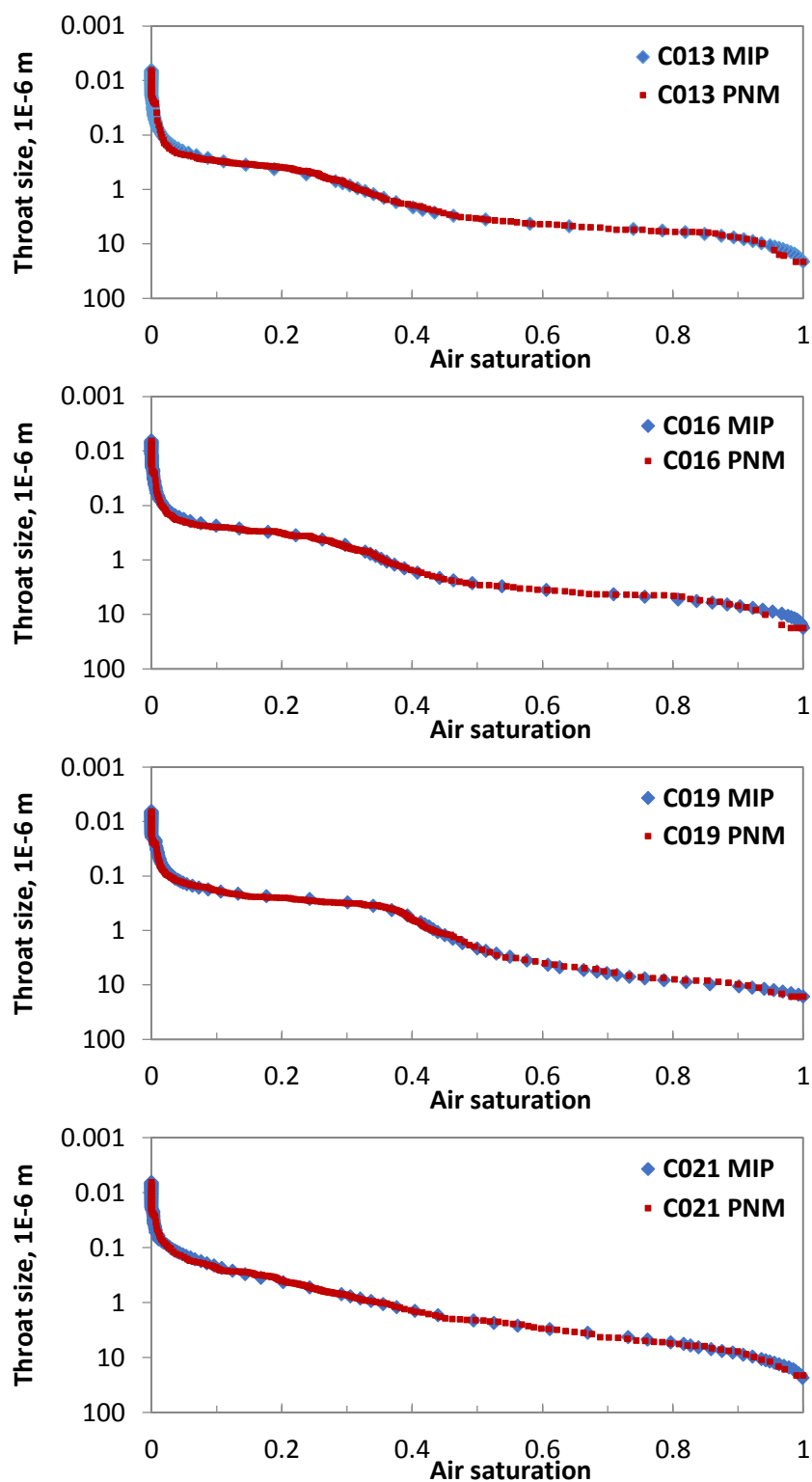


Figure 5.9 – Comparison of experimental (MIP) versus model-predicted (PNM) throat size distributions of carbonate samples.

The number frequencies of each PC determined from the spatially ordered networks of the final matched models are given with PC volume proportions in **Table 5.1** and as a bar chart diagram in **Fig. 5.10**. The number frequencies represent the spatial concentration or relative abundance of each PC in the rock microstructure (Jia et al., 2007). The difference between pore number and volume frequency distributions are apparent from **Table 5.1** and **Fig. 5.10**. For example, the smallest pore class (PC1) of carbonates makes up 45.5 to 69.7% of the pore count while it contributes just 28.3 to 41.3% of the pore volume. As mentioned previously, the frequency for the smallest pore class is more susceptible to image quality and processing (e.g., binarization) issues. After the model-predicted data adequately reproduces experimental MIP curve, no further adjustments are made to number frequencies of PCs within each network.

In network construction, the generation of distributions of a given property (e.g., inscribed pore and throat radii, aspect ratio, coordination number) defined within an allowed range is based on probability density functions, which are uniform, normal, log-normal or truncated Weibull distributions (Fenwick and Blunt, 1998a,b; Gao et al., 2011). In our model, uniform, and truncated Weibull distribution types are employed when necessary. Uniform distribution gives a random value between the allowed lower and upper boundaries, where all of the variable values in the range have equal probability. The inscribed radius is found by,

$$R = (R_{\max} - R_{\min})y + R_{\min} \quad (5.5)$$

where y is random variable between 0 and 1, $y \in [0,1]$. According to a truncated Weibull distribution, the variable y distributed between 0 and 1 is determined by,

$$y = \left(-\delta \ln \left(x \left(1 - e^{-1/\delta} \right) + e^{-1/\delta} \right) \right)^{1/\eta} \quad (5.6)$$

where x is a random number between 0 and 1, $x \in [0,1]$, δ and η are the parameters defining the shape of the distribution ($\delta > 0$). The distribution equation is expressed by scaling y between the minimum and maximum limits for a pore and then by substituting y into **Eq. 5.5**. Here, the maximum and minimum values of the network properties are obtained from previous characterization studies (**Chapter 4**).

Table 5.1 – Volume/number proportions of porosity attributed to each PC per sample.

		PC1	PC2	PC3	PC4	PC5	PC6
C013	Volume	0.283	0.118	0.180	0.203	0.166	0.050
	Number	0.455	0.151	0.070	0.023	0.209	0.093
C016	Volume	0.328	0.114	0.267	0.127	0.140	0.023
	Number	0.615	0.103	0.060	0.034	0.128	0.060
C019	Volume	0.413	0.087	0.108	0.076	0.217	0.099
	Number	0.697	0.099	0.026	0.017	0.099	0.062
C021	Volume	0.292	0.203	0.237	0.085	0.119	0.064
	Number	0.495	0.146	0.045	0.025	0.149	0.140

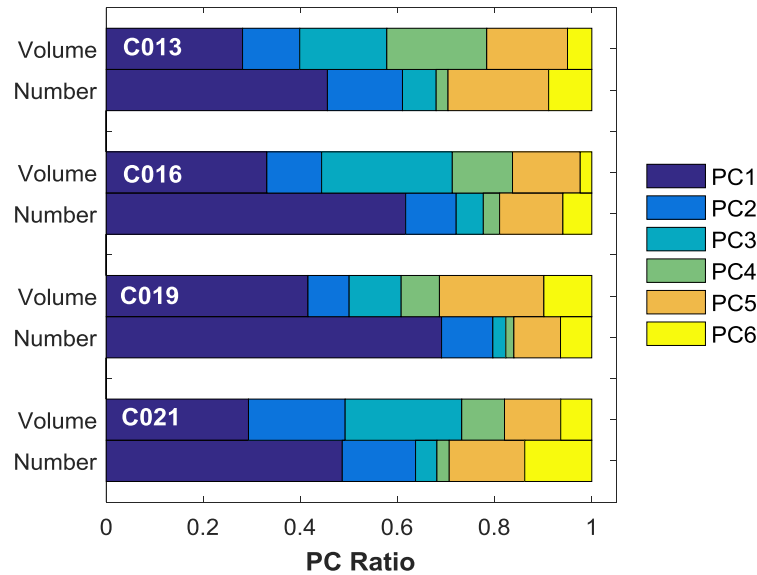


Figure 5.10 – Diagram of volume/number ratio of porosity attributed to each PC per sample.

5.1.2.2 Aspect ratio and pore body inscribed radius

For the unconsolidated systems where the minimum pore body size is greater than the maximum throat size ($R_t^{\max} \leq R_p^{\min}$), i.e. there is no overlap between pore body and throat size distributions, and with relatively narrow size distributions, pore body and throat radii are generated independently from each other (Fig. 5.11, left; Jerauld and Salter, 1990). Our carbonate samples, however, have a significant overlap interval

between their pore body and throat size distributions ($R_t^{\max} > R_p^{\min}$) as indicated in **Fig. 4.20**. If pore throat sizes are assigned from MIP-data while pore body radii are taken directly from SEM-data (**Table 4.7**), due to no correlation between throats and their adjacent pore bodies, the size contrast between connected pores and throats may be much greater than the allowed aspect ratio (size ratio of pore body to its adjacent throat) of the network.

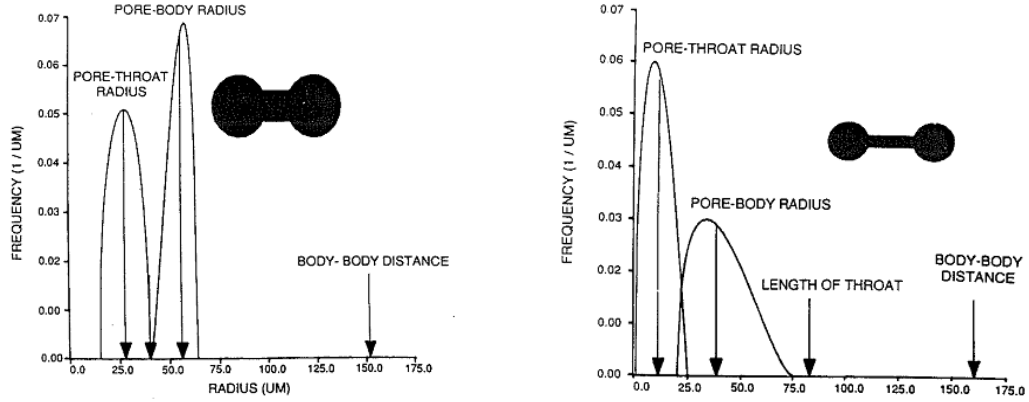


Figure 5.11 – Pore throat and body size distributions representative of unconsolidated (left; sphere-pack) and consolidated (right; Berea sandstone) porous media. Body-body distance: L_c (Jerauld and Salter, 1990).

In this model, instead, a spatially correlated size distribution which is typical for consolidated porous media is considered between pore bodies and their adjacent throats (**Fig. 5.11**, right; Jerauld and Salter, 1990). Aspect ratio is used to correlate predetermined throat sizes to inscribed radii of their connected pore bodies. Pore body radius (R_p) is expressed as follows (Fenwick and Blunt, 1998b; Valvatne and Blunt, 2004)

$$R_p = \max \left(\alpha \frac{\sum_{i=1}^Z R_{t,i}}{Z}, \max(R_{t,i}) \right) \quad (5.7)$$

where $R_{t,i}$ is the inscribed radius of the i^{th} connected throat, Z the coordination number ($Z=6$ in our case), and α the aspect ratio of pore body belonging to a particular PC. The inscribed radius of a pore body is found by multiplying its aspect ratio by the average

radius of its six connecting throats. In case R_p is smaller than the largest connecting throat, it is set to the size of that largest throat (Blunt, 1997a).

In the network, one of the six basic pore classes (PC) is assigned to the individual pore body and throat elements according to their relative abundances in the network system (**Table 5.1** and **Fig. 5.10**). Then, pore throat radii are uniformly distributed (**Eq. 5.5**) between cutoff minimum and maximum radius values specific to their PCs. As mentioned in **Section 4.3.5**, the average aspect ratio is calculated from the weighted average pore body (SEM) and throat sizes (MIP) of each pore class per sample and given in **Table 4.7**. Here, aspect ratio is assigned to individual pore bodies according to a truncated Weibull distribution (**Eq. 5.6**). The input parameters for aspect ratio distribution come from SEM and MIP-derived PC size boundaries as given in **Table 5.2**. In **Table 5.2**, the maximum aspect ratio of PC1 is far higher than that of the other pore classes for each sample due to infinitesimally small throat size limit of PC1 throats ($< 0.01 \mu\text{m}$). In case the minimum aspect ratio falls below one in a PC (i.e., the minimum pore body size is smaller than the maximum throat size), it is taken as unity. Then, **Eq. 5.6** is used by replacing R_{\min} and R_{\max} by α_{\min} and α_{\max} and by the appropriate δ parameters approximating average aspect ratios in **Table 5.2** ($\delta=0.003$ - 0.15 ; $\eta=1.5$).

Table 5.2 – SEM and MIP-derived average aspect ratios with their minimum and maximum limits.

	C013			C016			C019			C021		
	α_{\min}	α_{\max}	$\bar{\alpha}$	α_{\min}	α_{\max}	$\bar{\alpha}$	α_{\min}	α_{\max}	$\bar{\alpha}$	α_{\min}	α_{\max}	$\bar{\alpha}$
PC1	1.00	51.91	1.92	1.00	92.14	2.69	1.00	216.29	7.10	1.00	56.74	2.49
PC2	1.00	4.33	1.09	1.00	4.98	1.52	1.80	12.56	4.73	1.00	9.96	2.73
PC3	1.00	3.32	1.37	1.00	4.55	2.12	2.09	6.86	3.88	1.66	6.93	3.61
PC4	1.25	2.96	2.05	1.71	3.29	2.40	2.57	4.93	3.69	2.60	4.93	3.66
PC5	1.18	5.55	2.45	1.31	9.25	3.37	1.97	10.17	4.28	1.97	9.25	4.19
PC6	1.48	14.79	3.86	2.96	20.71	6.74	3.53	22.69	6.98	2.22	29.10	7.39

In the course of network construction, the input parameters may be exposed to some reasonable arrangements. For example, a pore body with PC1 may be connected with six throats where one or more of which belongs to a PC with larger throat size mode than the maximum possible pore body size of PC1. In this case, to meet the essential condition of $R_p \geq R_{t,i}$ (Eq. 5.7), pore body size is shifted to the size of its largest adjacent throat although this value is not defined in pore body size range of PC1.

Network-based aspect ratio is determined independently of PCs; because, as described in the previous paragraph, pore body and throat sizes have had a series of adjustments whenever necessary during network construction. Instead, the network is taken as a whole and aspect ratio is calculated from the ratio of each individual pore body to its throats connected one-by-one. **Table 5.3** gives the minimum, maximum, and mean aspect ratio outputs of the presented network models. To distinguish network-generated aspect ratio from the input aspect ratios defined for each PC, a single quotation mark (α') is used. The minimum aspect ratio of unity is the result of equated pore body size to its corresponding largest throat size. The distribution of aspect ratio values of pore body elements sorted in ascending order are shown in **Fig. 5.12**. From the network statistics, C013 has the lowest aspect ratio (that is to say its pore body sizes are closer to their associated throats) followed by C016, C021, and lastly C019. This is consistent with our experimental findings stated in **Section 4.3.5** and given in **Table 4.7**.

Table 5.3 – Network-measured aspect ratio (α') and lattice constant (L_c).

	C013	C016	C019	C021
α'_{\min}	1	1	1	1
α'_{\max}	8.15	9.37	14.82	14.03
$\bar{\alpha}'$	1.87	2.13	4.70	2.73
L_c , E-6 m	41.2	32.4	72.6	49.6

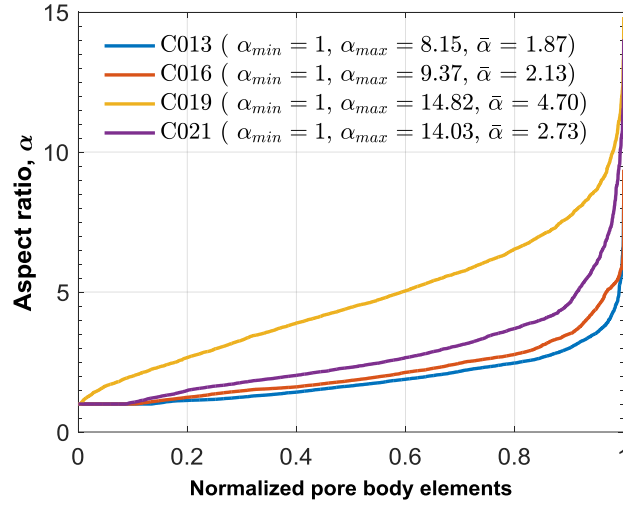


Figure 5.12 – Network-measured aspect ratio distributions of carbonate networks in ascending order.

5.1.2.3 Pore body and throat size distributions

The pore body and throat radii are uniformly distributed within the allowed size boundaries for each PC and plotted against the normalized number of network elements in **Fig. 5.13**. Besides, the frequency histograms of pore body and throat sizes measured in our constructed networks are given in **Fig. 5.14** for all samples. From the size distributions in **Figs. 5.13** and **5.14**, most of the pore throats have radii less than 1 μm and are much smaller than pore bodies. From the figures, C013 and C016 have narrower pore body size ranges with a lower maximum than the others. As mentioned previously, C013 has lower aspect ratio than others. That's why the overlap between pore body and throats sizes is the greatest for C013. Higher value of aspect ratio, keeping throat size distribution constant, skews the range of pore body frequency distribution curves towards the higher pore sizes. Therefore, the largest aspect ratio in C019 network leads to a more extended pore body size range (**Fig. 5.13c** and **5.14c**).

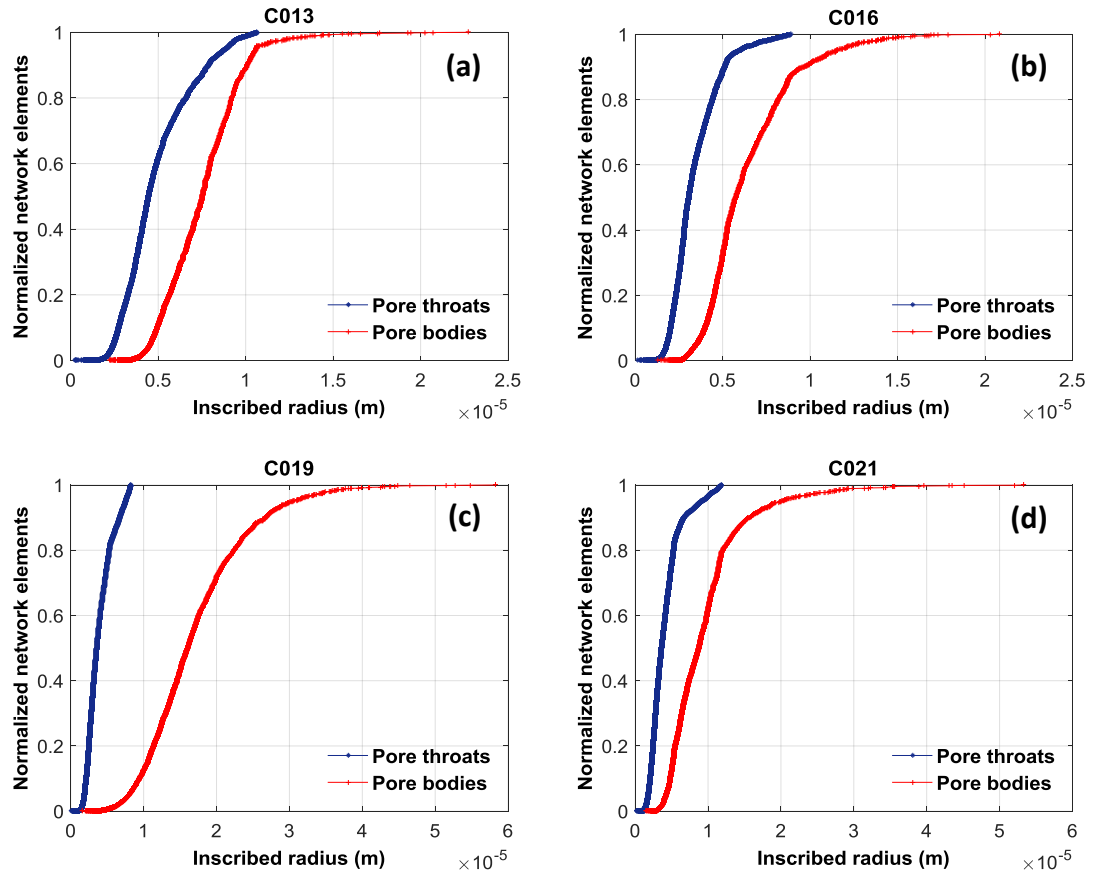


Figure 5.13 – Normalized network pore elements against pore body and throat radii for carbonate samples: a) C013, b) C016, c) C019, and d) C021.

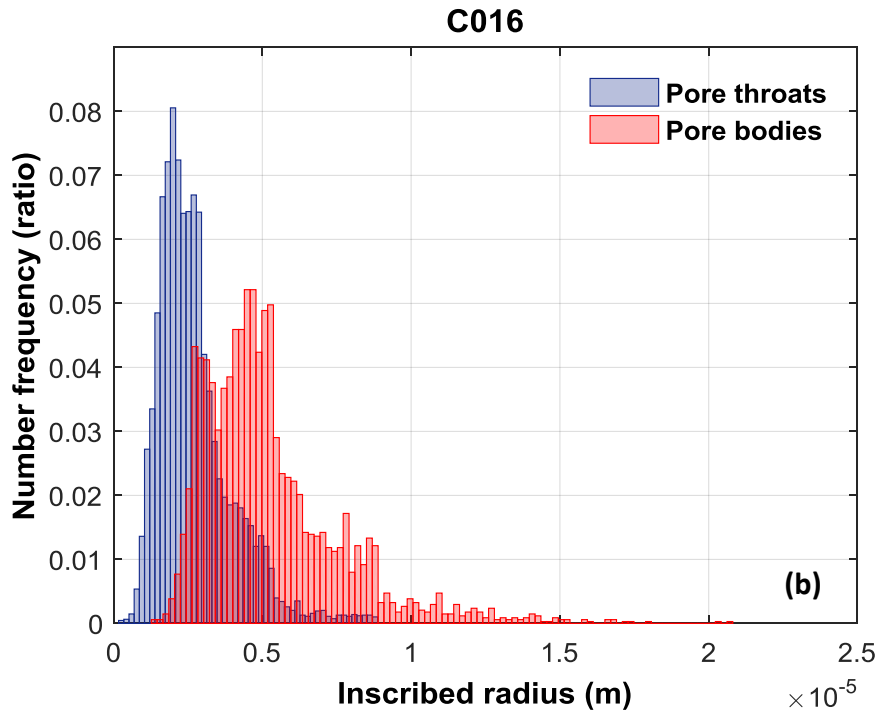
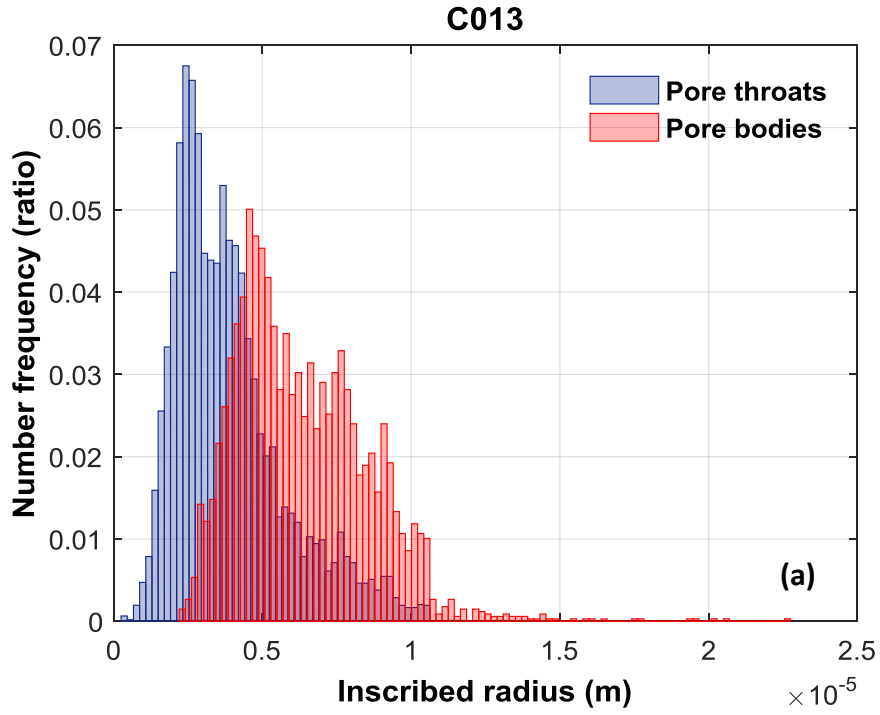


Figure 5.14 – Network-measured pore body and throat size frequency distributions of a) C013, b) C016, c) C019, and d) C021 (Cont'd).

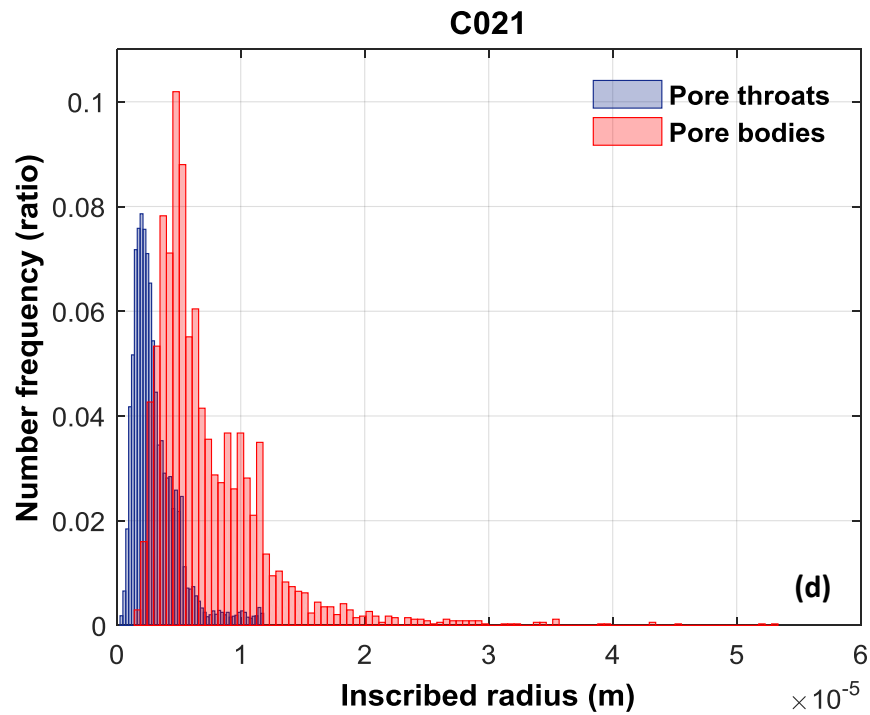
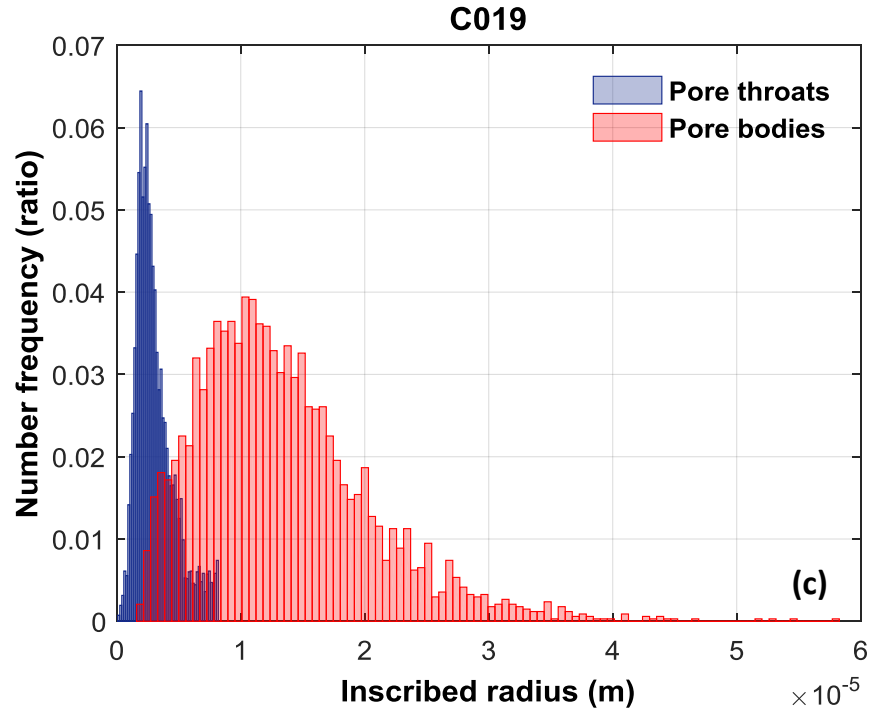


Figure 5.14 – Network-measured pore body and throat size frequency distributions of a) C013, b) C016, c) C019, and d) C021.

5.1.3 Pore body and throat lengths

In the model, the length of a pore network element depends on its inscribed radius. For this reason, pore lengths are determined after their inscribed radii are assigned. The length of a pore body is assumed to be equal to its inscribed diameter, i.e. $L_p = 2 \times R_p$ (Blunt, 1997a).

Jerauld and Salter (1990) defined the scale of a pore network as the distance between the centers of two adjacent pore bodies. Here, the scale of the network model is called as network lattice constant L_c and illustrated in **Fig. 5.15**. To determine fixed lattice spacing of carbonate networks, experimental porosity values of samples given in **Table 4.1** are equated to their network areal porosities by means of L_c as (Mogensen and Stenby, 1998)

$$\phi = \frac{\sum A_p + \sum A_t}{(n_x n_y n_z) L_c^2} \quad (5.8)$$

where L_c is the lattice constant, $n_x = n_y = n_z = n$ (model size), ϕ the core porosity, A_p and A_t are individual pore body and throat areas, respectively. In **Eq. 5.8**, both pore body and throat areas contribute to total pore space. The throat length connecting neighboring pore bodies I and J is then expressed by

$$L_{t,IJ} = L_c - (R_{p,I} + R_{p,J}) \quad (5.9)$$

where $R_{p,I}$ and $R_{p,J}$ are the radii of pore bodies adjoining that pore throat (**Fig. 5.15**).

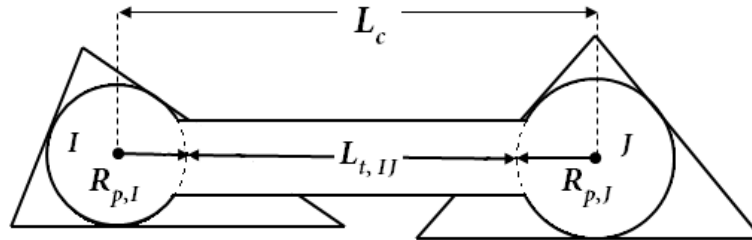


Figure 5.15 – Throat length between neighboring pore bodies I and J .

The interpore distances (L_c) of carbonate networks are found to be 41.2, 32.4, 72.6, and 49.6 μm for C013, C016, C019, and C021, respectively (**Table 5.3**). Based on the results, C019 network has relatively long distance between its node centers. The throat length distributions in ascending order are given in **Fig. 5.16**. In **Fig. 5.16**, pore throat length distributions verified that the length of any individual throat in a carbonate network system is always smaller than the lattice constant of that network. For example, the maximum throat length in C019 network is around 70 μm which is smaller than its lattice constant, 72.6 μm and this is also valid for other samples. It is important that allowing throat lengths to vary can lead to distortions in the resultant network. However, although the system pretends a more irregular structure, it still settles on a regular topology (Fenwick and Blunt, 1998a; Blunt et al., 2002).

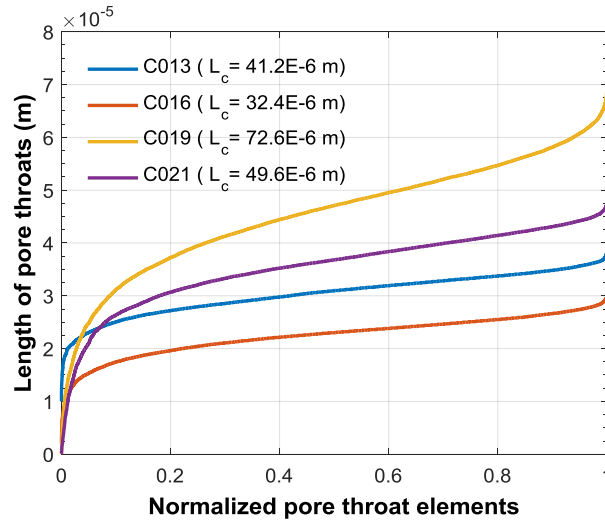


Figure 5.16 – Network-measured throat length distributions of carbonate networks in ascending order.

To sum up, in this section, the carbonate networks incorporating all the structural input parameters (shape factor, pore throat and body inscribed radii, aspect ratio, length, etc.) with the essential modifications have been constructed and the network structural outputs are obtained. Next, pore-level displacement mechanisms invoked in two-phase flow simulations are outlined and the algorithms followed in the simulations are summarized.

5.2 Fluid flow in the network

In this section, an overview of mathematical background of pore-level displacement mechanisms used for two-phase flow simulations in the model is given. Despite the highly chaotic porous system of reservoir rocks, the movement of fluids through them is governed by fundamental laws of fluid mechanics and capillarity (Kimbler and Caudle, 1957; Mohanty and Salter, 1982). Mostly Øren et al. (1998), Patzek (2001), Al-Futaisi and Patzek (2003), Valvatne and Blunt (2004), and Helland and Skjæveland (2004, 2006a) are followed for a comprehensive description of basic pore-scale flow processes.

In the model, flow is assumed to be quasi-static in which capillary forces control the flow regime at pore-level (Lenormand et al., 1983; Lenormand and Zarcone, 1984; Lenormand, 1986). Capillary number, N_{Ca} , is the ratio of viscous forces to capillary forces and expressed by

$$N_{Ca} = \mu v / \gamma \quad (5.10)$$

where μ is viscosity of the displacing phase (Pa.s), v total fluid velocity (m.s^{-1}) and γ interfacial tension between two phases (N.m^{-1}). Quasi-static assumption is reasonable for sufficiently slow flow of immiscible fluids satisfying low capillary number criterion ($N_{Ca} < 10^{-6}$; King, 1987; Jadhunandan and Morrow, 1995). It is typical of most of the oil-water displacement events in reservoir and low-rate coreflooding experiments (Mohanty and Salter, 1982; Blunt and Scher, 1995; Hilfer and Øren, 1996). The reservoir waterflooding displacements have capillary number less than 10^{-7} and also most coreflooding experiments are performed with capillary number lower than 10^{-6} (Lake, 1989; Dullien, 1992; Blunt, 1997b). Under capillarity-controlled conditions, the displacement process of one fluid by another is governed by the invasion percolation algorithm (Chandler et al., 1982; Wilkinson and Willemsen, 1983; Dias and Wilkinson, 1986). Based on the percolation algorithm, at each gradual change of capillary pressure, all menisci between fluid-fluid interfaces are kept static throughout the network and only one displacement happens with the consecutive pore-level event at a time. The displacement proceeds until all menisci within the network become stable (Reeve and

Celia, 1996). The effects of viscous forces are negligible except during pore-level events in pseudo-static models (Mohanty and Salter, 1982).

The capillary pressure at the pore level across the interface between two static immiscible fluids, oil and water in our case, is defined as

$$P_c = P_o - P_w = \gamma_{ow} \left(\frac{1}{r_1} + \frac{1}{r_2} \right) \quad (5.11)$$

where γ_{ow} is the oil-water interfacial tension, P_o and P_w stand for oil and water pressures, r_1 and r_2 are the principal radii of curvature on either sides of the oil-water interface.

During fluid invasion, two different types of fluid interfaces are formed in a non-circular cross-section: main terminal meniscus and corner arc (wedge) meniscus (Morrow and Mason, 1991; Piri, 2003). Main terminal meniscus is the one invading in the direction along the capillary tube separating bulk fluids from each other while the interface separating remaining wetting phase in the corners from bulk fluid is called as corner arc meniscus. **Figure 5.17** illustrates two types of interfaces created during oil drainage process in a capillary tube with irregular triangle cross-section.

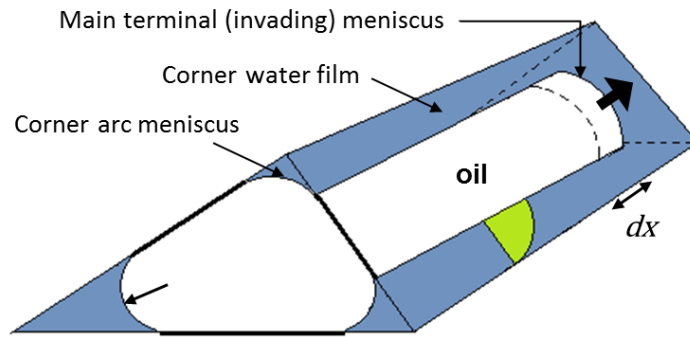


Figure 5.17 – A sketch of main terminal meniscus and corner arc meniscus in a triangular capillary tube during oil drainage.

The curvature of main invading meniscus is assumed to be spherical and, thus, the principal radii of interface are equal to each other, i.e. $r_1 = r_2 = r$ (Piri, 2003). From elementary geometry, the radius of interface is related to the radius of cylindrical

capillary tube and contact angle by $r = R/\cos \theta_c$ (**Fig. 5.18a**). Then, Young-Laplace equation expresses capillary pressure across an invading interface in a cylindrical capillary tube as

$$P_c = \frac{2\gamma_{ow}}{r} = \frac{2\gamma_{ow} \cos \theta_c}{R} \quad (5.12)$$

where r is the entry radius of curvature, R the inscribed radius, and θ_c the contact angle measured through the denser phase (water) (Dullien, 1992). The principal radii of corner arc menisci are believed to be perpendicular to each other which means that while $r_1 = r$, $r_2 = \infty$ (Mason and Morrow, 1991; Piri, 2003). Thus, to define the pressure difference across an arc meniscus (**Fig. 5.18b**), Young-Laplace equation turns into:

$$P_c = \gamma_{ow}/r \quad (5.13)$$

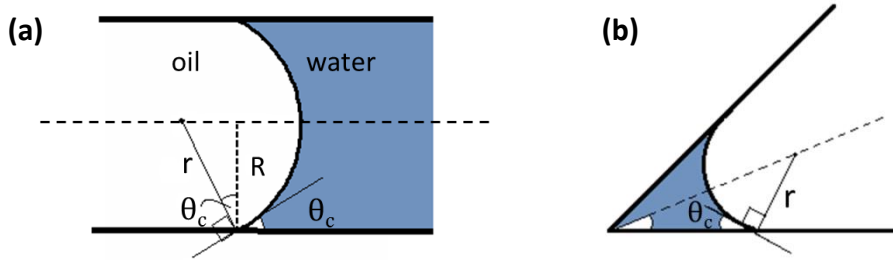


Figure 5.18 – Main terminal meniscus (a) and corner arc meniscus (b) in a capillary tube with triangular cross-section.

The constructed network model is aimed to simulate a sequence of quasi-static flooding processes in complex carbonate systems. After oil migration, due to wettability alteration, drainage (nonwetting phase displaces wetting phase) and imbibition (wetting phase displaces nonwetting phase) terminology for saturation changes leads to confusion in porous systems with nonuniform wettability. For this reason, hereafter, drainage and imbibition will refer to oil flooding and water flooding processes, respectively even for the mixed wettability conditions. Besides, wetting and nonwetting phase terms will correspond to water (or brine) and oil, respectively.

During a flooding process, fluid occupancy configurations in angular pore cross-sections differ with respect to subsequent pore-level displacement events. The possible

fluid configurations in an irregular triangle pore body or throat cross-section that may arise during the simulations are depicted by letters (Configurations A to I) in **Fig. 5.19**. Altered wettability on pore surfaces are marked by bold lines.

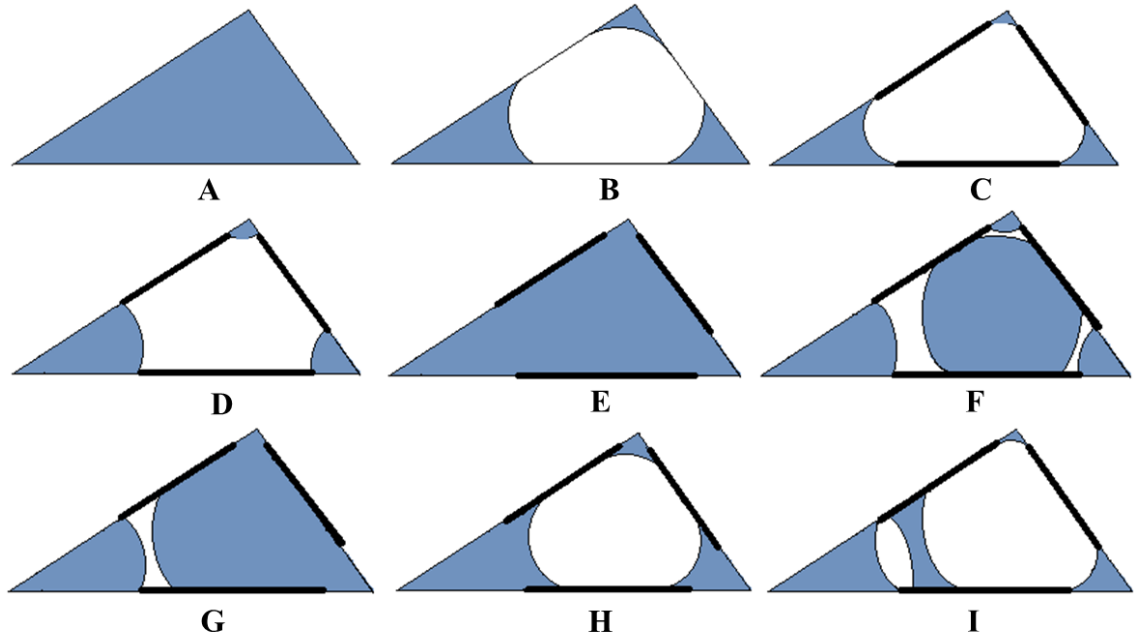


Figure 5.19 – Possible fluid configurations during primary drainage, secondary imbibition, and secondary drainage processes (Water is indicated in blue, and oil in white. The bold lines designate oil-wet surface regions after wettability change).

For the displacement of one fluid by another during any flooding event, the capillary entry pressure of target pore needs to be overcome. The following subsections describe how to calculate capillary entry pressure P_c^e for each possible displacement mechanism and the related criteria for creation of fluid layers in pore corners under mixed wettability conditions.

5.2.1 Primary drainage and threshold capillary pressure

Prior to primary drainage, the network is assumed to be fully water-saturated and water-wet. The initial configuration of all pore cross-sections is in the form of Configuration A (**Fig. 5.19**). Pore throats at the inlet face of the network are assumed to be in contact

with oil reservoir. Oil is the nonwetting phase of the porous medium, thus it firstly enters into the largest inlet throat having the lowest entry pressure. Invasion percolation algorithm progressively evaluates the accessible pore bodies and throats at each step, sorts their capillary entry pressures and addresses oil to the pore element in the sequence with the lowest P_c^e . The current capillary pressure of the system is raised to the entry pressure of the latest oil-drained pore. As oil invades into more capillaries, P_c climbs and water saturation declines in the network. At each step, overall saturations, conductances and other transport properties of each phase are recalculated. The drainage process continues until a predefined saturation or capillary pressure is reached or oil invades all the accessible pore bodies and throats in the network.

During primary drainage process, because only water is present initially in pore elements, oil invasion occurs from one pore to another through piston-type mechanism where the invading front of an oil-filled pore replaces the water from the center of its adjacent pores. The recently drained pore elements are symbolized as Configuration B (**Fig. 5.19**). To guarantee water presence in each corner i of a drained pore, the condition

$$\theta_R < 90^\circ - \beta_i \quad (5.14)$$

must be satisfied. By this way, water is connected throughout the network whether as bulk phase (Configuration A) or as corner water films (Configuration B). During primary drainage, as capillary pressure climbs, oil invades into smaller pores and also corner water area of oil-drained pores shrinks gradually with the movement of oil-water arc menisci towards the corners. The continuity of water along the network enables drainage of water to very low saturations.

The drainage capillary entry pressure is calculated by the generalization of so-called MS-P method (Mayer and Stowe, 1965; Princen, 1969a, 1969b, 1970) for irregular triangles (Ma et al., 1996; Øren et al., 1998; Patzek, 2001; Al-Futaisi and Patzek, 2003). MS-P method is based on equating the drainage entry radius of curvature r_d of corner arc menisci in an oil-drained pore to the first curvature of main invading

interface. For a small displacement of corner arc menisci dx (**Fig. 5.17**), the work of displacement is balanced by the change in surface energy as

$$P_c A_{eff} dx = (L_{ow} \gamma_{ow} + L_{os} \gamma_{os} - L_{os} \gamma_{ws}) dx \quad (5.15)$$

where A_{eff} is the cross-sectional area occupied by oil, L_{ow} and L_{os} are the interface lengths between oil-water (ow) and oil-solid wall (os), respectively. The effective area and length terms used in MS-P method are drawn in **Fig. 5.20** by modifying Fig. 10 in Ma et al. (1996) from equilateral to irregular triangular cross-section.

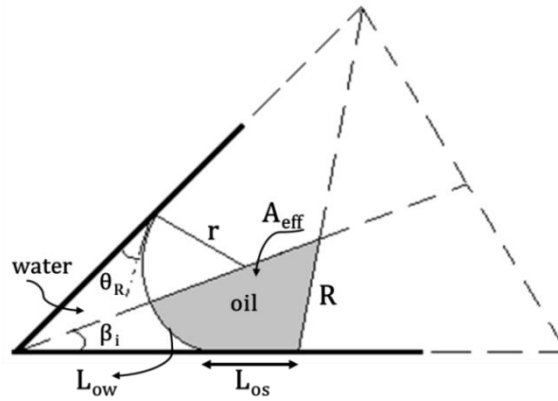


Figure 5.20 – Oil-occupied area and lengths used in MS-P method for a single corner of an irregular triangular cross-section (Modified from Fig. 10 in Ma et al., 1996).

Young's equation, an equilibrium horizontal balance between three phases (oil, water, solid),

$$\gamma_{os} = \gamma_{ws} + \gamma_{ow} \cos \theta_R \quad (5.16)$$

simplifies **Eq. 5.15** to

$$r_d = \frac{\gamma_{ow}}{P_c} = \frac{A_{eff}}{L_{os} \cos \theta_R + L_{ow}} = \frac{A_{eff}}{P_{eff}} \quad (5.17)$$

where drainage entry radius of curvature (r_d) is related to the receding contact angle (θ_R) and oil-occupied cross-sectional parameters termed as effective area (A_{eff}) and perimeter (P_{eff}). In the following part of the thesis, ow (oil-water) subscript will be

omitted. The elementary geometry relates the interface area and lengths to the essential geometric (G, β_i, R) and rock-fluid interaction properties $(\theta_R$ and $\gamma)$.

Shape factor of a triangular pore is related to its corner half-angles by **Eq. 5.1** (Patzek, 2001). Total area and perimeter of triangular-shaped pores are expressed as

$$A_T = R^2 / (4G) \quad (5.18)$$

$$P = R / (2G) \quad (5.19)$$

The effective oil-occupied area is the difference between total cross-sectional area and the water corner area A_{wc} :

$$A_{eff} = A_T - A_{wc} \quad (5.20)$$

The total area of fluid residing in the corners of a triangular pore after invasion is given by

$$A_{wc} = r_d^2 \sum_{i=1}^3 \left(\frac{\cos \theta_R \cos(\theta_R + \beta_i)}{\sin \beta_i} - \frac{\pi}{2} \left(1 - \frac{\theta_R + \beta_i}{90} \right) \right) = r_d^2 S_1 \quad (5.21)$$

The oil length contacting with wall L_{os} is the difference between total perimeter of the pore and the length of corner water L_{ws} :

$$L_{os} = P - L_{ws} \quad (5.22)$$

The length of water residing in the corners of a triangular pore after invasion is given by

$$L_{ws} = 2r_d \sum_{i=1}^3 \frac{\cos(\theta_R + \beta_i)}{\sin \beta_i} = 2r_d S_2 \quad (5.23)$$

The oil-water meniscus, thought as a slice of an imaginary circle with radius r_d , has the length of

$$L_{ow} = 2\pi r_d \sum_{i=1}^3 \left(\frac{90 - \theta_R - \beta_i}{180} \right) = \pi r_d \sum_{i=1}^3 \left(1 - \frac{\theta_R + \beta_i}{90} \right) = r_d S_3 \quad (5.24)$$

Then, substituting all the related geometrical expressions, **Eq. 5.17** becomes

$$r_d = \frac{\frac{R^2}{4G} - r_d^2 S_1}{\left(\frac{R}{2G} - 2r_d S_2 \right) \cos \theta_R + r_d S_3} \quad (5.25)$$

Equation 5.25 can be arranged in quadratic form for r_d as

$$(S_1 - 2 \cos \theta_R S_2 + S_3) r_d^2 + \frac{R}{2G} \cos \theta_R r_d - \frac{R^2}{4G} = 0 \quad (5.26)$$

Solving for r_d , **Eq. 5.26** is simplified to

$$r_d = \frac{R \cos \theta_R}{4GD} \left(-1 \pm \sqrt{1 + \frac{4GD}{\cos^2 \theta_R}} \right) \quad (5.27)$$

$$D = S_1 - 2 S_2 \cos \theta_R + S_3 \quad (5.28)$$

The solution for entry radius of curvature is the root which is less than the inscribed radius of the pore, i.e. $r_d < R$. Finally, drainage threshold capillary pressure of a pore body or throat is expressed by

$$P_{c,pd}^e = \frac{\gamma}{r_d} = \frac{4GD}{R \cos \theta_R} \frac{\gamma}{\left(-1 \pm \sqrt{1 + 4GD / \cos^2 \theta_R} \right)} \quad (5.29)$$

During computing threshold capillary pressures, it should be kept in mind that corner water exists in a corner i only if $\theta_R < 90^\circ - \beta_i$ (**Eq. 5.14**).

5.2.1.1 Wettability alteration and contact angle hysteresis

The wettability of porous system has paramount importance in flow behavior. It controls fluid distribution in a porous medium such that while wetting phase resides in micropores, crevices and rough surfaces of rocks, nonwetting phase tends to stay in the center of large pores, vugs and wide channels. Most hydrocarbon reservoirs are believed to be water-wet before oil migration (Abdallah et al., 2007). Prior to primary drainage, the pore space in our model is fully water-saturated, and hence, it is assumed to be water-wet. A constant receding contact angle smaller than 90° is assigned to network pore elements satisfying the condition in **Eq. 5.14** to ensure water presence in the corners of oil-occupied pores.

In our model, the well-known pore scale scenario of Kovscek et al. (1993) is used for wettability alteration description and development of mixed-wettability in porous medium. According to the proposed model of Kovscek et al. (1993), after oil

migrates into the center of a pore, thick water films lie along the solid pore walls and prevent the contact of bulk oil with solid surface. As oil invades into more capillaries in the pore space, capillary pressure climbs and consecutively water film coating the middle portions of the rock surface gets thinner. When capillary pressure inside pore space reaches its critical value (P_c^*), thick water films rupture into molecularly adsorbed films along the pore walls. Exceeding critical capillary pressure, polar organics of oil such as asphaltenes may collapse molecular water films and adsorb irreversibly onto the pore walls (Salathiel, 1973; Morrow et al., 1986). Then, oil-adsorbed pore walls become oil-wet. The degree of wettability change in an oil/water/rock system depends on many physical and chemical factors, namely composition of immiscible phases, pore surface mineralogy and roughness as well as temperature, initial water saturation, and duration of oil aging (Anderson, 1986; Hirasaki, 1991; Buckley et al., 1996). The wettability alteration generates mixed-wettability within individual pores in which the center of oil-invaded pore walls becomes oil-wet while the corners remain water-wet (Salathiel, 1973).

The contact angle hysteresis is defined as the difference between receding (reduction in water saturation) and advancing contact angles (increase in water saturation). The extent of contact angle hysteresis depends on both wettability alteration and surface roughness (Morrow, 1975; Kovscek et al., 1993). In the mixed-wet surfaces, the advancing angle is typically found to be significantly higher than water-wet surfaces due to higher tendency of aged pore surfaces to contact with oil phase ($\theta_A^{ww} < \theta_A^{mw}$). Besides wettability change, contact angle also depends on the direction of flow (Morrow, 1975). Attributed to surface roughness, advancing contact angle in a pore is always larger than or equal to receding contact angle independent of its wettability state ($\theta_R \leq \theta_A$). In the model, all of the oil-invaded pores are accepted to undergo wettability alteration and become mixed-wet. A wide range of advancing contact angles is used in flow simulations to analyze the effect of wettability conditions on flow behavior and residual saturation. The results are discussed in **Chapters 6 and 7** in detail.

In **Fig. 5.19**, Configuration A stands for the initial state of network pore elements, water-filled and water-wet pores. During primary drainage, inside the oil-

drained pores indicated as Configuration B, as P_c increases, oil-water corner arc menisci advances through the corners with no wettability alteration yet and corner water area shrinks gradually. After aging of oil-drained pores, Configuration B irreversibly turns into mixed-wet Configuration C. Configurations C to I represent mixed-wet pores following primary drainage.

5.2.2 Secondary imbibition and threshold capillary pressure

In comparison to primary drainage, water imbibition is somewhat more complex due to the contact angle hysteresis and the co-existence of water and oil in a single pore resulting in competition between flow mechanisms and oil entrapment (Lenormand et al., 1983; Prodanović and Bryant, 2006). Each pore in the network system has a different advancing contact angle satisfying $\theta_A \geq \theta_R$. During imbibition, water begins to enter into network via the smallest inlet pore throats with the highest entry pressure. The capillary pressure of the system declines stepwise. Main pore-level displacements observed during water imbibition are piston-type, pore body filling and snap-off mechanisms (Lenormand et al., 1983; Lenormand, 1986).

Two fluid configurations of **Fig. 5.19** are available in the network prior to secondary imbibition: Configuration A representing the water-filled, water-wet pores and Configuration C representing oil-drained, mixed-wet pores. Since the pores in Configuration A are already water-filled, water injection just affects Configuration C. Next, the description of each pore-level displacement mechanism is given with its corresponding threshold capillary pressure expression for different fluid configurations.

5.2.2.1 Piston-type advancement

In piston-type displacement mechanism, bulk oil in a pore is displaced by the frontal invading interface of one of its adjoining water-filled pores. Due to contact angle hysteresis, corner arc meniscus in each corner i of an oil-occupied pore (Configuration C in **Fig. 5.19**) stays pinned at the last position it reaches at the end of primary drainage

($L_{pd,i}$) as shown in **Fig. 5.21**. To accommodate for the capillary pressure drop, the pinned corner meniscus swells and its curvature decreases with the gradual increase of hinging contact angle $\theta_{h,i}$ from receding to advancing angle $\theta_R \leq \theta_{h,i} \leq \theta_A$ (**Fig. 5.21**). When hinging angle reaches advancing value, corner arc menisci has the same curvature with the invading interface and starts to move along the pore surface at advancing contact angle.

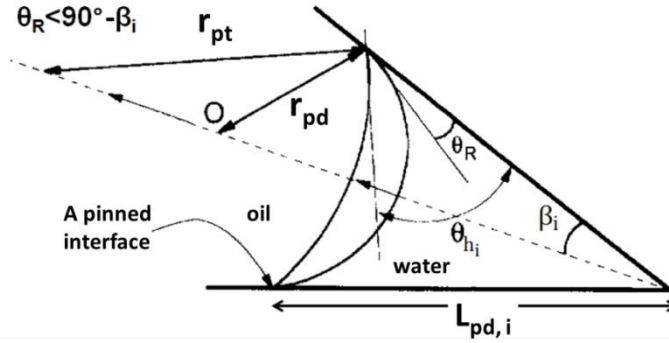


Figure 5.21 – Fluid configurations in a corner with pinned oil/water interface during imbibition (Modified from Fig. 5 in Ma et al., 1996).

From the similarity of triangles, if arc meniscus in an individual corner has not moved yet, its distance from the corner apex $L_{pd,i}$ is geometrically expressed as

$$L_{pd,i} = r_{pd} \frac{\cos(\theta_R + \beta_i)}{\sin \beta_i} \quad (5.30)$$

where $r_{pd} = \gamma / P_{c,pd}^{\max}$ is the minimum radius of curvature attained at maximum capillary pressure at the end of primary drainage. Since $L_{pd,i}$ decreases with $P_{c,pd}^{\max}$, maximum capillary pressure limit of primary drainage determines water-wet fraction of mixed-wet pores and so irreducible water saturation in the corners of oil-invaded pores. According to **Eq. 5.30**, it is noteworthy that in an oil-filled pore, the distance from corner oil-water meniscus to corner apex is the largest in the sharpest corner due to its smallest corner half-angle (β_1). Fassi-Fihri et al. (1995) stated that the pore geometry is a significant determinant in the wettability extent of pore surfaces. **Equation 5.30** reveals that the

length of water-wet surfaces $L_{pd,i}$ in the corners of two pore elements having similar shape factors (i.e., similar β_i) but different sizes (a relatively small and large pore) will be nearly the same. As shape factor and accordingly corner half-angles in a pore are independent of its pore size (**Eqs. 5.1–5.4**), smaller pore with the same shape factor will have larger fraction of water-wet surface ($L_{pd,i}$) on its total pore surface perimeter than the larger one. This is why smaller pores show more water-wet character during water invasion (Helland and Skjæveland, 2004, 2006a).

In the course of imbibition, capillary pressure of the porous medium progressively declines. Spontaneous water imbibition into previously oil-occupied pores continues until oil-water interface curvature becomes flat, i.e. P_c reaches zero. In mixed-wet medium, water imbibition continues in the forced manner where an external finite pressure is required to overcome the system capillary force (Mogensen and Stenby, 1998; Donaldson and Alam, 2008). Then, since water pressure exceeds oil pressure, oil-water interface bulges out toward the center (Configuration D in **Fig. 5.19**) and capillary pressure displays negative values (Hui and Blunt, 2000). In strongly water-wet pores, since the advancing angle never exceeds 90° , capillary pressure remains positive during imbibition (Configuration C in **Fig. 5.19**). The maximum advancing contact angle θ_A^{\max} corresponding to zero P_c with flat arc menisci is the limit for spontaneous piston-type imbibition and determined by (Ma et al., 1996)

$$\theta_A^{\max} = \cos^{-1} \left(\frac{-4G \sum_{i=1}^3 \cos(\theta_R + \beta_i)}{R \frac{P_{c,pd}^{\max}}{\gamma} - \cos \theta_R + 12 G \sin \theta_R} \right) \quad (5.31)$$

θ_A^{\max} depends on maximum capillary pressure at the end of primary drainage $P_{c,pd}^{\max}$, pore geometry (G, β_i, R) and θ_R . Based on **Eq. 5.31**, with the increase of $P_{c,pd}^{\max}$, the critical limit for spontaneous water invasion drops and imbibition continues mostly in forced manner. The normalized threshold capillary pressure ($P_{c,N} = R P_c^e / \gamma$) vs

advancing contact angle plots for different G -values from the study of Øren et al. (1998) are reproduced in **Fig. 5.22a**. According to **Fig. 5.22a**, spontaneous piston-type imbibition ($P_c > 0$) always occurs for advancing contact angles less than 90° , but it is also possible for advancing angles much larger than 90° depending on pore geometry (Øren et al., 1998).

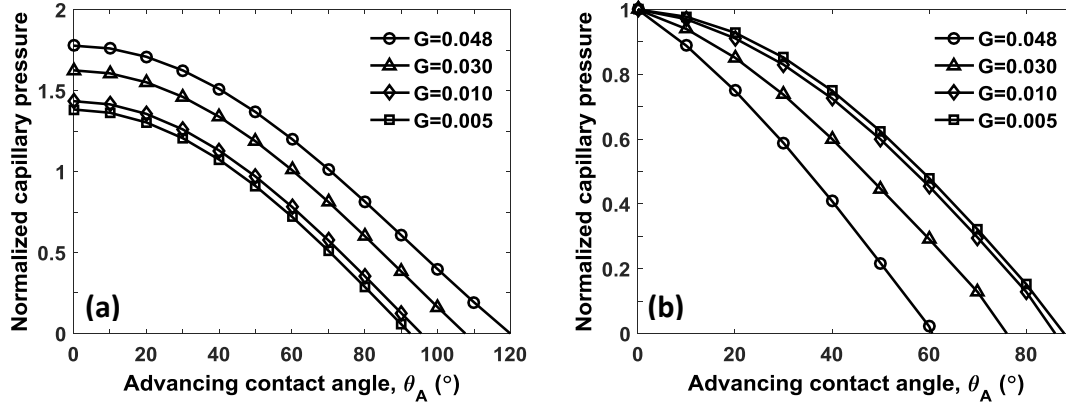


Figure 5.22 – Normalized threshold capillary pressure of a) piston-type displacement and b) snap-off for $\theta_R = 0^\circ$, $P_{c,N}^{\max} = 2$ (Reproduced from Øren et al., 1998).

If $\theta_A < \theta_A^{\max}$, capillary forces provide water to imbibe into the pore space spontaneously. The threshold capillary pressure for spontaneous piston-like displacement is again calculated from the MS-P method by equating the piston-type entry radius r_{pt} of pinned arc menisci to the main invading interface A_{eff}/P_{eff} . The geometric relations $(L_{os}, L_{ow}, A_{eff})$ used in MS-P method are modified by replacing r_d with r_{pt} , and θ_R with $\theta_{h,i}$. The difference with primary drainage is that, instead of corner arc menisci moving at a fixed receding contact angle, now the arc menisci are stuck at the last position of primary drainage and the hinging contact angle gradually increases from θ_R to θ_A ($\theta_R \leq \theta_{h,i} \leq \theta_A$) (**Fig. 5.21**). In contrast to primary drainage case, there is not an analytical solution of piston-type capillary entry pressure $P_{c,pt}^e$ because the hinging angle $\theta_{h,i}$ is a function of unknown entry radius of curvature r_{pt} .

The following nonlinear system of equations is solved iteratively for r_{pt} corresponding to $P_{c,pt}^e$.

$$\theta_{h,i} = \cos^{-1} \left(\frac{r_{pd}}{r_{pt}} \cos(\theta_R + \beta_i) \right) - \beta_i \quad (5.32)$$

$$A_{wc} = \sum_{i=1}^3 \left(L_{pd,i} r_{pt} \cos \theta_{h,i} - \frac{\pi}{2} r_{pt}^2 \left(1 - \frac{\theta_{h,i} + \beta_i}{90} \right) \right) \quad (5.33)$$

$$L_{ws} = 2 \sum_{i=1}^3 L_{pd,i} = 2 r_{pt} \sum_{i=1}^3 \frac{\cos(\theta_{h,i} + \beta_i)}{\sin \beta_i} \quad (5.34)$$

$$L_{ow} = 2\pi r_{pt} \sum_{i=1}^3 \left(\frac{90 - \theta_{h,i} - \beta_i}{180} \right) = \pi r_{pt} \sum_{i=1}^3 \left(1 - \frac{\theta_{h,i} + \beta_i}{90} \right) \quad (5.35)$$

$$r_{pt} = \frac{A_{eff}}{L_{os} \cos \theta_A + L_{ow}} \quad (5.36)$$

Capillary entry pressure for spontaneous piston-type imbibition is then $P_{c,pt}^e = \gamma / r_{pt}$.

During piston-type entry pressure calculations, our check points are $r_{pt} \geq r_{pd}$ (

$P_c \leq P_{c,pd}^{\max}$) and $\theta_R \leq \theta_{h,i} \leq \theta_A$.

If the contact angle hysteresis is too much, advancing angle exceeds its maximum limit for spontaneous piston-type displacement, i.e. $\theta_A > \theta_A^{\max}$. In this case, while corner arc menisci remained pinned, invading meniscus enters to the pore with a negative capillary pressure, known as forced imbibition.

In forced imbibition, if $\theta_A < 90^\circ + \beta_1$ where $\beta_1 = \min(\beta_i)$, invading meniscus is forced into the pore with a threshold capillary pressure of

$$P_{c,pt}^e = \frac{(1 + 2\sqrt{\pi G}) \gamma \cos \theta_A}{R} \quad (5.37)$$

If $\theta_A \geq 90^\circ + \beta_1$, entry capillary pressure is simply determined from **Eq. 5.29** after replacing θ_R by $(180 - \theta_A)$ as

$$P_{c, pt}^e = -P_{c, pd}^e (180 - \theta_A) \quad (5.38)$$

5.2.2.2 Pore body filling

Pore body filling is the movement of oil from the center of a pore body by the cooperative advancement of interfaces from water-invaded neighboring pore throats (Ryazanov, 2012). The threshold capillary pressure for pore body filling depends on the pore body size as well as the number and size of its adjacent oil-filled throats (Mohanty and Salter, 1982; Lenormand et al., 1983). Thus, for a pore body with coordination number Z , because at least one of its connected throats must be water-filled for piston-type imbibition, there are $Z - 1$ possible pore-body filling mechanisms denoted by I_k (I_1 to I_5 for $Z = 6$). In **Fig. 5.23**, some of the possible filling types for a pore body with coordination number of four ($Z = 4$) are illustrated (Blunt and Scher, 1995).

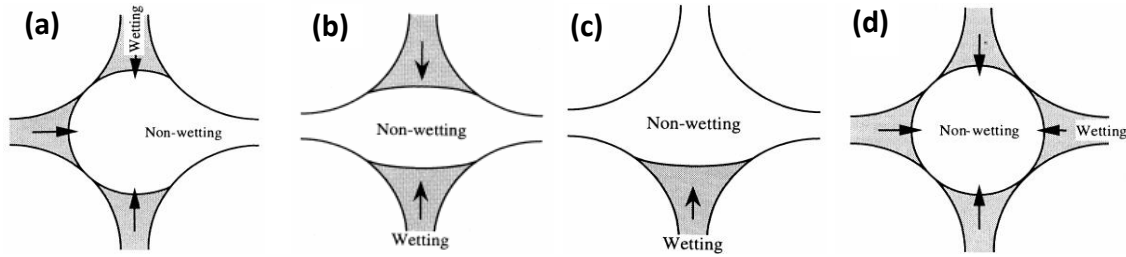


Figure 5.23 – Different types of pore body filling mechanisms for $Z = 4$: a) I_1 b) I_2 c) I_3 d) I_0 ($k = 0$ for snap-off) (Blunt and Scher, 1995).

In case only one of the connected throats occupies oil, i.e. I_1 in **Fig. 5.23a**, the imbibition process is similar to piston-type advancement with a similar capillary entry pressure as (Øren et al., 1998; Patzek, 2001)

$$P_{c, I_1}^e = P_{c, pt}^e \quad (5.39)$$

The mean or effective inscribed radius for a I_k mechanism is determined from

$$R_k = R_p + \sum_{i=1}^k (A_i R_{t,i} x_i) \quad (5.40)$$

where k is the number of adjacent oil-filled throats connected to a pore body, R_p the pore body inscribed radius, $R_{t,i}$ the radius of i^{th} connected oil-filled pore throat, x_i random number for $x_i \in [0,1]$, and A_i are the geometrical constants determining throat radii weight in each pore filling mechanism (Jia, 2005). The vector of geometrical constants employed in our model is taken as $A = [0, 0.5, 1.0, 5.0, 10.0, 30.0]$ (Lulla, 1999). Note that since I_1 is a piston-type displacement, its geometric constant is $A_1 = 0$.

For $I_k = I_2$ to I_5 mechanisms, a similar approach to Blunt's parametric model (1997b) is used for capillary entry pressure of noncircular pore shapes (Valvatne, 2004):

$$P_{c, I_k}^e = \frac{(1 + 2\sqrt{\pi G})\gamma \cos \theta_A}{R_k} \quad \text{for } k = 2 : 5 \quad (5.41)$$

Figure 5.24 gives the sorted distribution of resulting capillary entry pressures for particular pore body filling mechanisms at $\theta_R = 10^\circ$, $\theta_A = 60^\circ$ for C013. It is clear from the figure that, for a particular pore element, the corresponding threshold capillary pressures of pore-filling events decreases as k , the number of adjacent oil-filled throats to a pore body increases. The piston-type displacement I_1 has the highest capillary entry pressure among all.

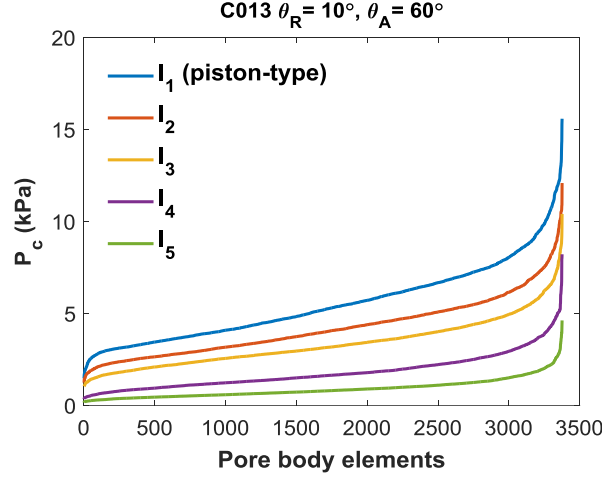


Figure 5.24 – Threshold capillary pressures of pore body filling mechanisms (I_k) in ascending order.

In forced piston-type imbibition into a pore body where $\theta_A > \theta_A^{\max}$, the capillary entry pressure does not depend on the number of adjacent oil-filled throats and is given by (Øren et al., 1998; Valvatne and Blunt, 2004)

$$P_{c,I_k}^e = \frac{(1 + 2\sqrt{\pi G}) \gamma \cos \theta_A}{R_p} \quad (5.42)$$

5.2.2.3 Oil layer formation and stability

If contact angle hysteresis is large enough to satisfy the condition $\theta_A \geq 90^\circ + \beta_i$ in a corner i of mixed-wet pores, during forced imbibition into the pore space, a second arc meniscus may form and so an intermediate oil layer may be left between water in the corner and water in the center (Configurations F and G in **Fig. 5.19**).

In micromodel studies, oil layers have been detected to bridge oil-wet surfaces along the central part of pore walls and brine in the crevices (Buckley, 1995, 1996). A geometrical criterion proposed by Blunt (1997b) has been widely used for conditioning oil layer existence in pore-scale models. It supposes that oil layers remain stable until two interfaces on either side of an oil layer meet due to the decrease in current capillary pressure during imbibition process. The critical capillary pressure below which oil layer

in corner i of a triangular mixed-wet pore ceases to exist is given by (Øren et al., 1998; Helland and Skjæveland, 2004)

$$P_{c,i}^{crit} = - \frac{\gamma(1-\xi_i^2)}{L_{pd,i} \left(\xi_i \cos \beta_i + \sqrt{1-\xi_i^2 \sin^2 \beta_i} \right)} \quad (5.43)$$

where $\xi_i = \frac{\cos \theta_A^{mw}}{\sin \beta_i} + 2$.

Equation 5.43 reveals that the formation of oil layers is suppressed at relatively low $P_{c,pd}^{\max}$, i.e. large $L_{pd,i}$ (Kallel et al., 2015). Even though the condition $\theta_a \geq 90^\circ + \beta_i$ is satisfied in a corner i , if $P_c \leq P_{c,i}^{crit}$, oil layer does not form. In triangular pores, the sharpest corner has the greatest potential for oil layer formation due to its smallest half-angle (β_1), accordingly greatest $L_{pd,i}$ and lowest $P_{c,i}^{crit}$. Based on the half-angles and critical collapse pressure values, oil layers can be present in all corners of a pore element like in Configuration F (**Fig. 5.19**). But, with the further decrease of P_c , most of the oil layers collapse and generally only the oil layer in the sharpest corner is left at the end of forced imbibition (Configuration G in **Fig. 5.19**). If oil layers collapse in a pore element, it turns into Configuration E in **Fig. 5.19**.

Based on **Eq. 5.43**, as θ_A^{mw} increases, the critical capillary pressure $P_{c,i}^{crit}$ below which oil layers no longer exist reduces. Therefore, in strongly oil-wet systems (large θ_A^{mw}), oil layers are stable for a greater range of capillary pressure during forced imbibition (Blunt, 1997b). Stable oil layers in the corners during forced imbibition play similar role as corner water films during primary drainage that they provide oil connectivity and significantly reduce residual oil saturation (Valvatne and Blunt, 2004).

5.2.2.4 Snap-off

In snap-off mechanism, as the water interfaces in the corners of previously oil-invaded pores swell during imbibition, they lose stability after a while and water in the corners

instantly fills the pore center. Snap-off makes a mixed-wet pore water-filled even though all of its adjacent pores are oil-occupied. As the pertinent capillary pressure declines during imbibition, more water accumulates in the corners and the pinned arc menisci swell gradually from θ_R to θ_A . When the hinging angle of arc meniscus at the sharpest corner reaches θ_A , it eventually moves towards the center of the pore element. Maximum advancing angle for spontaneous snap-off is given as

$$\theta_{A,so}^{\max} = 90^\circ - \beta_i \quad (5.44)$$

Therefore, contrary to piston-type displacement, spontaneous snap-off is possible only for advancing angles less than 90° . It is indicated in **Fig. 5.22b** again reproducing from the study of Øren et al. (1998).

If $\theta_A < \theta_{A,so}^{\max}$ in a triangular mixed-wet pore, all three arc menisci are concave and thereby their curvatures are positive (Configuration H in **Fig. 5.19**). When arc meniscus of the sharpest corner in a pore meets with one of the other arc menisci, they lose contact with the surface and coalesce. After snap-off, corner water spontaneously blocks the whole pore element as indicated in Configuration E (**Fig. 5.19**). Snap-off removes oil connectivity and causes disconnected oil droplets in the pore network. Depending on the advancing contact angle, arc menisci of the sharpest two corners may advance at θ_A (**Fig. 5.25a**) and meet or the sharpest corner may meet with the pinned arc menisci, $\theta_{h,3}$ at the most oblique corner (Øren et al., 1998). The radius of curvature for either case is given by

$$r_{so,ij} = R \left(\frac{\cot \beta_i + \cot \beta_j}{\cos(\theta_i + \beta_i) / \sin \beta_i + \cos(\theta_j + \beta_j) / \sin \beta_j} \right) \quad (5.45)$$

In the former case $(i, j) = (1, 2)$ and $\theta_1 = \theta_2 = \theta_A$ (**Fig. 5.25a**) and in the latter case $(i, j) = (1, 3)$ and $\theta_1 = \theta_A$; $\theta_3 = \theta_{h,3}$. For the latter case, since $\theta_{h,3}$ is a function of $r_{so,ij}$, capillary entry pressure is solved numerically. One of the cases offering the highest threshold capillary pressure (i.e. the smallest r_{so}) is favored for snap-off mechanism.

$$P_{c,so}^e = \frac{\gamma}{\min(r_{so,ij})} \quad (5.46)$$

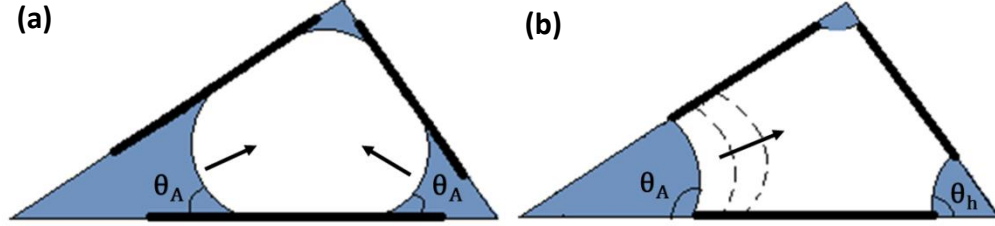


Figure 5.25 – The arc menisci configurations during a) spontaneous and b) forced snap-off events (Reproduced from Valvatne, 2004).

For $\theta_A = \theta_{A,so}^{\max}$, the corner meniscus of the sharpest corner is flat and so $P_{c,so}^e = 0$ (Al-Futaisi and Patzek, 2003). During forced snap-off ($\theta_A > \theta_{A,so}^{\max}$), all three corner menisci are convex with negative curvature (Configuration D in **Fig. 5.19**). When the hinging angle of arc menisci in the sharpest corner has reached θ_A as shown in **Fig. 5.25b**, it is no longer stable and snap-off occurs. The capillary entry pressure for forced snap-off depends on the relation between the smallest corner half-angle and advancing angle and is given by

$$P_{c,so}^e = \frac{\gamma}{r_{pd}} \frac{\cos(\theta_A + \beta_1)}{\cos(\theta_R + \beta_1)} \quad \text{if } \theta_A \leq 180^\circ - \beta_1 \quad (5.47)$$

and

$$P_{c,so}^e = \frac{\gamma}{r_{pd}} \frac{-1}{\cos(\theta_R + \beta_1)} \quad \text{if } \theta_A > 180^\circ - \beta_1 \quad (5.48)$$

As discussed previously, aspect ratio, i.e., pore-to-throat size ratio, controls snap-off (Roof, 1970). Large aspect ratio in porous systems leads to more snap-off and so extensive oil entrapment during imbibition (Chatzis et al., 1983). Wardlaw (1982) first related oil trapping to the wettability as well as pore geometry. Mogensen and Stenby (1998) used the criterion developed by Zhou et al. (1997) for snap-off occurrence in low

capillary number flows. It takes into account the effects of pore geometry and contact angle as

$$\alpha > \frac{2\kappa}{1 - \tan \theta_A \tan \beta_i} \quad (5.49)$$

where α is aspect ratio, κ geometry factor close to unity ($\kappa=1$ in the model), β_i corner half-angle, and θ_A advancing contact angle. If a particular pore throat meets the condition in **Eq. 5.49**, snap-off is allowed. The smallest corner half-angle (β_1) in each pore throat is used for snap-off occurrence condition in **Eq. 5.49**. According to this criterion, a smaller advancing angle, or corner half-angle provides a lower aspect ratio threshold. Therefore, snap-off becomes more favorable compared to other filling mechanisms in the irregular pores and water-wet medium.

In general, snap-off is evaluated only in pore throats of network models due to their relatively narrower sizes and greater possibility to stand with two adjacent oil-invaded pore bodies. In our model, besides pore throats, snap-off is also considered in pore bodies (I_0 , **Fig. 5.23d**) and pore body aspect ratio is proposed as

$$\alpha_{pb} = \frac{R_k}{\min(R_{t,i})} \text{ for } i=1:6 \quad (5.50)$$

where α_{pb} is pore body aspect ratio, R_k effective inscribed radius defined in **Eq. 5.40**, and $R_{t,i}$ inscribed radii of adjacent throats. It is conditioned in our model that if aspect ratio of a particular pore body, α_{pb} is greater than its snap-off criterion (**Eq. 5.49**) and its surrounding throats are all oil-filled yet, water imbibition via snap-off is possible. However, in pore bodies, snap-off is rarely favored over pore body filling because, due to their quite smaller sizes, throats are imbibed faster and a pore body surrounded by six oil-filled throats is occasionally encountered in a pore network during imbibition process.

In **Fig. 5.26**, the sorted piston-type and snap-off threshold capillary pressures of pore throats in C013 are given on the left side and their difference in individual pore throats (right; gray dots) with its sorted curve (right; red line) are given on the right side

for $\theta_R = 10^\circ$ and $\theta_A = 60^\circ$. Model outputs reveal that piston-type threshold pressure is always higher than snap-off threshold pressure ($P_{c,pt}^e - P_{c,so}^e > 0$). Therefore, even if the geometrical criterion (Eq. 5.49) is satisfied, snap-off only happens in a pore throat when any of its adjacent pore bodies are occupied by water and hence piston-type flow is impossible (Valvatne and Blunt, 2004). This is why snap-off mostly occurs at the early stages of imbibition when water clusters have not been formed yet across the network.

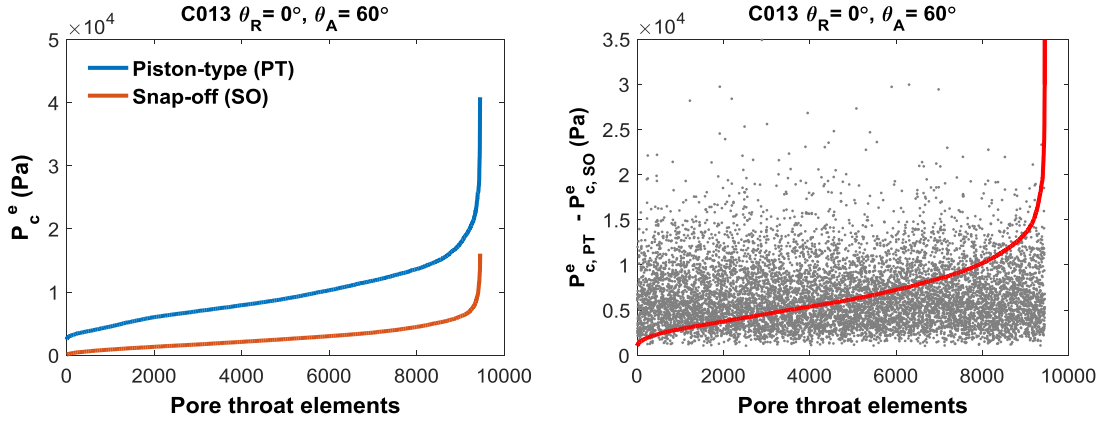


Figure 5.26 – Piston-type and snap-off capillary entry pressures (left) and their difference in individual throats (right; gray dots) and sorted in ascending order (right; red curve).

5.2.3 Secondary drainage and threshold capillary pressure

The last part of the flooding cycle is secondary drainage, i.e. oil re-invasion. Once no more oil can be displaced, oil again invades from the inlet face of the network. After water flooding, oil is still present within the network either as bulk phase, trapped oil blobs or as oil layers sandwiched in between water in the corner and in the center. Oil re-invasion may allow previously trapped oil to reconnect and be produced. Secondary drainage process is similar to primary drainage with essential modifications accounting for the oil presence in the network. To prevent ambiguity between receding contact angles of two drainage processes, θ_R and θ_r are used for primary and secondary drainage processes, respectively. Due to contact angle hysteresis, a different receding angle is defined for each mixed-wet pore body and throat in the range of $\theta_R < \theta_r < \theta_A$.

On the other hand, the same receding angle θ_R of pristine oil drainage is assigned to the water-wet pores and throats. Secondary drainage continues until the same maximum capillary pressure attained during primary drainage; however, it may finish at a lower capillary pressure due to contact angle hysteresis ($\theta_r > \theta_R$) and already existence of oil in the system ($P_{c, sd}^{\max} \leq P_{c, pd}^{\max}$).

Prior to secondary drainage, there are several oil-water combinations in the pore cross-sections. Firstly, oil-filled (Configurations C and D) and water-filled pores (Configurations A, E, F, and G) are identified in **Fig. 5.19**. Then, water-invaded mixed-wet pores are checked for oil-layer presence at the end of previously conducted imbibition process and evaluated separately in capillary entry pressure calculations. Helland and Skjæveland's work (2004, 2006a) is followed for the evaluation of secondary drainage threshold capillary pressures in each possible pore-level fluid configuration after the equations are modified from equilateral to scalene triangle cross-section.

Configuration A (**Fig. 5.19**) stands for the pores remain water-filled and accordingly water-wet all along the flooding cycle. Since the maximum capillary pressure of secondary drainage will not be allowed to exceed that of primary drainage, the water-wet pores in Configuration A will maintain their original state.

In Configuration C or D (**Fig. 5.19**), oil has already occupied the bulk region of pores and, accordingly, frontal oil invasion via main terminal menisci does not occur. The arc menisci are pinned at the intersection point of water-wet and oil-wet surfaces, $L_{pd,i}$ (**Eq. 5.30**). With the increase in current capillary pressure of the network system, the hinging angle of the pinned interfaces starts to shrink towards θ_r according to

$$\theta_{h,i} = \cos^{-1} \left(\frac{P_c}{P_{c, pd}^{\max}} \cos(\theta_R + \beta_i) \right) - \beta_i \quad (5.51)$$

Water-filled mixed-wet pores are checked for oil layer presence in any corner with the essential conditions of $\theta_A \geq 90^\circ + \beta_i$ and $P_c^{\min} \geq P_c^{crit}$ where P_c^{\min} is the

lowest capillary pressure reached at the end of secondary imbibition and P_c^{crit} is the critical capillary pressure for oil layer collapse (**Eq. 5.43**). Fully water-filled (no oil layer), mixed-wet pores are represented in Configuration E (**Fig. 5.19**). After oil re-invasion, Configuration E may turn into D or H depending on the relation between receding contact angle θ_r and half-angle of the sharpest corner β_1 .

If $\theta_r \geq 90^\circ - \beta_1$, the displacement is from Configuration E to D in a piston-type manner and threshold capillary pressure is calculated numerically from the nonlinear set of geometrical expressions given in **Eqs. 5.32–5.36** after replacing θ_A by θ_r and r_{pt} by r_{sd} . The piston-type entry radius of curvature r_{sd} gives capillary entry pressure as $P_{c,sd}^e = \gamma / r_{sd}$. In piston-type capillary entry pressure calculations, our check points are $r_{sd} \geq r_{pd}$ ($P_{c,sd}^{max} \leq P_{c,pd}^{max}$) and $\theta_r \leq \theta_{h,i} \leq \theta_A$.

In case $\theta_r < 90^\circ - \beta_1$, there are two possible displacements which are from Configuration E to C or E to H (**Fig. 5.19**). Firstly, the displacement from E to H is considered. In this case, since it seems like a typical primary drainage process, threshold capillary pressure is obtained from **Eq. 5.29** in which θ_R is replaced by θ_r . The corresponding distance of arc meniscus to apex in corner i is

$$L_i = \left| \frac{\gamma \cos(\theta_r + \beta_i)}{P_c \sin \beta_i} \right| \quad (5.52)$$

For $i=1$, if $L_i > L_{pd,i}$, the displacement is certainly from Configuration E to H. While the current capillary pressure climbs during oil re-invasion, arc menisci in Configuration H move smoothly towards the position of $L_{pd,i}$ at a constant contact angle θ_r . Thus, capillary entry pressure simply replicates **Eq. 5.29** for θ_r instead of θ_R

$$P_{c,sd}^e = P_{c,pd}^e(\theta_r) \quad (5.53)$$

If $L_i \leq L_{pd,i}$, the displacement actually occurs from Configuration E to C. Since the hinging contact angle changes gradually, threshold capillary pressure is again determined iteratively from **Eqs. 5.33–5.36** and **5.51** for r_{sd} .

While water flooding is progressed down to residual oil saturation S_{or} , most of the oil layers will have been collapsed until the end of water flooding. Water-filled mixed-wet pores with at least one oil layer are represented in Configurations F and G in **Fig. 5.19**. They exhibit a somewhat different behavior than Configuration E due to existence of oil layer(s). There are two oil-water arc menisci on either sides of oil layer in a single corner: inner meniscus separating oil layer from bulk water and outer meniscus separating oil layer from corner water film. Depending on the contact angle, three different scenarios for threshold capillary pressure expressions are defined for mixed-wet water-filled pores with at least one oil layer (Configuration G in **Fig. 5.19**).

If $\theta_r > 90^\circ + \beta_1$, the displacement is from Configuration G to D and capillary entry pressure is given by

$$P_{c,sd}^e = P_{c,pd}^e (180^\circ - \theta_r) \quad (5.54)$$

In this condition, after hinging angle of the inner meniscus decreases to θ_r , it may slide towards the center of the pore at a negative capillary pressure.

If $90^\circ - \beta_1 \leq \theta_r \leq 90^\circ + \beta_1$, the displacement is again from Configuration G to D. However, this time, the inner meniscus is pinned at its last position, $L_{imb,i}$ at the end of water flooding which is given by

$$L_{imb,i} = \left| r_{imb} \frac{\cos(\theta_A - \beta_i)}{\sin(\beta_i)} \right| \quad (5.55)$$

where $r_{imb} = \gamma / P_c^{\min}$ which is the maximum radius of curvature attained at minimum capillary pressure of secondary imbibition process. It is deduced from **Eq. 5.55** that $L_{imb,i}$ depends on the P_c^{\min} and θ_A . The capillary entry pressure is analogous to spontaneous piston-type imbibition and entry radius r_{sd} is calculated by solving the set of nonlinear equations given below.

$$\theta_{h,i} = \cos^{-1} \left(\frac{r_{imb}}{r_{sd}} \cos(\theta_A - \beta_i) \right) + \beta_i \quad (5.56)$$

$$A_{wc} = \sum_{i=1}^3 \left(L_{imb,i} r_{sd} \cos \theta_{h,i} - \frac{\pi}{2} r_{sd}^2 \left(1 - \frac{\theta_{h,i} - \beta_i}{90} \right) \right) \quad (5.57)$$

$$L_{ws} = 2 \sum_{i=1}^3 L_{imb,i} \quad (5.58)$$

$$L_{ow} = 2\pi r_{sd} \sum_{i=1}^3 \left(\frac{90 - \theta_{h,i} + \beta_i}{180} \right) = \pi r_{sd} \sum_{i=1}^3 \left(1 - \frac{\theta_{h,i} - \beta_i}{90} \right) \quad (5.59)$$

$$r_{sd} = \frac{A_{eff}}{L_{os} \cos \theta_r - L_{ow}} \quad (5.60)$$

The capillary entry pressure is ultimately determined from $P_{c,sd}^e = \gamma / r_{sd}$.

If $\theta_r < 90^\circ - \beta_1$ in a pore belonging to Configuration G, with the invasion of main invading meniscus from adjacent oil-filled pores, water layers may be left between oil layer and bulk oil at least one of the corners. In case water layers form, the displacement order is from Configuration G to I (**Fig. 5.19**) and threshold capillary pressure is calculated by **Eq. 5.53**. If the essential conditions are not satisfied for water layer formation, Configuration G is directly displaced to Configuration C whose capillary entry pressure is calculated again from **Eqs. 5.56–5.60** iteratively.

5.2.3.1 Water layer formation and stability

For a corner i with oil layer at the end of water flooding (Configuration F or G in **Fig. 5.19**), if the condition $\theta_r < 90^\circ - \beta_i$ is satisfied, with the oil re-invasion into the pore space, an intermediate water layer may form between oil layer and bulk oil. Configuration I in **Fig. 5.19** stands for the pore cross-section with intermediate oil and water layers on the sharpest and thus the most probable corner for oil layer formation and for its stability. Water layers remain stable until the two interfaces on either side of a

water layer meet with the increase in current capillary pressure. The geometrical capillary pressure criterion for a pore corner i over which water layer(s) cannot be stable and collapse is given by

$$P_{c,i}^{stab} = \frac{\gamma(\xi_i^2 - 1)}{L_{imb,i} \left(\xi_i \cos \beta_i - \sqrt{1 - \xi_i^2 \sin^2 \beta_i} \right)} \quad (5.61)$$

where $\xi_i = \frac{\cos \theta_r}{\sin \beta_i} - 2$.

If $P_c \geq P_{c,i}^{stab}$ in the corners of a pore element, water layers do not form and displacement occurs directly from Configuration F to C (**Fig. 5.19**).

The oil re-invasion may be spontaneous or forced depending on the minimum receding angle θ_r^{\min} . Oil spontaneously invades into a pore when its receding angle is greater than θ_r^{\min} and in a forced manner otherwise. For the water-occupied mixed-wet pores with at least one oil layer (Configuration F or G in **Fig. 5.19**), the minimum contact angle is expressed as (Helland and Skjæveland, 2004)

$$\theta_r^{\min} = \cos^{-1} \left(\frac{-4G \sum_{i=1}^3 \cos((180 - \theta_A) + \beta_i)}{R \frac{P_c^{\min}}{\gamma} - \cos(180 - \theta_A) + 12G \sin(180 - \theta_A)} \right) \quad (5.62)$$

If oil invasion occurs into entirely water-filled mixed-wet pores (Configuration E in **Fig. 5.19**), the minimum contact angle for spontaneous drainage is determined from **Eq. 5.31**.

5.2.4 Macroscopic fluid transport properties

At prescribed steps of any displacement event, the changes in the fluid configurations in the network are recorded. The areas occupied by fluid contents in each pore element and their overall saturations are evaluated stepwise. Then, the macroscopic flow properties, namely capillary pressure and relative permeability curves as a function of saturation and the oil recovery are determined in the pore network system.

5.2.4.1 Fluid areas and saturations

In a flooding process, at discrete steps, fractional oil and water areas in individual pore elements are calculated independently from each other. In our model, a mixed-wet pore element with noncircular cross-section may accommodate oil phase in the form of molecular surface films coating the oil-wet patches of pore wall, bulk phase in the center, disconnected oil droplets or intermediate oil layers on the corners. On the other side, water may be present in a pore element as bulk fluid, corner film or as intermediate layers.

If a pore element is fully water-saturated (Configuration A or E in **Fig. 5.19**), water area equals to the entire triangular cross-sectional area and found by **Eq. 5.18**. When oil occupies the bulk area of a drained pore element, water resides in the corners satisfying the condition of $\theta_R < 90^\circ - \beta_i$ (**Eq. 5.14**). If corner arc menisci at oil-water interface slide towards the corner apex during oil drainage (Configuration B or H in **Fig. 5.19**), the area occupied by corner water film in individual corners $A_{wc,i}$ depends on the position of arc menisci at prevailing capillary pressure of network and is calculated from **Eq. 5.21** where θ_r replaces θ_R and $r (= \gamma/P_c)$ replaces r_d in secondary drainage case (Configuration H in **Fig. 5.19**). While oil occupies the bulk area, if corner arc menisci is pinned at the intersection of oil-wet and water-wet surfaces (Configuration C or D in **Fig. 5.19**), the area occupied by water in an individual corner i is calculated from

$$A_{wc,i} = \left(\frac{L_{pd,i} \sin \beta_i}{\cos(\theta_{h,i} + \beta_i)} \right)^2 \left(\frac{\cos \theta_{h,i} \cos(\theta_{h,i} + \beta_i)}{\sin \beta_i} - \frac{\pi}{2} \left(1 - \frac{\theta_{h,i} + \beta_i}{90} \right) \right) \quad (5.63)$$

where the meniscus-apex distance $L_{pd,i}$ (**Eq. 5.30**) depends on the maximum capillary pressure of primary drainage and θ_i may be $\theta_R, \theta_A, \theta_r$, or $\theta_{h,i}$ depending on the circumstances mentioned previously for drainage and imbibition processes.

In an oil-invaded pore, total water corner area A_{wc} is the summation of water area in each corner as

$$A_{wc} = \sum_{i=1}^3 A_{wc_i} \quad (5.64)$$

and bulk oil area A_o is the difference between total pore area and total water area in the corners as given in **Eq. 5.20**.

If oil layers are present in water-occupied pores (Configuration F or G in **Fig. 5.19**), oil layer area in a single corner $A_{ol,i}$ is determined from the difference between areas of two arc menisci surrounded that oil layer. As indicated in **Fig. 5.27a**, the outermost arc meniscus between corner water film and oil layer is stuck at position $L_{pd,i}$, while its hinging angle increases from θ_R towards θ_A with further forced imbibition. The inner meniscus between oil layer and bulk water, on the other hand, moves through the corner with θ_A during forced imbibition. In **Fig. 5.27a**, the outermost ($\theta_{h,i}$) and innermost (θ_A) arc menisci are numbered as 1 and 2, respectively. The area of corner water film surrounded by outer meniscus $A_{wc,i}$ is found again from **Eq. 5.63** where $\theta_{h,i}$ replaces θ_i . The corner area covered by the inner arc menisci $A_{c,i}$ includes oil layer and corner water film and is determined from **Eq. 5.21** where θ_R is replaced by $180 - \theta_A$ and r_d by r which is the radius of curvature of inner meniscus, $r = \gamma/P_c$. Finally, oil layer area is

$$A_{ol,i} = A_{c,i} - A_{wc,i} \quad (5.65)$$

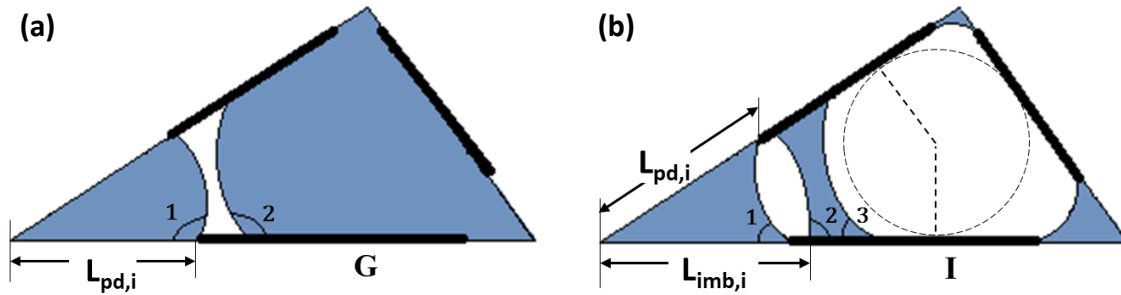


Figure 5.27 – Visualization of corner interfaces and contact angles in a) Configuration G and b) Configuration I for the sharpest corner i of triangular pore cross-section (Configuration G – 1: $\theta_{h,i}$, 2: θ_A , Configuration I – 1: $\theta_{h1,i}$, 2: $\theta_{h2,i}$, 3: θ_r).

For pore elements having water and oil layers together at least in the sharpest corner (**Fig. 5.27b**) after oil re-invasion, there are three corner oil-water interfaces. Here, the outermost ($\theta_{h1,i}$) and middle ($\theta_{h2,i}$) arc menisci numbered as 1 and 2 in **Fig. 5.27b** are pinned and while $\theta_{h1,i}$ is determined from **Eq. 5.51**, $\theta_{h2,i}$ is given by

$$\theta_{h2,i} = \cos^{-1} \left(\frac{P_c}{P_c^{\min}} \cos(\theta_A - \beta_i) \right) + \beta_i \quad (5.66)$$

Differently from the interfaces 1 and 2 in **Fig. 5.27b**, the innermost interface separating bulk oil from water layer moves freely towards the corner during oil re-invasion and its area ($A_{cor,i}$) covering water in corner, oil and water layers altogether is calculated from **Eq. 5.21** where θ_R is switched to θ_r and r_d to r ($= \gamma/P_c$). The corner water area $A_{wc,i}$ bounded by the outermost arc meniscus in **Fig. 5.27b** is calculated from **Eq. 5.63** where $\theta_{h,i}$ is replaced by $\theta_{h1,i}$. The area including corner water and oil layer $A_{c,i}$ is determined again by **Eq. 5.63** where $L_{pd,i}$ is changed to $L_{imb,i}$ and $\theta_{h,i}$ to $180 - \theta_{h2,i}$. Then, oil layer area is calculated from their difference (**Eq. 5.65**). Lastly, water layer area is the difference between total corner area and the area bordered by middle arc menisci and given as

$$A_{wl,i} = A_{cor,i} - A_{c,i} \quad (5.67)$$

In primary drainage, because water maintains continuity across the network either as corner films in the angular corners of drained pores or as bulk phase in the capillary-bound micropores, water trapping is not considered in the model. During water invasion, trapped oil volume is determined using the capillary pressure at which oil is first trapped. During spontaneous imbibition, piston-type displacement allows oil clusters to move in a connected manner, and trapped oil is mainly resulted as a consequence of snap-off event. In secondary oil flooding, the previously formed trapped oil is mostly reconnected. The irreducible water after oil re-invasion is due to undrained water-filled pores as well as oil-invaded pores with continuous water films in the angular

corners and also with water layers surrounded by oil layers and bulk oil. The volume of molecular surface films on oil-wet patches of pore walls occupies a little fraction of total pore volume.

For saturation calculations, at progressive steps, the volume of oil phase in each pore body and throat including oil either as bulk phase, surface film, trapped phase or as a layer, are added together and divided by the total pore volume to obtain overall oil saturation of the network expressed as

$$S_o = \frac{\sum_{nodes} (A_o L) + \sum_{links} (A_o L)}{V_T} \quad (5.68)$$

where V_T is the total pore volume of the network (m^3). Then, from definition, water saturation is

$$S_w = 1 - S_o \quad (5.69)$$

5.2.4.2 Fluid conductance, absolute and relative permeabilities

In the simulations, flow is allowed to occur only through the side of the network normal to inlet and outlet faces, the other sides are assumed to be impervious to flow. For a given applied pressure gradient, the absolute permeability of the network is calculated using Darcy's law as

$$k_a = \frac{q_T}{A} \mu \frac{L}{\Delta P} \quad (5.70)$$

where q_T is the total single phase flow rate of the model ($m^3.s^{-1}$), ΔP pressure difference applied between the inlet and outlet ends in either fluid across network (Pa), μ the fluid viscosity (Pa.s), L the length of model along flow direction (m), and A the cross-sectional area of model (m^2) normal to flow direction (x -direction in **Fig. 5.28**).

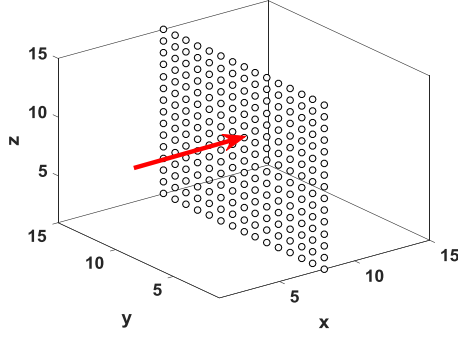


Figure 5.28 Any sectional plane ($x = 8$) within the pore network perpendicular to flow direction ($n = 15$).

For quasi-static and incompressible flow, volume conservation is applied to every pore body as (Blunt, 1997a)

$$\sum_J q_{p,IJ} = 0 \quad J = 1, 2, \dots, Z \quad (5.71)$$

where p refers to water or oil phase, I refers to a particular pore body in the model and J one of its neighboring pore bodies connected via their mutual throat IJ as indicated in **Fig. 5.15**.

For laminar flow of incompressible immiscible phases, the volumetric flow rate of phase p between neighboring pore bodies I and J is prescribed by Hagen-Poiseuille's law as

$$q_{p,IJ} = g_{p,IJ} \nabla P_{p,IJ} = g_{p,IJ} \frac{(P_{p,I} - P_{p,J})}{L_{IJ}} \quad (5.72)$$

where $g_{p,IJ}$ is the hydraulic conductance ($\text{m}^4 \cdot \text{Pa}^{-1} \cdot \text{s}^{-1}$), $P_{p,I}$ and $P_{p,J}$ pore body pressures and L_{IJ} the distance between the centers of adjoining pore bodies.

The hydraulic conductance of a pore element depends on its geometric and fluid properties. Using Hagen-Poiseuille's law for laminar flow in a circular tube, the conductance g for completely water-filled pores (Configuration A in **Fig. 5.19**) is computed analytically as

$$g = \frac{\pi R^4}{8\mu} \quad (5.73)$$

where R is the inscribed radius of pore element. If more than one phase occupies pore cross-section, **Eq. 5.73** is modified for the bulk phase flowing through the center of pore element as (Mogensen and Stenby, 1998)

$$g_b = \frac{\pi R_{eff}^4}{8\mu} \quad (5.74)$$

where the effective radius of the bulk phase is $R_{eff} = \sqrt{A_b/\pi}$. The conductance of corner water film is given by

$$g_c = \frac{A_{wc} r^2}{B\mu} \quad (5.75)$$

where A_{wc} is the corner water area, r the radius of curvature of arc meniscus, and B the dimensionless resistance factor accounting for lower conductance of corner water due to insulation effect of pore walls. The dimensionless resistance factor B used in flow simulations of various flooding processes is taken from standard values in the literature (Ransohoff and Radke, 1988).

If an oil layer (forced imbibition) or oil and water layers together (secondary drainage) exist in a corner of pore elements, due to complex geometries of intermediate layers, layer conductance is approximated by corner flow conductance (**Eq. 5.75**) where A_{wc} is replaced either by A_{ol} or A_{wl} for oil or water layer conductance, respectively. Although having a considerable ratio in pore volume, the trapped oil is not included in conductance calculations. It hangs as isolated blobs in porous medium and has zero conductance. On the other hand, although molecular surface oil films on oil-wet patches of mixed-wet pores have infinitesimally small volume, they still provide substantial oil conductance.

The overall conductance of a phase p between two neighboring pore bodies I and J , $g_{p,IJ}$ is assumed to be harmonic mean of the conductances of a unit flow channel consisting of two pore bodies and their mutual pore throat (Patzek, 2001) as

$$\frac{L_{IJ}}{g_{p,IJ}} = \frac{L_t}{g_{p,t}} + \frac{1}{2} \left(\frac{L_I}{g_{p,I}} + \frac{L_J}{g_{p,J}} \right) \quad (5.76)$$

where subscript t refers to pore throat. **Equations 5.71–5.76** yield a system of linear algebraic equations for unknown pore body (node) pressures. For matrix solution of unknown node pressures ($\vec{AP} = b$), the pressure boundaries of both phases at inlet and

outlet faces of network model are specified as $P_{in}=1$ psia and $P_{out}=0$ psia, respectively (Blunt, 1997a; Al-Futaisi and Patzek, 2003; Jia, 2005). To dampen boundary effects in relative permeability predictions, the inlet and outlet faces of the network are excluded in the simulations ($i=2:(n-1)$) (Jia et al., 2007). In matrix solution of nodal pressures of water and oil phases, since water has continuity all along the network, its matrix size is equal to total number of nodes except the ones located on the inlet and outlet faces ($n^3-2n^2=2925$ for $n=15$). On the other hand, matrix size of oil-invaded nodes increases stepwise during primary drainage. This is indicated in **Fig. 5.29** that while the node number is equal for all steps in water phase (= 2925), the number of oil-filled nodes in pressure matrix increases progressively and reaches nearly the total node number in the network at the end of primary drainage.

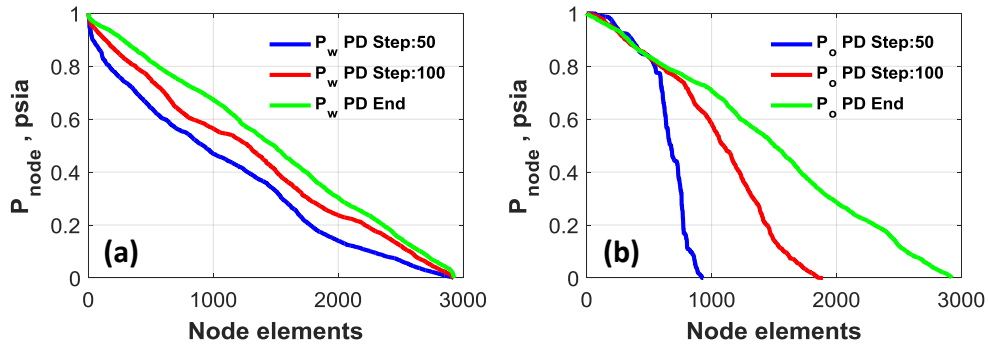


Figure 5.29 – Number of nodes in pressure matrix of a) water and b) oil phases under unit pressure difference during primary drainage ($n=15$).

After pore body pressures are determined, total flow rate through the network (q_T) is computed from **Eq. 5.72** using any sectional plane within network perpendicular to flow direction as indicated in **Fig. 5.28**. Knowing the total flow rate of network model allows us to determine its absolute permeability from **Eq. 5.70** at the beginning of primary oil flooding when the system is fully saturated with a single phase, water. Then, in the progressive displacement steps, relative permeability for each phase p having at least one cluster continuous from inlet to outlet is calculated from the ratio of flow rate of the phase (water or oil) to total flow rate as

$$k_{rp} = q_p / q_T \quad (5.77)$$

5.2.5 Summary of displacement processes

In the carbonate networks, two-phase flow simulations are intended to be performed in the sequence of primary drainage with wettability alteration followed by secondary imbibition and oil re-invasion. In this chapter, for each part of the flooding cycle, the possible fluid configurations in a single pore are considered and approximate expressions are given for their capillary entry pressure. The oil and water layer formation and stability equations are utilized to check whether intermediate layers are present in mixed-wet systems and affect the flow performances. The algorithms followed during drainage-imbibition-secondary drainage cycle are summarized in **Appendix B**.

CHAPTER 6

NETWORK SIMULATION RESULTS

The representative pore network models of Middle East carbonates are constructed in the previous chapter. Then, three consecutive fluid displacements, namely primary drainage with wettability alteration, secondary imbibition including spontaneous imbibition followed by forced water flooding, and lastly secondary drainage are simulated in the simplified pore networks. For the carbonate samples under investigation, the pore structure properties of the network are kept constant throughout the simulations of a complete drainage-imbibition-secondary drainage cycle. The respective macroscopic transport properties, namely capillary pressure and relative permeability curves and their hysteresis loops are obtained for two-phase flow under nonuniform wettability conditions. In this section, predictions of our network model are presented together with an extensive analysis of the behavioral differences of carbonate samples. The key roles of wettability and pore structure characteristics on flow properties are discussed.

6.1 Primary drainage simulation results

As mentioned in **Chapter 5**, the network is initially full of water, thus the system is assumed to be water-wet and a uniform receding contact angle ($< 90^\circ$) is assigned to all pore bodies and throats. The oil migration into the water-filled medium may be called as pristine drainage (Kovscek et al., 1993). During primary drainage, oil tends to invade into the widest pores with the lowest capillary entry pressure among all accessible nodes and links. The current capillary pressure of the system increases progressively with the oil invasion into smaller pores. Here, oil remains connected to inlet face all along the

drainage process while water is always continuous from inlet to outlet to be displaced without trapping. In case the maximum capillary pressure $P_{c,pd}^{\max}$ is not limited, oil fills the entire network and water saturation reaches almost zero when the water resides only in angular corners of drained pores (Kovscek et al., 1993). However, this is not a realistic scenario for mimicking natural reservoir conditions. Carbonate reservoirs, in particular, have substantial amount of microporosity in their pore system which usually holds capillary-bound water entire its lifetime and leads to nonzero residual water saturation (Cantrell and Hagerty, 1999, 2003; Hebert et al., 2015).

The water saturation at the end of primary drainage is called as initial (connate) water saturation S_{wi} . In many pore-scale modeling studies, a predefined maximum capillary pressure or initial water saturation is set artificially to finalize the drainage process (e.g., $S_{wi}= 8.3\%$ in Blunt, 1997b; $S_{wi}= 2\%$ in Hui et al., 2000; $S_{wi}= 6\%$ for $P_c^{\max} = 188$ kPa in Al-Futaisi and Patzek, 2004; 0.5% clay volume proportion in Al-Kharusi and Blunt, 2008). In our model, mercury intrusion measurements (MIP) are utilized to decide on threshold pore diameter, i.e. on the fraction of the accessible pore space during primary drainage (**Figs. 4.16** and **4.19a**). In **Fig. 6.1**, MIP throat size distribution together with its incremental volume data is plotted for C013. The first region of bimodal throat size distribution with large pores represents for macropores and the second region for micropores. Referring to **Section 4.3.4**, based on the incremental mercury volume data, the first region of macropores are subdivided into multiple intervals and classified as PC6 to PC2 in descending size order and the second region with micropores is classified as PC1 involving the micro-scale pores of the network ($R \leq 0.711 \mu\text{m}$). Note that, despite the relatively low abundance of macroporosity PCs with larger throat size ranges (**Table 5.1**), they topologically connect more than 70% of the total C013 pore volume accessible to nonwetting phase seen in **Fig. 6.1** (Xu and Torres-Verdin, 2013). Due to high pressure application (33,000 psia \approx 227,527 kPa), most of the micropores are intruded during MIP experiment. However, in oil-water systems, oil may not enter into micropores due to their extremely large threshold pressures. Briefly stated, oil invasion in our model is allowed to continue until only PC1 throats representing

microporosity of carbonate samples are left undrained and no further displacement occurs after $S_w = S_{wi}$. Similar to our conditioning of threshold radius to determine what fraction of the pore space is accessible, Valvatne (2004) chose a throat size limit of about 0.1 μm for oil drainage into a mixed-wet intergranular carbonate network and 2% water saturation is left. In the study of Kallel et al. (2015), another example, for a wide range of size distribution (from 1 to 152 μm), the micropore threshold is determined as 5 μm representing 18% of the total pore volume of a heterogeneous microporous carbonate network; however, they allowed oil to drain micropores as well resulting in near-zero connate water saturation.

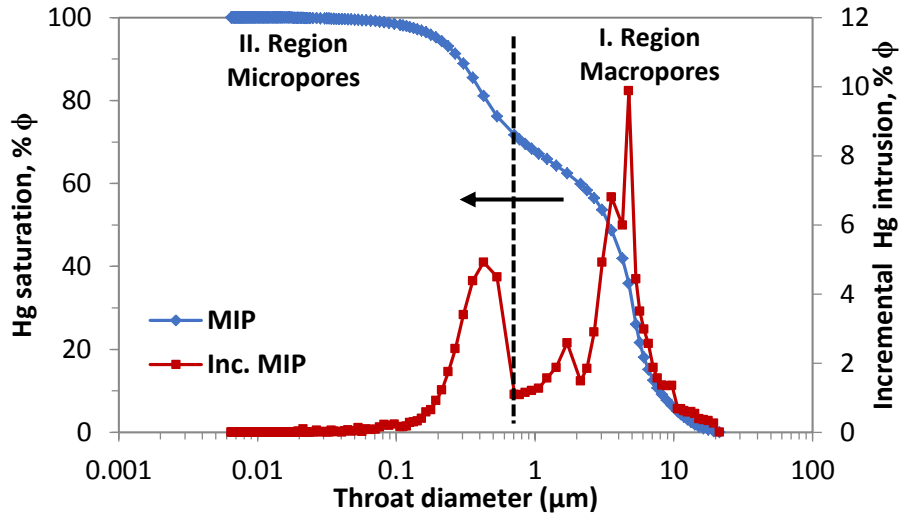


Figure 6.1 – Cumulative and incremental volume curves of high-pressure MIP throat size distribution for C013.

After defining the essential criteria of initial oil migration in the model, primary drainage experiments of carbonates are simulated at various receding contact angles θ_R . Capillary pressure and relative permeability measurements are highly reproducible for each carbonate network. In order to check consistency between the results, some of the drainage simulations are repeated and because θ_R is kept constant, only small variations are encountered in the network due to random selection of the intermediate corner half-

angle within the allowed range of $\beta_{2,\min} \leq \beta_2 \leq \beta_{2,\max}$ (Valvatne, 2004; **Eqs. 5.2–5.3**).

The basic fluid properties used in the simulations are listed in **Table 6.1**.

Table 6.1 –Fluid properties used in flow simulations.

Property	Value
Oil-water interfacial tension, γ_{ow} (10^{-3} N/m)	34
Fluid viscosity, μ (10^{-3} Pa.s)	1
Fluid density, ρ (kg/m^3)	1000

Figure 6.2 represents the pore occupancy histograms corresponding to piston-like displacements during primary drainage in C013 network ($n = 15$). It illustrates the number of oil- and still water-occupied nodes and links stepwise for strongly water-wet case, i.e. $\theta_R = 0^\circ$ throughout the network. Each step data is recorded after the next consecutive 50 pores are invaded during flooding process in order to reduce time-consuming matrix inversion of nodal pressures (Al-Futaisi and Patzek, 2003; Jia et al., 2005). According to **Fig. 6.2**, node elements with lower entry pressure are invaded mostly in the first half of the drainage process and while oil drains almost all nodes (**Fig. 6.2a**) at the end, it proceeds to invade into links until only micropores (PC1 links) are left behind (**Fig. 6.2b**). Primary drainage ends when only micropores and the isolated nodes surrounded completely by micropores remain undrained. After primary drainage, the water is present in the network either as bulk phase in micropores and rarely in isolated nodes or as wetting films in the corners of drained pores.

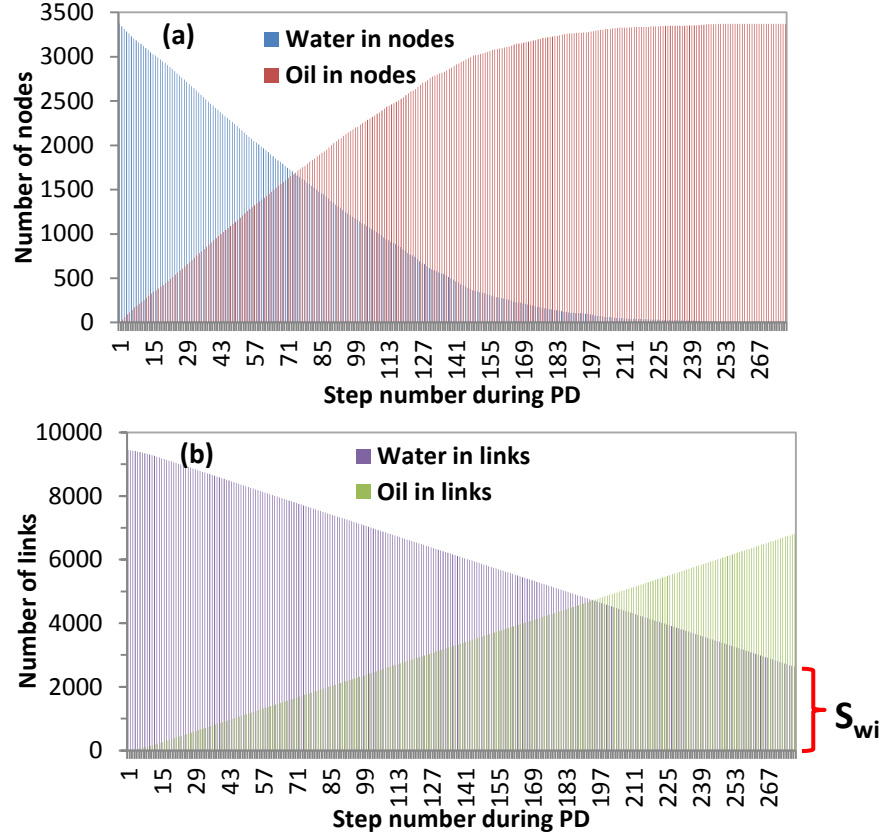


Figure 6.2 – Pore occupancy histograms for a) nodes and b) links in C013 during primary drainage (PD).

The predicted primary drainage P_c and k_r curves are shown in **Figs. 6.3** and **6.4** respectively for $\theta_R = 0^\circ$. For the sake of clarity, P_c and k_r curves are plotted in both linear (left) and semi-logarithmic scales (right). Since the first region of dual throat size distribution curve is realized in our simulations, the resulting P_c curves of carbonate samples exhibit unimodal character. **Figure 6.3** reveals that C013 has the greatest amount of initial water saturation S_{wi} , followed by C016, C021, and lastly C019. The minimum capillary pressure $P_{c,pd}^{min}$ where oil initially enters into the system follows the same order with S_{wi} (from C013 to C019 in descending order) whereas the maximum capillary pressures $P_{c,pd}^{max}$ at the end of oil migration are almost the same for all samples. The outputs of primary drainage for each sample are summarized in **Table 6.2**.

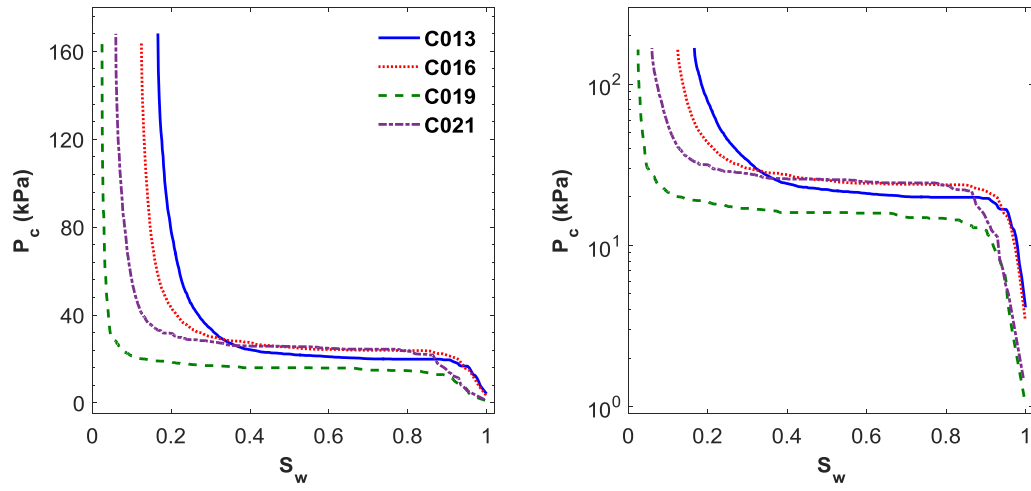


Figure 6.3 – Predicted primary drainage P_c curves of carbonate networks for $\theta_R = 0^\circ$.

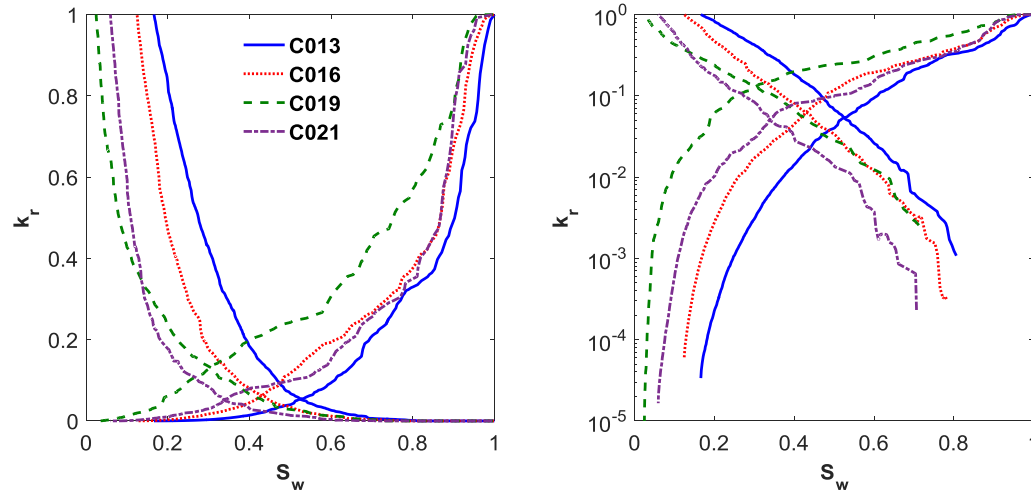


Figure 6.4 – Predicted primary drainage k_r curves of carbonate networks for $\theta_R = 0^\circ$.

Table 6.2 – Primary drainage simulation results for $\theta_R = 0^\circ$.

Sample	$P_{c, pd}^{\min}$, kPa	P_c^* , kPa	S_w^*	$P_{c, pd}^{\max}$, kPa	S_{wi}	q_t , E-14 m ³ /s	k_a , mD	k_a^+ , mD
C013	4.1	19.9	0.881	168.2	0.166	21.3	473	180
C016	3.5	23.8	0.841	164.3	0.124	6.05	185	122
C019	1.1	14.4	0.833	164.4	0.025	7.65	115	115
C021	1.5	24.4	0.771	168.0	0.059	10.5	212	168

(*oil breakthrough, ⁺ laboratory-measured permeability corrected from air to brine)

In **Fig. 6.3**, after oil is introduced into the medium, P_c of the network increases modestly up to around $S_w = 0.8$. Earlier on primary drainage, most of the oil-invaded pores form various dendritic branches and do not have accessibility yet, i.e. not connected to outside (Mohanty and Salter, 1982). As a result, k_{ro} is zero until S_w exceeds 0.8 in **Fig. 6.4**. Also, the rapid decrease of k_{rw} at relatively large S_w (**Fig. 6.4**) can be explained by this fact. When the slope of P_c curve changes notably, an oil continuum extending from inlet to the outlet face of the network is achieved and oil breakthrough happens. The breakthrough capillary pressures P_c^* of the carbonate networks are in the range of 14.4 to 24.4 kPa and given in **Table 6.2** with their corresponding water saturations S_w^* . Immediately past breakthrough, there is a large flat transition zone for all samples especially for C019 where most of the well-connected pore bodies are invaded without much change in P_c but a significant decrease in S_w . Following that flat transition zone, P_c increases again to invade most of the relatively small pore throats. In C019, a sudden increase in P_c with slight contribution to oil saturation is evident after $P_c > 30$ kPa. This is due to oil entrance into the smallest accessible pores whose volume fraction in the network is very little. On P_c curves, the pass from the flat transition zone to the last region of the drainage curve is controlled by the corner shape of the drained pores (Diaz et al., 1987). The pass in P_c curves is the sharpest for C019 followed by C021, than C016 in contrast to the curved smooth transition in C013. This is because greater correlation (i.e. overlap) between pore body and throat size distributions (**Figs. 5.13** and **5.14**) leads to smoother transition from large pores region to extremely small ones in drainage curves (Mohanty and Salter, 1982; Diaz et al., 1987).

The trends in P_c and k_r behaviors depend on the wettability state and pore geometry of the particular porous medium under study. As θ_R is kept constant, for the same wettability conditions, the differences in P_c and k_r curves of carbonates are

basically attributed to their pore size frequency distributions (**Fig. 5.14**). During the network construction, firstly pore throats are determined and then pore bodies are established using average aspect ratios for each PC per sample (**Eq. 5.7**) so as to correlate pore bodies to their connected throats. Referring to pore-throat classification method in **Chapter 4**, throat size ranges per PC are the same for all carbonates (**Fig. 4.21**) and so the difference in P_c and k_r behaviors of carbonates is mainly due to their aspect ratios. The greater aspect ratio of C019 (almost twice the others, **Table 5.3**) skews its pore body size distribution towards the higher sizes as indicated in **Fig. 5.14c** and thus its capillary pressure at the initial oil invasion ($P_{c,pd}^{\min} = 1.1 \text{ kPa}$ in **Table 6.2**) and also all through the drainage process is lower than that of the other samples (**Fig. 6.3**). In the same manner, lower aspect ratio of C013 results in much more small pore bodies and reduces the size contrast between pore bodies and their connected throats (**Fig. 5.14a**). Having relatively small-sized pore bodies, the capillary pressure of C013 at the initial oil invasion is the largest among all ($P_{c,pd}^{\min} = 4.1 \text{ kPa}$ in **Table 6.2**). Due to closer size range (i.e. larger overlap) between pore bodies and throats in C013 pore network, oil intrudes into relatively small pores earlier which provides connection between oil-drained branches effectively and so oil breakthrough occurs faster ($P_c^* = 19.9 \text{ kPa}$ at $S_w = 0.881$ in **Table 6.2**). For this reason, its P_c curve is below P_c curves of C016 and C021 all along the transition zone in **Fig. 6.3**. During drainage, the final oil saturation is the least for C013, and so, its transition zone is the shortest (**Fig. 6.3**).

In **Fig. 6.4**, a gradual decrease is remarked in k_{rw} of carbonate samples whereas k_{ro} increases smoothly from zero up to one (at S_{wi}). The difference in k_r behavior may be related to sites of oil and water phases in the network; while oil occupies the center of pores, water is present either as bulk phase or corner film of drained pores and hence, due to its sensitivity to pore irregularities, k_{rw} may probe the structural properties of the network (Xiong et al., 2016). Due to size correlation between pore bodies and their connected throats, through the pass from larger PCs to smaller during drainage, discrete rather than smooth k_{rw} curves are noticed for around $S_w > 0.6$. The initial

record of k_{rw} is equal to unity because the system is full of water. At the end of oil drainage, water occupies only micropores ($\leq 0.711 \mu\text{m}$) and the corners of drained pores. The remaining water residing in micropores is nearly immobile and does not contribute to the flow. Water filaments remained in the corners of drained pores shrink gradually with the pressure increase up to $P_{c,pd}^{\max}$. Water always has continuum throughout the network even at S_{wi} , so k_{rw} never becomes zero at the end of drainage. Oil firstly invades into larger pores and thus its saturation increases quickly in the earlier stages of the process, i.e. $S_w > 0.8$ in **Fig. 6.4a**. Oil-invaded pores are dispersed widely until oil clusters form a broad spread elongating throughout of network, i.e. oil breakthrough happens and k_{ro} stays nearly zero. When the effective saturation is achieved ($S_w < 0.8$ in **Fig. 6.4**), displacing phase (oil) interconnects the majority of pore network, dominates flow (Diaz et al., 1987) and k_{ro} increases rapidly. The cross-point of k_{rw} and k_{ro} curves moves through the left side with the increase in pore-throat aspect ratio.

PC1 links, representing micropores in our model, are the smallest pores in carbonate networks whose radii are less than $0.711 \mu\text{m}$ and they always remain water-filled. They make the major contribution to initial water saturation S_{wi} at the end of drainage. Although PC1 covers quite large portion in all carbonate networks (0.433 to 0.697 in **Table 5.1**), due to wider pore bodies in C019, the ratio of volume occupied by PC1 links in its network is comparatively too little. The lowest residual water saturation is therefore obtained in C019 network ($S_{wi} = 0.023$ in **Table 6.2**). Again, because the size of pore bodies is closer to their connected throats in C013, undrained PC1 links have a considerable volume ratio in total pore volume and a remarkable water saturation remains at the end of drainage ($S_{wi} = 0.166$ in **Table 6.2**). The minimum throat size for oil entrance is the same for all carbonates ($0.711 \mu\text{m}$); hence, their maximum capillary pressures at the end of drainage process $P_{c,pd}^{\max}$ are close to each other and in the range of 164 to 168 kPa for $\theta_R = 0^\circ$ in **Table 6.2**.

At the start of primary drainage, the system is full of water and therefore the first record of water effective permeability gives the absolute (single) permeability k_a of the network. The model-predicted absolute permeabilities are given in **Table 6.2**. The core permeabilities of carbonates measured with air at ambient conditions (**Table 4.1**) are corrected to permeability for brine at reservoir conditions using Swanson's empirical equation (**Eq. 4.6**) and listed in **Table 6.2** for comparison with model-predicted values. The model tends to overestimate the experimentally determined permeabilities but still within the same order of magnitude. Carbonate samples are generally heterogeneous and may have anisotropy in their permeability (Mostaghimi et al., 2013), so the difference between measured and predicted values is not surprising. When compared to the measured data, only C019 network displays, by coincidence, almost identical permeability to its core permeability. The difference is the greatest for C013. The discrepancy in model-predicted permeabilities may partially be attributed to the difference in their microporosity (PC1) proportions (first column in **Table 5.1**). The samples with larger fraction of PC1 have lower permeability. Accurate representation of micropores provides fair prediction of single and multiphase properties (Øren et al., 2002; Harland et al., 2015). From Darcy's law, the permeability of a porous rock is proportional to the flow rate normal to flow plane (**Eq. 5.71**). Total flow rate of water in the beginning of drainage is given in **Table 6.2**. There is obviously a close relation between flow rate and permeability of samples. The general correlation between permeability and entry pressure fails here due to the complex multiscale pore system of our carbonates. In addition to microporosity item, an adequate determination of the topology of carbonates rocks (i.e., connectivity) accounts for better permeability predictions through the pore networks (Jivkov et al., 2013).

In our model, all pores are sufficiently water-wet prior to drainage and satisfy the criterion $\theta_R < 90^\circ - \beta_i$ to keep water in their corners after oil invasion. Water saturation in the angular corners of oil-drained pores S_{wc} is calculated during the drainage process. Because corner water is a little portion of drained pores, S_{wc} is expected to be very small. The water corner film saturations in nodes, links and whole system elements are plotted against overall water saturation in **Fig. 6.5** for each carbonate network. From the

plots, it is observed that the corner water saturation accounts for no more than 3% of the total pore volume despite its critical role in water continuity throughout the network. At the same P_c , the distance of oil-water arc menisci to corner apex L_i depending on θ_R and β_i is the same for identical corner half-angles (**Eq. 5.52**). Accordingly, because there are much more links than nodes in pore network, S_{wc} of links is greater than S_{wc} of nodes at each step. In **Fig. 6.5**, for all samples, after a short fluctuation period in the beginning especially in C019 and C021 due to oil entrance into wide pores at the inlet boundary, the system comes to equilibrium. In the course of process, S_{wc} climbs at a steady rate in response to the increment in oil-drained pore amount. Once most of the possible pores are drained, S_{wc} reaches its peak value (e.g., at $S_w = 0.4$ for C013). Then, with the further increment of P_c , the corner menisci in oil-invaded pores move through the apex, S_{wc} decreases sharply and comes to near zero at the end of process.

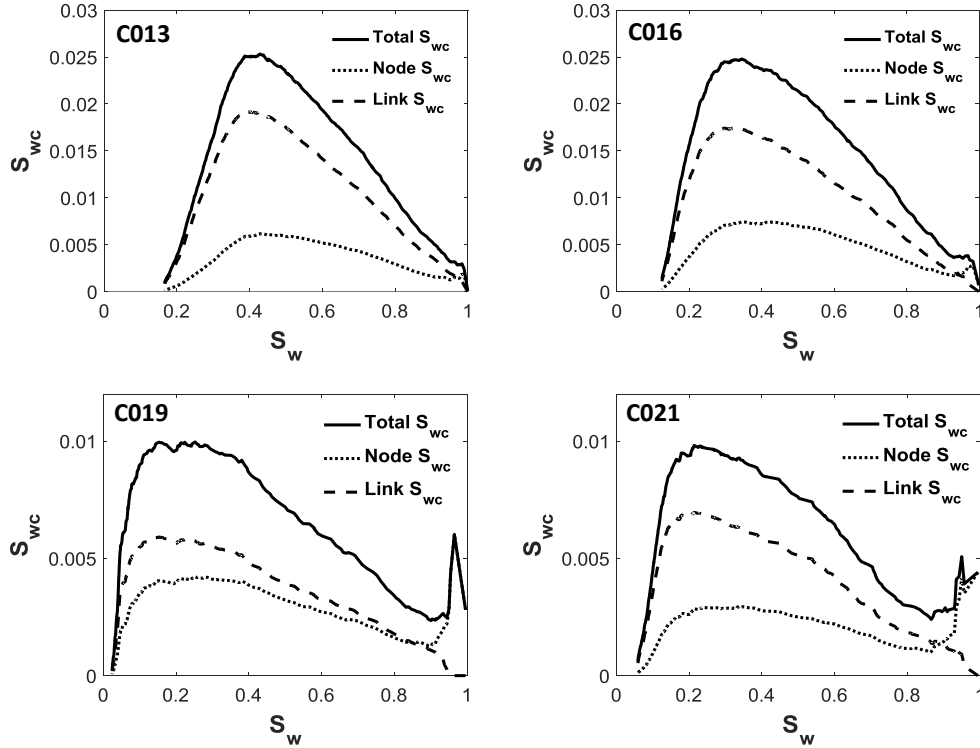


Figure 6.5 – Corner water saturation S_{wc} in carbonate networks during primary drainage at $\theta_R = 0^\circ$.

The initial (connate) water saturation following primary drainage changes with respect to both the pore structure and local wettability conditions (Chang et al., 1997; Høiland et al., 2007). Our carbonate samples having different structural properties are simulated at the same wettability condition ($\theta_R = 0^\circ$) and their behavioral differences are investigated above. Freer et al. (2002) reported experimentally that, as opposed to general acceptance of $\theta_R = 0^\circ$, receding contact angles may reach up to 50° on aged surfaces following oil drainage. Now, P_c and k_r curves of a single sample (i.e. same geometric structure) are calculated under different but uniform wettability conditions ($\theta_R = 0^\circ$ to 50°) and presented in **Figs. 6.6** and **6.7** for C013 and C019, respectively. According to **Figs. 6.6** and **6.7**, the increase in θ_R making the medium less water-wet slightly decreases the capillary entry pressures ($P_c^e \propto \cos \theta$) and $P_{c,pd}^{\max}$ attained at the end of drainage. The initial water saturations do not decrease so much (from 0.166 to 0.161 for C013 and from 0.0245 to 0.0235 for C019) against the change in θ_R . The volume of water-filled micropores which is the major contribution to initial water saturation is the same for each θ_R case, whereas the volume of corner water films in oil-invaded pores decreases with respect to the increment in θ_R which has a minor fraction in total pore volume as indicated in **Fig. 6.8**. Supporting our results, Anderson (1987a) showed the insensitivity of the drainage P_c to the wettability for θ_R less than 50° by experimental measurements with uniformly wetted reservoir cores using mercury measurements and attributed this insensitivity to the pore geometry effects.

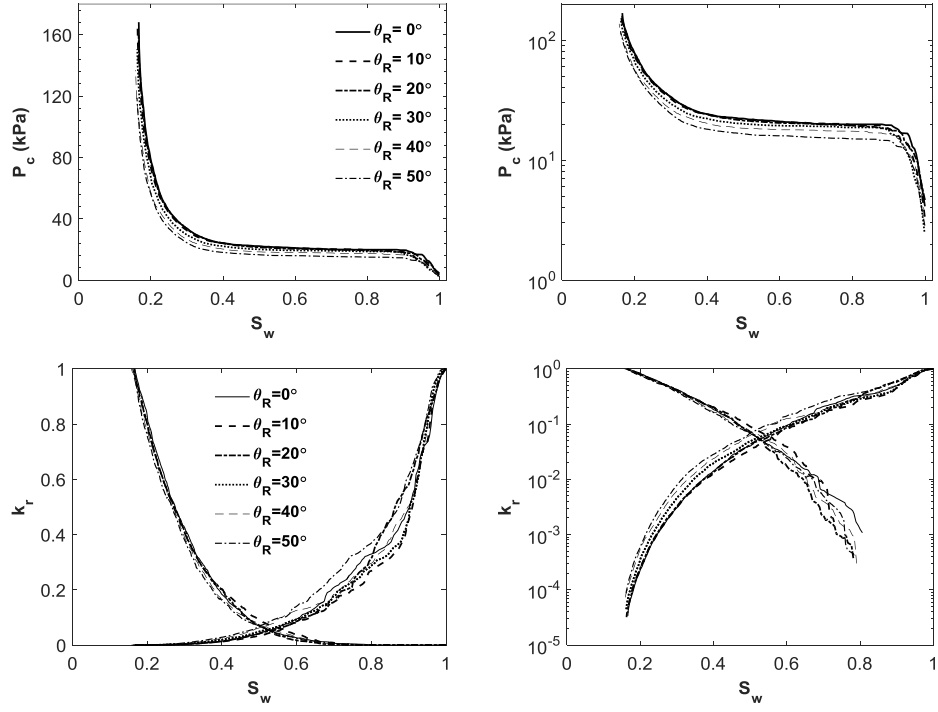


Figure 6.6 – Predicted primary drainage P_c and k_r curves of C013 at different θ_R .

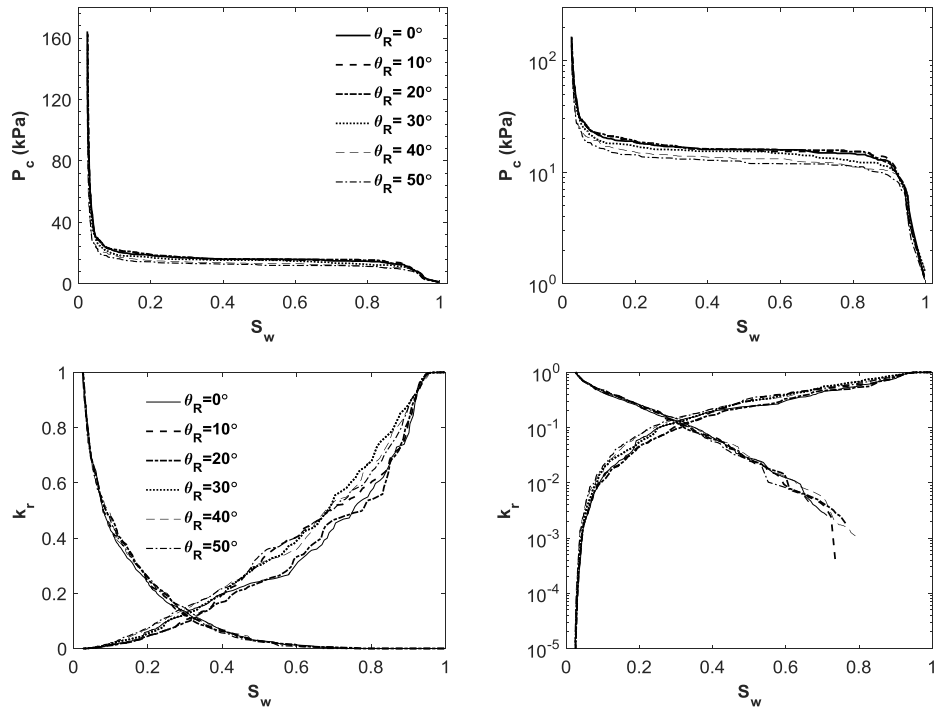


Figure 6.7 – Predicted primary drainage P_c and k_r curves of C019 at different θ_R .

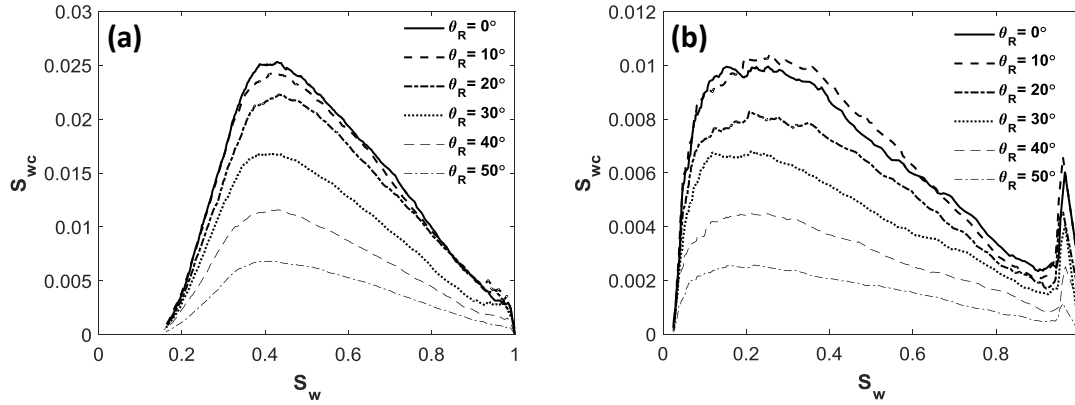


Figure 6.8 – Corner water saturation S_{wc} of a) C013 and b) C019 during primary drainage at different θ_R .

The linear and semi-log plots of relative permeability curves in **Figs. 6.6** and **6.7** indicate that the cross-over point for the relative permeability curves moves slightly through lower S_w as the system becomes less water-wet. The oil relative permeability k_{ro} is mostly insensitive to θ_R . Only in the initial stage of drainage process for $k_{ro} < 0.1$, a small fluctuation of k_{ro} is noticed in semi-log plots (**Figs. 6.6** and **6.7**, right). The water relative permeability k_{rw} , despite some irregularities between the curves, has a general tendency to increase slightly with θ_R for a given S_w . Due to P_c drop with θ_R increment, at the same S_w , more water is freely flow in the central part of porous medium which is the reason for its relatively high conductivity and so high k_{rw} .

6.2 Mixed-wettability development

As described in **Section 5.2.1.1**, after primary drainage, the surface water films lying between bulk oil and pore walls may rupture to molecularly thin films and eventually pore walls in the central part of drained pores becomes oil-wet while the corners remain water-wet (Kovscek et al., 1993; Configuration C in **Fig. 5.19**). Mixed-wettability in which distinct water-wet and oil-wet surfaces coexist in a single pore dominates the medium thereafter (Salathiel, 1973; Anderson, 1986). In our model, all of the drained

pores are assumed to experience wettability alteration and then no further change in wettability occurs in the subsequent flooding processes. Prior to water imbibition, still water-occupied (mostly micropores) and oil-drained pores are identified in the model and assigned as water-wet and mixed-wet, respectively. The number fraction of mixed-wet pores in a porous medium (after Heiba et al., 1983) is denoted by f_{mw} . In an entirely water-wet medium, $f_{mw} = 0$ while in a perfectly oil-wet medium, $f_{mw} = 1$ (Sahimi, 2011). The resulting mixed-wet fractions in nodes (f_{mw_N}) and links (f_{mw_L}) for each carbonate network are given in **Table 6.3**. Oil has invaded into most of the nodes due to their large sizes; thus, very few nodes remain water-filled and the mixed-wet fraction in nodes reaches almost one (**Table 6.3**). The nodes remained water-filled are the ones surrounded only by PC1 links. They have no connection with the invading fluid and are seldom encountered in the model. On the contrary, among the links, micropore population (PC1) has a significant ratio. Accordingly, water-wet links that are never contacted by oil still have a considerable ratio after primary drainage and mixed-wet fraction of links changes from 0.52 to 0.63 (**Table 6.3**).

Table 6.3 – Number fraction of mixed-wet nodes and links and their overall in carbonate networks for $\theta_R = 0^\circ$.

Sample	C013	C016	C019	C021
f_{mw_N}	0.999	0.996	0.993	0.997
f_{mw_L}	0.628	0.591	0.516	0.619
f_{mw}	0.716	0.687	0.630	0.709

In the network, the advancing angle of both water-wet and mixed-wet pores will be larger than their receding angles due to the direction of displacement, known as contact angle hysteresis. At the same time, mixed-wet pores will have larger advancing angles than water-wet pores after wettability alteration.

6.3 Secondary imbibition simulation results

Water is flooded across the network right after primary drainage. Contrary to primary drainage, both immiscible oil and water phases present in the medium at the outset of water imbibition. While oil occupies the center of drained pores, water resides in the sharp corners of oil-drained pores and also as bulk phase of mostly micropores. The water saturation of the network is not zero prior to imbibition, but equal to the initial water saturation S_{wi} . The water-wet micropores occupying most of the initial water saturation eventually reconnect during the water imbibition (Diaz et al., 1987). Water tends to invade the narrowest pores first. Thus, obviously seen in the pore occupancy histograms in **Fig. 6.9**, the remaining oil-filled pores after imbibition are mainly the wide nodes (**Fig. 6.9a**) while most of the small-sized links are imbibed (**Fig. 6.9b**).

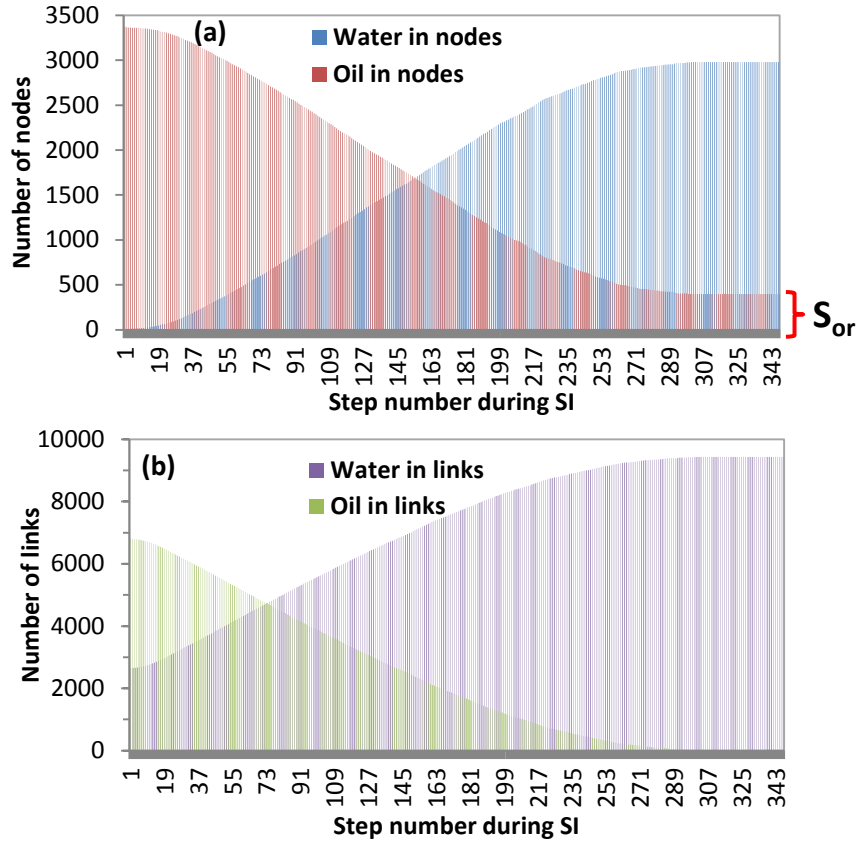


Figure 6.9 – Pore occupancy histograms for a) nodes and b) links of C013 during secondary imbibition (SI).

Three main cases representing different mixed-wettability levels are realized in the secondary imbibition simulations. Three cases stand for a water-wet (*Case 1*), an intermediate-wet (*Case 2*), and an oil-wet (*Case 3*) condition, respectively. Their contact angle ranges for receding angle θ_R and advancing angles in water-wet θ_A^{ww} and mixed-wet θ_A^{mw} pores are given in **Table 6.4**. For arranging the contact angle ranges, the experimental study of Treiber et al. (1972) on wettability characterization of 55 oil reservoirs (25 of them were carbonate and the rest were silicic) is utilized. The strongly wetting fluids have contact angle less than 30° (Jerauld and Salter, 1990). Notice in **Table 6.4** that while $\theta_R = 0^\circ$ in *Case 1* represents an initially strong water-wet rock, the value of $\theta_R = 30^\circ$ in *Case 2* and *3* corresponds to initially weakly water-wet rocks. Many researchers state that wettability alterations that have occurred in actual reservoirs are nonuniform i.e. the contact angles are not identical for all water-wet or mixed-wet pores. Due to the lack of an experimental or numerical methodology universal for pore-scale wettability status identification and related parameters (fraction and spatial distribution of mixed-wet pores, contact angle ranges) (Ryazanov, 2012; Gharbi and Blunt, 2012; Kallel et al., 2015), water-wet and mixed-wet advancing angles are uniformly distributed within their prescribed ranges in our model.

Table 6.4 – Contact angle ranges of different wettability cases used in secondary imbibition runs.

Case	θ_R ($^\circ$)	θ_A^{ww} ($^\circ$)	θ_A^{mw} ($^\circ$)
1	0	10 – 20	20 – 75
2	30	40 – 50	75 – 105
3	30	40 – 60	125 – 170

The secondary imbibition is simulated for each wettability case. **Table 6.5** lists the essential outputs of the secondary imbibition along with the primary and secondary drainage processes namely endpoint saturations and relative permeabilities as well as final capillary pressures for each case. Differently from drainage process, three possible pore-level flow mechanisms, namely piston-type, pore body filling and snap-off are

evaluated during imbibition. The resulting statistics of displacement events under each case are given as histograms in **Fig. 6.10**. It is obvious in **Fig. 6.10** that pore-level events depend significantly on the prevalent wettability conditions.

Table 6.5 – Secondary imbibition simulation results for carbonate samples under different wettability cases.

Case	Sample	S_{wi}	$P_{c, pd}^{\max}$ (kPa)	S_{or}	k_{rw} at S_{or}	P_c^{\min} (kPa)	S_{wirr}	$P_{c, sd}^{\max}$ (kPa)
1	C013	0.166	168	0.098	0.561	1.654	0.174	50
	C016	0.124	164	0.221	0.377	1.905	0.128	80
	C019	0.025	164	0.492	0.048	0.318	0.044	118
	C021	0.059	168	0.460	0.108	0.308	0.063	103
2	C013	0.162	151	0.191	0.478	-151	0.170	151
	C016	0.121	149	0.214	0.475	-149	0.127	149
	C019	0.025	153	0.222	0.477	-153	0.034	153
	C021	0.056	153	0.207	0.471	-153	0.065	153
3	C013	0.162	151	0.002	1	-151	0.219	151
	C016	0.121	149	0.004	1	-149	0.165	149
	C019	0.025	153	0.006	0.955	-153	0.052	153
	C021	0.056	153	0.002	0.986	-153	0.102	153

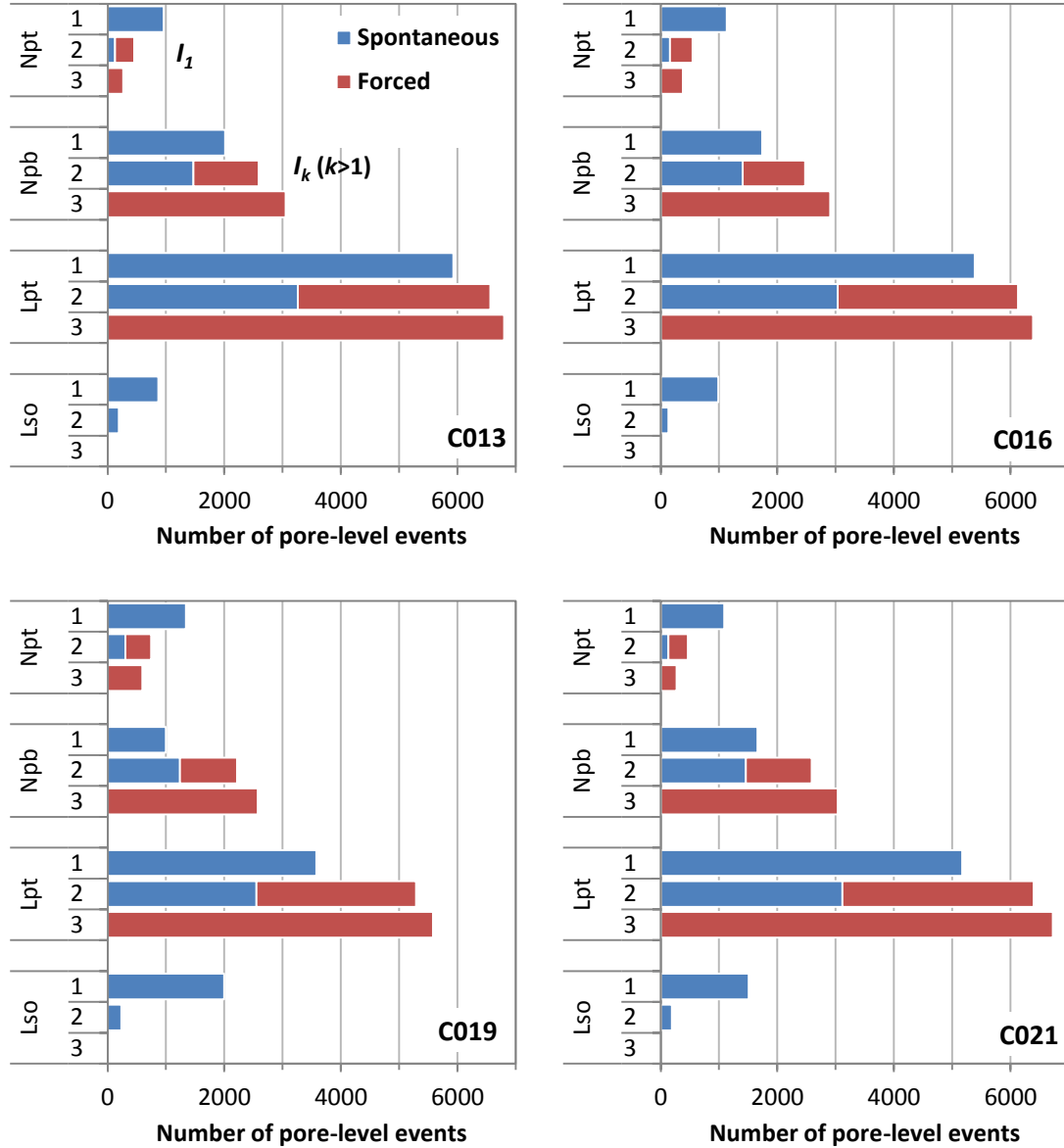


Figure 6.10 – Number of pore-level displacement events during secondary imbibition
(N: node, L: link, pt: piston-type, pb: pore body filling, so: snap-off,
1: Case 1, 2: Case 2, 3: Case 3).

The frontal displacement (piston-type) of water is always preferred to snap-off due to its higher P_c^e (see **Fig. 5.26**). In case the frontal displacement is not possible in a pore yet, i.e. any of its adjacent pores (nodes) or throats (links) is not water-occupied and the geometrical criterion given by **Eq. 5.49** is satisfied, snap-off ensues in the model. In **Fig. 6.11**, the cumulative number of filling mechanisms in links per sample is

plotted stepwise for *Case 1*. It is clear from the figure that snap-off initiates water invasion followed by the piston-type advancement and mostly occurs in the early stages of imbibition. Because adjacent throats of a pore body are imbibed faster than pore body itself due to their relatively small size, a pore body surrounded by six oil-filled throats is occasionally encountered in the early stages of imbibition process. For this reason, snap-off events are too rare in pore bodies (< 22) and not plotted in **Fig. 6.10**.

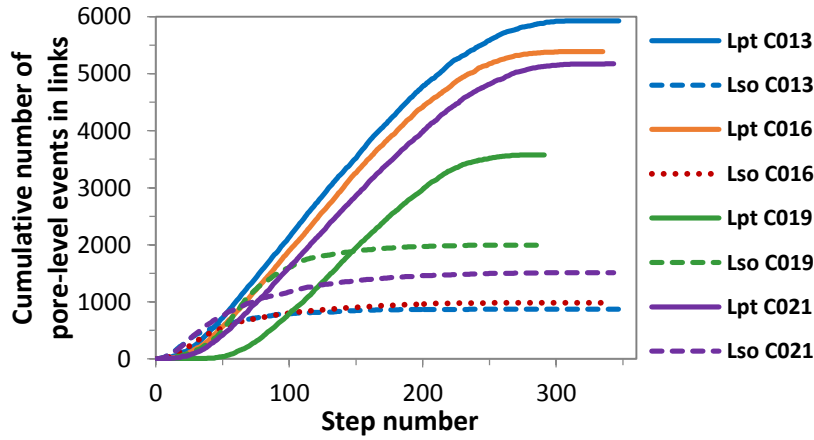


Figure 6.11 – Cumulative number of pore-level displacement events in links stepwise during secondary imbibition (*Case 1*) (L: link, pt: piston-type, so: snap-off).

After snap-off, the pore body or throat is instantly filled with water and the oil phase in the center of recently imbibed pore is cut off and completely surrounded by bulk water. The trapped oil blobs are dispersed in the pore space and due to lack of a continuous path, they cannot flow towards the outside and may constitute significant amount of residual oil saturation S_{or} . In our carbonate networks, extensive snap-off is possible because the high aspect ratio of samples easily meets the geometrical criterion in **Eq. 5.49**. In order to keep snap-off event and accordingly residual oil saturation at a reasonable level, a 0.5 probability is conditioned in the model for snap-off occurrence whenever it is possible during imbibition. For comparison, a probability value of 0.6 was used for snap-off occurrence in Jia's pore network model of diatomites (2005).

The predicted P_c and k_r curves are presented in **Figs. 6.12, 6.13, and 6.14** for *Case 1, 2, and 3*, respectively. Because the geometrical and topological properties of a

single carbonate network are the same for all simulations, the major factor for the variation in their P_c and k_r results is the wettability, i.e. the contact angles being randomly assigned to pore systems. Now, the trace of P_c and k_r curves for each wettability case will be analyzed separately.

Case 1: The system is still weakly water-wet after primary drainage because the advancing angle is smaller than 90° . The pore network spontaneously imbibes water because P_c of the system is always positive. From the histograms in **Fig. 6.10**, it is seen that water invades pore bodies through piston-type and different pore body filling mechanisms. The main difference in pore-level statistics is in the throats (links) of carbonate networks. While C013 links have the highest rank in piston-type displacement (L_{pt} in **Fig. 6.10**), C019 links have the maximum snap-off ratio (L_{so} in **Fig. 6.10**). Based on snap-off criterion in **Eq. 5.49**, under the same wettability conditions (*Case 1*), larger aspect ratio makes snap-off more favorable compared to other filling mechanisms. This explains the largest S_{or} in C019 with its greatest aspect ratio (**Table 5.3**), followed by C021, C016, and lastly C013 in **Fig. 6.12**. The residual oil is a consequence of trapped oil in water-invaded mixed-wet pores and more importantly the remaining oil-filled nodes at the end of imbibition process.

Secondary imbibition starts at $P_{c,pd}^{\max}$. In the early stages, infinitely small S_w increments are observed against large P_c drop in **Fig. 6.12a** as a result of the water imbibition into the smallest available pores and the swelling of pinned corner menisci in previously oil-drained pores. Analogous to the oil breakthrough in primary drainage, first bending of P_c curves in **Fig. 6.12a** below 15 kPa is considered as water breakthrough where a spanning cluster of bulk water is established extending from the inlet to outlet face of the network (Diaz et al., 1987). The water breakthrough in secondary imbibition is found to take place at around 10, 13.5, 9, and 5.5 kPa for C013, C016, C019, and C021, respectively. In order to get a water continuum throughout the network, C019 is exposed to further P_c decrease due to its wider pore bodies among all.

Secondary imbibition is allowed to continue until $-P_{c, pd}^{\max}$ (**Table 6.5**), but at around 1.65, 1.90, 0.50, 0.87 kPa for samples C013, C016, C019, and C021, respectively most of the accessible pores are invaded and no more remarkable change occurs in the saturation of the network.

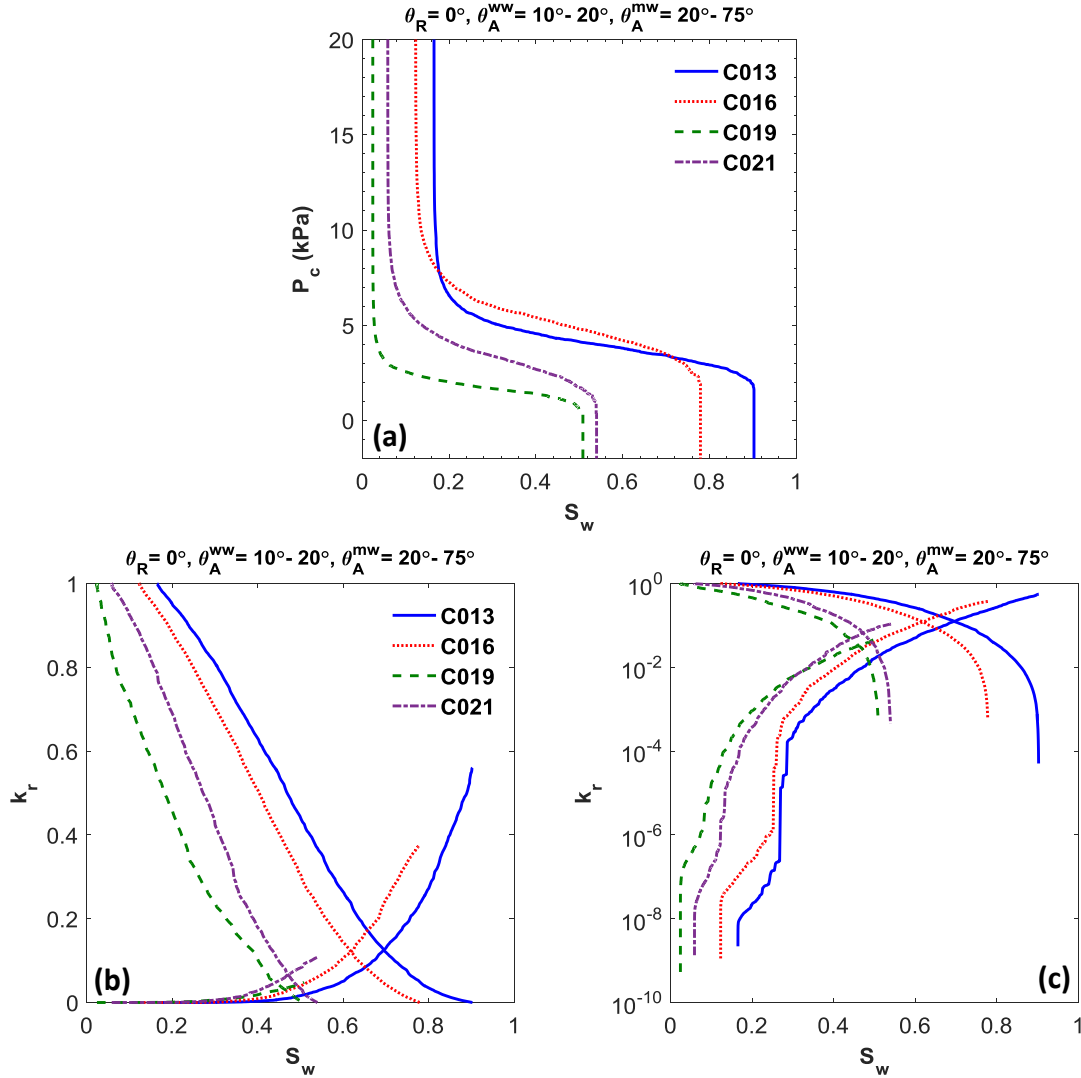


Figure 6.12 – Secondary imbibition P_c and k_r curves of carbonate networks for Case 1.

During spontaneous imbibition, as piston-type displacement allows oil to move in a connected manner with the least residual, trapped oil is mainly resulted from snap-off. Snap-off weakens water continuity (or k_{rw}) due to disconnected oil droplets around.

The trapped oil interrupts the pore channels filled with water more than connected oil clusters (Jerauld and Salter, 1990). From the relative permeability curves in **Fig. 6.12b** and output data in **Table 6.5**, as expected, C019 has the lowest endpoint k_{rw} (at S_{or}) under *Case 1* as a result of its largest residual oil.

In the beginning of imbibition, water resides mostly in micropores and pore corners, so due to little water occupancy in the medium, k_{rw} is quite low ($< 10^{-8}$) as clearly seen in **Fig. 6.12c**, the semi-log plot of k_r curves. **Fig. 6.12c** also reveals that at the same water saturation ($S_w < 0.3$), k_{rw} is relatively high for the networks with wider pore bodies (i.e. larger α) due to better water conductance through wide pores. Similarly, k_{ro} is the lowest for C019 because oil in its large pores is replaced by water resulting in the largest decrease in its oil conductance compared to the others (**Fig. 6.12c**). S_{or} is the minimum saturation where oil no longer flows across the network, and thus k_{ro} is zero for $S_o \leq S_{or}$. C013 with the least residual oil saturation has the greatest k_{rw} at S_{or} (0.561 in **Table 6.5**).

Case 2: The advancing angle of mixed-wet pores is uniformly distributed between 75° and 105° to represent intermediate-wet system including both water-wet and oil-wet surfaces in previously oil-drained pores (**Table 6.4**). Thus, in the intermediate-wet media of carbonates, spontaneous imbibition is followed by forced imbibition.

P_c and k_r curves for *Case 2* in **Fig. 6.13** reveal that the residual oil saturations of carbonates are close to each other and change from 0.19 to 0.22 (**Table 6.5**). Differently from *Case 1*, the advancing angle exceeds 90° in *Case 2* and water imbibition continues in forced manner after P_c crosses $P_c = 0$ line. Based on P_c curves in **Fig. 6.13a**, the switch from spontaneous to forced imbibition occurs at around $S_w = 0.3$ for all samples. Depending upon the dominant pore-level flow mechanisms, the amount of oil produced by spontaneous imbibition is significantly smaller than that produced by forced imbibition.

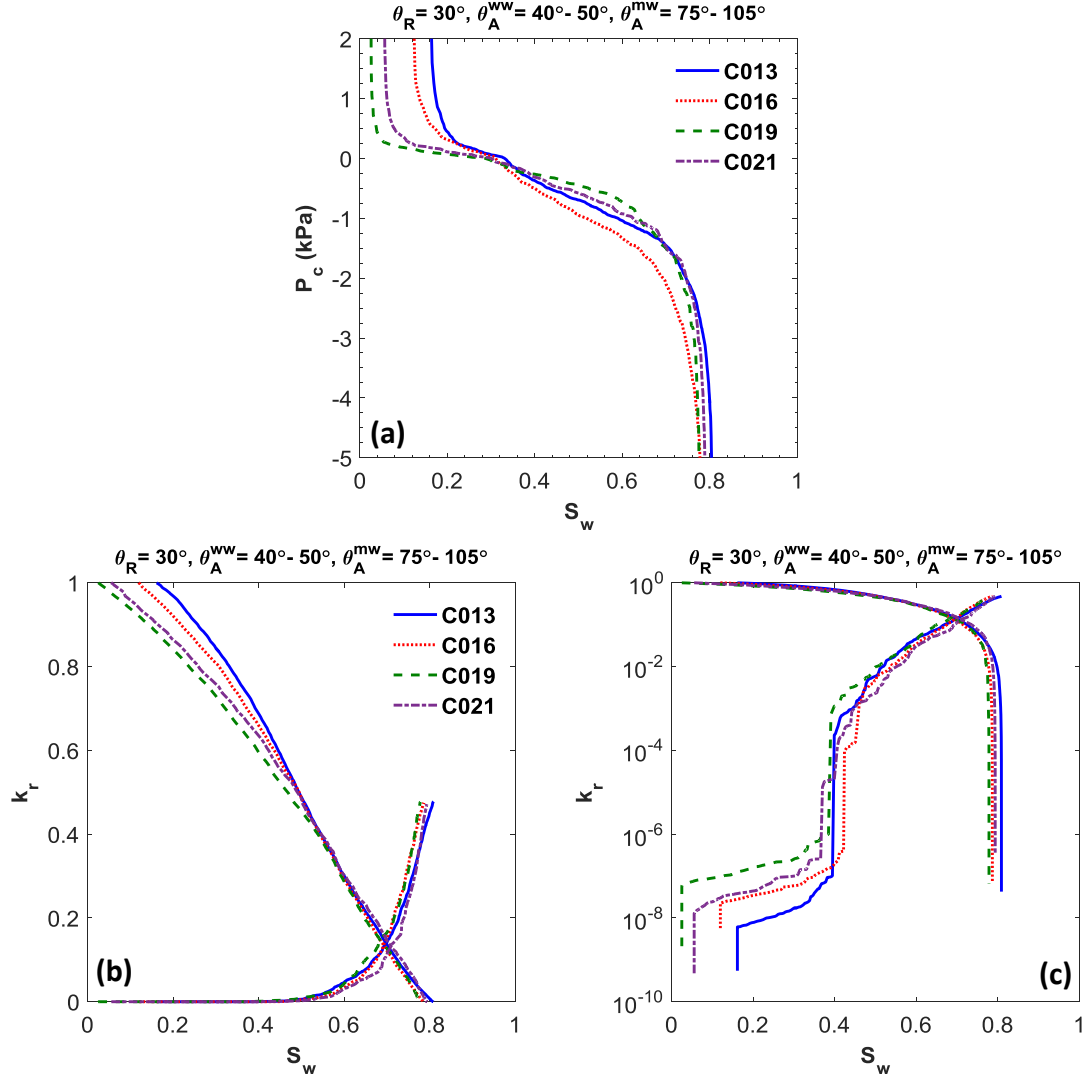


Figure 6.13 – Secondary imbibition P_c and k_r curves of carbonate networks for *Case 2*.

From the histograms of pore-level events in **Fig. 6.10**, nodes are generally filled through pore body filling (I_k) with at least two adjacent oil-filled links. Again from **Fig. 6.10**, while snap-off plays a minor role during spontaneous imbibition of links, forced imbibition is completely dominated by piston-type advancement. For $\theta_A > 90^\circ$, snap-off P_c^e is too low compared to piston-type P_c^e . Therefore, even if the geometrical criterion for snap-off is met (**Eq. 5.49**), due to its lower P_c^e , snap off is mostly suppressed during forced imbibition in mixed-wet systems (Kovscek et al., 1993; Øren

et al., 1998; Blunt et al., 2002). Here, according to **Table 6.5**, as compared to *Case 1*, the only increase in S_{or} occurs for C013. The reason is that snap-off events are less frequent in C013 under *Case 1* due to its lower aspect ratio (see **Fig. 6.10**) and when the system becomes more oil-wet (larger θ_A^{mw} in *Case 2*), trapped oil amount during forced imbibition without oil layers exceeds snap-off effect in C013. While C016 P_c has the earliest breakthrough in spontaneous imbibition, it needs further pressure decline to reach the same S_w of the other samples in forced imbibition zone. This may be attributed to the arrangement of its pore elements, i.e. better positioning between similar-sized pores inside the network.

The pores having $\theta_A < 90^\circ$ are invaded during spontaneous imbibition. From k_r curves in **Fig. 6.13**, during spontaneous imbibition, water preferentially invades the narrowest pores, and as a consequence k_{rw} is very low ($< 10^{-6}$ for $S_w < 0.3$). After around $S_w = 0.3$, water enters into pores with negative P_c ($\theta_A > 90^\circ$) over a significant range of saturation. As S_w reaches about 0.4, water establishes a spanning pathway across the network and a sudden increase is observed in k_{rw} (3-4 orders of magnitude) followed by a more steady increase thereafter. **Figure 6.13b** depicts that the endpoint k_{rw} (at S_{or}) is almost the same for all carbonates and no more than 0.5 (**Table 6.5**). Compared to the k_{ro} at S_{or} in *Case 1* ($> 10^{-4}$ in **Fig. 6.12c**), k_{ro} drops to lower values in *Case 2* ($< 10^{-4}$ in **Fig. 6.13c**).

Contact angle hysteresis is not much in *Case 2* (mostly $\theta_A < 90^\circ + \beta_i$), but still some intermediate oil layers form during forced imbibition (see **Section 5.2.2.3**). Oil layer saturation S_{ol} in node and link systems of C013 during imbibition process is plotted against step number and overall water saturation in **Figs. 6.14a** and **6.14b**, respectively. **Figure 6.14** shows that S_{ol} is too low, i.e. not exceed 0.42% (summation of S_{ol} in nodes and links) along the imbibition process. Oil layer formation begins at around 80th step of imbibition in nodes, and 120th step in links (each step covers 50 consecutive invasions) (**Fig. 6.14a**). The change in S_{ol} does not show a smooth trend,

rather a substantial amount of zigzagging on the saturation curves most probably due to seldom layer creation in the network. As S_w goes beyond 0.6, despite some small increments, S_{ol} of both nodes and links declines until almost zero at the end (**Fig. 6.14b**). The decline is a result of collapse of most of the previously formed oil layers ($P_c < P_{c,i}^{crit}$) and also the further drainage of remaining oil layers in the system.

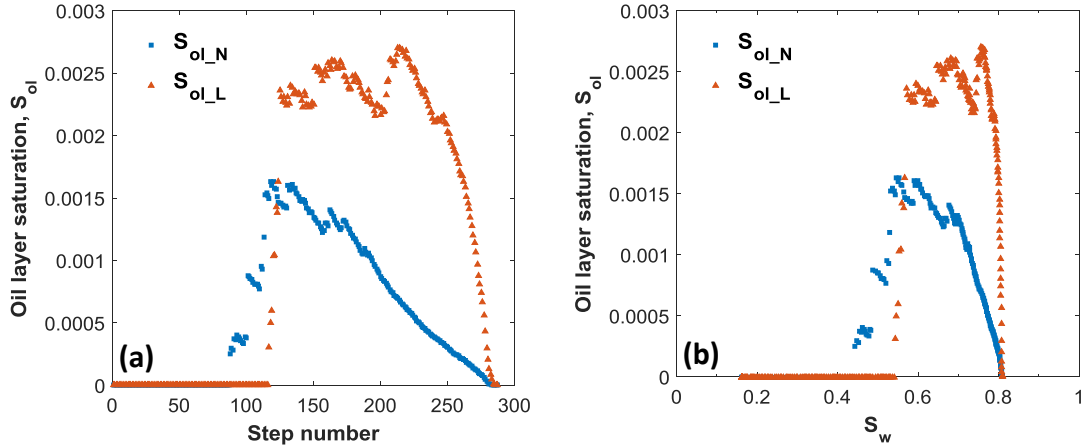


Figure 6.14 – Oil layer saturation in a) node and b) link systems of C013 during forced imbibition under Case 2 (N: node, L: link, ol: oil layer).

Oil layers do provide oil continuity up to low saturations while they have very low conductance in the medium (Al-Kharusi and Blunt, 2008). Here, it is remarkable that continuity of a phase is the critical factor for its relative permeability rather than how much of it is present in the system. For instance, S_{or} in C016 is nearly the same for Case 1 and 2 (~ 0.2 in **Table 6.5**), but although k_{ro} of Case 2 is larger than that of Case 1 throughout the imbibition process, its k_{ro} towards the end ($S_w > 0.8$ in **Fig. 6.13c**) falls to much smaller values ($< 10^{-6}$) compared to endpoint k_{ro} in Case 1 ($< 10^{-3}$) due to connectivity of oil phase by means of remaining thin oil layers with low conductance. The instant decrease of k_{ro} near S_{or} in **Fig. 6.13c** is directly correlated to the substantial reduction in oil layer saturation in **Fig. 6.14b**. The final P_c where no further imbibition occurs is nearly the same for all samples (-149 to -153 kPa in **Table 6.5**). It is deduced

from the simulation results that pore structural differences of the carbonate networks have less impact on their P_c and k_r behaviors under *Case 2* compared to water-wet conditions in *Case 1*.

Case 3: The advancing angle of oil-wet surfaces is allowed to be greater than 90° for *Case 3* representing an oil-wet system (**Table 6.4**). Under oil-wet conditions, the secondary imbibition is entirely dominated by forced piston-type advancement regime and proceeds like oil migration process (Al-Futaisi and Patzek, 2004). Obviously, there is no change in water saturation of carbonates until forced imbibition begins ($P_c < 0$) in **Fig. 6.15a**.

According to the pore-level flow histograms in **Fig. 6.10**, nodes are mostly filled through pore body filling mechanism (I_k) under *Case 3*. Snap-off is completely suppressed and only piston-type flow occurs in links. Inferred to the significant degree of contact angle hysteresis in *Case 3* ($\theta_A \geq 90^\circ + \beta_i$), many intermediate oil layers are created in the pore space during forced piston-type imbibition. These oil layers provide oil connectivity down to very low oil saturations in the network and accordingly efficient oil recovery (Kovscek et al., 1993). From the curves, S_{or} is almost zero for all oil-wet carbonate systems ($< 0.6\%$ in **Table 6.5**). The water-filled mixed-wet pores are checked at each step for the survival of their oil layers at the prevailing P_c . If the recent P_c goes down the critical capillary pressure $P_{c,i}^{crit}$ (**Eq. 5.43**), the oil layer on corner i no longer exists. Masalmeh (2002) conducted imbibition experiments on several cores from different carbonate fields in Middle East and some clastic rocks and, similar to our results, the residual oil saturation S_{or} was found to decrease 15 to 20 saturation units with the increase in oil-wetness of the medium.

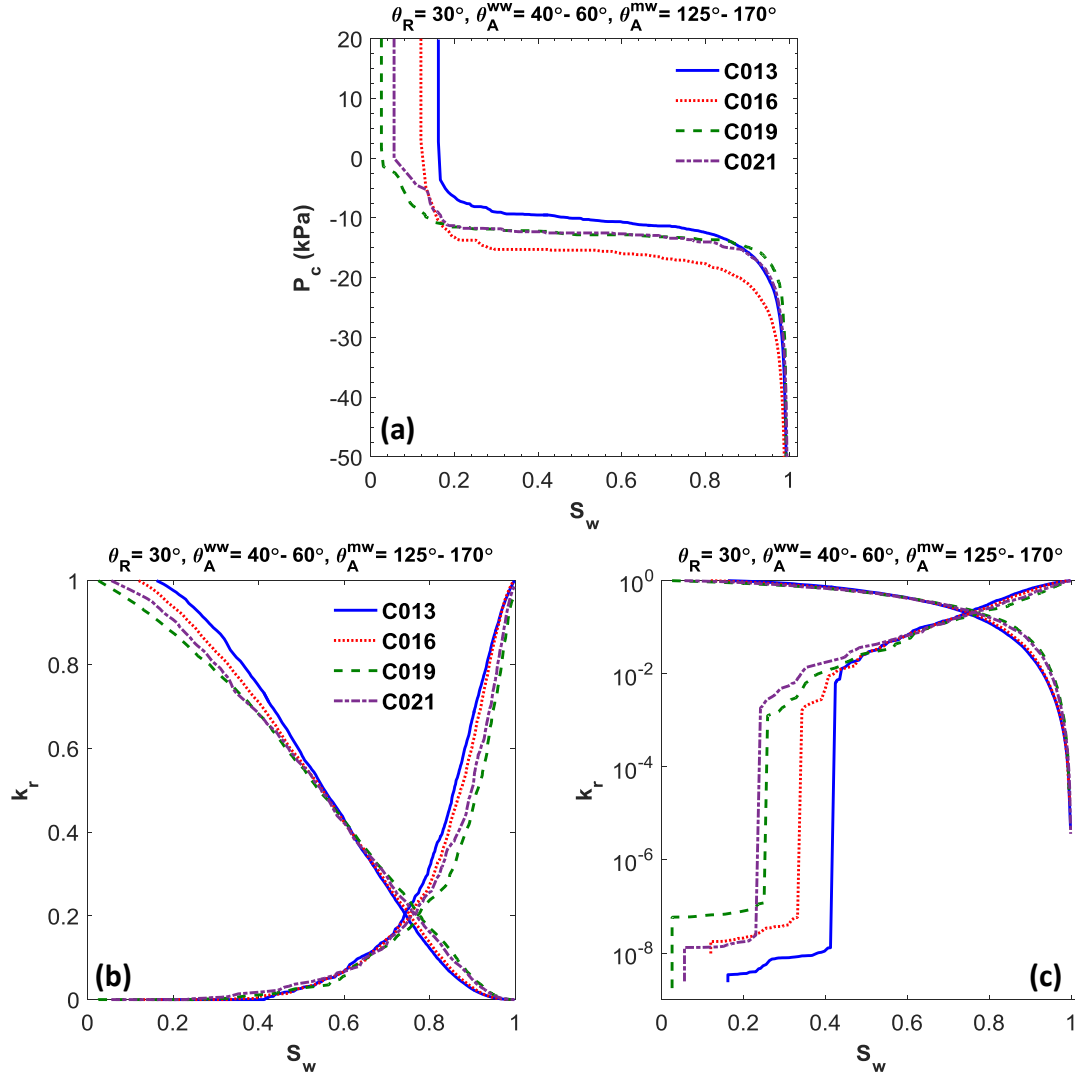


Figure 6.15 – Secondary imbibition P_c and k_r curves of carbonate networks for Case 3.

The oil layer saturation S_{ol} during imbibition in node and link systems of C013 is plotted against step number and overall water saturation in **Figs. 6.16a** and **6.16b**, respectively. From **Fig. 6.16a**, at the early steps of imbibition, up to around 20, oil layer formation does not begin. By the progressive invasion of water into the system, oil layers are created in near most of the corners of both nodes and links. The oil layer saturation reaches its maximum in the node and link systems at nearly 110th and 150th steps corresponding to overall water saturation S_w of 0.72 and 0.85 in **Fig. 6.16b**, respectively. Afterwards, the further decrease of system P_c exceeds the critical collapse

pressure $P_{c,i}^{crit}$ of most of the pores having oil layer(s). These oil layers cannot persist any longer and disappear quite steeply. Besides, the drainage of remaining oil layers continues down to very low values ($S_{ol} < 5 \times 10^{-4}$) towards the end of water flooding process. Note that while the peak value of the total S_{ol} in C013 was smaller than 0.42% for *Case 2* (Fig. 6.14), it is around 4.5% for *Case 3* (Fig. 6.16).

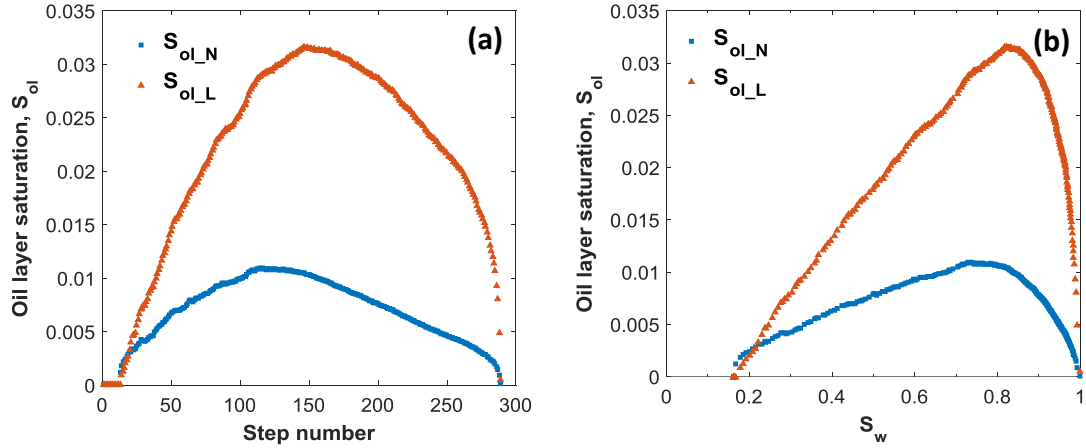


Figure 6.16 – Oil layer saturation in a) node and b) link systems of C013 during forced imbibition under *Case 3* (N: node, L: link, ol: oil layer).

According to k_r curves in Fig. 6.15, initially water filling of the narrowest pores and swelling of corner water take place for $S_w < 0.4$ and result in extremely small k_{rw} ($< 10^{-7}$). Then, in consequence of achieving a broad water continuity across the network, a huge jump is observed in k_{rw} (around 4-6 orders of magnitude). Oil layer presence in the pore network prevents isolated oil clusters and makes all the remaining oil connected through the outside. This explains the quite large k_{rw} in *Case 3*. Besides, due to oil layer shrinkage with the decrease in P_c , oil layer conductance weakens and k_{ro} gets very low values ($< 10^{-5}$) towards the end of forced imbibition. Note that although oil saturation falls to much less values through the end of imbibition in *Case 3* compared to *Case 2* (Table 6.5), the endpoint k_{ro} in *Case 3* ($< 10^{-5}$ in Fig. 6.15c) is higher than that in *Case 2* ($< 10^{-7}$ in Fig. 6.13c) owing to the presence of much more oil layers left at the end.

Similar to *Case 2*, there is a strong correlation between k_{ro} (**Fig. 6.15c**) and S_{ol} trends (**Fig. 6.16b**) for $S_w > 0.8$. The curved decrease in k_{ro} close to S_{or} is the consequence of the collapse of most of the oil layers and the drainage of remaining oil layers through the end.

If water and oil relative permeabilities for three wettability cases per sample are compared (**Figs. 6.12, 6.13, and 6.15**), the endpoint k_{rw} seems to increase with the oil-wetness of the medium. This observation is consistent with the experimental study of Masalmeh (2001) on both carbonate and sandstone core samples. The main reason why k_{rw} in *Case 3* reaches its maximum (~ 1 in **Table 6.5**) is related to extensive oil layer presence and hence less disruption of the connectedness of water clusters. k_{ro} at S_{or} is the highest for *Case 1*, because a considerable amount of pores is left oil-filled in the network and oil flows predominantly in the pore centers. The cross-point between k_{rw} and k_{ro} curves shift to right side with the increase in the oil-wetness, i.e. in θ_A^{mw} . Lastly, under all wetting circumstances, endpoint k_{rw} (at S_{or}) is lower than or equal to k_{ro} at S_{wi} ("Fluid flow in porous media: facts," 2016). Because, during drainage process, due to permanent continuity of water in the porous system, corner water continues water drainage until very low saturations and does not disrupt the connectivity of oil occupying the pore center. On the contrary, residual oil presents as isolated droplets in the central part of pore network and weakens water continuity during imbibition.

6.4 Secondary drainage simulation results

Following oil production through secondary imbibition, oil is re-invaded into the system. The dependence of pore-level distributions of the phases and their flow behaviors upon the saturation history of the porous medium and the direction of saturation change causes hysteresis in contact angle, capillary pressure and relative permeability curves. As described in **Section 5.2.3**, to realize contact angle hysteresis between the flooding

cycles, θ_r is assigned to each mixed-wet pore in between θ_R and θ_A , while θ_r is equal to θ_R in water-wet pores. The sorted distributions of θ_A and θ_r depending on wettability state of individual network pores are plotted in **Fig. 6.17** for C013 under *Case 3*. Due to the rareness of water-wet nodes in the network, the advancing angles in water-wet nodes θ_A^{ww} are just a few blue dots in the range of 40° - 60° (**Table 6.4**). The receding angle in water-wet links ($\theta_r = 30^\circ$) are at the base of Link θ_r curve in **Fig. 6.17**. However, since almost all nodes are mixed-wet (**Table 6.3**), there is not a distinct period in Node θ_r curve for $\theta_r = 30^\circ$.

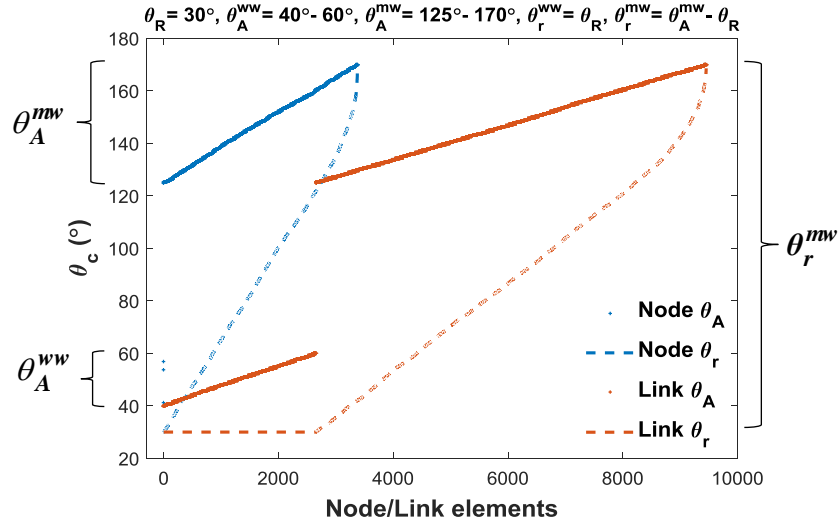


Figure 6.17 – Distribution of the receding and advancing angles in water-wet (ww) and mixed-wet (mw) nodes/links of C013 under *Case 3*.

Primary drainage, secondary imbibition, and secondary drainage phases of a flooding cycle differ with respect to the initial state of pore-level fluid distributions in the network (**Fig. 5.19**). The algorithm complexity increases with the diversity in initial possible oil-water combinations to be evaluated in the flow simulations (**Appendix B**). As each upcoming flooding offers additional fluid configurations in a single pore, much more possibilities have to be taken into account in oil re-invasion modeling. In brief, secondary drainage depends on the entire sequence of previous displacement processes, i.e. saturation history (Hui and Blunt, 2000).

Secondary drainage percolation is similar to primary drainage except with the essential modifications for the oil involvement within the network either as bulk phase, trapped oil blobs or as oil layers. Again, only piston-type advancement is considered and pores are allowed to be drained in the direction of P_c^e increase. Secondary drainage may provide previously trapped oil to be reconnected and produced in the upcoming recovery processes (Blunt, 1997b).

In the beginning of secondary drainage, water-occupied pores are checked for oil-layer existence at P_c^{\min} . The piston-type capillary entry pressures of nodes and links with/without oil layer(s) are computed separately following the aforementioned equations appropriate for their configurations (Configuration E or G in **Fig. 5.19**) given in **Section 5.2.3**. The secondary drainage P_c^e calculated for each possible displacement of C013 nodes and links are plotted in **Figs. 6.18–6.20** for *Case 1*, 2 and 3, respectively. P_c^e plots represent separate dots belonging to P_c^e of individual nodes and links as well as their sorted forms in ascending order. In **Fig. 6.18**, due to lack of oil layers in *Case 1*, only Configuration E (**Fig. 5.19**) is recognized for pore elements prior to secondary drainage. θ_r in *Case 1* mostly obeys to the condition of $\theta_r < 90^\circ - \beta_1$, therefore the displacement happens predominantly from Configuration E to H in **Fig. 6.18**.

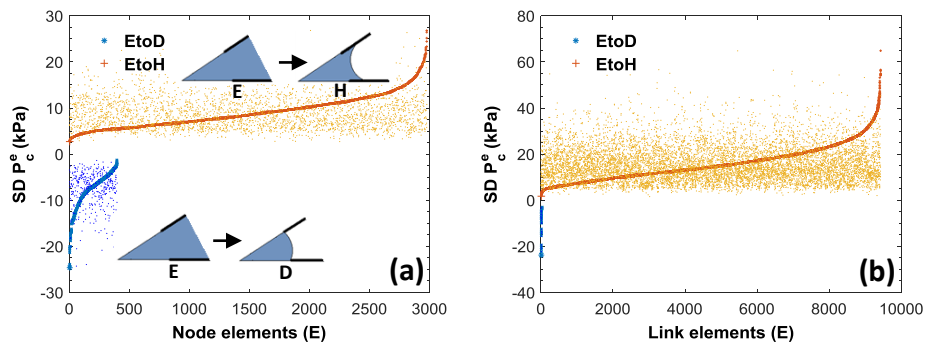


Figure 6.18 – Secondary drainage P_c^e of water-filled a) nodes and b) links of C013 under *Case 1*.

Prior to secondary drainage, since oil layer occurrence is seldom under *Case 2*, nodes and links in Configuration E dominate the system in **Fig. 6.19**. On the contrary, under *Case 3*, the majority of water-filled mixed-wet nodes and links occupy at least one oil layer at the end of imbibition and so Configuration G competes with E, especially in nodes (**Fig. 6.20**). In displacement from Configuration G to D, (1) and (2) refer to the conditions $\theta_r > 90^\circ + \beta_1$ and $90^\circ - \beta_1 \leq \theta_r \leq 90^\circ + \beta_1$, respectively. Since θ_r has a wide range from smaller than 90° to larger by far, depending on the relation between receding angle and corner half-angles, P_c^e of pore elements may take positive or negative values as demonstrated in **Figs. 6.18–6.20**.

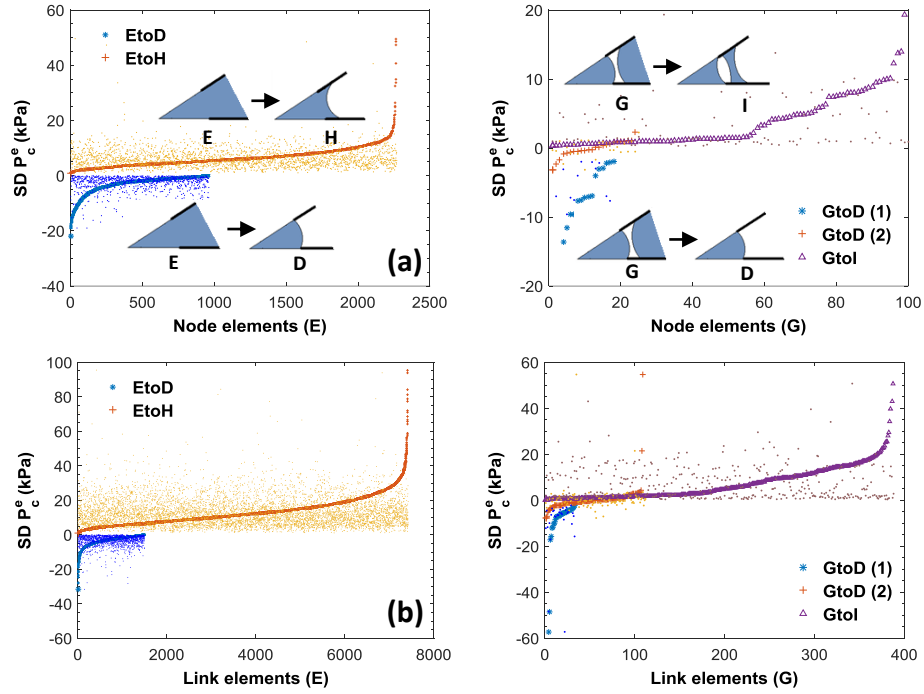


Figure 6.19 – Secondary drainage P_c^e of water-filled a) nodes and b) links of C013 under *Case 2*.

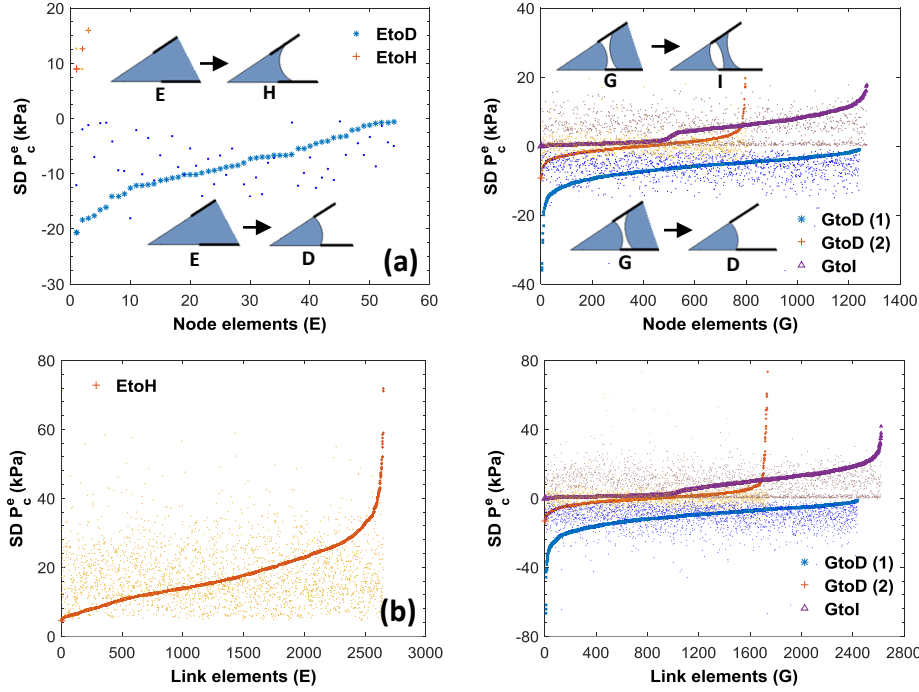


Figure 6.20 – Secondary drainage P_c^e of water-filled a) nodes and b) links of C013 under Case 3.

P_c hysteresis curves of complete flooding cycles for all three wettability cases per sample are plotted in **Figs. 6.21–6.24** with their enlarged versions on the right side (the enlarged intervals are signified by right braces). The resulting curves clearly show the hysteresis between flooding loops. Due to the contact angle hysteresis and presence of oil in the system, secondary drainage (SD) P_c curve does not coincide with primary P_c curve and lies between primary drainage (PD) and imbibition (SI) curves along the process. Due to wettability change, the breakthrough capillary pressure P_c^* in secondary drainage of each carbonate network is generally somewhat less than its primary drainage P_c^* which agrees with the experimental findings of Chatzis and Dullien (1981) on three sandstone samples and Masalmeh (2001) on several carbonates and sandstones of different wettability. Only for *Case 1* of C019 in **Fig. 6.23a**, there is an unusual trend where SD curve slightly steps up on PD curve. This is probably resulted from its lower primary breakthrough pressure than the others for $\theta_R = 0^\circ$ (**Table 6.2**). Due to

significant S_{or} in C019 under *Case 1*, most of the largest pores are already oil-filled prior to secondary drainage. Therefore, C019 reaches oil breakthrough at a greater P_c compared to its primary case and so its transition region in secondary drainage P_c curve where most of the pores with similar size (i.e., similar P_c^e) are invaded is just above the primary P_c curve. The oil re-invasion mostly occurs above $P_c = 0$ for all samples. Secondary drainage ends when all possible pores are invaded until the current pressure of the network reaches uttermost $P_{c,pd}^{\max}$. Based on P_c hysteresis curves in **Figs. 6.21–6.24**, secondary drainage is completed at a lower pressure (50 to 118 kPa) than the allowed limit of $P_{c,pd}^{\max}$ (164 to 168 kPa) only for *Case 1* (**Table 6.5**). This is the consequence of spontaneous imbibition process in *Case 1* where no oil layer is available in the network prior to secondary drainage to continue oil drainage until high pressures.

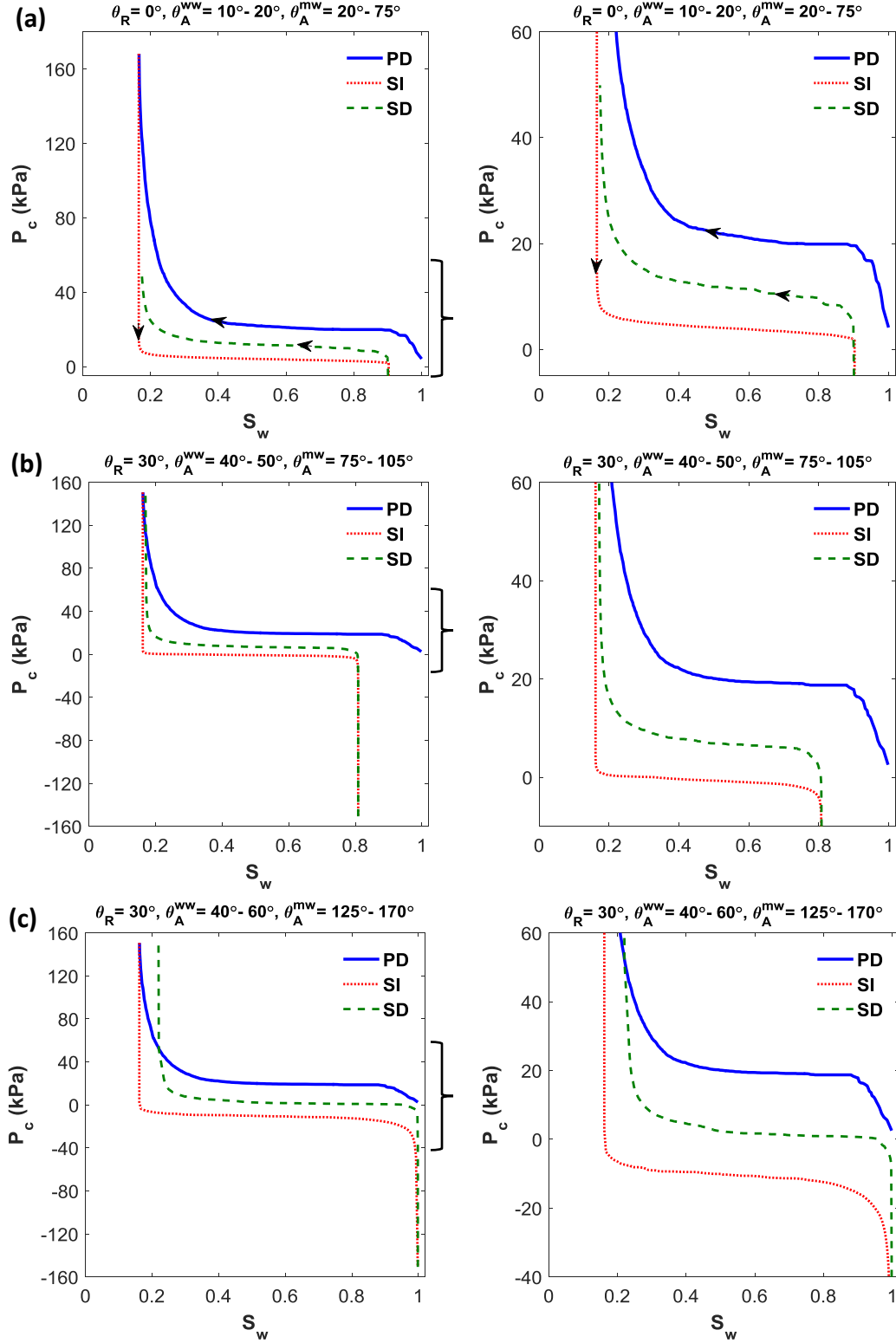


Figure 6.21 – P_c hysteresis curves of C013 (left) and their enlarged versions (right; enlarged intervals signified by right braces) for a) Case 1, b) Case 2, c) Case 3 (PD: primary drainage, SI: secondary imbibition, SD: secondary drainage).

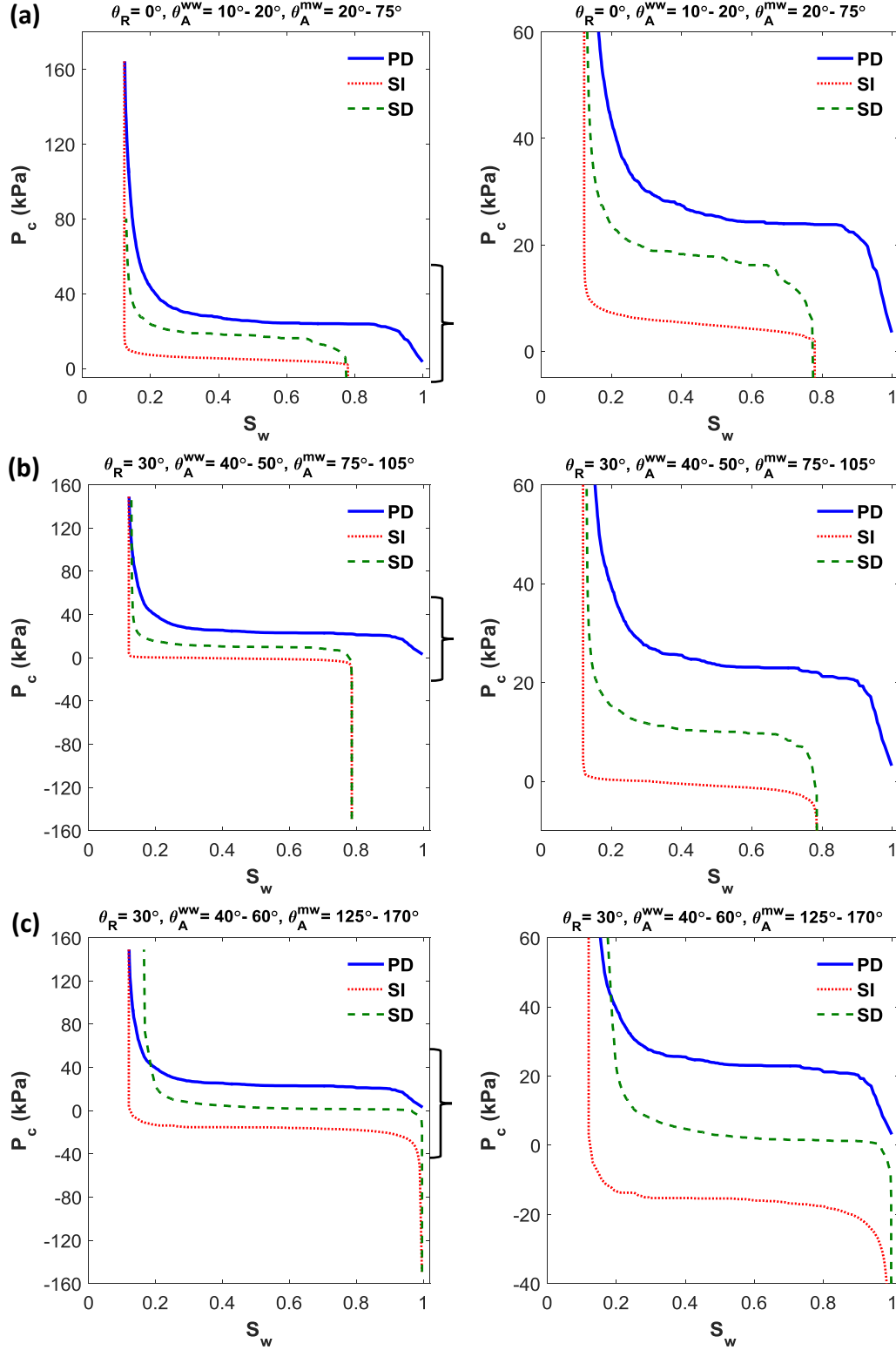


Figure 6.22 – P_c hysteresis curves of C016 (left) and their enlarged versions (right; enlarged intervals signified by right braces) for a) Case 1, b) Case 2, c) Case 3 (PD: primary drainage, SI: secondary imbibition, SD: secondary drainage).

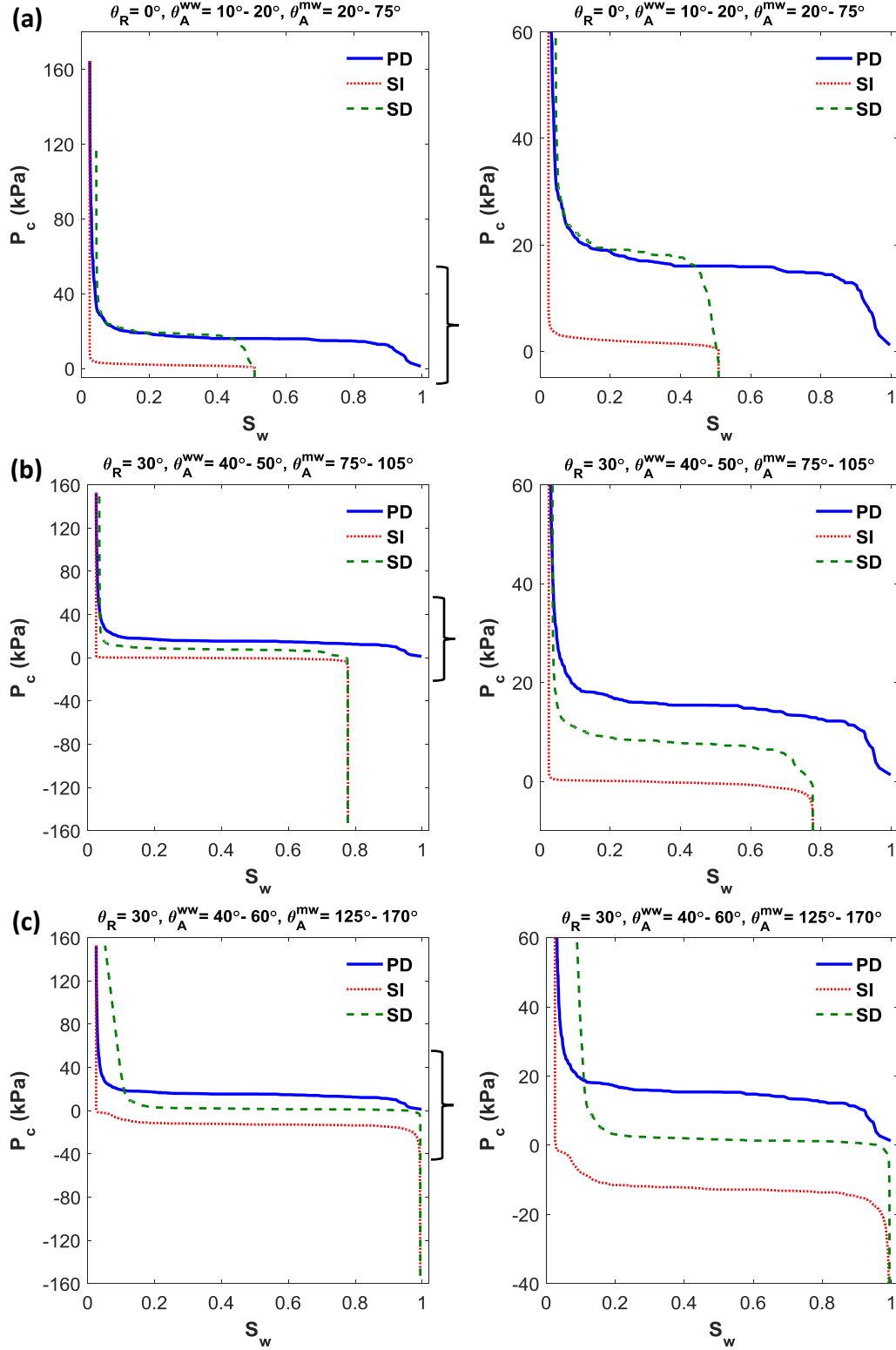


Figure 6.23 – P_c hysteresis curves of C019 (left) and their enlarged versions (right; enlarged intervals signified by right braces) for a) Case 1, b) Case 2, c) Case 3 (PD: primary drainage, SI: secondary imbibition, SD: secondary drainage).

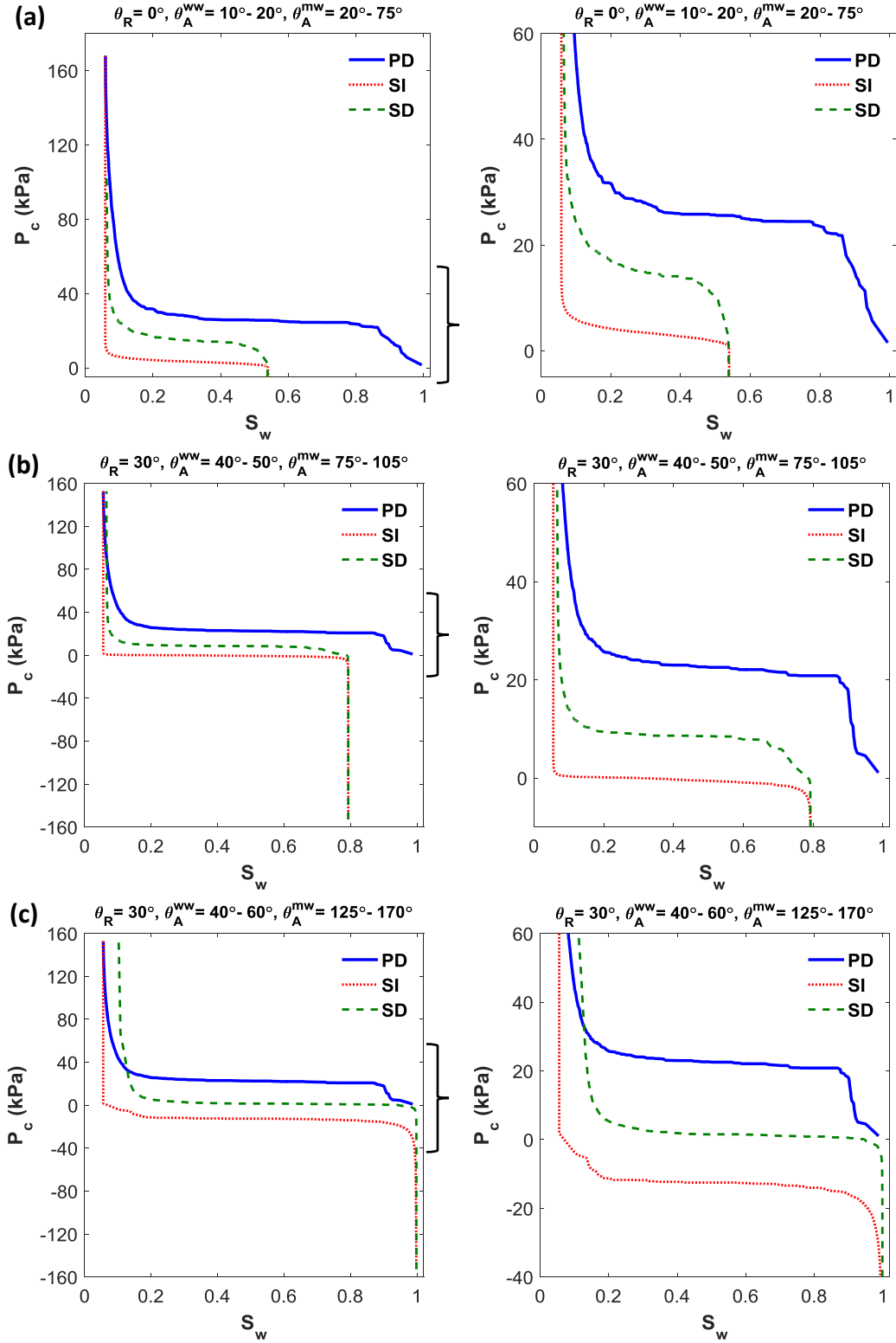


Figure 6.24 – P_c hysteresis curves of C021 (left) and their enlarged versions (right; enlarged intervals signified by right braces) for a) Case 1, b) Case 2, c) Case 3 (PD: primary drainage, SI: secondary imbibition, SD: secondary drainage).

Similar to our simulation results, Masalmeh (2001) experimentally presented the significant hysteresis in P_c curves of both carbonate and sandstone samples and attributed this hysteresis trend to contact angle hysteresis, wettability change and fluid trapping. For water-wet media, P_c curves formed closed hysteresis loops because no water trapping was expected (Fig. 6.25a). However, extra hysteresis was observed for mixed-wet carbonates; P_c curves of secondary drainage did not end at the same S_w as primary drainage which was related to water trapping. For instance, P_c hysteresis curves of carbonates in Fig. 6.25b and 6.25c shows a shift of 2-3 saturation units in residual water between primary and secondary drainage processes. Similar to our model results (Figs. 6.21-6.24), secondary drainage mostly occurred at positive P_c (Fig. 6.25). It was concluded that due to contact angle hysteresis, mixed-wet rocks might behave as water-wet during secondary drainage and as oil-wet during imbibition.

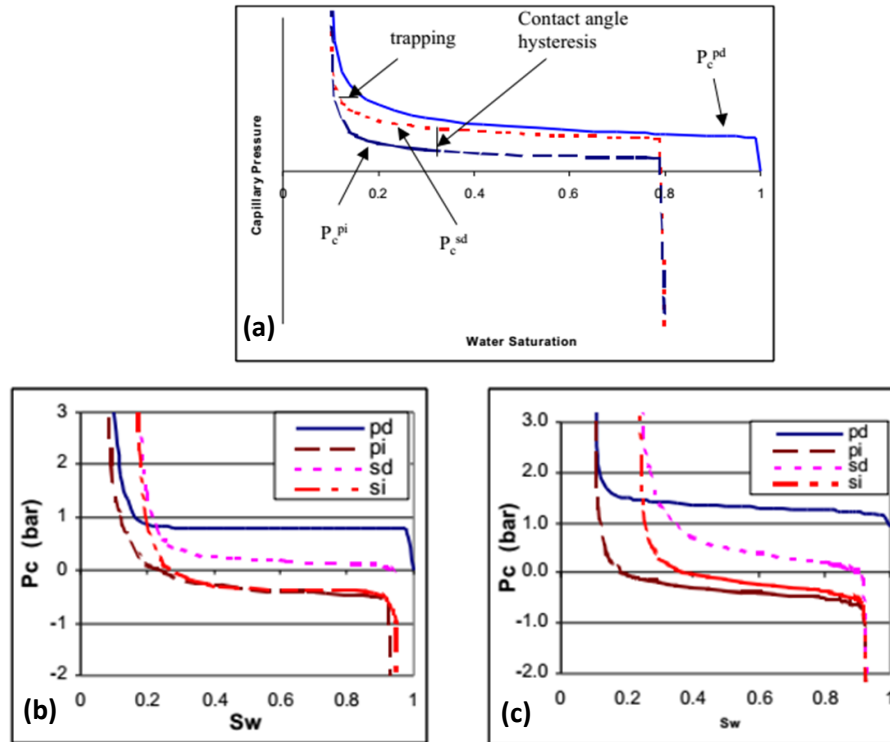


Figure 6.25 – Experimental P_c hysteresis curves of water-wet sandstone (a) and two mixed-wet limestone samples from the same formation (b-c) (Masalmeh, 2001) (Note: Primary imbibition (pi) in Masalmeh's paper refers to secondary imbibition (SI) in our model).

The minimum receding angle in a pore determines whether oil re-invasion is spontaneous or forced into that pore. In our model, θ_r^{\min} is found to be around 90° for all wettability cases (Eq. 5.65 or 5.34). Oil spontaneously invades into a pore when its receding angle is greater than θ_r^{\min} and forced drainage occurs otherwise. In *Case 1*, since θ_A is smaller than 90° , θ_r never exceeds θ_r^{\min} and hence only forced drainage occurs. In *Case 2*, although θ_A may be larger than 90° , its maximum limit is not much (105°) and thus, again the forced drainage dominates the process. Differently, in *Case 3*, θ_r is distributed in a large extent (from 30° up to 170°) and both spontaneous and forced drainage take place as indicated in Fig. 6.26 for C013.

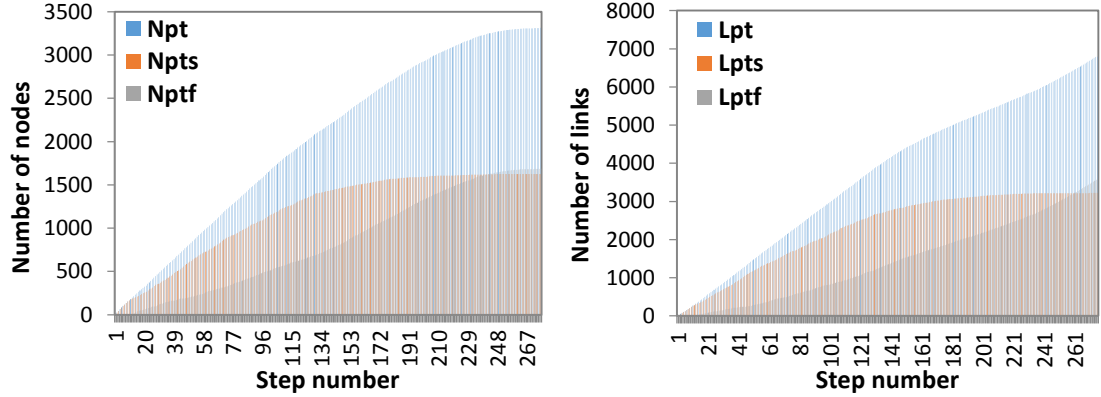


Figure 6.26 – Number frequencies of piston-type displacements in nodes and links of C013 for *Case 3* during secondary drainage (N: node, L: link, pt: piston-type, s: spontaneous, f: forced).

Notice that oil layers available in the water-filled pores prior to secondary drainage (at P_c^{\min}) will stay stable unless oil re-invasion occurs in these pores. Because P_c increases during drainage, it never drops below critical collapse pressure $P_{c,i}^{crit}$. In the case of stable oil layers, oil refills the oil layers progressively (Kovscek et al., 1993). After oil re-invasion into the pores having at least one oil layer, if water layer is formed (from Configuration G to I in Fig. 5.19), while oil layer gets thicker, water layer gets thinner in response to P_c climb. However, when the current P_c exceeds $P_{c,i}^{stab}$ (Eq.

5.61), water layer lining between oil layer and oil in the center collapses and oil layer in the corner merges with the oil in the very center. **Figures 6.27a** and **6.27b** exhibit the decrease in oil layer saturation S_{ol} of water-filled nodes and links (Configuration G in **Fig. 5.19**) under *Case 2* and *Case 3* for C013, respectively. From the S_{ol} trends, there is a continuous drop in S_{ol} due to oil layer collapse with the oil re-invasion into previously water-filled pores during secondary drainage.

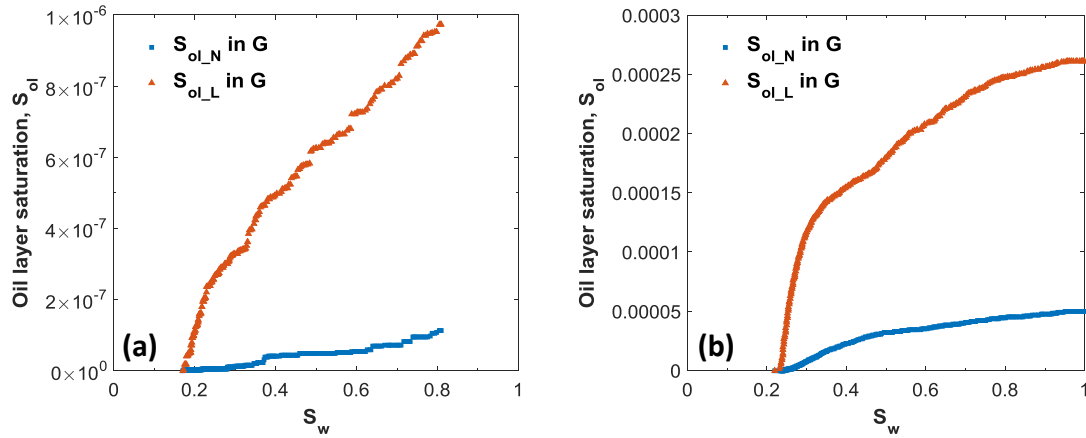


Figure 6.27 – Oil layer saturation in previously water-filled pores of C013 under a) *Case 2* and b) *Case 3* during secondary drainage (N: node, L: link, ol: oil layer).

Table 6.5 depicts that the residual water saturation S_{wirr} is always more than the initial (irreducible) water saturation S_{wi} (Salathiel, 1973). Especially for *Case 3*, the difference between S_{wirr} and S_{wi} remarkably increases as a result of large wettability change. For this reason, the secondary drainage curve does not join the primary drainage curve at the completion of subsequent drainage process. Our carbonate systems are assumed to be initially water-wet (strongly or weakly), thus water always maintains continuity along the network and is assumed not to be trapped under any circumstances in drainage simulations (Kovscek et al., 1993). In Masalmeh's experimental study on Middle East carbonates (2001, 2002), the observed difference between residual water saturations was up to 15 saturation units in mixed-wet systems and related to the water trapping during secondary drainage. In our case, as in primary drainage, a major

contribution to irreducible water is due to carbonate network's microporosity (PC1 links). Although water trapping is not implemented in our model, still, a noticeable increase in residual water for each wettability case, especially for *Case 3*, is observed due to the newly generated oil-water configurations in the network, the additional water-filled pores after oil re-invasion and the intermediate water layers on the pore corners. The displacement from Configuration E to H (**Fig. 5.19**) that is commonly observed in *Case 1* and *Case 2* causes slight increase in corner water saturation due to the longer distance from corner arc menisci to apex L_i in oil-filled pores without oil layer(s) compared to the pinned menisci distance $L_{pd,i}$ of primary drainage. On the other hand, the water layer(s) in the system (from Configuration G to I in **Fig. 5.19**), dominant in *Case 3*, contribute to the further residual water if $P_{c,sd}^{\max}$ is not enough for the collapse of water layers in the network.

The saturation of water layer S_{wl} during oilflooding a previously waterflooded medium together with the saturation of its adjacent oil layer S_{ol} is plotted against S_w in **Figs. 6.28** and **6.29** for *Case 2* and *3* of C013, respectively. In both figures, there is a clear coincidence between the saturation trends of oil and water layers along the process. Since much less number of oil layers exist in *Case 2*, S_{ol} and S_{wl} values are too low in **Fig. 6.28** as compared to **Fig. 6.29**. It is also remarkable that S_{wl} is nearly 3 to 5 orders of magnitude greater than its corresponding S_{ol} . The layer saturations in **Fig. 6.28** increase modestly until the very end of drainage where they start to decline around $S_w < 0.2$. Since oil preferentially occupies the larger pores first, the rate of layer saturation in nodes stabilizes before the end of process ($S_w < 0.3$) while it continues to increase in small-sized links through the end. In **Fig. 6.29**, the rate of continuous climb in oil and water layer saturations increases around $S_w = 0.4$ in nodes and 0.5 in links with the forced oil invasion into smaller pores. At the end of secondary drainage (around $S_w = 0.2$), a remarkable amount of layer saturation is left behind which is regarded as the residual water saturation but unlike water in micropores, it is mobile and in a continuous

path throughout the network. In case the secondary drainage is allowed to proceed until all possible invasions occur, i.e. $P_{c, sd}^{\max}$ is not limited, a close to or even smaller residual water than S_{wi} would be possible in the model (at a quite high pressure level for reservoir conditions ($> 6,000$ psi)).

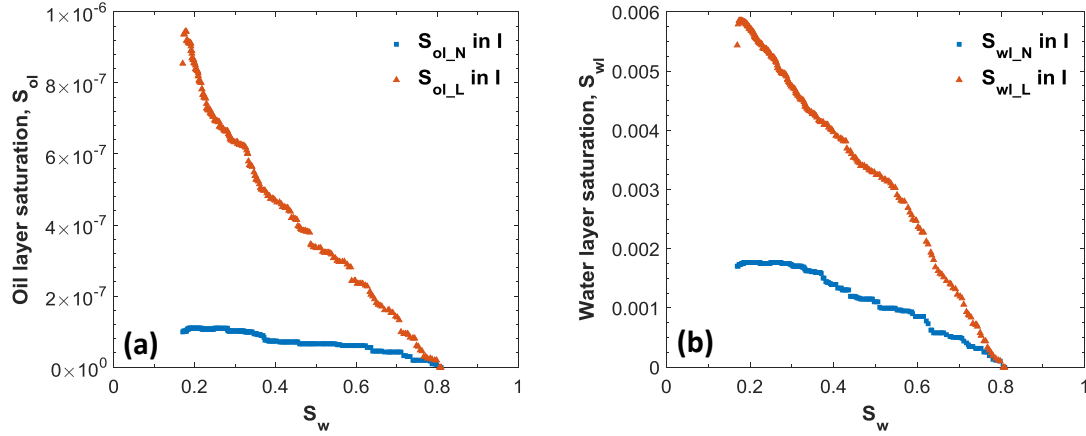


Figure 6.28 – Oil (a) and water layer saturations (b) of C013 during secondary drainage for Case 2 (N: node, L: link, ol: oil layer, wl: water layer).

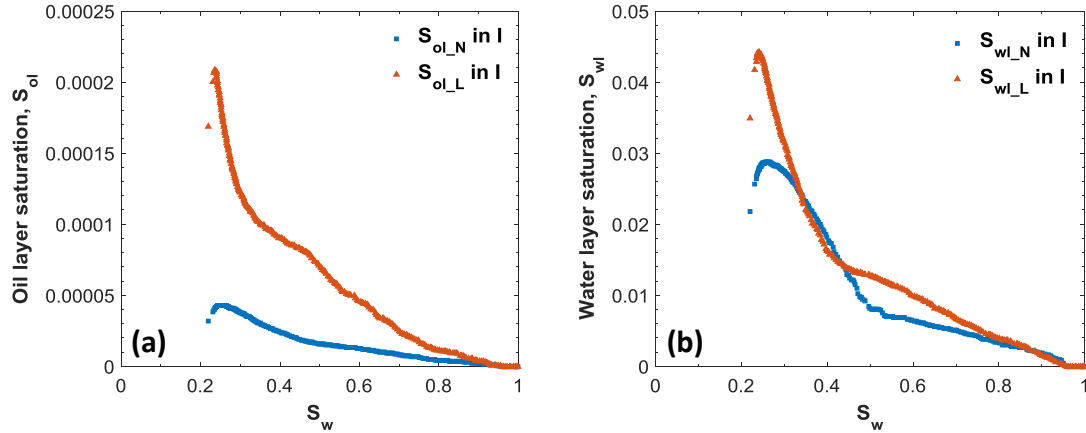


Figure 6.29 – Oil (a) and water layer saturations (b) of C013 during secondary drainage for Case 3 (N: node, L: link, ol: oil layer, wl: water layer).

The variety in fluid configurations in pore cross-sections makes it tricky to obtain reasonable relative permeability data for secondary drainage flow (Jerauld and Salter, 1990). Owing to the difficulties inherent in k_r measurements in our developed

model, k_r of samples having higher aspect ratio (C019) is not predicted well especially for *Case 1*. For this reason, k_r hysteresis curves under each wettability case are plotted only for C013 in the linear (left) and semi-log scales (right) in **Fig. 6.30** for the representation purpose.

The measured k_r hysteresis loops in C013 support the experimental observations done in strongly to moderately wetting systems (Jerauld and Salter, 1990; Masalmeh, 2001) such that k_{ro} shows more hysteresis than k_{rw} in capillary-dominated flows for each wettability case (left side of **Fig. 6.30**). Also k_{ro} hysteresis between flooding phases of a loop increases from **Fig. 6.30a** to **6.30c** with the increase in contact angle hysteresis. k_{ro} in SD is larger than in PD at a given S_w due to oil presence active in transport prior to drainage as bulk fluid in the largest pores, surface films and corner layers (if available) in the mixed-wet systems. Due to the same reason, differently from primary drainage, k_{ro} is not zero prior to secondary drainage. SD endpoint k_{ro} (at S_{wirr}) does not reach unity only in *Case 3* at the end of drainage process (**Fig. 6.30c**) because, as described before, the maximum capillary pressure $P_{c, sd}^{max}$ is not enough for the collapse of most of the water layers available in the network (**Fig. 6.29b**). Accordingly, substantial amount of flowing water remains and oil does not entirely dominate the system at the completion of SD. Foremost, SD k_{ro} crosses over PD k_{ro} and its slope increases for $S_w < 0.3$ under *Case 3* (**Fig. 6.30c**) due to the start of water layer collapse through the end of SD (**Fig. 6.29b**). Likewise, in Masalmeh's experiments (2001), while endpoint k_{ro} was found to be more than 1 for strongly water-wet samples, it was around 0.2 for oil-wet samples. These observations are in contradiction with most of the existing hysteresis models assuming that k_{ro} end points originate from the primary drainage curve.

The imbibition k_{ro} lies above the drainage (PD and SD) curves, i.e. imbibition k_{ro} is generally greater than drainage k_{ro} in the flooding cycle for each wettability case. Because while oil moves almost as a whole during water flooding except the

isolated oil droplets in the center of water-imbibed pores, oil forms disconnected clusters during primary drainage and needs time to get connectedness throughout the porous medium until S_w decreases to around 0.5. From semi-log plots (on the right side of **Fig. 6.30**), endpoint k_{ro} of imbibition generally drops downward ($< 10^{-4}$) as compared to k_{ro} at the breakthrough of primary drainage since fewer large pores are occupied by oil through the end of imbibition (Masalmeh, 2001; Dernaika et al., 2012). Due to permanent continuity of water extending from the inlet to outlet face of the network either as bulk fluid, corner or surface films, or as corner layer, the minimum k_{rw} gets much less values as compared to the minimum of k_{ro} under any circumstances either in imbibition or drainage processes. In general, the endpoint k_{rw} at S_{or} increases as oil-wetness increases (**Table 6.5**), because the trapped oil in less oil-wet cases hinders water movement throughout the network and thus reduces its imbibition k_{rw} (Masalmeh, 2001, 2002). k_{rw} reaches its smallest value at the end of secondary drainage for *Case 3* because of the thin water layers available in the network (on the right side of **Fig. 6.30c**).

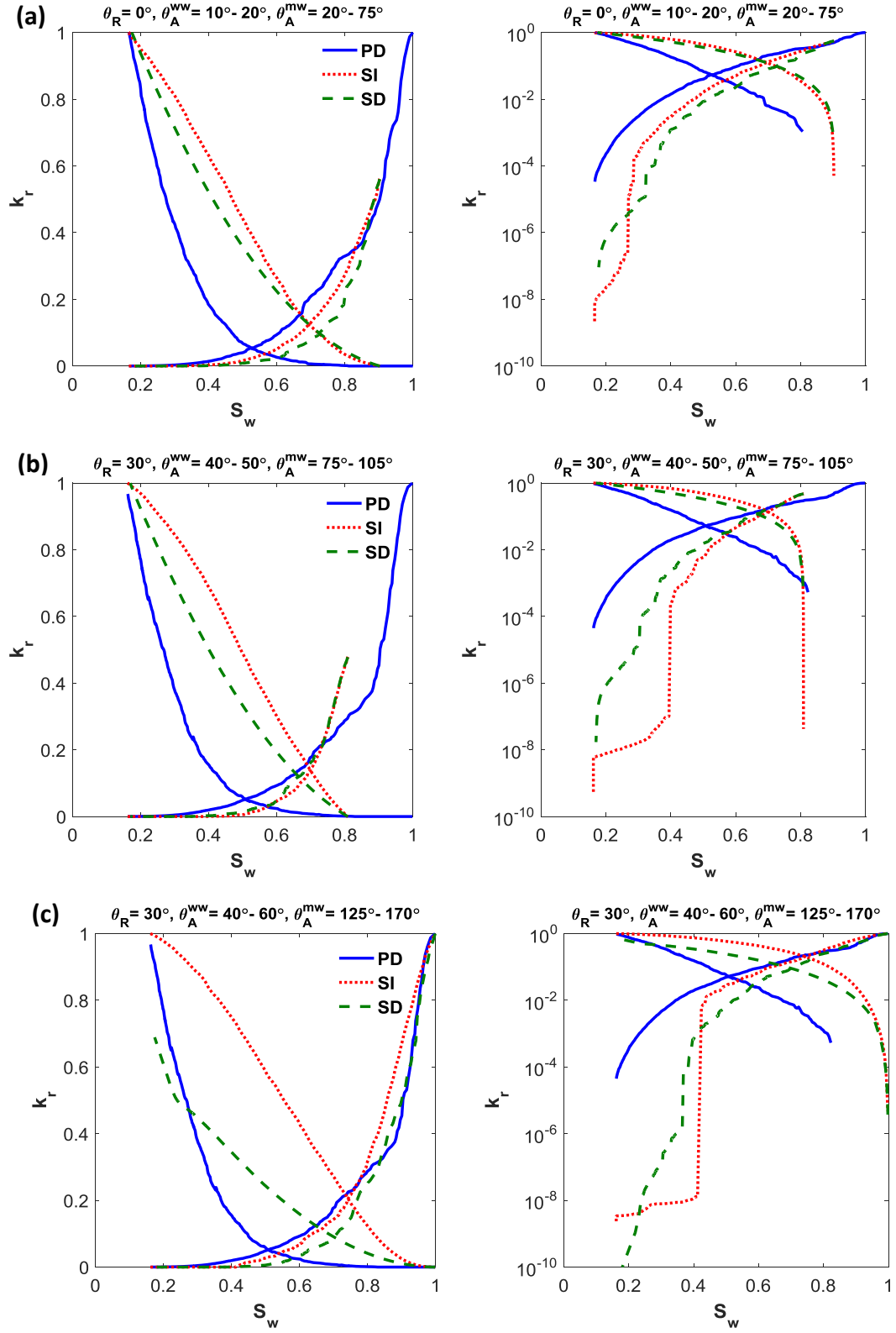


Figure 6.30 – k_r hysteresis curves in a flooding cycle of C013 for a) Case 1, b) Case 2, c) Case 3 (PD: primary drainage, SI: secondary imbibition, SD: secondary drainage).

CHAPTER 7

SENSITIVITY STUDIES OF WETTABILITY AND PORE STRUCTURE EFFECTS ON TWO-PHASE FLOW PROPERTIES

In this section, a sensitivity study is performed to investigate the effects of wettability characteristics and structural features of porous medium on the two-phase flow behavior during different flooding patterns. The significant controlling parameters of wettability, namely advancing contact angle, initial water saturation following primary drainage, and mixed-wet fraction and the basic geometric properties in the pore network are varied systematically and the change in macroscopic transport properties, flow regimes, and residual saturations are analyzed briefly for each in turn.

7.1 Effect of advancing contact angle during secondary imbibition

The effect of advancing contact angle on imbibition P_c and k_r curves, pore-level displacement mechanisms, and residual oil saturation are investigated for the carbonate samples C013 and C019. By taking into consideration the sensitivity studies of Blunt (1997b) and Al-Futaisi and Patzek (2003) which are explained in **Chapter 2**, the advancing angle of mixed-wet pores θ_A^{mw} is split into very narrow ranges between 0° and 180° to trace in step the dependence of two-phase flow properties on medium wettability. The contact angles are uniformly distributed within each narrow range. The receding contact angle during primary drainage θ_R is taken as zero and the advancing contact angle in water-wet pores θ_A^{ww} is uniformly distributed between 0° and 10° for each case.

For different wettability cases in mixed-wet pores (θ_A^{mw}), primary drainage and secondary imbibition P_c curves of C013 and C019 are given in **Fig. 7.1a** and **7.1b**, respectively. **Figure 7.1** indicates that the range of advancing contact angle plays a significant role on the behavior of P_c curves. The hysteresis between primary drainage and secondary imbibition P_c curves grows with the increment of θ_A^{mw} (e.g., Masalmeh, 2001; Al-Futaisi and Patzek, 2003). P_c is positive until 90° resulting in spontaneous imbibition. By the increase of θ_A^{mw} from 0° to 90° , P_c curves get flatter and closer to $P_c = 0$ line (80° - 90° , 89° - 91° in **Fig. 7.1**) When θ_A^{mw} exceeds 90° , P_c goes below $P_c = 0$ line and since then forced imbibition commences in the medium. With the further increase of θ_A^{mw} from 120° through 180° , the breakthrough P_c during forced imbibition drops to lower values (-5.57 kPa for $\theta_A^{mw}=170^\circ$ - 180°). Accordingly, imbibition P_c curve mirrors (i.e. is analogous to) the primary drainage curve more and more at greater advancing angle ranges (Kovscek et al., 1993; Al-Futaisi and Patzek, 2003).

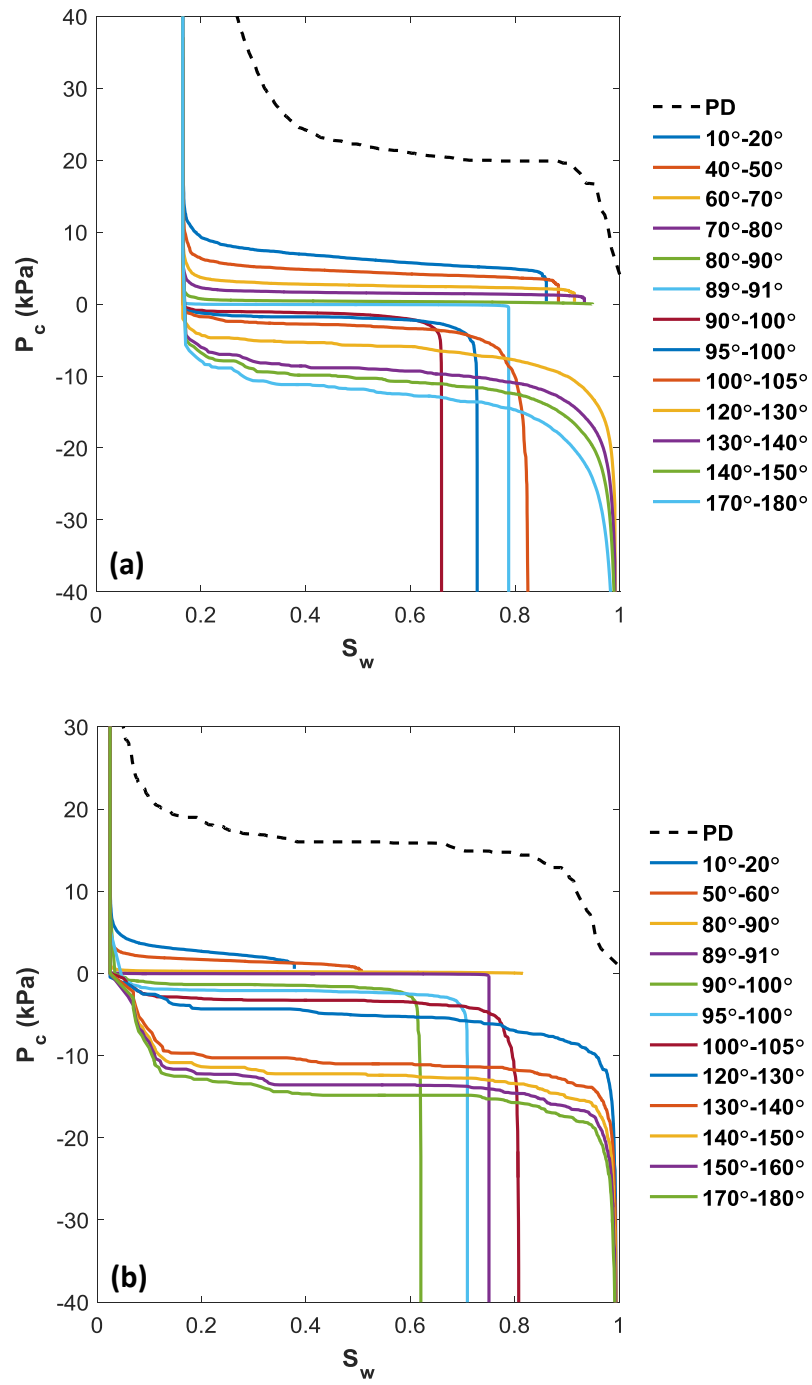


Figure 7.1 – Secondary imbibition P_c curves of a) C013 and b) C019 as a function of advancing contact angle.

The residual oil saturation S_{or} and the pore-level displacement events experienced in nodes and links for each average θ_A^{mw} case are summarized in **Figs. 7.2** and **7.3**, respectively. The results clearly illustrate the strong impact of surface wettability (θ_A^{mw}) on residual oil and the change in pore-level events. As said before, snap-off is the dominant mechanism for oil entrapment in strongly water-wet conditions (Dullien, 1992). During spontaneous imbibition, snap-off displacement in links is replaced by piston-type advance through the transition from strongly to weakly water-wet conditions (see Lso and Lpt from 0° to 90° in **Figs. 7.3a** and **7.3b**). In **Fig. 7.2**, by the increase of θ_A^{mw} , S_{or} decreases until around 90° due to inhibited snap-off events and better connection of both oil and water phases through piston-type flow in links. Higher oil recovery is therefore achieved in weakly water-wet systems than in strongly water-wet systems similar to those experimentally reported for sandstone core samples by Morrow et al. (1986). Snap-off is completely suppressed all beyond θ_A^{mw} of 90° , because during forced imbibition, it has virtually never happened due to its quite low capillary entry pressure as compared to piston-type flow.

In **Fig. 7.2**, there is a sharp jump in S_{or} right after 90° which is the result of switch from spontaneous to forced imbibition without intermediate oil layers. Approximately between 90° and 100° , as average advancing contact angle is not generally enough to satisfy the geometric condition for oil layer formation ($\theta_A^{mw} \geq 90^\circ + \beta_i$), forced piston-type displacement causes dendritic oil clusters in the medium. It reflects the weakly oil-wet systems resulting in extremely large residual oil ($S_{or} > 0.4$) and hence very poor recovery. However, some oil layers in the sharpest corners are allowed to be created even for advancing angles close to 90° ($Npt+ol$ and $Lpt+ol$ in **Figs. 7.3a** and **7.3b**). From weakly to strongly oil-wet conditions, layer formation increasingly continues and hence S_{or} decreases gradually. When the extent of advancing contact angle meets the geometric requirement, i.e. when θ_A^{mw} reaches around 125° in our model, almost all forced piston-type events give rise to oil layer

creation (**Fig. 7.3**). After the average advancing contact angle of 125° , the curves representing piston-type events with oil layer formation in **Figs. 7.3a** and **7.3b** (N_{pt+ol} and L_{pt+ol}) coincides with the total piston-type events (N_{pt} and L_{pt}), i.e. almost all piston-type water invasion into the pores create at least one intermediate oil layer near the corner. Referring to **Section 5.2.2.3**, due to decrease in critical capillary pressure for oil layer collapse at larger θ_A^{mw} , oil layers persist until a more negative capillary pressure (with a greater absolute value) during imbibition (Blunt, 1997b). The oil layers enhance oil connectedness, thus there is almost no oil left in the medium for average $\theta_A^{mw} > 125^\circ$ in **Fig. 7.2**. The change in residual oil saturation S_{or} with respect to advancing contact angle θ_A^{mw} in mixed-wet systems, indicated in **Fig. 7.2**, exhibits a similar trend to the relation between S_{or} and θ_A^{mw} in the sensitivity studies of Al-Futaisi and Patzek (2003; **Fig. 2.8**) conducted on a sample of Bentheimer sandstone and of Blunt (1997b; **Fig. 2.6**). The similarity of our S_{or} vs θ_A^{mw} curves is much more with the former study, because in the former study arbitrary triangles were used for pore cross-section approximation as in our model while in Blunt's study (1997b), square pore elements were used in which case snap-off was no longer possible beyond a contact angle θ_A^{mw} of 45° .

To sum up, advancing contact angle effect on S_{or} asserts that the greatest oil recovery is possible in strongly oil-wet media ($\theta_A^{mw} > 125^\circ$) by means of oil layer drainage. However, although theoretically strongly oil-wet reservoirs offer the greatest recovery, in the light of previous pore-scale modeling studies on wettability effects (Anderson, 1987b; Dixit et al., 1999), weakly water-wet systems are considered more productive in the short term. Because oil layers have very low conductivity, the recovery process after breakthrough occurs very slowly at more negative capillary pressures (Kovscek et al., 1993). Consequently, as clearly showed in **Fig. 2.7** of Blunt's waterflooding recovery curves for four flow regimes with different wettabilities (1997b), more than 100 pore volumes of water injection is required in a strongly oil-wet medium to reach greater oil recovery than in a weakly water-wet system.

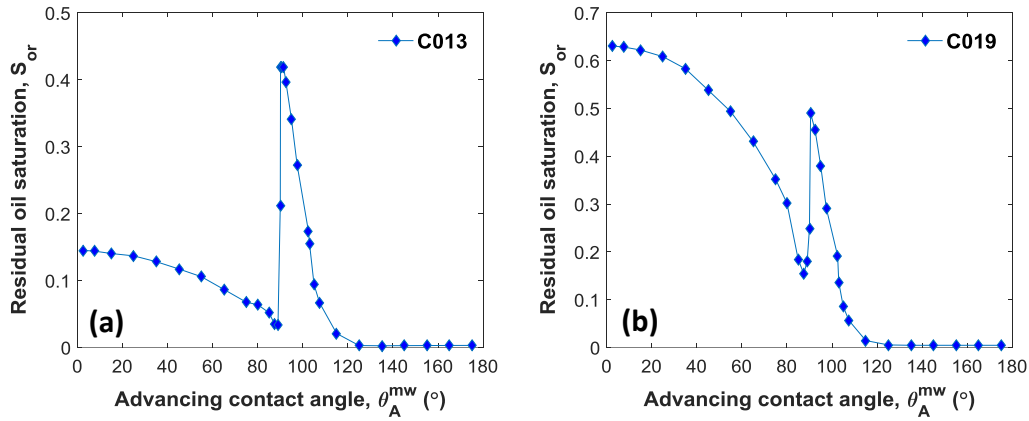


Figure 7.2 – Residual oil saturation in a) C013 and b) C019 as a function of advancing contact angle during secondary imbibition.

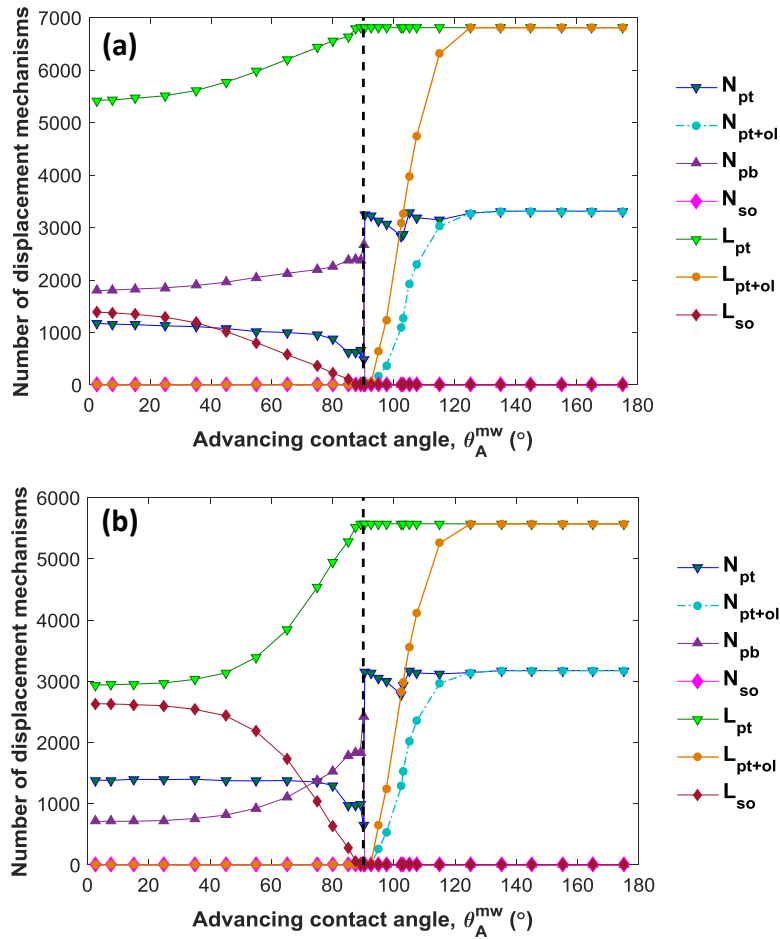


Figure 7.3 – Secondary imbibition pore-level displacement events in a) C013 and b) C019 in response to average advancing contact angle (N: node, L: link, pt: piston-type, pb: pore-body filling, so: snap-off, ol: oil layer).

7.2 Effect of receding contact angle during secondary drainage

The strong effect of advancing contact angle on secondary imbibition is investigated in the previous section. As mentioned earlier, due to contact angle hysteresis, the receding contact angle in mixed-wet pores θ_r is not the same with primary receding contact angle θ_R of initially water-wet medium. The receding contact angle after ageing θ_r depends on both primary receding angle and advancing angle ($\theta_R < \theta_r < \theta_A$), thus the macroscopic properties and flow behavior during secondary drainage will also change accordingly. In the network model, θ_r is randomly selected between θ_R and θ_A^{mw} for each mixed-wet pore. Since θ_R is constant, θ_r changes with respect to the change in θ_A^{mw} . The model-derived linear relationship between the average advancing angle and its corresponding average receding angle in mixed-wet pores is given in **Fig. 7.4**. From the resulting curve, the maximum degree of receding contact angle in mixed-wet pores is nearly 90° .

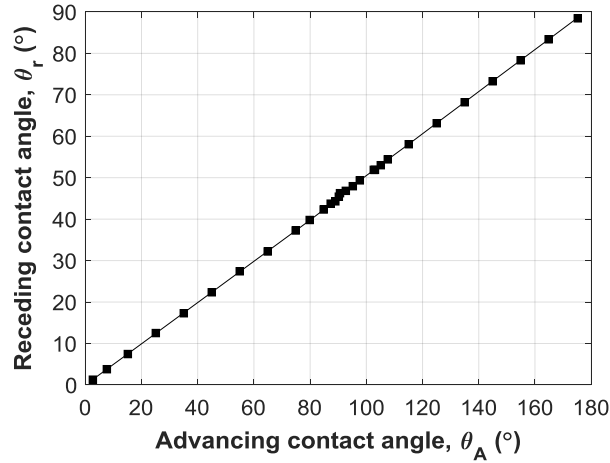


Figure 7.4 – The average advancing contact angle with its corresponding average receding contact angle in mixed-wet pores.

The variability of irreducible water saturation S_{wirr} at the end of secondary drainage in response to the receding contact angle is plotted in **Fig. 7.5** together with initial water saturation S_{wi} of 0.166 and 0.02 for C013 and C019 respectively (red lines

on **Fig. 7.5**). Besides, the number of spontaneous and forced piston-type events and available water oil layers at each receding angle range are demonstrated in **Fig. 7.6** in order to explain the trend of irreducible water saturation in **Fig. 7.5**. According to **Fig. 7.6**, while θ_r up to 45° is only dominated by forced drainage, spontaneous drainage also takes place increasingly afterwards.

Based on **Fig. 7.5**, S_{wirr} decreases until θ_r of 40° - 55° corresponding to θ_A^{mw} of around 90° (**Fig. 7.4**). Observe from **Fig. 7.6** that for θ_r smaller than 45° (θ_A^{mw} smaller than 90°), only forced piston-type drainage occurs and since the geometric condition of $\theta_A \geq 90^\circ + \beta_i$ is not satisfied in any corner, no oil layers exist in the network. Therefore, the water-filled mixed-wet pores are all in Configuration E prior to oil re-invasion (**Fig. 5.19**). Due to dominant snap-off mechanism at low θ_A^{mw} , especially in C019, significant amount of trapped oil is left in the network. This trapped oil disrupts water continuity to be swept through the outside during water displacement via secondary oil flooding and much more nodes and links remain water-filled compared to primary drainage. This situation is indicated in **Fig. 7.5** where the difference between S_{wirr} and S_{wi} is the highest at the lowest θ_r for the water-wet media ($\theta_r < 45^\circ$). In addition to the remaining water-filled pores which is the prominent reason for S_{wirr} , as described in **Section 5.2.3**, if the displacement occurs from Configuration E to H (**Fig. 5.19**), corner water volume increases after oil re-entry since the distance to apex L_i will be longer than the pinned menisci distance of primary drainage case $L_{pd,i}$ (Configuration H vs D in **Fig. 5.19**). However, the increase in corner volume has minor effect in irreducible water saturation when compared to water-occupied pores left after secondary drainage. During the increase of θ_r from 0° through 45° , owing to less oil trapping and less frequent displacement from E to H (**Fig. 5.19**), S_{wirr} gets closer to S_{wi} in **Fig. 7.5**.

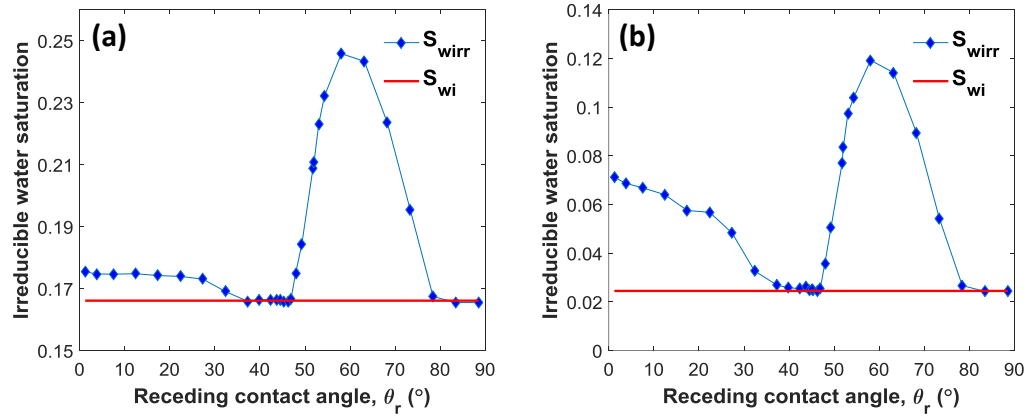


Figure 7.5 – Irreducible water saturation in a) C013 and b) C019 as a function of receding contact angle during secondary drainage with constant S_{wi} of 0.166 and 0.02 (red lines).

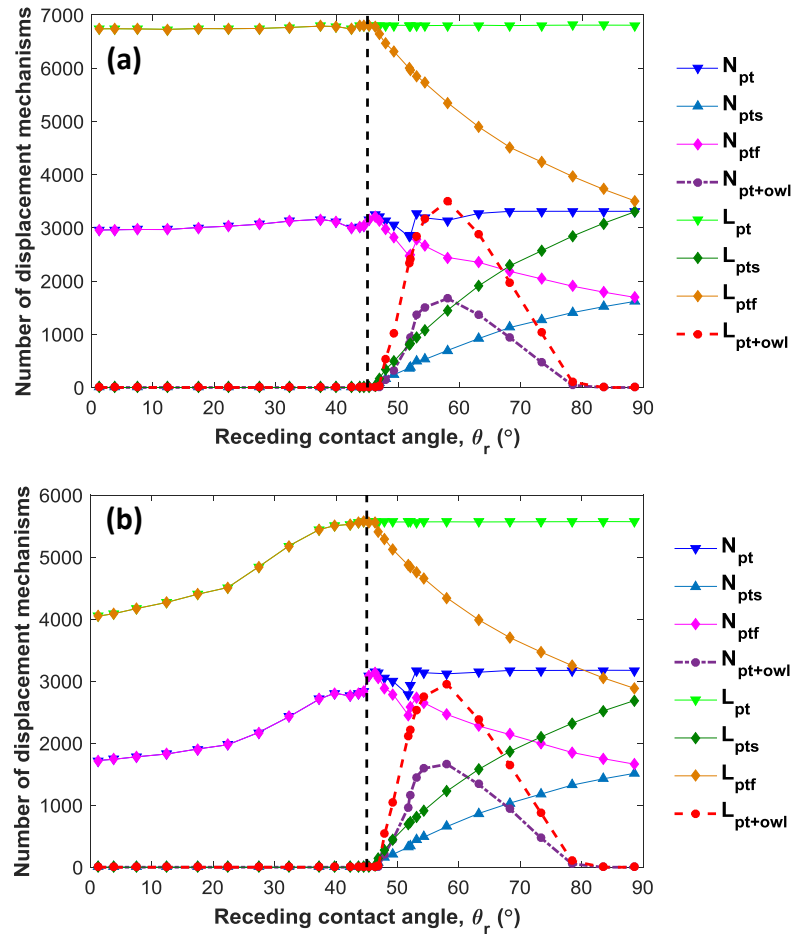


Figure 7.6 – Secondary drainage pore-level displacement events in a) C013 and b) C019 in response to average receding contact angle (N: node, L: link, pt: piston-type, s: spontaneous, f: forced, owl: oil and water layers).

As discussed in the previous section, for $\theta_A^{mw} > 90^\circ$, oil layers begin to form during forced imbibition. In case oil layers are present prior to oil re-invasion (Configuration G in **Fig. 5.19**), when geometric requirement of $\theta_r < 90^\circ - \beta_i$ is satisfied and the network pressure does not exceed the maximum allowable pressure for layer stability ($P_c^e < P_{c,i}^{stab}$ in **Eq. 5.61**), water layers are formed in the mixed-wet pores (Configuration I in **Fig. 5.19**). According to **Fig. 7.5**, the irreducible water saturation increases progressively from 45° until 60° and then reduces again to S_{wi} level at around 80° . This trend is well-correlated with water layer occurrence shown in **Fig. 7.6**. By the formation of water layers for $\theta_r > 45^\circ$, S_{wirr} increases since many water layers are stable within the range of imposed capillary pressure at the end of secondary drainage process. The maximum number of water layers exists at around θ_r of 60° since both θ_A^{mw} ($\sim 120^\circ$) and its corresponding θ_r (**Fig. 7.4**) have the highest suitability for oil and water layer formations, respectively. For the presence of at least one water layer in the sharpest corner of a pore element, the condition $\theta_r < 90^\circ - \beta_1$ must be met (**Section 5.2.3.1**). From **Fig. 5.4**, the smallest corner half-angle β_1 changes in the range of 4° to 20° but mostly below 10° in our network systems. Therefore, water layer formation is geometrically almost impossible for $\theta_r > 80^\circ$ (N_{pt+owl} and L_{pt+owl} trends in **Fig. 7.6**) which leads to nearly the same water saturation as primary drainage (**Fig. 7.5**). For $\theta_r > 80^\circ$ without water layers, if the maximum capillary pressure is not limited ($P_{c,sd}^{max} \leq P_{c,pd}^{max}$), it is possible to reach S_{wirr} less than S_{wi} due to the contact angle hysteresis ($\theta_r > \theta_R$). Furthermore, through the end of secondary drainage, both oil and water phases maintain their continuity across the network (Kovscek et al., 1993). The larger contact angle provides more pore drainage (smaller P_c^e) and also shrinkage of corner water saturation owing to the smaller distance of pinned oil-water interface to corner apex L_i (**Eq. 5.52**).

7.3 Effect of initial water saturation on transport properties and residual oil

The maximum capillary pressure reached at the end of primary drainage $P_{c,pd}^{\max}$ determines the initial water saturation and the rate of oil-migrated pores undergoing a pertinent wettability change. In our model, a minimum pore size limit is set at $0.711 \mu\text{m}$ where oil cannot intrude any pore smaller. In this section, in order to inspect the effect of residual water on the following imbibition and secondary drainage processes, S_{wi} is varied sequentially through gradual lowering of the imposed $P_{c,pd}^{\max}$ and all other parameters are kept constant. Several simulations are conducted to analyze S_{wi} effect under two different wettability conditions for C013 representing water-wet (20° to 55°) and oil-wet (120° to 155°) systems (Al-Futaisi and Patzek, 2004).

Capillary pressure curves produced at gradually lowered $P_{c,pd}^{\max}$ values in water-wet and oil-wet conditions are given in **Figs. 7.7** and **7.8** for C013, respectively. The resulting P_c plots prove that lower $P_{c,pd}^{\max}$ corresponds to larger initial water saturation S_{wi} at the end of primary drainage. Accordingly, each $P_{c,pd}^{\max}$ results in a network with a different degree of wettability. The change in mixed-wet fraction and endpoint saturations for a complete drainage-imbibition-secondary drainage cycle upon a controlled decrease in $P_{c,pd}^{\max}$ is listed in **Tables 7.1** and **7.2** for water-wet and oil-wet conditions, respectively. While f_{mw_N} and f_{mw_L} are the fractions of mixed-wet nodes and links, f_{mw} stands for the overall mixed-wettability ratio of the porous medium. For the purpose of visualization, the dependence of residual oil and irreducible water saturations on S_{wi} is shown for both wettability cases in **Fig. 7.9**. **Tables 7.1** and **7.2** reveal that oil succeeds to invade into fewer relatively small pores as $P_{c,pd}^{\max}$ lowers and thus the fraction of both mixed-wet nodes f_{mw_N} and f_{mw_L} decreases in the media which is consistent with Salathiel's (1973) experimental observations in mixed-wet

rocks. Besides, Jadhunandan and Morrow (1995) experimentally showed the increase in oil-wetness character of Berea sandstone by the reduction of its connate water saturation.

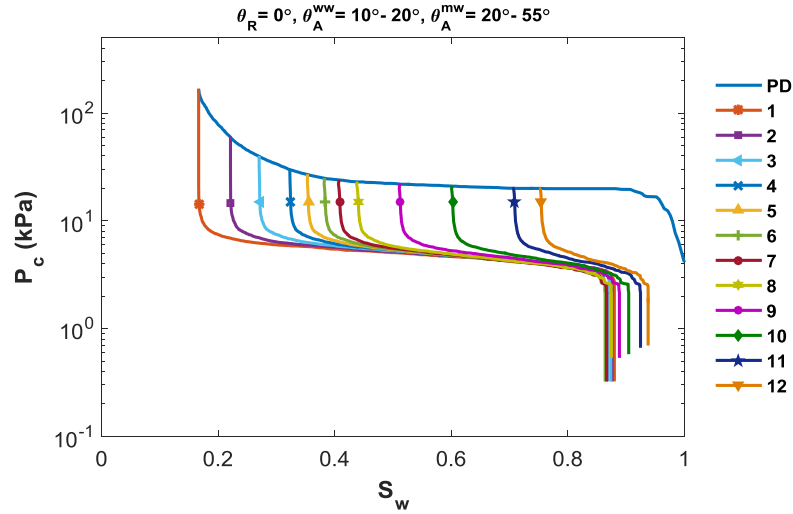


Figure 7.7 – Secondary imbibition P_c curves at varying $P_{c,pd}^{max}$ cases for water-wet system of C013.

Table 7.1 – Simulation results of a complete flooding cycle at varying $P_{c,pd}^{max}$ cases for water-wet system of C013.

Case	$P_{c,pd}^{max}$, kPa	f_{mw_N}	f_{mw_L}	f_{mw}	S_{wi}	S_{or}	$k_{rw} @ S_{or}$	S_{wirr}
1	168.19	0.999	0.631	0.719	0.166	0.120	0.596	0.174
2	60.74	0.996	0.552	0.658	0.220	0.124	0.579	0.224
3	40.07	0.988	0.483	0.603	0.269	0.127	0.583	0.272
4	30.17	0.962	0.416	0.546	0.320	0.133	0.561	0.331
5	27.08	0.936	0.380	0.512	0.350	0.135	0.527	0.365
6	25.00	0.900	0.341	0.474	0.379	<u>0.136</u>	0.523	0.416
7	24.04	0.863	0.316	0.446	0.404	0.134	0.558	0.491
8	23.06	0.805	0.286	0.410	0.436	0.125	0.647	0.521
9	22.04	0.682	0.233	0.340	0.509	0.112	0.983	0.580
10	21.04	0.538	0.176	0.262	0.599	0.096	1.000	0.799
11	20.06	0.385	0.119	0.182	0.706	0.076	1.000	0.842
12	20.00	0.322	0.098	0.151	0.752	0.062	1.000	0.855

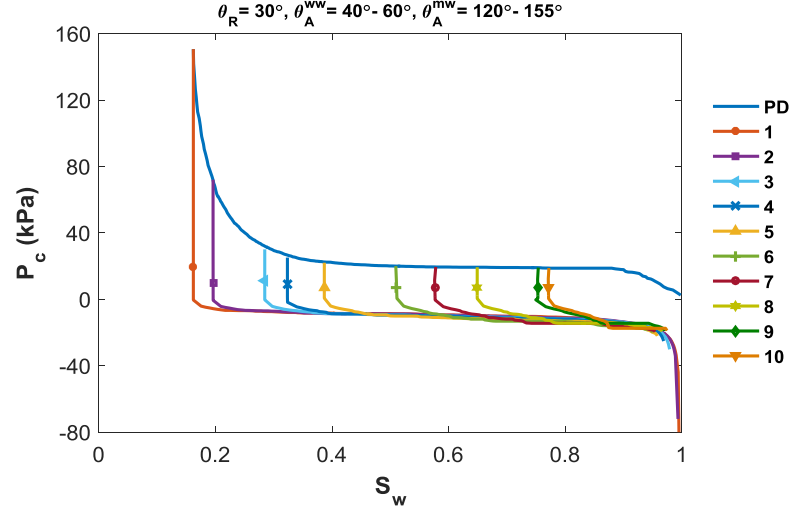


Figure 7.8 – Secondary imbibition P_c curves at varying $P_{c,pd}^{max}$ cases for oil-wet system of C013.

Table 7.2 – Simulation results of a complete flooding cycle at varying $P_{c,pd}^{max}$ cases for oil-wet system of C013.

Case	$P_{c,pd}^{max}$ (kPa)	f_{mw_N}	f_{mw_L}	f_{mw}	S_{wi}	S_{or}	$k_{rw} @ S_{or}$	S_{wirr}
1	150.66	0.999	0.630	0.718	0.162	0.002	0.998	0.182
2	72.01	0.998	0.580	0.679	0.196	0.007	0.993	0.213
3	30.09	0.974	0.439	0.566	0.296	0.021	0.970	0.302
4	25.14	0.936	0.384	0.515	0.339	0.031	0.917	0.342
5	22.04	0.851	0.311	0.440	0.404	0.042	0.887	0.406
6	20.00	0.669	0.224	0.330	0.509	<u>0.050</u>	0.950	0.512
7	19.51	0.575	0.187	0.279	0.575	0.046	1.000	0.593
8	19.32	0.460	0.147	0.222	0.660	0.034	1.000	0.663
9	19.07	0.324	0.100	0.153	0.752	0.028	1.000	0.872
10	18.74	0.156	0.044	0.071	0.880	0.013	1.000	0.880

Based on the simulation results, S_{or} increases up to a certain $P_{c,pd}^{max}$ (25 kPa for water-wet system in **Table 7.1** and 20 kPa for oil-wet system in **Table 7.2**). The residual oil saturation S_{or} increases against large decrease in $P_{c,pd}^{max}$. For low S_{wi} , the increase of S_{or} in parallel to S_{wi} validates the experimental findings of Salathiel (1973) and modeling study of Blunt (1997b). Since the majority of the system has undergone wettability change at lower S_{wi} (i.e. larger f_{mw}), oil phase better spans mixed-wet

surfaces and maintains strong continuity throughout the network. This results in less S_{or} accompanied by higher network permeability to water (endpoint k_{rw} in **Tables 7.1** and **7.2**).

It is described in **Section 5.2.2** that the corner arc menisci in a mixed-wet pore are pinned at the location they attained at $P_{c,pd}^{\max}$. The length of pinned oil-water menisci to corner apex prior to water imbibition $L_{pd,i}$ is a function of receding contact angle and $P_{c,pd}^{\max}$ as well as pore corner geometry (β_i) (**Eq. 5.30**). As $P_{c,pd}^{\max}$ decreases, the corner menisci settle further away from the pore corners and $L_{pd,i}$ increases. In both water-wet and oil-wet cases, this leads to larger corner water saturation. In addition, for oil-wet case, oil layer presence depends on $L_{pd,i}$ (or $P_{c,pd}^{\max}$ in **Eq. 5.43**). Because the critical capillary pressure for layer stability $P_{c,i}^{crit}$ increases in response to decrease in $P_{c,pd}^{\max}$, oil layers remain stable for a narrower P_c range and hence more oil trapping occurs. It is noticeable in **Fig. 7.9** that S_{or} increase in oil-wet network (from 0.002 to 0.050 in **Table 7.2**) is more prominent than S_{or} increase in water-wet network (from 0.120 to 0.136 in **Table 7.1**) due to the effect of inhibited oil layer existence in oil-wet case.

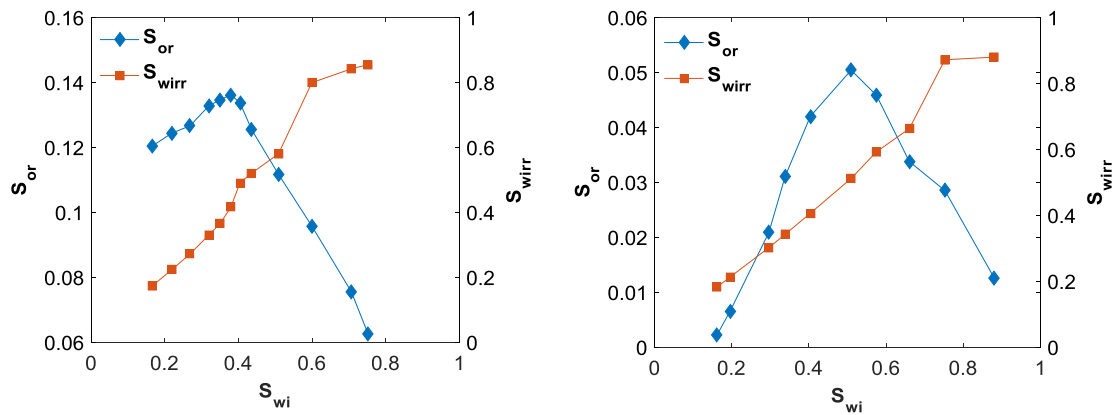


Figure 7.9 – The change in S_{or} and S_{wirr} in response to S_{wi} for a) water-wet and b) oil-wet systems of C013.

Further increase of S_{wi} decreases S_{or} for both wettability conditions as shown in **Fig. 7.9** (after 0.379 for water-wet case in **Table 7.1** and 0.509 for oil-wet case in **Table 7.2**). Because oil saturation severely decreases at the end of primary drainage ($1 - S_{wi}$), it is easier to displace this small amount of oil from the network during imbibition. Several network modeling studies confirm our model-derived S_{or} versus S_{wi} relation. For instance, similar behavior of S_{or} as a function of S_{wi} is observed in modeling studies of Blunt (1997b) and of Kallel et al. (2015) studying two network systems, namely a homogeneous Berea sandstone and a heterogeneous microporous carbonate. Lastly, the irreducible water saturation S_{wirr} also increases with the reduction in $P_{c, pd}^{\max}$ and is always larger than S_{wi} due to the presence of more water-filled pores, the increase in corner water volume in oil-invaded pores and the remaining water layers (for oil-wet case) at the end of secondary drainage (see **Fig. 7.5**).

7.4 Effect of mixed-wettability fraction on transport properties and residual oil

In the previous part, the effect of S_{wi} on the mixed-wet fraction of the porous medium and accordingly endpoint saturations and k_{rw} is probed for a drainage-imbibition-secondary drainage cycle under water-wet and oil-wet conditions. While S_{wi} is a limiting factor for the extensity of mixed-wet pores in the network, the rate of ageing in readily oil-drained pores following primary drainage is also one of the major determinants of medium wettability. It is mentioned in **Section 5.2.1.1** that the pore walls of an oil-invaded pore away from the corners undergo wettability reversal when the critical capillary pressure of surface water films exceeds the maximum disjoining pressure (Kovscek et al., 1993). In our fundamental model, all the oil-migrated pores are assumed to be exposed to water film rupture and assigned as mixed-wet thereafter. The resulting mixed-wet fractions of carbonate networks are given in **Table 6.3**. Based on the scenario of Kovscek et al. (1993), the surface water films coating the large pores are thick and thus mineral surfaces are not exposed to wettability change. Besides, water-

filled pores (mostly micropores) always remain water-wet. Then, only the intermediate-sized pores experience wettability change after pristine drainage. In this section, the effect of the extent of wettability alteration will be analyzed for C013 network under a large contact angle hysteresis ($\theta_A^{ww} = 40^\circ\text{--}60^\circ$ and $\theta_A^{mw} = 125^\circ\text{--}170^\circ$). Here, two different scenarios are examined to inspect the behavior of two-phase flow: mixed-wetness fraction is varied in nodes and links together in the first part and in nodes alone in the second part.

In the first part, oil-occupied nodes and links following primary drainage are correlated with their sizes (inscribed radii) to decide on whether their surface wettability is altered or not. In this scenario, oil-filled pores larger than a specified threshold size and the already water-filled pores remain water-wet while the others become mixed-wet. The simulations at discrete maximum size limits above which oil-filled pores remain water-wet are summarized in **Table 7.3**. In **Fig. 7.10**, the resulting secondary imbibition P_c and k_r curves under different f_{mw} cases are demonstrated. As the allowable size boundary for wettability change declines at each case in **Table 7.3**, f_{mw_N} and f_{mw_L} decrease stepwise. The first case in **Table 7.3** is our existing model where only water-filled micropores and their surrounding nodes remain water-wet. In the last case (10th), the system is accepted entirely water-wet ($f_{mw} = 0$). Therefore, P_c curve never drops below $P_c = 0$ line in **Fig. 7.10a**. According to the trend of P_c curves in **Fig. 7.10a**, as oil-wetness increases (i.e. f_{mw}), saturation range of spontaneous imbibition is shrunk and correspondingly forced imbibition covers a wider saturation range. As f_{mw} steps up, the upper size boundary of mixed-wet pores increases and hence forced imbibition starts earlier, i.e. at a greater negative P_c (smaller in absolute value) from the former one. This is the reason for shortening of transition period from spontaneous to forced imbibition in response to increase in f_{mw} in **Fig. 7.10a**.

Table 7.3 – Simulation results of a complete flooding cycle at varying f_{mw} cases for oil-wet system of C013.

Case	R , E-6 (m)	f_{mw_N}	f_{mw_L}	f_{mw}	S_{or}	$k_{rw} @ S_{or}$	S_{wirr}
1	Model	0.999	0.630	0.718	0.002	1.000	0.174
2	15	0.994	0.630	0.717	0.013	0.988	0.172
3	12	0.981	0.630	0.714	0.024	0.935	0.172
4	10	0.934	0.624	0.698	0.035	0.895	0.171
5	9	0.853	0.610	0.668	0.054	0.807	0.176
6	8	0.734	0.586	0.621	<u>0.056</u>	0.811	0.168
7	7	0.604	0.555	0.567	0.050	0.850	0.171
8	5	0.318	0.467	0.432	0.041	0.883	0.168
9	4	0.117	0.348	0.293	0.030	0.927	0.165
10	–	0	0	0	0.098	0.620	0.167

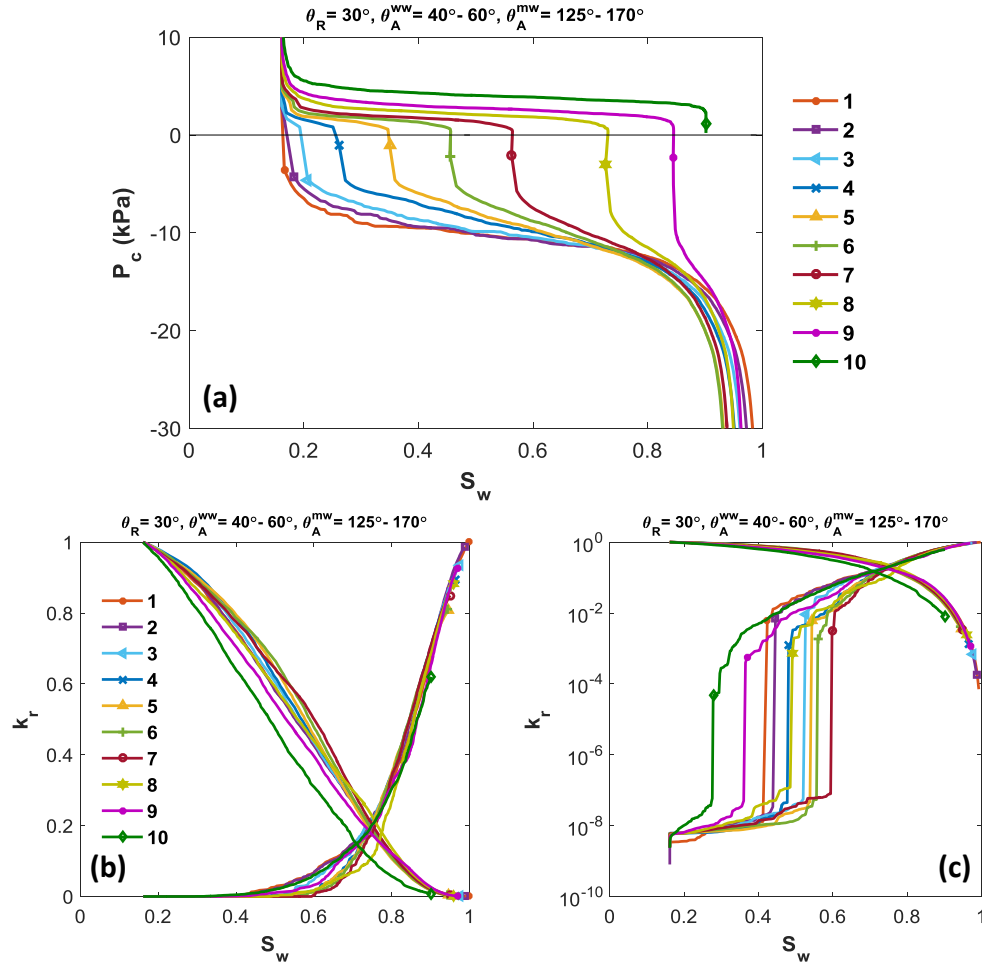


Figure 7.10 – Secondary imbibition P_c and k_r curves at varying f_{mw} cases for oil-wet system of C013.

According to **Table 7.3**, S_{or} has a local maximum at completely water-wet case (0.098 at $f_{mw} = 0$) due to dominant snap-off mechanism ($\theta_A^{ww} = 40^\circ$ - 60°). Again in **Table 7.3**, the minimum S_{or} is in our fundamental model which is the most oil-wet case ($f_{mw} = 0.793$). Due to micropores which remain water-filled throughout all flooding cycles, the mixed-wet fraction never reaches unity in the model. Owing to almost no trapped oil in our original model (1st case in **Table 7.3**), water continuity is undamaged by the isolated oil blobs and so endpoint k_{rw} reaches one. From latter to former cases for mixed-wet conditions in **Table 7.3** (from 9th to 1st case), by the increase of f_{mw} , S_{or} grows up to 0.056 until oil-wet regions span throughout the network (Blunt, 1997b). Then, the well-connectivity between oil-wet surfaces and accordingly between intermediate oil layers allows S_{or} to drop until almost zero in the model ($S_{or} = 0.002$ for 1st case in **Table 7.3**). In **Table 7.3**, the endpoint k_{rw} changes parallel to residual oil saturation of the system. A case with larger S_{or} corresponds to relatively low k_{rw} and k_{ro} at the same S_w (**Figs. 7.10b**) due to phase discontinuities inside the network as a result of trapped oil and lack of interconnected oil layers. For instance, k_{rw} and k_{ro} curves of the completely water-wet medium (10th case in **Table 7.3**) lie at the outermost of all in **Fig. 7.10**, i.e. completely water-wet case has generally the lowest k_{rw} and k_{ro} values throughout the imbibition process. In addition, the irreducible water saturation of secondary drainage S_{wirr} is greater than the initial water saturation S_{wi} for each case (**Table 7.3**).

The impact of fractional wettability (f_{mw}) on residual oil saturation S_{or} is also evaluated in Gharbi and Blunt's (2012) pore network modeling study for a set of six carbonate samples, two of which were from a deep saline Middle East aquifer. Similar to our findings, S_{or} tends to increase in response to decrease in f_{mw} . Beginning from a fully water-wet condition, S_{or} reaches its maximum at weakly mixed-wet case $f_{mw} =$

0.25 and then declines sharply to very low saturations as oil-wetness increases. For $f_{mw} \geq 0.75$, oil is produced efficiently due to large numbers of oil layers in the medium.

In the second part of this section, the influence of only mixed-wet fraction of the nodes is investigated on flooding cycle. In this scenario, since links are always smaller than their connected nodes, the wettability of the links is kept constant and the extent of wettability alteration in nodes is studied depending on their pore classes (PC). As given in **Table 7.4**, the wettability distribution of nodes is changed sequentially starting from the existing model where almost all nodes are mixed-wet (f_{mw_N} in **Table 6.3**). Then, each following case is conducted by adding the next largest pore class nodes to the former water-wet population. In the last case, all nodes are assigned as water-wet ($f_{mw_N} = 0$).

Figure 7.11 illustrates the resulting P_c and k_r curves under different f_{mw_N} cases. **Figure 7.11a** indicates that with the increase of water-wet nodes in the system, spontaneous imbibition interval widens. For the 1st case in **Table 7.4** representing our actual model, because the only water-wet pores in the network are micropores (PC1 links) and they are already water-filled, water invasion starts directly into mixed-wet pores. Therefore, spontaneous imbibition does not occur in our base model (**Fig. 7.11a**). S_{or} changes parallel to the rate of mixed-wettability and accordingly to spontaneous imbibition. Spontaneous imbibition in water-wet nodes accounts for large residual oil. By the increase in water-wetness in node elements, S_{or} increases around two orders of magnitude (from 0.002 to 0.186 in **Table 7.4**). According to **Figs. 7.11b-c**, the cross-point between k_{rw} and k_{ro} curves shifts to left side as water-wetness increases. The endpoint k_{rw} (at S_{or}) decreases in response to the rise in S_{or} (**Table 7.4**). In **Figs. 7.11b-c**, k_{ro} curve for water-wet case lie at the outermost due to larger trapped oil. Again S_{wirr} exceeds S_{wi} in each case mostly as a result of additional water-wet nodes and intermediate water layers remained stable until the end of secondary drainage (**Table 7.4**). Besides, S_{wirr} declines through less mixed-wet cases due to less water layer presence in the medium after secondary drainage.

Table 7.4 – Simulation results of a complete flooding cycle at varying f_{mw_N} cases for oil-wet system of C013.

Case	N_{ww}	f_{mw_N}	f_{mw_L}	f_{mw}	S_{or}	$k_{rw} @ S_{or}$	S_{wirr}
1	Model	0.999	0.630	0.718	0.002	1.000	0.182
2	PC6	0.896	0.630	0.693	0.024	0.943	0.179
3	PC5-6	0.690	0.630	0.644	0.058	0.803	0.179
4	PC4-6	0.666	0.630	0.639	0.062	0.781	0.178
5	PC3-6	0.606	0.630	0.624	0.075	0.746	0.178
6	PC2-6	0.450	0.630	0.587	0.112	0.607	0.174
7	PC1-6	0	0.630	0.480	0.186	0.417	0.172

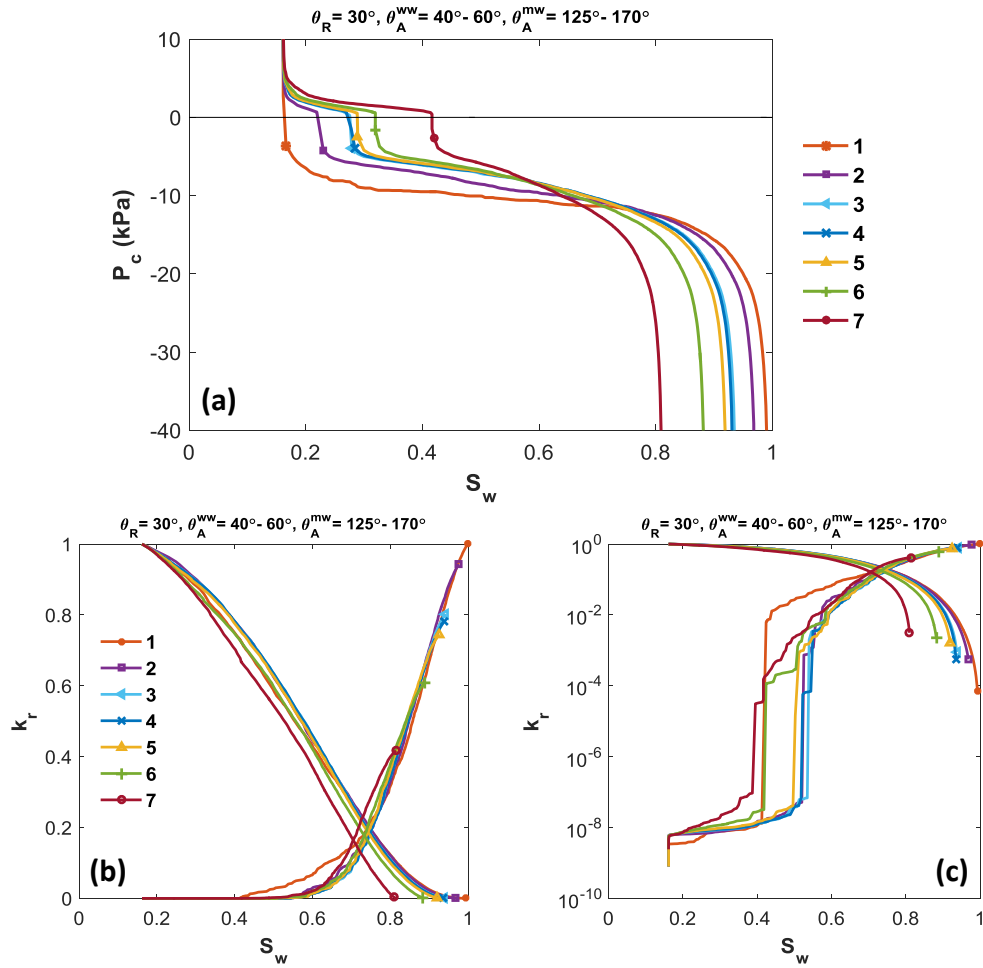


Figure 7.11 – Secondary imbibition P_c and k_r curves at varying f_{mw_N} cases for oil-wet system of C013.

7.5 Effect of the structural properties on transport properties and residual oil

In **Chapter 6**, the macroscopic flow properties of the carbonate samples have been discussed comparatively for different wettability cases. Under the same wettability conditions, most of the characteristic differences between P_c and k_r curves and residual saturations of carbonates are related to their aspect ratio, i.e. the ratio of large-sized nodes to small-sized links inside network. Aspect ratio has been used to correlate pore body size to experimental (MIP) throat size. It determines the overlap between pore body and throat size distributions. From our results, one can infer that one of most significant structural properties of a pore system is its aspect ratio (e.g., Jerauld and Salter, 1990). It plays a dominant role on flow regimes and oil recovery. Since aspect ratio has already been studied in the previous chapter, in the following subsections, the effects of other structural properties of the network, namely model size and pore shape are investigated to understand their influence on flow properties and residual saturation in a complete flooding cycle.

7.5.1 Network model size

In the current model, a cubic network system of model size $n=15$ is used for flow simulations. Because of the much more CPU time requirement of larger networks, the minimum model size overcoming end effects and enough to discern trends in flow properties is preferred (Jerauld and Salter, 1990; Xu et al., 1999; Jia et al., 2007). In order to test the dependency of our flow predictions on the variability of network sizes larger than 15 and to check the necessity for a larger model, the networks with $n=20$ ($20 \times 20 \times 20$) and $25 \times 15 \times 15$ are also assessed in this section.

For three networks with different model sizes, the predicted P_c and k_r curves of C013 and C019 under water-wet and oil-wet conditions (*Case 2* and *3* in **Table 6.4**) are given in **Figs. 7.12** and **7.13**, respectively. From the results, S_{or} is highly insensitive to models larger than $n=15$ verifying aforementioned preliminary works of Chatzis and Dullien (1985), Dullien et al. (1986), and Diaz et al. (1987) that the network sizes of 15

nodes per edge and greater is sufficient for sensible reproducibility of flow properties. Only S_{or} of C019 network in water-wet condition (**Fig. 7.12b**) decreases slightly (from 0.492 to 0.444) as model enlarges and accordingly its endpoint k_{rw} slightly reaches up while k_{ro} declines more than the others.

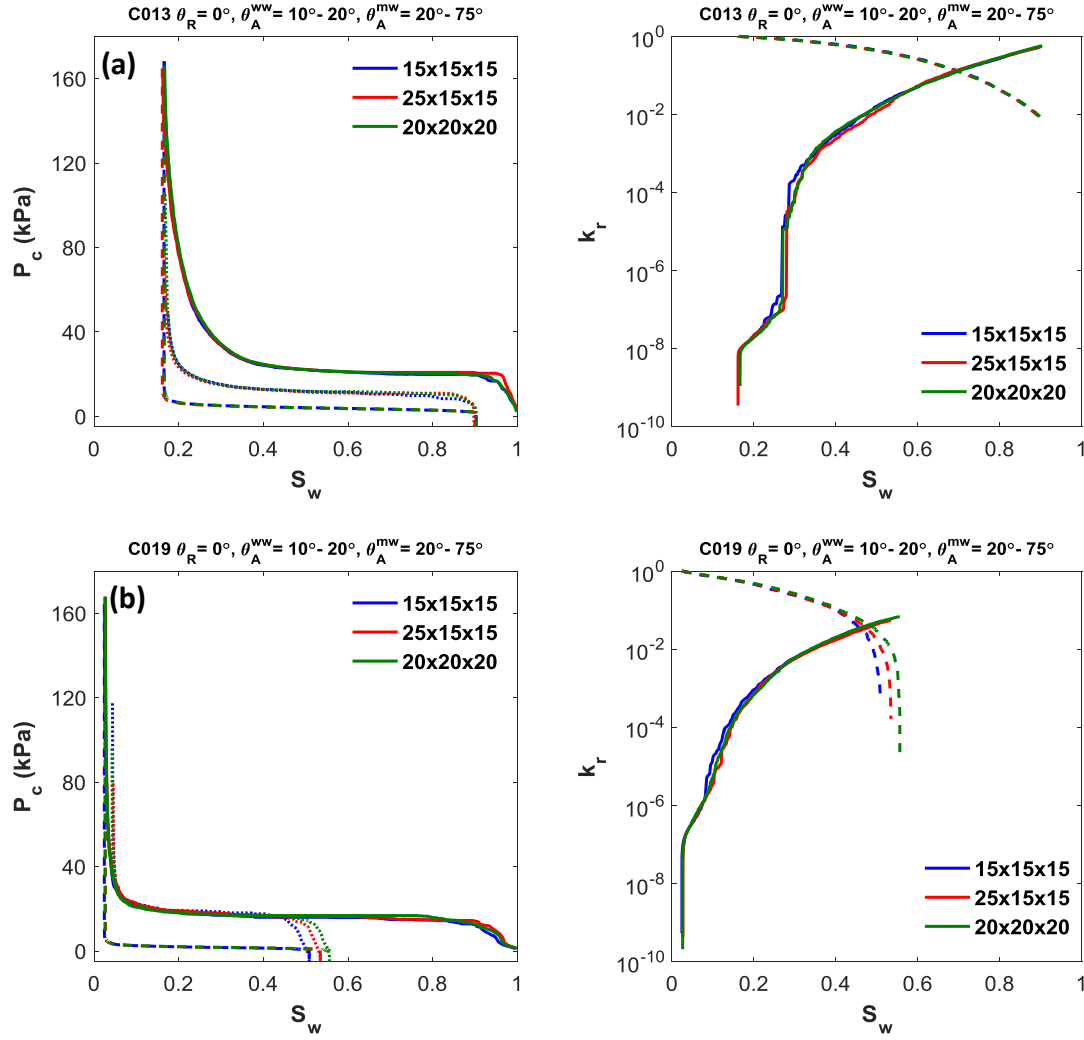


Figure 7.12 – P_c and k_r curves of water-wet networks with different model sizes for a) C013 and b) C019.

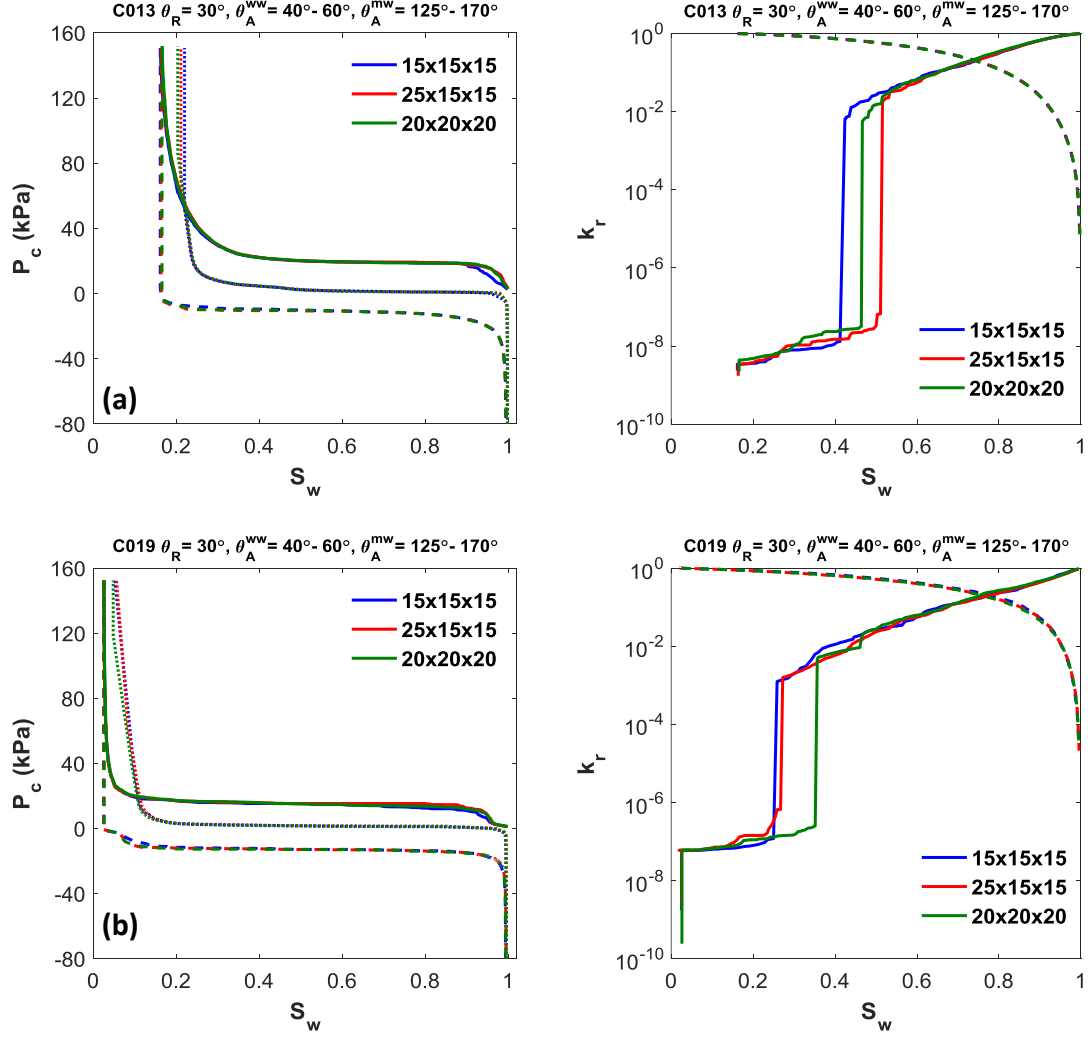


Figure 7.13 – P_c and k_r curves of oil-wet networks with different model sizes for a) C013 and b) C019.

On P_c curves during primary drainage, the first region from initial oil entrance to breakthrough point is the most sensitive region to the model size and boundary effects (Mohanty and Salter, 1982). In the beginning of primary drainage P_c curves, there are small fluctuations under water-wet and oil-wet conditions especially in C013 in response to change in model size (**Figs. 7.12a** and **7.13a**). Foremost, the statement of Mohanty and Salter (1982) is verified in our simulations that the longer networks have sharper turn from the first region to oil breakthrough point. It is remarkable in k_r curves of oil-wet media (**Fig. 7.13**) that the jump in k_{rw} associated with the enhanced water

continuity along the network first occurs in the smallest network. Referring to the number ratio of micropores (PC1) in **Table 5.1**, nearly the same initial water saturation S_{wi} is obtained for each case. Lastly, the irreducible water saturations S_{wirr} of networks with different model sizes are almost the same and close to S_{wi} in water-wet condition (**Figs. 7.12**). Contrarily, S_{wirr} in oil-wet networks all exceed their S_{wi} but slightly decrease as model size increases (**Table 7.13**). In summary, despite small variations in P_c and k_r curves, there is not a significant difference in flow predictions for the three networks whose sizes are greater than or equal to 15.

7.5.2 Shape factor

Referring to **Section 5.1.1**, shape factors are derived from SEM images of carbonate thin sections. The resulting shape factor histograms reveal that the majority of our carbonate pores are in the range of irregular triangles, i.e. $G < 0.048$ (**Fig. 4.26**). In our fundamental network, shape factors are arbitrarily assigned from the image-derived distribution data to the network pore elements (**Fig. 5.5b**). To test the variability in flow parameters against shape factor range of triangular pores, besides our original case [0.01,0.048], additional simulations are conducted at fixed shape factors of 0.048 and 0.024 where the former one stands for equilateral triangles and the latter one is the half of it (Al-Kharusi and Blunt, 2008). The corner half-angles for each shape factor range are plotted in **Fig. 7.14**. For each network with different shape factor range, water is allowed to retain in all the corners of oil-filled pores obeying the condition of $\theta_R + \beta_i < 90^\circ$. The half-angles in equilateral pores are almost the same and equal to 30° (**Fig. 7.14c**), while the largest discrepancy between half-angles in a single pore is observed for $G = 0.024$ (**Fig. 7.14b**).

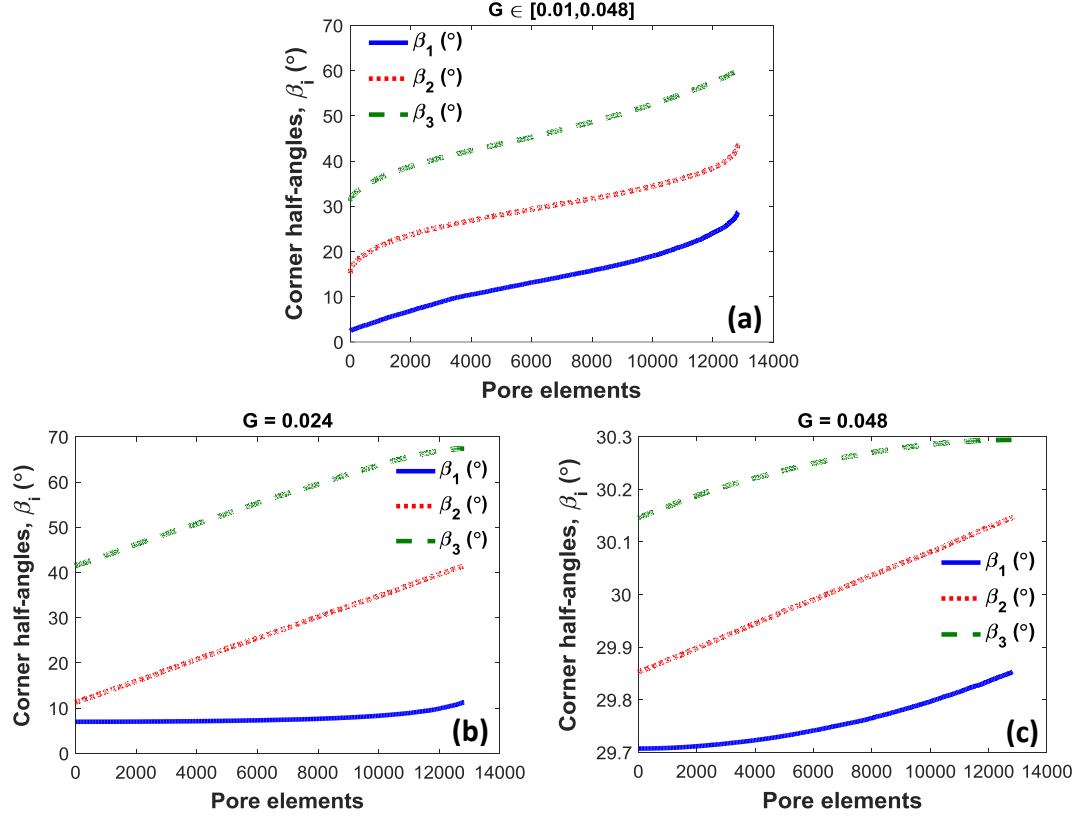


Figure 7.14 – Corner half-angles β_i of individual pore elements in ascending order for a) $G \in [0.01, 0.04811]$, b) $G = 0.024$, and c) $G = 0.048$.

Figures 7.15 and **7.16** compares the predicted P_c hysteresis curves and secondary imbibition k_r curves of C013 and C019 for different shape factor cases under water-wet and oil-wet conditions, respectively. In **Fig. 7.15**, while P_c curves of our base model match well with $G = 0.024$ case, the equilateral pores of $G = 0.048$ allow a lower residual oil saturation in water-wet conditions. It is shown in **Fig. 5.22** that as pore shapes in the network become more regular (i.e. as G increases), the capillary entry pressure P_c^e of spontaneous imbibition by piston-type displacement increases while P_c^e of snap-off reduces making piston-type flow more common than snap-off. Snap-off, the dominant mechanism in water-wet systems, is suppressed to a large extent for $G = 0.048$ since the smallest corner half-angle β_1 of pore throats is quite large at equilateral pores (30°) compared to highly sharp corners in other networks ($\beta_1^{\min} \approx 2.5^\circ$ for $G \in$

[0.01,0.048] and $\beta_1^{\min} \approx 7^\circ$ for $G = 0.024$ in **Fig. 7.14**). The reduction in β_1 increases the snap-off possibility as given in **Eq. 5.49**. The drop in S_{or} is more remarkable for C019 due to its greater potential for snap-off. Our observation of S_{or} decrease for more regular pore shapes in water-wet medium is inconsistent with Mason and Morrow's study (1991) in which less S_{or} is found for more irregular triangles. Based on k_r curves at water-wet case (**Fig. 7.15**), due to less residual oil in the medium, the networks with $G = 0.048$ reaches higher k_{rw} and lower k_{ro} at the endpoint (i.e. at $1 - S_{or}$).

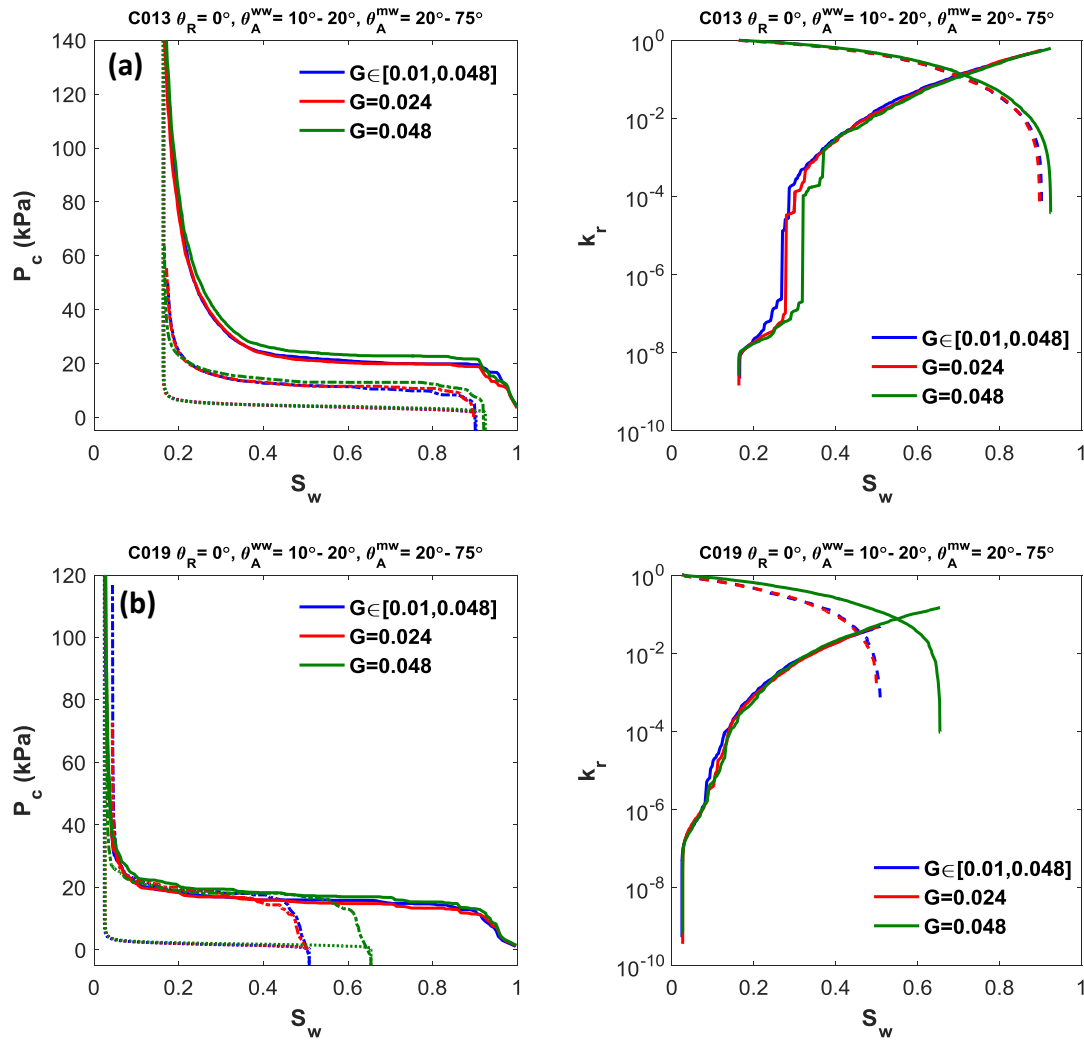


Figure 7.15 – P_c and k_r curves of water-wet networks with different shape factors for a) C013 and b) C019.

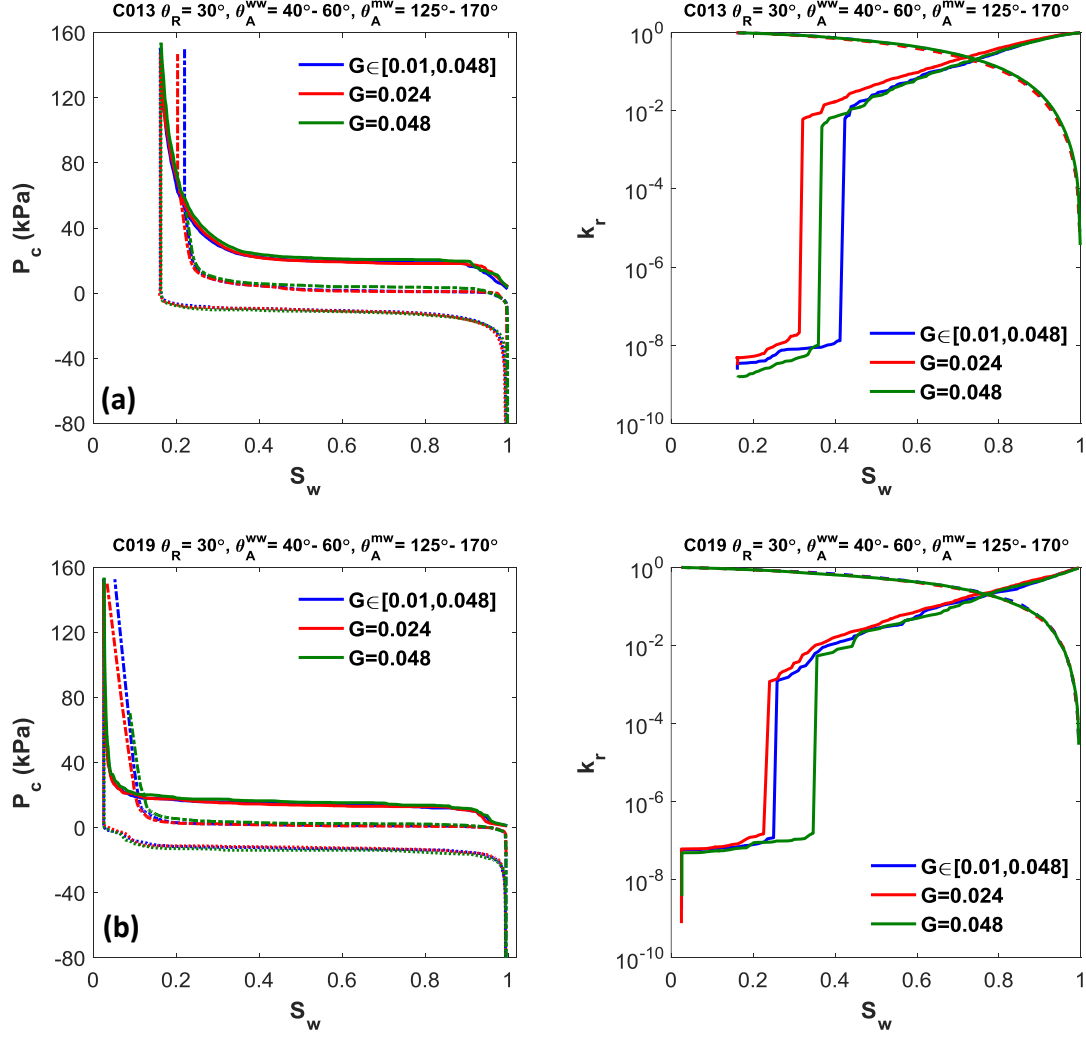


Figure 7.16 – P_c and k_r curves of oil-wet networks with different shape factors for a) C013 and b) C019.

In oil-wet conditions, there is not a significant variation in P_c hysteresis curves for both of the samples C013 and C019 as shown in **Fig. 7.16**. Due to oil layer presence in forced imbibition, S_{or} is almost zero at the end of water flooding. The irreducible water saturation S_{wirr} is a bit larger for our present model with $G \in [0.01, 0.048]$ due to the geometry of pore corners. As the smallest corner half-angle β_1 is the minimum in our model (**Fig. 7.14**), much more water layers are left in the network ($\theta_r < 90^\circ - \beta_1$) and this results in larger S_{wirr} at the end of secondary drainage. Secondary drainage is

completed at a smaller capillary pressure $P_{c, sd}^{\max}$ in the network of $G = 0.048$. Secondary imbibition k_{ro} curves of samples C013 and C019 for different shape factors match perfectly. The difference is observed in k_{rw} for $S_w < 0.4$ due to variation in the transition from the small-sized pores to larger pores with a sharp climb ($k_{rw} > 10^{-3}$) as a result of enhanced water continuity throughout the network.

For different ranges of triangle shape factors, the predictions of P_c and k_r curves are similar to each other especially for oil-wet case. S_{or} in water-wet case decreases for equilateral triangular pores due to inhibited snap-off mechanism. The sensitivity results indicate that the degree of pore geometry irregularity may have an important effect on the flow results under water-wet conditions, but for oil-wet case, the precise assignment of shape factor has a minor effect as long as triangular cross-section shape is assigned to individual pore network elements and water is allowed to be retained in the corners of oil-drained pores (Al-Kharusi and Blunt, 2008).

CHAPTER 8

CONCLUSIONS

In this thesis, a representative capillary-dominated network model for mixed-wet Middle East carbonates has been developed for the prediction of difficult to measure flow properties such as relative permeability. Our proposed model combines

- a detailed description of the carbonate pore structure,
- a reasonable characterization of wettability conditions and
- a full description of possible cross-sectional fluid configurations for two-phase flow with the appropriate pore-scale physics.

The major conclusions from our investigations of the newly developed model are summarized below.

Pore network characterization elements of complex, representative Middle East carbonate samples determined via SEM-based image analysis and physical core measurements provide the basis for future PNM studies of multiphase flow in carbonates. They are essential for a detailed representation of complex pore systems and serve to populate subsequent models. In contrast to conventional PNM studies, multiscale pore structure characterization and fundamental pore-throat classification approaches have been developed and used in the present work.

- Pore-size distributions obtained at two magnifications have been merged into a multiscale pore system by renormalizing 750X porosities to compensate for the missing large areas in the total 750X image area.
- The average coordination numbers predominantly range from 3 to 5.

- The cumulative distributions of shape factor indicate that triangle-shaped cross sections dominate the carbonate pore shapes.
- Based on a new proposed pore-throat classification approach, a strong spatial correlation is accepted between pore body and throat size distributions and 6 main pore-throat classes have been identified with their unique pore body- and throat-size ranges.
- The pore body to throat aspect ratio, calculated from weighted average pore body and throat sizes, is generally large (> 2.5) increasing the possibility of snap-off.

A pore-scale 3D cubic lattice is proposed as the basis of each carbonate pore network.

- Model size is chosen on the order of 15 nodes per edge. In sensitivity analysis, a significant change is not observed in flow predictions for the networks of $n \geq 15$.
- Irregular triangle-shaped cross-sections with $G \in [0.01, 0.04811]$ dominate the carbonate pore geometry. Sensitivity to the pore geometry irregularity is found to be rather large in water-wet systems while it has a minor effect in oil-wet media as long as triangular cross-section shape is used.
- Arranging the interconnected 3D network as a bundle of capillary tubes, network throat size distributions are modified by mercury intrusion data and the resulting models reveal the relative abundances of each pore class in carbonate networks.
- For the spatially correlated carbonate networks, the network-generated average aspect ratios are found to be 1.87, 2.13, 4.70, and 2.73 for C013, C016, C019, and C021, respectively.

In our representative network models, three consecutive fluid displacements, namely primary drainage with wettability alteration, secondary imbibition including spontaneous imbibition followed by forced imbibition (waterflooding), and lastly secondary drainage have been simulated. The resulting P_c and k_r curves display a significant dependency on the interaction of pore structure, wettability, and saturation history.

- The networks with larger microporosity (PC1 links) proportion are found to have lower absolute permeability. The model tends to overestimate the core-measured absolute permeabilities but still within the same order of magnitude.
- Micropores in our model ($R < 0.711 \mu\text{m}$) make the major contribution to the initial water saturation.
- Corner water saturation accounts for no more than 3% of the total pore volume despite its critical role in water continuity throughout the network.
- The primary drainage P_c and k_r curves show strong dependency on the pore structure (aspect ratio) and the pore-scale displacement processes.
- Wettability ($\theta_R \leq 50^\circ$) has a minor effect on the primary drainage P_c and k_r curves.
- The resulting mixed-wet fractions of carbonate networks change from 0.63 to 0.71. While almost all pore bodies are exposed to wettability change, approximately one third of the throats are never contacted by oil and remain water-wet.

The secondary imbibition simulations are conducted mainly at three different wettability levels: water-wet, intermediate-wet, and oil-wet cases. Here, the wettability levels refer to the contact angles of wettability-altered (aged) surfaces in mixed-wet pores right after oil migration. The results indicate that the wettability effects on P_c and k_r curves, residual oil S_{or} and the pore-level displacement mechanisms may be quite substantial.

- During spontaneous imbibition, snap-off becomes dominant in the systems with high aspect ratio and results in larger trapped oil.
- During forced imbibition, snap-off is completely inhibited and only piston-type displacement occurs.
- In forced imbibition, with the increase in contact angle hysteresis, a significant increase in oil layers formation occurs on the corners of mixed-wet pores.

- The geometrically based oil layers existence scenario (Blunt, 1997b) produces near-zero oil residuals ($< 0.6\%$) for strongly oil-wet cases ($\theta_A^{mw} > 125^\circ$).
- The endpoint k_{rw} (at S_{or}) seems to increase as oil-wetness increases as a result of extensive oil layer presence and hence less disruption of the water connectedness.
- The instant decrease of k_{ro} near S_{or} is directly correlated to the substantial reduction in S_{ol} through the end of waterflooding.
- In sensitivity studies on θ_A^{mw} , there is a sharp jump in S_{or} right after 90° as a result of switch from spontaneous to forced imbibition without intermediate oil layers reflecting weakly oil-wet systems with very poor recovery.
- From weakly to strongly oil-wet conditions, layer formation continues increasingly and accordingly S_{or} decreases up to near-zero around $\theta_A^{mw} > 125^\circ$.

Secondary drainage depends on the previously conducted primary drainage and secondary imbibition processes. The variety in pore occupancy configurations makes it tricky to simulate secondary drainage and to achieve reasonable P_c and k_r data.

- Secondary drainage mostly occurs at positive P_c for all wettability cases.
- Secondary drainage in water-wet case is completed at a lower pressure than the allowed limit due to lack of oil layers prior to oil re-invasion.
- There is a clear coincidence between the saturation trends of oil and water layers (S_{ol} and S_{wl}) along the secondary drainage process.
- A significant hysteresis in drainage-imbibition-secondary drainage P_c curves is obtained due to contact angle hysteresis. Extra hysteresis is seen when oil-wetness increased.
- The irreducible (residual) water saturation S_{wirr} is always more than the initial water saturation S_{wi} . Especially for oil-wet case, the difference between S_{wirr}

and S_{wi} remarkably increases. Therefore, the resulting P_c curves do not form a closed hysteresis loop in oil-wet systems.

- Based on the measured k_r hysteresis loops in C013, k_{ro} shows more hysteresis than k_{rw} in capillary-dominated flows for all wettability cases.
- SD endpoint k_{ro} (at S_{wirr}) does not reach unity only in oil-wet case, because substantial amount of flowing water remain and oil cannot fully dominate the system at the end.
- The resulting k_r curves reveal that the continuity of a phase is the critical factor for its relative permeability rather than how much of it is present in the system.
- The thin layer existence of a phase is found to be critically important on its relative permeability at low saturations.

CHAPTER 9

RECOMMENDATIONS FOR FUTURE WORK

The newly developed pore network model is a useful tool for capillary-controlled two-phase flow in nonuniformly wetted carbonate pore systems. The experimental flow data of our carbonate samples which is essential for a quantitative match of model simulation results was not available. In this thesis, rather, we have focused on understanding pore-level displacement processes that produce the complex experimental hysteresis trends. The experimental or modeling studies including drainage-imbibition-secondary drainage processes together in carbonate reservoirs are limited. Therefore, the experimental studies of Masalmeh (2001, 2002) analyzing the P_c and k_r hysteresis trends of Middle East carbonates were valuable sources for the qualitative comparison and validation of our model predictions.

- Our simulation results represent the general trend that the more strongly oil-wet media lead to lower oil residuals by means of abundant presence of oil layers. However, near-zero oil residuals for strongly oil-wet cases ($\theta_A^{mw} > 125^\circ$) is not realistic. Therefore, in the following studies, the geometrically based oil layers existence scenario (Blunt, 1997b) is aimed to be modified by a more restrictive condition giving reasonable nonzero residual oil saturations. Besides oil layer criterion, an improved geometrical description of intermediate layer area and also the conductivity approximations of corner and layer phases are intended to be derived and implemented in the model.

- Water trapping is not allowed in our model, but still, a noticeable increase in residual water is observed for each wettability case, especially for oil-wet case, due to the new oil-water configurations, the additional water-filled pores after oil re-invasion and the intermediate water layers on the pore corners. In the upcoming simulations, water trapping after wettability change will also be considered and thus greater residual water is expected at the end of secondary drainage.
- From the sensitivity analysis, the higher oil recovery is possible for strongly oil-wet case through intermediate oil layers ($\theta_A^{mw} > 125^\circ$). However, while the ultimate recovery increases through more oil-wet case, due to low conductance of oil layers, waterflooding may have to be continued for a very long period and this increases the cost of the field development.

To enhance our network representation and model predictions:

- 3D micro-CT imaging, if possible at multi resolutions, can be used to determine 3D connectivity and to capture larger porosity features such as vugs and fractures.
- If experimental P_c and k_r hysteresis data are available, they can be used to anchor the pore network model results. A quantitative match of model predictions can provide
 - accurate characterization of the wettability and
 - modification of pre-existing geometrical layer existence criteria.
- A micromodel experimental approach can be incorporated to compare, validate and advance our network model.
- The model results can be implicated to field scale displacements by data integration for a comprehensive analysis of flow and transport at all scales.

In the future studies, our model can be extended and improved to realize

- three phase flow with much more complex pore occupancies and multiple displacements for many interesting subjects as solution gas drive and higher-order (water-alternating-gas) floods,
- wettability alteration due to salinity effects,
- dynamic effects incorporating high flow rates (fracture flow), high viscosities (polymer flooding), or low interfacial tensions (surfactant flooding),
- capillary trapping of dense supercritical sCO_2 in carbonate and sandstone saline aquifers,
- pore-scale flow in unconventional resources.

REFERENCES

- Abdallah, W., Buckley, J.S., Carnegie, A., Edwards, J., Herold, B., Fordham, E., Graue, A., Habashy, T., Seleznev, N., Signer, C., Hussain, H., Montaron, B., Ziauddin, M., 2007. Fundamentals of wettability. *Oilf. Rev.*, 44–61.
- Adler, P.M., Jacquin, C.G., Quiblier, J.A., 1990. Flow in simulated porous media. *Int. J. Multiph. Flow* 16, 691–712. doi:10.1016/0301-9322(90)90025-E
- Adler, P.M., Thovert, J.F., 1998. Real porous media: local geometry and macroscopic properties. *Appl. Mech. Rev.* 51, 537. doi:10.1115/1.3099022
- Ahlbrandt, T.S., Charpentier, R.R., Klett, T.R., Schmoker, J.W., Schenk, C.J. and Ulmishek, G.F., 2005. Global resource estimates from total petroleum systems, AAPG Memoir No.86, Tulsa, Oklahoma, USA.
- Akin, S., Schembre, J.M., Bhat, S.K., Kovsky, A.R., 2000. Spontaneous imbibition characteristics of diatomite. *J. Pet. Sci. Eng.* 25, 149–165. doi:10.1016/S0920-4105(00)00010-3
- Al Sayari, S.S., 2009. The influence of wettability and carbon dioxide injection on hydrocarbon recovery. PhD Thesis. London: Imperial College.
- Al-Futaisi, A., Patzek, T.W., 2004. Secondary imbibition in NAPL-invaded mixed-wet sediments. *J. Contam. Hydrol.* 74, 61–81. doi:10.1016/j.jconhyd.2004.02.005
- Al-Futaisi, A., Patzek, T.W., 2003. Impact of wettability alteration on two-phase flow characteristics of sandstones: A quasi-static description. *Water Resour. Res.* 39, 1042–1054. doi:10.1029/2002WR001366
- Al-Gharbi, M., Blunt, M.J., 2005. Dynamic network modeling of two-phase drainage in porous media. *Phys. Rev. E* 71, 16308. doi:10.1103/PhysRevE.71.016308
- Al-Kharusi, A.S., Blunt, M.J., 2008. Multiphase flow predictions from carbonate pore space images using extracted network models. *Water Resour. Res.* 44, 1–14. doi:10.1029/2006WR005695
- Al-Kharusi, A.S., Blunt, M.J., 2007. Network extraction from sandstone and carbonate pore space images. *J. Pet. Sci. Eng.* 56, 219–231. doi:10.1016/j.petrol.2006.09.003
- Anderson, W.G., 1986. Wettability literature survey- Part 2: Wettability measurement. *J. Pet. Technol.* 38, 1246–1262. doi:10.2118/13933-PA

Anderson, W.G., 1987a. Wettability literature survey - Part 4: Effects of wettability on capillary pressure. *J. Pet. Technol.* 39, 1283–1300. doi:10.2118/15271-PA

Anderson, W.G., 1987b. Wettability literature survey - Part 6: Effect of wettability on waterflooding. *J. Pet. Technol.* 39, 1605–1622. doi:10.2118/16471-PA

Arns, C.H., Bauget, F., Limaye, A., Sakellariou, A., Senden, T.J., Sheppard, A.P., Sok, R.M., Pinczewski, W.V., Bakke, S., Berge, L.I., Øren, P.E., Knackstedt, M.A., 2005. Pore- scale characterization of carbonates using x-ray microtomography. *Soc. Pet. Eng. J.* 10 (4), 475–484.

Arns, J.Y., Sheppard, A.P., Arns, C.H., Knackstedt, M.A., Yelkhovsky, A., Pinczewski, W.V., 2007. Pore-level validation of representative pore networks obtained from micro-CT images. In: *Proceedings of the annual symposium of the society of core analysis, SCA2007-A26*, Calgary, Canada.

Bakke, S., Øren, P.E., 1997. 3-D pore-scale modelling of sandstones and flow simulations in the pore networks. *Soc. Pet. Eng.* 2, 136-149. <http://dx.doi.org/10.2118/35479-PA>

Bauer, D., Youssef, S., Fleury, M., Békri, S., Rosenberg, E., Vizika, O., 2012. Improving the estimations of petrophysical transport behavior of carbonate rocks using a dual pore network approach combined with computed microtomography. *Transp. Porous Media* 94, 505–524. doi:10.1007/s11242-012-9941-z

Beckingham, L.E., Peters, C.A., Um, W., Jones, K.W., Lindquist, W.B., 2013. 2D and 3D imaging resolution trade-offs in quantifying pore throats for prediction of permeability. *Adv. Water Resour.* 62, 1–12. doi:10.1016/j.advwatres.2013.08.010

Békri, S., Xu, K., Yousefian, F., Adler, P.M., Thovert, J.F., Muller, J., Iden, K., Psyllos, A., Stubos, A.K., Ioannidis, M.A., 2000. Pore geometry and transport properties in North Sea chalk. *J. Pet. Sci. Eng.* 25, 107–134. doi:10.1016/S0920-4105(00)00008-5

Berg, R.R., 1975. Capillary pressures in stratigraphic traps. *Am. Assoc. Pet. Geol. Bull.* 59, 939–956. doi:10.1306/83D91EF7-16C7-11D7-8645000102C1865D

Biswal, B., Manwart, C., Hilfer, R., Bakke, S., Øren, P.E., 1999. Quantitative analysis of experimental and synthetic microstructures for sedimentary rock. *Phys. A Stat. Mech. its Appl.* 273, 452–475. doi:10.1016/S0378-4371(99)00248-4

Biswal, B., Øren, P.E., Held, R.J., Bakke, S., Hilfer, R., 2007. Stochastic multiscale model for carbonate rocks. *Phys. Rev. E* 75, 61303. doi:10.1103/PhysRevE.75.061303

Blunt, M.J., King, P., 1991. Relative permeabilities from two- and three-dimensional pore-scale network modelling. *Transp. Porous Media* 6, 407–433. doi:10.1007/BF00136349

- Blunt, M.J., King, M.J., Scher, H., 1992. Simulation and theory of two-phase flow in porous media. *Phys. Rev. A* 46(12), 7680-7699. doi:10.1103/PhysRevA.46.7680
- Blunt, M.J., Scher, H., 1995. Pore-level modeling of wetting. *Phys. Rev. E* 52, 6387–6403. doi:10.1103/PhysRevE.52.6387
- Blunt, M.J., 1997a. Effects of heterogeneity and wetting on relative permeability using pore level modeling. *SPE J.* 2, 70–87. doi: 10.2118/36762-PA
- Blunt, M.J., 1997b. Pore level modeling of the effects of wettability. *SPE J.* 2, 494–510. doi:10.2118/38435-PA
- Blunt, M.J., 1998. Physically-based network modeling of multiphase flow in intermediate-wet porous media. *J. Pet. Sci. Eng.* 20, 117–125. doi:10.1016/S0920-4105(98)00010-2
- Blunt, M.J., 2001. Flow in porous media - pore-network models and multiphase flow. *Curr. Opin. Colloid Interface Sci.* 6, 197–207. doi: 10.1016/S1359-0294(01)00084-X
- Blunt, M.J., Jackson, M.D., Piri, M., Valvatne, P.H., 2002. Detailed physics, predictive capabilities and macroscopic consequences for pore-network models of multiphase flow. *Adv. Water Resour.* 25, 1069–1089. doi:10.1016/S0309-1708(02)00049-0
- Blunt, M.J., Bijeljic, B., Dong, H., Gharbi, O., Iglauer, S., Mostaghimi, P., Paluszny, A., Pentland, C., 2013. Pore-scale imaging and modelling. *Adv. Water Resour.* 51, 197–216. doi:10.1016/j.advwatres.2012.03.003
- Bondi, A., 1964. van der Waals volumes and radii. *J. Phys. Chem.* 68, 441–451. doi:10.1021/j100785a001
- Bryant, S., Blunt, M.J., 1992. Prediction of relative permeability in simple porous media. *Phys. Rev. A* 46, 2004–2011. doi:10.1103/PhysRevA.46.2004
- Bryant, S.L., King, P.R., Mellor, D.W., 1993a. Network model evaluation of permeability and spatial correlation in a real random sphere packing. *Transp. Porous Media* 11, 53–70. doi:10.1007/BF00614635
- Bryant, S.L., Mellor, D.W., Cade, C.A., 1993b. Physically representative network models of transport in porous media. *AIChE J.* 39, 387–396. doi:10.1002/aic.690390303
- Buckley, J.S., 1995. Asphaltene precipitation and crude oil wetting. *SPE Adv. Technol. Ser.* 3, 53–59. doi:10.2118/26675-PA
- Buckley, J.S., Bousseau, C., Liu, Y., 1996. Wetting alteration by brine and crude oil: from contact angles to cores. *SPE J.* 1, 341–350. doi:10.2118/30765-PA

Buckley, J.S. 1996. Mechanisms and consequences of wettability alteration by crude oils. PhD Thesis, Heriot-Watt University, Edinburgh, Scotland.

Cantrell, D.L., Hagerty, R.M., 1999. Microporosity in Arab formation carbonates, Saudi Arabia. *GeoArabia* 4, 129–154.

Cantrell, D.L., Hagerty, R.M., 2003. Reservoir rock classification, Arab-D reservoir, Ghawar Field, Saudi Arabia. *GeoArabia, J. Middle East Pet. Geosci.* 8, 435–462.

Celia, M.A., Reeves, P.C., Ferrand, L.A., 1995. Recent advances in pore scale models for multiphase flow in porous media. *Rev. Geophys.* 33, 1049–1057. doi:10.1029/95RG00248

Chandler, R., Koplik, J., Lerman, K., Willemsen, J.F., 1982. Capillary displacement and percolation in porous media. *J. Fluid Mech.* 119, 249–267. doi:10.1017/S0022112082001335

Chang, Y.C., Mohanty, K.K., Huang, D.D., Honarpour, M.M., 1997. The impact of wettability and core-scale heterogeneities on relative permeability. *J. Pet. Sci. Eng.* 18, 1–19. doi:10.1016/S0920-4105(97)00006-5

Chatzis, I., Dullien, F.A.L., 1977. Modelling pore structure by 2-D And 3-D networks with application to sandstones. *J. Can. Pet. Technol.* doi:10.2118/77-01-09

Chatzis, I., Dullien, F.A.L., 1981. Mercury porosimetry curves of sandstones. Mechanisms of mercury penetration and withdrawal. *Powder Technol.* 29, 117–125. doi:10.1016/0032-5910(81)85010-3

Chatzis, I., Morrow, N., Lim, H., 1983. Magnitude and detailed structure of residual oil saturation. *Old SPE J.* 23, 311–326. doi:10.2118/10681-PA

Chatzis, I., Dullien, F.A.L., 1985. The modeling of mercury porosimetry and the relative permeability of mercury in sandstones using percolation theory. *Int. Chem. Eng.; (United States)* 25:1.

Chatzis, I., Jewlal, D.M., Ioannidis, M.A., 1997. Core sample permeability estimation using statistical image analysis, in: SCA 9723, International Symposium of the Society of Core Analysts. Calgary, Canada.

Choquette, P.W., Pray, L.C., 1970. Geologic nomenclature and classification of porosity in sedimentary carbonates. *Am. Assoc. Pet. Geol. Bull.* 54(2), 207–250.

Clerke, E.A., Mueller, H.W., Phillips, E.C., Eyvazzadeh, R.Y., Jones, D.H., Ramamoorthy, R., Srivastava, A., 2008. Application of Thomeer Hyperbolas to decode the pore systems, facies and reservoir properties of the Upper Jurassic Arab D limestone, Ghawar field, Saudi Arabia: A “Rosetta Stone” approach. *GeoArabia* 13, 113–160.

Clerke, E., 2009. Permeability, relative permeability, microscopic displacement efficiency and pore geometry of M₁ bimodal pore systems in Arab-D limestone. SPE J. 14, 1–12. doi:10.2118/105259-PA

Cnudde, V., Boone, M.N., 2013. High-resolution X-ray computed tomography in geosciences: A review of the current technology and applications. Earth-Science Rev. 123, 1–17. doi:10.1016/j.earscirev.2013.04.003

Coenen, J., Tchouparova, E., Jing, X., 2004. Measurement parameters and resolution aspects of micro x-ray tomography for advanced core analysis.

Constantinides, G.N., Payatakes, A.C., 1996. Network simulation of steady-state two-phase flow in consolidated porous media. AIChE J. 42, 369–382. doi:10.1002/aic.690420207

Crain's Petrophysical Handbook - Mineral properties tables, Retrieved from <https://www.spec2000.net/05-mineralprops.htm>, last visited on February 2015.

Curtis, M.E., Ambrose, R.J., Sondergeld, C.H., 2010. Structural characterization of gas shales on the micro- and nano-scales, in: Canadian Unconventional Resources and International Petroleum Conference. SPE. doi:10.2118/137693-MS

Dahle, H.K., Celia, M.A., 1999. A dynamic network model for two-phase immiscible flow. Comput. Geosci. 3, 1–22. doi:10.1023/A:1011522808132

Dandekar, A.Y., 2006. Petroleum reservoir rock and fluid properties. CRC/Taylor & Francis.

Dernaika M.R., Kalam, M.Z., Basoni, M.A., Skjæveland, S.M., 2012. Hysteresis of capillary pressure, resistivity index and relative permeability in different carbonate rock types. Petrophysics 53(5), 315–331.

Dias, M.M., Wilkinson, D., 1986. Percolation with trapping. J. Phys. A (Mathematical Gen. 19, 3131–3146. doi:10.1088/0305-4470/19/15/034

Diaz, C.E., Chatzis, I., Dullien, F.A.L., 1987. Simulation of capillary pressure curves using bond correlated site percolation on a simple cubic network. Transp. Porous Media 2, 215–240. doi:10.1007/BF00165783

Dixit, A.B., McDougall, S.R., Sorbie, K.S., 1998. A pore-level investigation of relative permeability hysteresis in water-wet systems. SPE J. 3, 115–123. doi:10.2118/37233-PA

Dixit, A.B., McDougall, S.R., Sorbie, K.S., Buckley, J.S., 1999. Pore-scale modeling of wettability effects and their influence on oil recovery. SPE Reserv. Eval. Eng. 2, 25–36. doi:10.2118/54454-PA

Dixit, A.B., Buckley, J.S., McDougall, S.R., Sorbie, K.S., 2000. Empirical measures of wettability in porous media and the relationship between them derived from pore-scale modelling. *Transp. Porous Media* 40, 27–54. doi:10.1023/A:1006687829177

Donaldson, E.C., Alam, W., 2008. *Wettability*. Gulf Pub. Co.

Dong, H., Fjeldstad, S., Roth, S., Bakke, S., Øren, P.E., 2008. Pore network modelling on carbonate: A comparative study of different micro-CT network extraction methods. *Proc. Int. Symp. Soc. Core Anal.* 2008–2031.

Dong, H., Blunt, M.J., 2009. Pore-network extraction from micro-computerized-tomography images. *Phys. Rev. E - Stat. Nonlinear, Soft Matter Phys.* 80, 1–11. doi:10.1103/PhysRevE.80.036307

Dullien, F.A.L., Batra, V.K., 1970. Determination of the structure of porous media. *Ind. Eng. Chem.* 6, 25–53. doi:10.1021/ie50730a004

Dullien, F.A.L., Lai, F.S.Y., MacDonald, I.F., 1986. Hydraulic continuity of residual wetting phase in porous media. *J. Colloid Interface Sci.* 109, 201–218. doi:10.1016/0021-9797(86)90295-X

Dullien, F.A.L., 1992. *Porous media: fluid transport and pore structure*. Academic Press.

Dunsmuir, J.H., Ferguson, S.R., D'Amico, K.L., Stokes, J.P., 1991. X-Ray microtomography: A new tool for the characterization of porous media, in: *SPE Annual Technical Conference and Exhibition*. doi:10.2118/22860-MS

Edmundson, H., Raymer, L.L., 1979. Radioactive logging parameters for common minerals. *Log Anal.* 20, 38–47.

Ehrlich, R., Kennedy, S.K., Crabtree, S.J., Cannon, R.L., 1984. Petrographic image analysis; I, Analysis of reservoir pore complexes. *J. Sediment. Res.* 54, 1365–1378. doi:10.1306/212F85DF-2B24-11D7-8648000102C1865D

Ehrlich, R., Crabtree, S.J., Horkowitz, K.O., Horkowitz, J.P., 1991a. Petrography and reservoir physics I: objective classification of reservoir porosity. *Am. Assoc. Pet. Geol. Bull.* doi:10.1306/0C9B2989-1710-11D7-8645000102C1865D

Ehrlich, R., Etris, E.L., Brumfield, D., Yuan, L.P., Crabtree, S.J., 1991b. Petrography and reservoir physics III: Physical models for permeability and formation factor. *Am. Assoc. Pet. Geol. Bull.* doi:10.1306/0C9B299D-1710-11D7-8645000102C1865D

Etris, E.L., Brumfield, D.S., Ehrlich, R., Crabtree, S.J., 1988. Relations between pores, throats and permeability: A petrographic/physical analysis of some carbonate grainstones and packstones. *Carbonates and Evaporites* 3, 17–32. doi:10.1007/BF03174409

Fassi-Fihri, O., Robin, M., Rosenberg, E., 1995. Wettability studies at the pore level: A new approach by the use of cryo-scanning electron microscopy. SPE Form. Eval. 10, 11–19. doi:10.2118/22596-PA

Fatt, I., 1956. The network model of porous media. Pet. Trans. AIME 207, 144–181.

Fenwick, D.H., Blunt, M.J., 1998a. Three-dimensional modeling of three phase imbibition and drainage. Adv. Water Resour. 21, 121–143. doi:10.1016/S0309-1708(96)00037-1

Fenwick, D., Blunt, M.J., 1998b. Network modeling of three-phase flow in porous media. SPE J. 3, 5–8. doi:10.2118/38881-PA

Fischer, U., Celia, M.A., 1999. Prediction of relative and absolute permeabilities for gas and water from soil water retention curves using a pore-scale network model. Water Resour. Res. 35, 1089–1100. doi:10.1029/1998WR900048

Flannery, B.P., Deckman, H.W., Roberge, W.G., D'amico, K.L. 1987. Three-dimensional X-ray microtomography. Science, 237, 1439–1444, <http://dx.doi.org/10.2118/75192-MS>

Fluid flow in porous media: facts, Retrieved from <http://www.jgmaas.com/scores/facts.html>, last visited on February 2005.

Frank, S., Narayanan, R., Hansen, P., Allen, D.F., Albrechtsen, T., Steinhardt, H., Raven, M.J., Fordham, E., Bize, E., Rose, D.A., 2005. Carbonate rock typing using NMR data: A case study from Al Shaheen Field, Offshore Qatar, in: International Petroleum Technology Conference. doi:10.2523/IPTC-10889-MS

Freer, E.M., Svitova, T.F., Radke, C.J., 2002. Aging of the crude oil/brine interface: Implications for mixed wettability. SPE 75188. Proceedings of the 13th SPE/DOE Symposium on Improved Oil Recovery, Tulsa, Oklahoma.

Funk, J.J., Choinski, M.C., Saxman, B.B., Callender, C.A., 1989. Characterization of carbonate porosity using petrophysical properties and image analysis, in: Middle East Oil Show. Society of Petroleum Engineers. doi:10.2118/17943-MS

Gao, S., Meegoda, J.N., Hu, L., 2011. Geometrical and topological characteristics of the void space in random packing of equal size spheres, in: EMI Proceedings 2011 Conference. Boston, pp. 181–191.

Gharbi, O., Blunt, M.J., 2012. The impact of wettability and connectivity on relative permeability in carbonates: A pore network modeling analysis. Water Resour. Res. 48, 1–14. doi:10.1029/2012WR011877

Giesche, H., 2006. Mercury porosimetry: A general (practical) overview. Part. Part. Syst. Charact. 23, 9–19. doi:10.1002/ppsc.200601009

Gomes, J.S., Ribeiro, M.T., Strohmenger, C.J., Naghban, S., Kalam, M.Z., 2008. Carbonate reservoir rock typing - The link between geology and SCAL, in: Abu Dhabi International Petroleum Exhibition and Conference. doi:10.2118/118284-MS

Gouze, P., Hassani, R., Bernard, D., Coudrain-Ribstein, A., 2001. Calcul de l'évolution de la perméabilité des réservoirs sédimentaires contenant des argiles; application à la zone de la faille de Bray (bassin de Paris). Bull. la Société Géologique Fr. 172.

Graton, L.C., Fraser, H.J., 1935. Systematic packing of spheres: with particular relation to porosity and permeability. J. Geol. 43, 785–909. doi:10.1086/624386

Gundogar, A.S., Ross, C.M., Akin, S., Kovscek, A.R., 2016. Multiscale pore structure characterization of Middle East carbonates. J. Pet. Sci. Eng. 146, 570–583. doi:10.1016/j.petrol.2016.07.018

Harland, S.R., Wood, R.A., Curtis, A., Van Dijke, M.I.J., Stratford, K., Jiang, Z., Kallel, W., Sorbie, K., 2015. Quantifying flow in variably wet microporous carbonates using object-based geological modeling and both lattice-Boltzmann and pore-network fluid flow simulations. Am. Assoc. Pet. Geol. Bull. 99, 1827–1860. doi:10.1306/04231514122

Hazlett, R.D., 1995. Simulation of capillary-dominated displacements in microtomographic images of reservoir rocks. Transp. Porous Media 20, 21–35. doi:10.1007/BF00616924

Hebert, V., Garing, C., Luquot, L., Pezard, P.A., Gouze, P., 2015. Multi-scale X-ray tomography analysis of carbonate porosity. Geol. Soc. London, Spec. Publ. 406, 61–79. doi:10.1144/SP406.12

Heiba, A.A., Davis, H.T., Scriven, L.E., 1983. Effect of wettability on two-phase relative permeabilities and capillary pressures, in: SPE Annual Technical Conference and Exhibition. Society of Petroleum Engineers. doi:10.2118/12172-MS

Heiba, A.A., Sahimi, M., Scriven, L.E., Davis, H.T., 1992. Percolation theory of two-phase relative permeability. SPE Reserv. Eng. 7, 123–132. doi:10.2118/11015-PA

Heijmans, H., 1995. Mathematical morphology: A modern approach in image processing based on algebra and geometry. SIAM Rev. doi:doi:10.1137/1037001

Helland, J.O., Skjæveland, S.M., 2004. Physically-based capillary pressure correlation for mixed-wet reservoirs from a bundle-of-tubes model, in: SPE/DOE Symposium on Improved Oil Recovery. Society of Petroleum Engineers, Tulsa, Oklahoma. doi:10.2118/89428-MS

- Helland, J.O., Skjæveland, S.M., 2006a. Physically based capillary pressure correlation for mixed-wet reservoirs from a bundle-of-tubes model. *SPE J.* 11, 171–180. doi:10.2118/89428-PA
- Helland, J.O., Skjæveland, S.M., 2006b. Three-phase mixed-wet capillary pressure curves from a bundle of triangular tubes model. *J. Pet. Sci. Eng.* 52, 100–130. doi:10.1016/j.petrol.2006.03.018
- Helland, J.O., Ryazanov, A.V., van Dijke, M.I.J., 2008. Characterization of pore shapes for pore network models. doi:10.3997/2214-4609.20146420
- Hicks, P.J., Deans, H.A., Narayanan, K., 1992. Distribution of residual oil in heterogeneous carbonate cores using X-Ray CT. *SPE Form. Eval.* 7, 235–240. doi:10.2118/21574-PA
- Hilfer, R., 1995. Transport and relaxation phenomena in porous media, in: *Adv. Chem. Phys.* John Wiley & Sons, Inc., pp. 299–424. doi:10.1002/9780470141519.ch3
- Hilfer, R., Øren, P.E., 1996. Dimensional analysis of pore scale and field scale immiscible displacement. *Transp. Porous Media* 22, 53–72. doi:10.1007/BF00974311
- Hilpert, M., Miller, C.T., 2001. Pore-morphology-based simulation of drainage in totally wetting porous media. *Adv. Water Resour.* 24, 243–255. doi:10.1016/S0309-1708(00)00056-7
- Hilpert, M., Glantz, R., Miller, C.T., 2003. Calibration of a pore network model by a pore morphological analysis. *Transp. Porous Media* 51, 267–285. doi:10.1023/A:1022384431481
- Hirasaki, G.J., 1991. Wettability: fundamentals and surface forces. *SPE Form. Eval.* 6, 217–226. doi:10.2118/17367-PA
- Høiland, L.K., Spildo, K., Skauge, A., 2007. Fluid flow properties for different classes of intermediate wettability as studied by network modelling. *Transp. Porous Media* 70, 127–146. doi:10.1007/s11242-006-9088-x
- Hughes, R.G., Blunt, M.J., 2000. Pore scale modeling of rate effects in imbibition. 295–322.
- Hui, M.H., Blunt, M.J., 2000. Effects of wettability on three-phase flow in porous media. *J. Phys. Chem. B* 104, 3833–3845. doi:10.1021/jp9933222
- Ioannidis, M.A., Chatzis, I., Payatakes, A.C., 1991. A mercury porosimeter for investigating capillary phenomena and microdisplacement mechanisms in capillary networks. *J. Colloid Interface Sci.* 143, 22–36. doi:10.1016/0021-9797(91)90434-A

Ioannidis, M.A., Chatzis, I., 1993a. A mixed-percolation model of capillary hysteresis and entrapment in mercury porosimetry. *J. Colloid Interface Sci.* 161, 278–291. doi:10.1006/jcis.1993.1468

Ioannidis, M.A., Chatzis, I., 1993b. Network modelling of pore structure and transport properties of porous media. *Chem. Eng. Sci.* 48, 951–972. doi:10.1016/0009-2509(93)80333-L

Ioannidis, M.A., Chatzis, I., Sudicky, E.A., 1993. The effect of spatial correlations on the accessibility characteristics of three-dimensional cubic networks as related to drainage displacements in porous media. *Water Resour. Res.* 29, 1777–1785. doi:10.1029/93WR00385

Ioannidis, M.A., Kwiecien, M.J., Chatzis, I., Macdonald, I.F., Dullien, F.A.L., 1997. Comprehensive pore structure characterization using 3D computer reconstruction and stochastic modeling, in: *SPE Annual Technical Conference and Exhibition*. Society of Petroleum Engineers. doi:10.2118/38713-MS

Ioannidis, M.A., Chatzis, I., 2000. On the geometry and topology of 3D stochastic porous media. *J. Colloid Interface Sci.* 229, 323–334. doi:10.1006/jcis.2000.7055

Jadhunandan, P.P., Morrow, N.R., 1995. Effect of wettability on waterflood recovery for crude-oil/brine/rock systems. *SPE Reserv. Eng.* 10. doi:10.2118/22597-PA

Jerauld, G.R., Salter, S.J., 1990. The effect of pore-structure on hysteresis in relative permeability and capillary pressure: Pore-level modeling. *Transp. Porous Media* 5, 103–151. doi:10.1007/BF00144600

Jia, L., 2005. Reservoir definition through integration of multiphase petrophysical data. PhD Thesis, Stanford University, CA, USA.

Jia, L., Ross, C.M., Kovscek, A.R., 2007. A pore-network-modeling approach to predict petrophysical properties of diatomaceous reservoir rock. *SPE Reserv. Eval. Eng.* 10, 597–608. doi:10.2118/93806-PA

Jiang, Z., Wu, K., Couples, G., Van Dijke, M.I.J., Sorbie, K.S., Ma, J., 2007. Efficient extraction of networks from three-dimensional porous media. *Water Resour. Res.* 43, 1–17. doi:10.1029/2006WR005780

Jiang, Z., Van Dijke, M.I.J., Sorbie, K.S., Couples, G.D., 2013. Representation of multiscale heterogeneity via multiscale pore networks. *Water Resour. Res.* 49, 5437–5449. doi:10.1002/wrcr.20304

Jivkov, A.P., Hollis, C., Etiese, F., McDonald, S.A., Withers, P.J., 2013. A novel architecture for pore network modelling with applications to permeability of porous media. *J. Hydrol.* 486, 246–258. doi:10.1016/j.jhydrol.2013.01.045

- Joekar-Niasar, V., Prodanović, M., Wildenschild, D., Hassanizadeh, S.M., 2010. Network model investigation of interfacial area, capillary pressure and saturation relationships in granular porous media. *Water Resour. Res.* 46, n/a-n/a. doi:10.1029/2009WR008585
- Joshi, M., 1974. A class of stochastic models for porous media. University Microfilms, Ann Arbor Mich.
- Kallel, W., van Dijke, M.I.J., Sorbie, K.S., Wood, R., Jiang, Z., Harland, S., 2015. Modelling the effect of wettability distributions on oil recovery from microporous carbonate reservoirs. *Adv. Water Resour.* 0, 1–12. doi:10.1016/j.advwatres.2015.05.025
- Kamath, J., Lee, S.H., Jensen, C.L., Narr, W., Wu, H., 1998. Modeling fluid flow in complex naturally fractured reservoirs. *Spe* 39547. doi:10.2523/39547-MS
- Kaminsky, R., Radke, C.J., 1997. Asphaltenes, water films, and wettability reversal. *SPE J.* 2, 485–493. doi:10.2118/39087-PA
- Keller, L.M., Holzer, L., Wepf, R., Gasser, P., Münch, B., Marschall, P., 2011. On the application of focused ion beam nanotomography in characterizing the 3D pore space geometry of Opalinus clay. *Phys. Chem. Earth, Parts A/B/C* 36, 1539–1544. doi:10.1016/j.pce.2011.07.010
- Kendall, M., Moran, P.A.P., 1963. Geometrical probability. Hafner Pub. Co., New York.
- Ketcham, R.A., Carlson, W.D., 2001. Acquisition, optimization and interpretation of X-ray computed tomographic imagery: applications to the geosciences. *Comput. Geosci.* 27, 381–400. doi:10.1016/S0098-3004(00)00116-3
- Kimbler, O.K., Caudle, B.H., 1957. New techniques for study of fluid flow and phase distribution in porous media, *Oil and Gas J.*, 55(50) 85.
- King, P.R., 1987. The fractal nature of viscous fingering in porous media. *J. Phys. A. Math. Gen.* 20, L529–L534. doi:10.1088/0305-4470/20/8/008
- Knackstedt, M.A., Sahimi, M., Sheppard, A.P., 2000. Invasion percolation with long-range correlations: first-order phase transition and nonuniversal scaling properties. *Phys. Rev. E* 61(5), 4920–4934.
- Knackstedt, M.A., Sheppard, A.P., Sahimi, M., 2001. Pore network modelling of two-phase flow in porous rock: the effect of correlated heterogeneity. *Adv. Water Resour.* 24, 257–277.

Knackstedt, M.A., Arns, C.H., Ghou, A., Sakellariou, A., Senden, T.J., Sheppard, A.P., Sok, R.M., Nguyen, V., Pinczewski, W.V., 2006. 3D imaging and characterization of the pore space of carbonate core; implications to single and two phase flow properties. SPWLA 47th Annual Logging Symposium, 1–15.

Knackstedt, M.A., Arns, C.H., Sok, R.M., Sheppard, A.P., 2007. 3D pore scale characterisation of carbonate core: relating pore types and interconnectivity to petrophysical and multiphase flow properties. In: Extended abstract, International Petroleum Technology Conference, Abu Dhabi, December 2007, IPTC 11775.

Knackstedt, M.A., Sok, R.M., Sheppard, A.P., Latham, S.J., Madadi, M., Varslot, T., Arns, C.H., Bachle, G., Eberli, G., 2008. Probing pore systems in carbonates: Correlations to petrophysical properties. Paper presented at the 49th Annual Logging Symposium, Austin, Texas, 25–28 May.

Knackstedt, M.A., Jaime, P., Butcher, A., Botha, P., Middleton, J., Sok, R., 2010. Integrating reservoir characterization: 3D dynamic, petrophysical and geological description of reservoir facies, in: SPE Asia Pacific Oil and Gas Conference and Exhibition. Society of Petroleum Engineers. doi:10.2118/133981-MS

Koplik, J., Lin, C., Vermette, M., 1984. Conductivity and permeability from microgeometry. *J. Appl. Phys.* 56, 3127–3131. doi:10.1063/1.333872

Koplik, J., Lasseter, T.J., 1985. Two-phase flow in random network models of porous media. *Soc. Pet. Eng. J.* 25, 89–100. doi:10.2118/11014-PA

Kovscek, A.R., Wong, H., Radke, C.J., 1993. A pore-level scenario for the development of mixed wettability in oil reservoirs. *AIChE J.* 39(6), 1072–1085. doi:10.1002/aic.690390616

Krumbein, W.C., 1935. Thin-section mechanical analysis of indurated sediments. *J. Geol.* 43, 482–496. doi:10.1086/624330

Kwiecien, M.J., Macdonald, I.F., Dullien, F.A.L., 1990. Three-dimensional reconstruction of porous media from serial section data. *J. Microsc.* 159, 343–359. doi:10.1111/j.1365-2818.1990.tb03039.x

Lake, L.W., 1989. Enhanced oil recovery. Prentice Hall.

Laroche, C., Vizika, O., 2005. Two-phase flow properties prediction from small-scale data using pore-network modeling. *Transp. Porous Media* 61, 77–91. doi:10.1007/s11242-004-6797-x

Lehmann, P., Wyss, P., Flisch, A., Lehmann, E., Vontobel, P., Krafczyk, M., Kaestner, A., Beckmann, F., Gygi, A., Flühler, H., 2006. Tomographical imaging and mathematical description of porous media used for the prediction of fluid distribution. *Vadose Zo. J.* 5, 80–97. doi:10.2136/vzj2004.0177

Lemmens, H., Butcher, A., Botha, P.W., 2010. FIB/SEM and automated mineralogy for core and cuttings analysis, in: SPE Russian Oil and Gas Conference and Exhibition. Society of Petroleum Engineers. doi:10.2118/136327-MS

Lemmens, H., Richards, D., 2013. Multiscale imaging of shale samples in the scanning electron microscope, in Camp, W., Diaz, E., Wawak, B., *Electron Microsc. shale Hydrocarb. Reserv.: AAPG Mem.* 102, 27–36. doi:10.1306/13391702M1023582

Lenormand, R., Zarcone, C., Sarr, A., 1983. Mechanisms of the displacement of one fluid by another in a network of capillary ducts. *J. Fluid Mech.* 135, 337. doi:10.1017/S0022112083003110

Lenormand, R., Zarcone, C., 1984. Role of roughness and edges during imbibition in square capillaries. *Proc. SPE Annu. Tech. Conf. Exhib.* doi:10.2523/13264-MS

Lenormand, R., 1986. Scaling laws for immiscible displacements with capillary and viscous fingering, in: SPE Annual Technical Conference and Exhibition. Society of Petroleum Engineers. doi:10.2118/15390-MS

Lerdahl, T.R., Oren, P.-E., Bakke, S., 2000. A predictive network model for three-phase flow in porous media, in: SPE/DOE Improved Oil Recovery Symposium. Society of Petroleum Engineers. doi:10.2118/59311-MS

Li, X., Yortsos, Y.C., 1995. Visualization and simulation of bubble growth in pore networks. *AIChE J.* 41, 214–222. doi:10.1002/aic.690410203

Li, Y., Laidlaw, W.G., Wardlaw, N.C., 1986. Sensitivity of drainage and imbibition to pore structures as revealed by computer simulation of displacement process. *Adv. Colloid Interface Sci.* 26, 1–68. doi:10.1016/0001-8686(86)80014-8

Li, Y., Wardlaw, N.C., 1986a. The influence of wettability and critical pore-throat size ratio on snap-off. *J. Colloid Interface Sci.* 109, 461–472. doi:10.1016/0021-9797(86)90324-3

Li, Y., Wardlaw, N.C., 1986b. Mechanisms of nonwetting phase trapping during imbibition at slow rates. *J. Colloid Interface Sci.* 109, 473–486. doi:10.1016/0021-9797(86)90325-5

Liang, Z.R., Philippi, P.C., Fernandes, C.P., Magnani, F.S., 1999. Prediction of Permeability from the Skeleton of Three-Dimensional Pore Structure. *SPE Reserv. Eval. Eng.* 2, 161–168. doi:10.2118/56006-PA

- Lindquist, W.B., Lee, S.M., Coker, D.A., Jones, K.W., Spanne, P., 1996. Medial axis analysis of void structure in three-dimensional tomographic images of porous media. *J. Geophys. Res.* 101, 8297. doi:10.1029/95JB03039
- Lowry, M.I., Miller, C.T., 1995. Pore-scale modeling of nonwetting-phase residual in porous media. *Water Resour. Res.* 31, 455–473. doi:10.1029/94WR02849
- Lucia, F.J., 2007. Carbonate reservoir characterization: an integrated approach. Springer.
- Lucia, F.J., 1995. Rock-fabric/petrophysical classification of carbonate pore space for reservoir characterization. *Am. Assoc. Pet. Geol. Bull.* 79, 1275–1300. doi:10.1306/7834D4A4-1721-11D7-8645000102C1865D
- Lulla, R.N., 1999. Pore scale modeling of flow in 3-D random networks, Student Report. Earth Sciences Library (Branner), Stanford University, CA, USA.
- Ma, S., Mason, G., Morrow, N.R., 1996. Effect of contact angle on drainage and imbibition in regular polygonal tubes. *Colloids Surfaces A Physicochem. Eng. Asp.* 117, 273–291. doi:10.1016/0927-7757(96)03702-8
- Man, H.N., Jing, X.D., 1999. Network modelling of wettability and pore geometry effects on electrical resistivity and capillary pressure. *J. Pet. Sci. Eng.* 24, 255–267. doi:10.1016/S0920-4105(99)00047-9
- Man, H.N., Jing, X.D., 2000. Pore network modelling of electrical resistivity and capillary pressure characteristics. *Transp. Porous Media* 41, 263–286. doi:10.1023/A:1006612100346
- Mani, V., Mohanty, K.K., 1998. Pore-level network modeling of three-phase capillary pressure and relative permeability curves. *SPE J.* 3, 238–248. doi:10.2118/50942-PA
- Mani, V., Mohanty, K.K., 1999. Effect of pore-space spatial correlations on two-phase flow in porous media. *J. Pet. Sci. Eng.* 23, 173–188. doi:10.1016/S0920-4105(99)0015-7
- Manwart, C., Hilfer, R., 1999. On the reconstruction of random media using Monte Carlo methods. *Physical Review E*, 59, 5596–5599. doi:10.1103/PhysRevE.59.5596
- Manwart, C., Torquato, S. and Hilfer, R. 2000. Stochastic reconstruction of sandstones. *Physical Review E*, 62, 893–899.
- Marzouk, I., Takezaki, H., Suzuki, M., 1998. New classification of carbonate rocks for reservoir characterization, in: Abu Dhabi International Petroleum Exhibition and Conference. Society of Petroleum Engineers. doi:10.2118/49475-MS
- Masalmeh, S.K., 2001. Experimental measurements of capillary pressure and relative permeability hysteresis. in: SCA 2001-23. Edinburgh, 1–13.

Masalmeh, S.K., 2002. The effect of wettability on saturation functions and impact on carbonate reservoirs in the Middle East, in: Abu Dhabi International Petroleum Exhibition and Conference. Society of Petroleum Engineers. doi:10.2118/78515-MS

Masalmeh, S.K., 2003. The effect of wettability heterogeneity on capillary pressure and relative permeability. *J. Pet. Sci. Eng.* 39, 399–408. doi:10.1016/S0920-4105(03)00078-0

Masalmeh, S.K., Jing, X.D., 2004. Carbonate SCAL: characterisation of carbonate rock types for determination of saturation functions and residual oil saturations, in: SCA2004-08. Abu Dhabi, UAE, 1–12.

Masalmeh, S.K., Jing, X.D., 2006. Capillary pressure characteristics of carbonate reservoirs: Relationship between drainage and imbibition curves. *Int. Symp. Soc. Core Anal. Trondheim, Norway*, 1–14.

Mason, G., Morrow, N.R., 1991. Capillary behavior of a perfectly wetting liquid in irregular triangular tubes. *J. Colloid Interface Sci.* 141, 262–274. doi:10.1016/0021-9797(91)90321-X

Mayagoitia, V., Rojas, F., Kornhauser, I., Pérez-Aguilar, H., 1997. Modeling of porous media and surface structures: their true essence as networks. *Langmuir* 13, 1327–1331. doi:10.1021/LA950812M

Mayer, R.P., Stowe, R.A., 1965. Mercury porosimetry-breakthrough pressure for penetration between packed spheres. *J. Colloid Sci.* 20, 893–911. doi:10.1016/0095-8522(65)90061-9

McCreesh, C.A., Ehrlich, R., Crabtree, S.J., 1991. Petrography and reservoir physics II: Relating thin section porosity to capillary pressure, the association between pore types and throat size. *Am. Assoc. Pet. Geol. Bull.* doi:10.1306/0C9B2993-1710-11D7-8645000102C1865D

McDougall, S.R., Sorbie, K.S., 1995. The impact of wettability on waterflooding: Pore-scale simulation. *SPE Reserv. Eng.* 10, 208–213. doi:10.2118/25271-PA

McDougall, S.R., Sorbie, K.S., 1997. The application of network modelling techniques to multiphase flow in porous media. *Pet. Geosci.* 3, 161–169. doi:10.1144/petgeo.3.2.161

Moctezuma, A., Békri, S., Laroche, C., Vizika, O., 2003. A dual network model for relative permeability of bimodal rocks: Application in a vuggy carbonate, in: SCA2003-12. Pau, France, 22–25.

Mogensen, K., Stenby, E.H., 1998. A dynamic two-phase pore-scale model of imbibition. *Transp. Porous Media* 32, 299–327. doi:10.1023/a:1006578721129

Mohanty, K.K., Salter, S.J., 1982. Multiphase flow in porous media: II. Pore-level modeling, in: SPE Annual Technical Conference and Exhibition. doi:10.2118/11018-MS

Moore, C.H., 2001. Carbonate reservoirs: Porosity evolution and diagenesis in a sequence stratigraphic framework. Elsevier, Amsterdam, *Developments in Sedimentology* Volume 55, 444.

Morrow, N.R., 1971. Small-scale packing heterogeneities in porous sedimentary rocks. *Am. Assoc. Pet. Geol. Bull.* 55, 514–522.

Morrow, N.R., 1975. The effects of surface roughness on contact: Angle with special reference to petroleum recovery. *J. Can. Pet. Technol.* 14. doi:10.2118/75-04-04

Morrow, N.R., Lim, H.T., Ward, J.S., 1986. Effect of crude-oil-induced wettability changes on oil recovery. *SPE Form. Eval.* 1, 89–103. doi:10.2118/13215-PA

Mostaghimi, P., Blunt, M.J., Bijeljic, B., 2013. Computations of absolute permeability on micro-CT images. *Math. Geosci.* 45, 103–125. doi:10.1007/s11004-012-9431-4

Nguyen, V.H., Sheppard, A.P., Knackstedt, M. a., Val Pinczewski, W., 2006. The effect of displacement rate on imbibition relative permeability and residual saturation. *J. Pet. Sci. Eng.* 52, 54–70. doi:10.1016/j.petrol.2006.03.020

Okabe, H., Blunt, M.J., 2004. Prediction of permeability for porous media reconstructed using multiple-point statistics. *Phys. Rev. E - Stat. Nonlinear, Soft Matter Phys.* 70, 1–2. doi:10.1103/PhysRevE.70.066135

Or, D., Tuller, M., 1999. Liquid retention and interfacial area in variably saturated porous media: Upscaling from single-pore to sample-scale model. *Water Resour. Res.* 35, 3591–3605. doi:10.1029/1999WR900262

Øren, P.E., Pinczewski, W. V, 1994. The effect of wettability and spreading coefficients on the recovery of waterflood residual oil by miscible gasflooding. *SPE Form. Eval.* 9, 149–156. doi:10.2118/24881-PA

Øren, P.E., Bakke, S., Arntzen, O.J., 1998. Extending predictive capabilities to network models. *SPE J.* 3, 324–336. doi:10.2118/52052-PA

Øren, P.E., Antonsen, F., Rueslåtten, H.G., Bakke, S., 2002. Numerical simulations of NMR responses for improved interpretations of NMR measurements in reservoir rocks, in: SPE Annual Technical Conference and Exhibition. doi:10.2118/77398-MS

Øren, P.E., Bakke, S., 2002. Process based reconstruction of sandstones and prediction of transport properties. *Transp. Porous Media* 46, 311–343. doi:10.1023/A:1015031122338

- Øren, P.E., Bakke, S., 2003. Reconstruction of Berea sandstone and pore-scale modelling of wettability effects. *J. Pet. Sci. Eng.* 39, 177–199. doi:10.1016/S0920-4105(03)00062-7
- Pamukcu, A.S., Gualda, G.A.R., 2010. Quantitative 3D petrography using X-ray tomography 2: Combining information at various resolutions. *Geosphere* 6, 775–781. doi:10.1130/GES00565.1
- Patzek, T.W., 2001. Verification of a complete pore network simulator of drainage and imbibition. *SPE J.* 6, 144–156. doi:10.2118/71310-PA
- Patzek, T.W., Silin, D.B., 2001. Shape factor correlations of hydraulic conductance in noncircular capillaries. *J. Colloid Interface Sci.* 236, 295–304. doi:10.1006/jcis.2000.7414
- Peng, S., Hu, Q., Dultz, S., Zhang, M., 2012. Using X-ray computed tomography in pore structure characterization for a Berea sandstone: Resolution effect. *J. Hydrol.* 472, 254–261. doi:10.1016/j.jhydrol.2012.09.034
- Pereira, G.G., Pinczewski, W. V., Chan, D.Y.C., Paterson, L., Øren, P.E., 1996. Pore-scale network model for drainage-dominated three-phase flow in porous media. *Transp. Porous Media* 24, 167–201. doi:10.1007/BF00139844
- Piri, M., 2003. Pore-scale modelling of three-phase flow. PhD Thesis, Imperial College London.
- Piri, M., Blunt, M.J., 2005. Three-dimensional mixed-wet random pore-scale network modeling of two- and three-phase flow in porous media. *Phys. Rev. E* 71, 26301-26302. doi:10.1103/PhysRevE.71.026301-2
- Pittman, E.D., 1971. Microporosity in carbonate rocks: Geological notes. *Am. Assoc. Pet. Geol. Bull.* 55, 1873–1878.
- Princen, H.M., 1969a. Capillary phenomena in assemblies of parallel cylinders: I. Capillary rise between two cylinders. *J. Colloid Interface Sci.* 30, 69–75. doi:10.1016/0021-9797(69)90379-8
- Princen, H.M., 1969b. Capillary phenomena in assemblies of parallel cylinders: II. Capillary rise in systems with more than two cylinders. *J. Colloid Interface Sci.* 30, 359–371. doi:10.1016/0021-9797(69)90403-2
- Princen, H.M., 1970. Capillary phenomena in assemblies of parallel cylinders: III. Liquid Columns between Horizontal Parallel Cylinders. *J. Colloid Interface Sci.* 34, 171–184. doi:10.1016/0021-9797(70)90167-0

- Prodanović, M., Bryant, S.L., 2006. A level set method for determining critical curvatures for drainage and imbibition. *J. Colloid Interface Sci.* 304, 442–458. doi:10.1016/j.jcis.2006.08.048
- Prodanović, M., Lindquist, W.B., Seright, R.S., 2007. 3D image-based characterization of fluid displacement in a Berea core. *Adv. Water Resour.* 30, 214–226. doi:10.1016/j.advwatres.2005.05.015
- Prodanović, M., Mehmani, A., Sheppard, A.P., 2014. Imaged-based multiscale network modelling of microporosity in carbonates. *Geol. Soc. London, Spec. Publ.* 406, SP406-9. doi:10.1144/SP406.9
- Quiblier, J.A., 1984. A new three-dimensional modeling technique for studying porous media. *J. Colloid Interface Sci.* 98, 84–102. doi:10.1016/0021-9797(84)90481-8
- Rajaram, H., Ferrand, L.A., Celia, M.A., 1997. Prediction of relative permeabilities for unconsolidated soils using pore-scale network models. *Water Resour. Res.* 33, 43–52. doi:10.1029/96WR02841
- Ramakrishnan, T.S., Ramamoorthy, R., Fordham, E., Schwartz, L., Herron, M., Saito, N., Rabaute, A., 2001. A model-based interpretation methodology for evaluating carbonate reservoirs, in: *SPE Annual Technical Conference and Exhibition*. Society of Petroleum Engineers. doi:10.2118/71704-MS
- Ransohoff, T.C., Radke, C.J., 1988. Laminar flow of a wetting liquid along the corners of a predominantly gas-occupied noncircular pore. *J. Colloid Interface Sci.* 121, 392–401. doi:10.1016/0021-9797(88)90442-0
- Raoof, A., Hassanizadeh, S.M., 2010. A new method for generating pore-network models of porous media. *Transp. Porous Media* 81, 391–407. doi:10.1007/s11242-009-9412-3
- Reeves, P.C., Celia, M.A., 1996. A functional relationship between capillary pressure, saturation, and interfacial area as revealed by a pore-scale network model. *Water Resour. Res.* 32, 2345–2358. doi:10.1029/96WR01105
- Roof, J.G., 1970. Snap-off of oil droplets in water-wet pores. *Soc. Pet. Eng. J.* 85–90. doi:10.2118/2504-PA
- Rose, W., Bruce, W.A., 1949. Evaluation of capillary character in petroleum reservoir rock. *J. Pet. Technol.* 1, 127–142. doi:10.2118/949127-G
- Ross, C.M., Callender, C.A., Turbeville, J.B., Funk, J.J., 1995. Modeling of capillary pressure behavior using standard open hole wireline log data: Demonstrated on carbonates from the Middle East. *SPE Annu. Tech. Conf. Exhib.* doi:10.2118/30543-MS

Ross, C.M., Kovscek, A.R., 2002. Pore microstructure and fluid distribution in a diatomaceous reservoir. *Spe* 75190 1–9. doi:10.2118/75190-MS

Ryazanov, A.V., van Dijke, M.I.J., Sorbie, K.S., 2009. Two-phase pore-network modelling: Existence of oil layers during water invasion. *Transp. Porous Media* 80, 79–99. doi:10.1007/s11242-009-9345-x

Ryazanov, A.V., van Dijke, M.I.J., Sorbie, K.S., 2010. Pore-network prediction of residual oil saturation based on oil layer drainage in mixed-wet systems, in: *SPE Improved Oil Recovery Symposium*. SPE. doi:10.2118/129919-MS

Ryazanov, A.V., 2012. Pore-scale network modelling of residual oil saturation in mixed-wet systems. PhD Thesis, Heriot-Watt University, Edinburgh, Scotland.

Sahimi, M., 1993. Flow phenomena in rocks: From continuum models to fractals, percolation, cellular automata, and simulated annealing. *Rev. Mod. Phys.* 65, 1393–1534. doi:10.1103/RevModPhys.65.1393

Sahimi, M., 2011. Flow and transport in porous media and fractured rock. Wiley-VCH Verlag GmbH & Co. KGaA, Weinheim, Germany. doi:10.1002/9783527636693

Sahu, B.K., 1968. Thin-section size analysis and the moment problem. *Sedimentology* 10, 147–151. doi:10.1111/j.1365-3091.1968.tb01107.x

Salathiel, R.A., 1973. Oil recovery by surface film drainage in mixed-wettability rocks. *J. Pet. Technol.* 25, 1216–1224. doi:10.2118/4104-PA

Saller, A.H., Pollitt, D., Dickson, J.A.D., 2014. Diagenesis and porosity development in the First Eocene reservoir at the giant Wafra Field, Partitioned Zone, Saudi Arabia and Kuwait. *Am. Assoc. Pet. Geol. Bull.* 98, 1185–1212. doi:10.1306/12021313040

Schembre, J.M., Kovscek, A.R., 2003. A technique for measuring two-phase relative permeability in porous media via X-ray CT measurements. *J. Pet. Sci. Eng.* 39, 159–174. doi:10.1016/S0920-4105(03)00046-9

Schlumberger, Carbonate Reservoirs 2007, accessed March 15, 2015. http://www.slb.com/~media/Files/industry_challenges/carbonates/brochures/cb_carbonate_reservoirs_07os003.pdf

Serra, J., 1982. Image analysis and mathematical morphology. Academic Press.

Sheppard, A.P., Sok, R.M., Averdunk, H., 2005. Improved pore network extraction methods, in: the International Symposium of the Society of Core Analysts . Toronto.

Silin, D.B., Guodong, J., Patzek, T.W., 2003. Robust determination of the pore space morphology in sedimentary rocks. *Proc. SPE Annu. Tech. Conf. Exhib.* 69–70. doi:10.2523/84296-MS

Silin, D.B., Patzek, T.W., 2006. Pore space morphology analysis using maximal inscribed spheres. *Phys. A Stat. Mech. its Appl.* 371, 336–360. doi:10.1016/j.physa.2006.04.048

Singh, K., Bijeljic, B., Blunt, M.J., 2016. Imaging of oil layers, curvature and contact angle in a mixed-wet and a water-wet carbonate rock. *Water Resour. Res.* 52, 1716–1728. doi:10.1002/2015WR018072

Skalinski, M., Kenter, J.A.M., 2015. Carbonate petrophysical rock typing: integrating geological attributes and petrophysical properties while linking with dynamic behaviour. *Geol. Soc. London, Spec. Publ.* 406, 229–259. doi:10.1144/SP406.6

Sok, R.M., Knackstedt, M.A., Sheppard, A.P., Pinczewski, W.V., Lindquist, W.B., Venkatarangan, A., Paterson, L., 2002. Direct and stochastic generation of network models from tomographic images; effect of topology on residual saturations. *Transp. Porous Media* 46, 345–372. doi:10.1023/A:1015034924371

Sok, R.M., Arns, C., Knackstedt, M.A., Senden, T., Sheppard, A.P., Averdunk, H., Pinczewski, W.V., Okabe, H., 2007. Estimation of petrophysical parameters from 3D images of carbonate core. *SPWLA Middle East Reg. Symp.* 1–15.

Sok, R.M., Varslot, T., Ghous, A., Latham, S., Sheppard, A.P., Knackstedt, M.A., 2010. Pore scale characterization of carbonates at multiple scales: Integration of micro-CT, BSEM, and FIBSEM. *Petrophysics* 51, 379–387.

Sorbie, K.S., Ryazanov, A. V, Van Dijke, M.I.J., 2011. The structure of residual oil as a function of wettability alteration using pore-scale network modelling, in: *Society of Core Analysts*. Austin, United States, 1–12.

Stauffer, D., Aharony, A., 1994. *Introduction to percolation theory*. Taylor & Francis.

Sun, S.Q., 1995. Dolomite reservoirs: porosity evolution and reservoir characteristics. *Am. Assoc. Pet. Geol. Bull.* 79, 186–204.

Sung, R.R., Clerke, E.A., Buiting, J.J., Ait Ettajer, T., 2013. Integrated geology, sedimentology, and petrophysics application technology for multi-modal carbonate reservoirs. *Int. Pet. Technol. Conf.* 4253–4262. doi:10.2523/16988-ABSTRACT

Swanson, B.F., 1980. Rationalising the influence of crude wetting on reservoir fluid flow with electrical resistivity behavior. *JPT*, August 1980, 1459-1464.

Swanson, B.F., 1981. A simple correlation between permeabilities and mercury capillary pressures. *J. Pet. Technol.* 33, 2498–2504. doi:10.2118/8234-PA

Thomeer, J.H.M., 1983. Air permeability as a function of three pore-network parameters. *J. Pet. Technol.* 35, 809–814. doi:10.2118/10922-PA

Tissot, B.P., Welte, D.H., 1978. *Petroleum formation and occurrence*. Springer Berlin Heidelberg, Berlin, Heidelberg. doi:10.1007/978-3-642-96446-6

Tomutsa, L., Silin, D.B., Radmilovic, V., 2007. Analysis of chalk petrophysical properties by means of submicron-scale pore imaging and modeling. *SPE Reserv. Eval. Eng.* 10, 285–293. doi:10.2118/99558-PA

Treiber, L.E., Archer, D.L., Owens, W.W., 1972. A laboratory evaluation of the wettability of fifty oil-producing reservoirs. *Soc. Pet. Eng. J.* 531–540. doi:10.2118/3526-PA

Tsakiroglou, C.D., Payatakes, A.C., 1991. Effects of pore-size correlations on mercury porosimetry curves. *J. Colloid Interface Sci.* 146, 479–494. doi:10.1016/0021-9797(91)90212-Q

Tsakiroglou, C.D., Payatakes, A.C., 2000. Characterization of the pore structure of reservoir rocks with the aid of serial sectioning analysis, mercury porosimetry and network simulation. *Adv. Water Resour.* 23, 773–789. doi:10.1016/S0309-1708(00)00002-6

Tsakiroglou, C.D., Burganos, V.N., Jacobsen, J., 2004. Pore-structure analysis by using nitrogen sorption and mercury intrusion data. *AIChE J.* 50, 489–510. doi:10.1002/aic.10043

Tuller, M., Or, D., Dudley, L.M., 1999. Adsorption and capillary condensation in porous media: Liquid retention and interfacial configurations in angular pores. *Water Resour. Res.* 35, 1949–1964. doi:10.1029/1999WR900098

Turner, M.L., Knüfing, L., Arns, C.H., Sakellariou, A., Senden, T.J., Sheppard, A.P., Sok, R.M., Limaye, A., Pinczewski, W.V., Knackstedt, M.A., 2004. Three-dimensional imaging of multiphase flow in porous media. *Phys. A Stat. Mech. its Appl.* 339, 166–172. doi:10.1016/j.physa.2004.03.059

Valvatne, P.H., 2004. Predictive pore-scale modelling of multiphase flow. PhD Thesis, Imperial College, London.

Valvatne, P.H., Blunt, M.J., 2004. Predictive pore-scale modeling of two-phase flow in mixed wet media. *Water Resour. Res.* 40, 1–21. doi:10.1029/2003WR002627

Van Dijke, M.I.J., Sorbie, K.S., 2002. Pore-scale network model for three-phase flow in mixed-wet porous media. *Phys. Rev. E* 66, 46302. doi:10.1103/PhysRevE.66.046302

- Van Dijke, M.I.J., Sorbie, K.S., 2006. Existence of fluid layers in the corners of a capillary with non-uniform wettability. *J. Colloid Interface Sci.* 293, 455–463. doi:10.1016/j.jcis.2005.06.059
- Vinegar, H.J., Wellington, S.L., 1987. Tomographic imaging of three-phase flow experiments. *Rev. Sci. Instrum.* 58, 96–107. doi:10.1063/1.1139522
- Vogel, H.J., Roth, K., 2001. Quantitative morphology and network representation of soil pore structure. *Adv. Water Resour.* 24, 233–242. doi:10.1016/S0309-1708(00)00055-5
- Wardlaw, N.C., 1982. Effects of geometry, wettability, viscosity and interfacial tension on trapping in single pore-throat pairs. *J. Can. Pet. Technol.* 21, 21–27. doi:10.2118/82-03-01
- Wardlaw, N.C., Li, Y., Forbes, D., 1987. Pore-throat size correlation from capillary pressure curves. *Transp. Porous Media* 2, 597–614. doi:10.1007/BF00192157
- Washburn, E.W., 1921. Note on a method of determining the distribution of pore sizes in a porous material. *Proc. Natl. Acad. Sci. U. S. A.* 7, 115–6.
- Wildenschild, D., Sheppard, A.P., 2013. X-ray imaging and analysis techniques for quantifying pore-scale structure and processes in subsurface porous medium systems. *Adv. Water Resour.* 51, 217–246. doi:10.1016/j.advwatres.2012.07.018
- Wilkinson, D., Willemsen, J.F., 1983. Invasion percolation: a new form of percolation theory. *J. Phys. A. Math. Gen.* 16, 3365–3376. doi:10.1088/0305-4470/16/14/028
- Wirth, R., 2009. Focused Ion Beam (FIB) combined with SEM and TEM: Advanced analytical tools for studies of chemical composition, microstructure and crystal structure in geomaterials on a nanometre scale. *Chem. Geol.* 261 (3), 217–229.
- Xiong, Q., Baychev, T.G., Jivkov, A.P., 2016. Review of pore network modelling of porous media: Experimental characterisations, network constructions and applications to reactive transport. *J. Contam. Hydrol.* 192, 101–117. doi:10.1016/j.jconhyd.2016.07.002
- Xu, B., Kamath, J., Yortsos, Y.C., Lee, S.H., 1999. Use of pore-network models to simulate laboratory corefloods in a heterogeneous carbonate sample. *Spe 57664-Pa* 5–8. doi:10.2118/57664-PA
- Xu, C., Torres-Verdín, C., 2013. Quantifying fluid distribution and phase connectivity with a simple 3D cubic pore network model constrained by NMR and MICP data. *Comput. Geosci.* 61, 94–103. doi:10.1016/j.cageo.2013.08.003

Yanuka, M., Dullien, F.A.L., Elrick, D., 1986. Percolation processes and porous media: I. Geometrical and topological model of porous media using a three-dimensional joint pore size distribution. *J. Colloid Interface Sci.* 112, 24–41. doi:10.1016/0021-9797(86)90066-4

Zhao, X., Blunt, M.J., Yao, J., 2010. Pore-scale modeling: Effects of wettability on waterflood oil recovery. *J. Pet. Sci. Eng.* 71, 169–178. doi:10.1016/j.petrol.2010.01.011

Zhou, D., Blunt, M.J., Orr, F., 1997. Hydrocarbon drainage along corners of noncircular capillaries. *J. Colloid Interface Sci.* 187, 11–21. doi:10.1006/jcis.1996.4699

Zhou, Y., 2013. Pore scale modeling of capillary pressure curves in 2D rock images. PhD Thesis, University of Stavanger, Norway.

APPENDIX A

MOSAIC IMAGES OF CARBONATE SAMPLES



Figure A.1 – C013 Mosaic. Black represents epoxy-filled pores and white represents rock matrix.

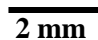
75X  **2 mm**



Figure A.2 – C016 Mosaic. Black represents epoxy-filled pores and white represents rock matrix.

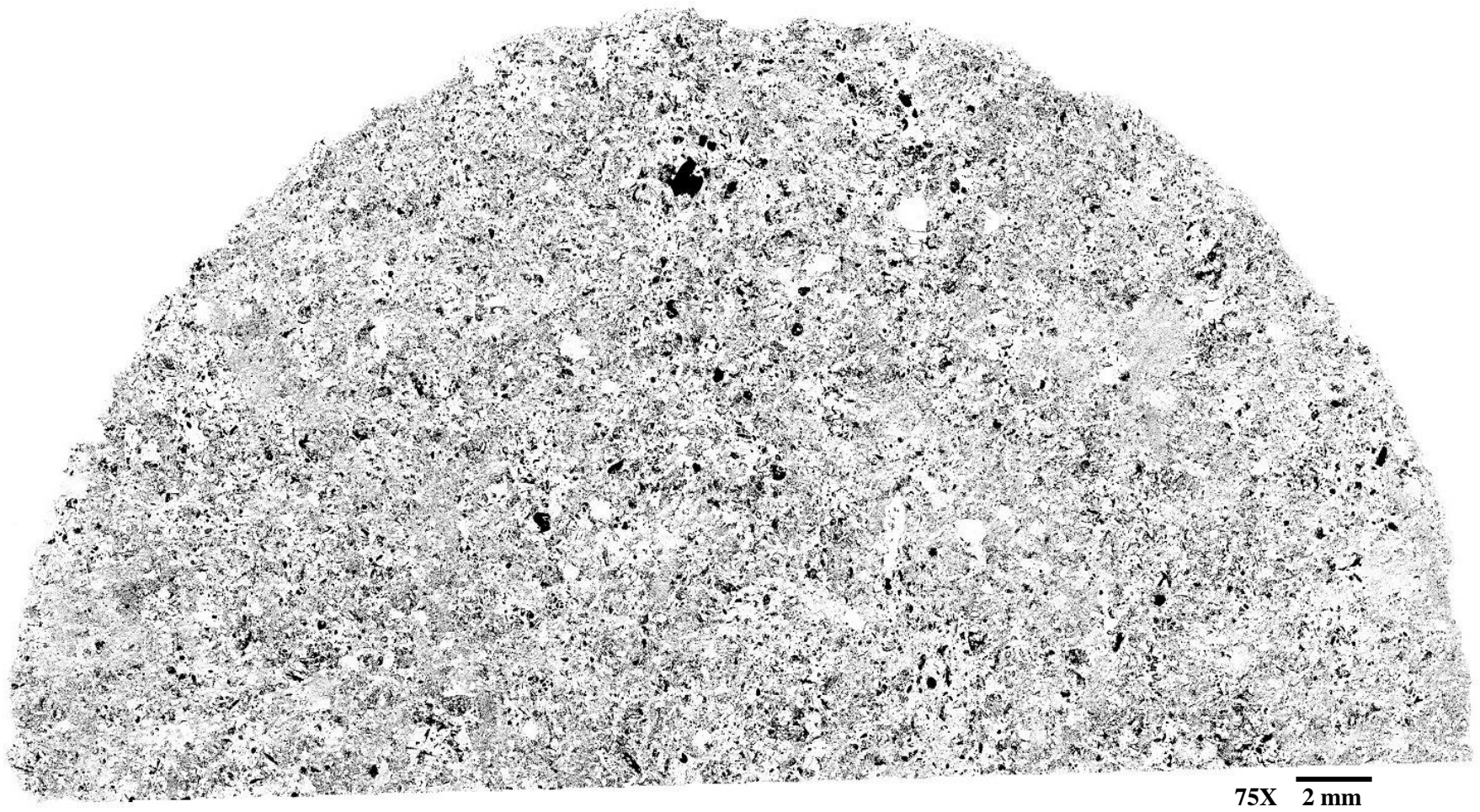
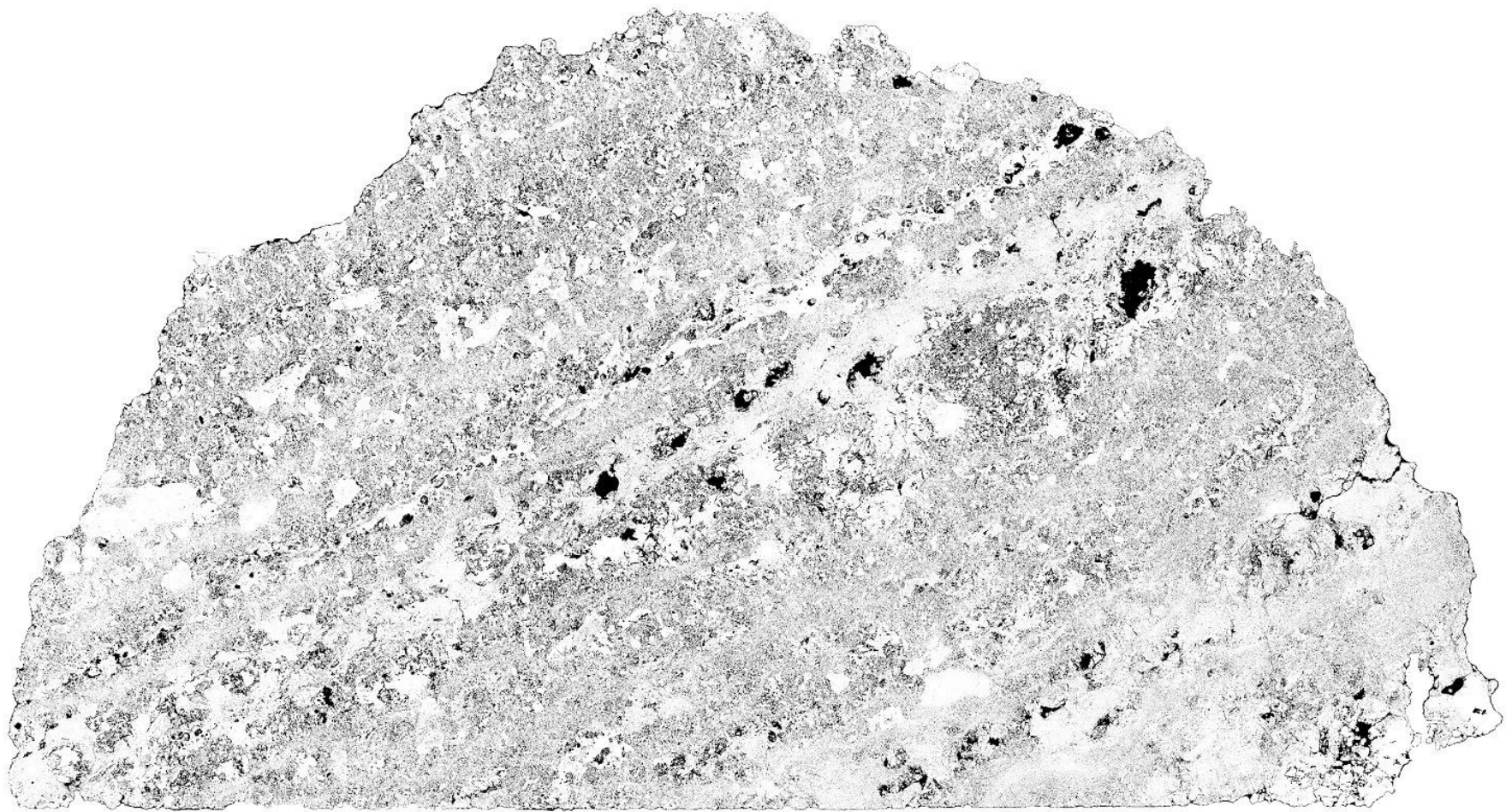


Figure A.3 – C019 Mosaic. Black represents epoxy-filled pores and white represents rock matrix.



75X 2 mm

Figure A.4 – C021 Mosaic. Black represents epoxy-filled pores and white represents rock matrix.

APPENDIX B

ALGORITHMS FOR TWO-PHASE FLOW SIMULATIONS IN THE PORE NETWORKS

B.1 Algorithm of primary drainage simulation

1. The entire network is filled with water. All pore elements (nodes and links) are in the form of Configuration A in **Fig. 5.19**.
2. A constant receding contact angle is assigned to all pore elements in the network.
3. Piston-type threshold capillary pressures P_c^e of all nodes and links in the network are calculated according to MS-P method given in **Section 5.2.1**.
4. Initially, P_c^e of inlet links are gathered in a common stack and rank in increasing order. Oil invasion starts when oil is first introduced into the medium through the largest link (the lowest P_c^e) at the inlet face of the network.
5. Since water is the sole phase present in the network prior to primary drainage simulation, the first relative permeability data is the absolute permeability of the network indeed.

At each of the following steps:

6. P_c^e of all accessible pores in which at least one of the connected pores is oil-filled are added into pressure stack and sorted in ascending order. The one with the minimum P_c^e in the stack is the next node or link to be invaded and the current capillary pressure is raised to its P_c^e . The oil-drained pores are turned into Configuration B in **Fig. 5.19**.

7. The water and oil areas in individual nodes and links in the form of either bulk phase, surface or corner films (valid for water) are evaluated for the current P_c as given in **Section 5.2.4.1**. The overall water saturation is recalculated which is the summation of water volume in individual pores divided by total pore volume.
8. Under a unit pressure gradient, as described in **Section 5.2.4.2**, the conductance of phases in individual pore elements, total flow rate and relative permeabilities of water and oil phases are updated.
9. The process continues in this manner until maximum capillary pressure $P_{c,pd}^{\max}$ where no further invasion is possible in the network.

B.2 Algorithm of secondary imbibition simulation

1. Water invasion starts from $P_{c,pd}^{\max}$ right after primary drainage. In the beginning of the process, oil-drained (Configuration B) and still water-filled (Configuration A) pores are identified (**Fig. 5.19**).
2. The wettability of oil-drained pores changes from water-wet to mixed-wet (from Configuration B to C in **Fig. 5.19**) and water-filled pores remain water-wet (Configuration A in **Fig. 5.19**). Advancing contact angles are randomly distributed to water-wet and mixed-wet pores in their allowed ranges. Due to contact angle hysteresis, advancing angle exceeds receding angle even for the water-wet pores ($\theta_R < \theta_A$). Besides, advancing angle of a water-wet pore ($< 90^\circ$) is always smaller than that of a mixed-wet pore ($\theta_A^{mw} > \theta_A^{ww}$).
3. Maximum advancing angle θ_A^{\max} of each pore element for spontaneous piston-type imbibition is calculated from **Eq. 5.31**.
4. Piston-type P_c^e of nodes for all possible I_k events ($k=1:5$) and of links are computed as described in **Section 5.2.2**. Likewise, snap-off P_c^e of nodes and links are computed.

5. Again, water flooding starts at the inlet boundary of the network. It invades first into the smallest inlet link with the greatest P_c^e .

At each of the following steps:

6. The available nodes and links for piston-type invasion with at least one connected water-filled pore or the pores which are surrounded by only oil-occupied pores but convenient for snap-off displacement satisfying the criteria given in **Eq. 5.49** are ranked in descending order. The next pore element to be imbibed is the one with the maximum P_c^e from the stack list involving all available nodes and links.

7. The critical capillary pressure $P_{c,i}^{crit}$ for oil layer existence is determined from **Eq. 5.43** for each corner of triangular pore elements.

8. After each iteration, oil layer presence in the network is updated for the current P_c . While recently water-invaded mixed-wet pores are checked for oil layer formation, the preexisting oil layer(s) in already water-filled pores are checked whether they collapse with the recent decrease in P_c during forced imbibition or still survive. If oil layer(s) are created in a pore, its configuration changes from Configuration C to F or to G (**Fig. 5.19**). After oil layers rupture, pore configuration is altered from Configuration F or G to E (**Fig. 5.19**).

9. Hinging contact angle of pinned arc menisci in the corners of mixed-wet pores are evaluated for the recent P_c (**Eq. 5.32**).

10. The areas of water phase which may be present in a single pore as corner or bulk phase and oil phase as thin surface films, bulk phase, trapped or intermediate layers are calculated according to **Section 5.2.4.1**. Next, the overall water saturation of the network is determined.

11. The conductances of water and oil phases in individual pore elements in the form of corner or surface films, bulk phase, or intermediate oil layers are computed. Then, the total flow rates and relative permeabilities of water and oil phases are updated.

12. The minimum imposed capillary pressure during imbibition P_c^{\min} is set to be $-P_{c,pd}^{\max}$ when oil remains only in the largest oil-filled pores and as surface films, intermediate layers or trapped droplets in water-occupied mixed-wet pores.

B.3 Algorithm of secondary drainage simulation

- 1.** Oil re-invasion starts from the lowest pressure reached at the end of secondary imbibition, $P_c^{\min} (= -P_{c,pd}^{\max})$.
- 2.** For water-wet pores, the receding angle in secondary drainage is exactly the same as in primary drainage, i.e. $\theta_r^{ww} = \theta_R$. In the mixed-wet pores, the receding angle in secondary drainage is uniformly distributed between its receding angle in primary drainage and advancing angle satisfying the condition of $\theta_R < \theta_r^{mw} < \theta_A$.
- 3.** Prior to secondary drainage (at the end of water flooding), the existence of oil layers in any corners of water-filled, mixed-wet nodes and links is controlled using the conditions of $\theta_A > 90^\circ + \beta_i$ and $P_c^{\min} > P_{c,i}^{crit}$.
- 4.** In the beginning of oil re-invasion, the appropriate configuration of each node and link in the network is identified from **Fig. 5.19**. Mixed-wet water-filled pores with (Configuration F or G) or without oil layers (Configuration E) are distinguished.
- 5.** In the pores with oil layer(s) (Configuration F or G in **Fig. 5.19**), the critical capillary pressure $P_{c,i}^{stab}$ for water layer stability is found from **Eq. 5.61** for each corner i having oil layer.
- 6.** After oil re-invasion, the pore cross-sections may take different versions (**Fig. 5.19**). Configuration E may change to D or H and Configuration G to D or I depending on the relation between θ_r and half-angle of the sharpest corner β_1 . Piston-type P_c^e of nodes and links are calculated using the aforementioned appropriate equations for their configurations in **Section 5.2.3**.

7. Minimum receding angle θ_r^{\min} of nodes and links for spontaneous drainage are found from **Eq. 5.62** or **5.31** depending on whether any oil layer exists in the pore or not.

8. Oil first invades into the largest link with the lowest P_c^e at the inlet face of network.

At each of the following steps:

9. The list of P_c^e of all accessible nodes and links with at least one connected oil-filled pore is revised and ranked in ascending order. The next pore element to be drained is the one with the lowest P_c^e in the list.

10. Water layer presence in oil re-invaded pores (Configuration I in **Fig. 5.19**) is checked stepwise. If $P_c \geq P_c^{stab}$, water layer collapses and pore cross-section turns into Configuration D in **Fig. 5.19**.

11. Hinging contact angle of pinned arc menisci in mixed-wet pore corners are updated for the current P_c (**Eq. 5.51** or **5.56**).

12. The areas of water phase which may be present in a single pore as corner or bulk phase or as intermediate layers and oil phase as bulk phase, thin surface films, trapped oil or as intermediate layers are calculated according to **Section 5.2.4.1**. Next, the overall water saturation of the network is determined.

13. The conductance of water and oil phases in individual pore elements is recalculated. Then, relative permeabilities of water and oil phases based on their total flow rates across the network are updated.

14. During secondary drainage process, the displacement from Configuration E to H is progressively checked for the condition described in **Section 5.2.3** ($L_i > L_{pd,i}$), and in case it is not satisfied, the displacement is revised to be directly from E to C. Likewise, the transition from Configuration G to I where water layers form is checked at each step and if $P_c \geq P_{c,i}^{stab}$, the displacement is altered as from G to C (**Fig. 5.19**).

15. Secondary drainage ends up when all possible pores are drained until the maximum capillary pressure of primary drainage ($P_{c,sd}^{\max} \leq P_{c,pd}^{\max}$) is achieved in the model.

CURRICULUM VITAE

PERSONAL INFORMATION

Surname, Name : Gundogar, S. Asli
Nationality : Turkish (TC)
Date and Place of Birth: 5 March 1985, Corum
Marital Status : Single
Phone : +90 312 210 48 85
Fax : +90 312 210 28 95
Email : e134077@metu.edu.tr
aslimgun@gmail.com

EDUCATION

Degree	Institution	Year of Graduation
MS	METU Petroleum and Nat. Gas Engineering	2010
BS	METU Petroleum and Nat. Gas Engineering	2007
High School	Eti Anadolu High School, Corum	2002

WORK EXPERIENCE

Year	Place	Enrollment
2014–2015	Stanford University SUPRI-A Res. Group	Visiting Research Student
2007–2014	METU Petroleum and Nat. Gas Engineering	Research Assistant
2006-2007	METU Petroleum and Nat. Gas Engineering	Student Assistant
2006 July	N.V.Turkse Perenco /Ankara	Intern Eng. Student
2005 August	TPAO / Adiyaman	Intern Eng. Student

FOREIGN LANGUAGES

Advanced English, Basic Spanish

PUBLICATIONS

1. Gundogar, A.S., Ross, C.M., Akin, S., Kovscek, A.R., 2016. Multiscale pore structure characterization of Middle East carbonates. J. Pet. Sci. Eng. 146, 570–583.
doi:10.1016/j.petrol.2016.07.018

2. Gundogar, A.S., Kok, M.V., 2014. Thermal characterization, combustion and kinetics of different origin crude oils. *Fuel* 123, 59–65. doi:10.1016/j.fuel.2014.01.058
3. Kok, M.V., Gundogar, A.S., 2013. DSC study on combustion and pyrolysis behaviors of Turkish crude oils. *Fuel Process. Technol.* 116, 110–115. doi:10.1016/j.fuproc.2013.05.001
4. Kok, M. V., Gundogar, A.S., 2010. Effect of different clay concentrations on crude oil combustion kinetics by thermogravimetry. *J. Therm. Anal. Calorim.* 99, 779–783. doi:10.1007/s10973-009-0377-9

HONORS & AWARDS

2014–2015 The Scientific and Technological Research Council of Turkey (TUBITAK) International Research Fellowship Programme (2214-A)

2010–2014 The Scientific and Technological Research Council of Turkey (TUBITAK) National Scholarship Programme for PhD Students (2211-A)

2007–2009 The Scientific and Technological Research Council of Turkey (TUBITAK) National Scholarship Programme for MSc Students (2210-A)

2010 August IEA Greenhouse Gas R&D Program International Interdisciplinary CCS Summer School held at Loneyarbyen, Svalbard, Norway. All costs covered by the organization (The Gas Tech. Centre NTNU-SINTEF, BIGCCS and SUCCESS)

2009–2010 Academic Year Graduate Courses Performance Award (Grad. School of Natural and Appl. Sciences, METU)

HOBBIES

Literature, Argentine tango, analog photography, trekking.